NATIONAL TECHNICAL UNIVERSITY OF ATHENS
SCHOOL OF CHEMICAL ENGINEERING
MATERIALS SCIENCE & ENGINEERING DEPARTMENT

PhD Dissertation

Quantitative Analysis and Defect Assessment Using Infrared Thermographic Approaches

PANAGIOTIS I. THEODORAKEAS
CHEMICAL ENGINEER

SUPERVISOR:
MARIA KOUI, PROFESSOR NTUA

ATHENS 2013

Advisory Committee

- Koui Maria, Professor NTUA (Supervisor)
- Maldague Xavier, Professor Université Laval
- Yfantis Dimitrios, Professor NTUA

PhD Dissertation Committee

- Yfantis Dimitrios, Professor NTUA
- Maldague Xavier, Professor Université Laval
- Batis Giorgos, Professor NTUA
- Dimotikali Dimitra, Professor NTUA
- Karagianni Stefania-Haido, Professor NTUA
- Koui Maria, Professor NTUA
- Karantonis Antonis, Lecturer NTUA

Every progress, every creation
is the organisation of new conditions of change.

Guy Debord

PREFACE

The present dissertation was conducted in the Materials Science and Engineering Department of Chemical Engineering School in NTUA in collaboration with the Computer Vision and Systems Laboratory (CVSL) of Electrical and Computer Engineering Department in Université Laval. In this point, I would like to thank everyone who contributed for the implementation of this work.

First of all, I would like to express my grateful thanks to Prof. Maria Koui who, along with the supervision of the present dissertation, she trusted me as her colleague all these years of our coexistence in NTUA. I highly value the opportunity to work with her in a professional and demanding, but at the same time friendly atmosphere, and I will always be thankful for her continuing guidance, mentorship and encouragement, which were expended beyond our common scientific activities. Her concerns regarding new scientific perspectives, her methodology to approach issues regardless their difficulty gradient, and her selflessness to provide any information and advice, are some of her characteristics which strongly influenced me and acted as the driving force for the implementation of this dissertation.

Additionally, I would like to express my special appreciation and thanks to Prof. Xavier Maldague, co-supervisor of this thesis and member of the advisory committee. The simplicity in his ordinary life completely contrasts his research activities and innovations, indicating the actual role of a professor. Despite the fact that the distance between the two laboratories was long enough embedding me to spend more time testing under his guidance, through his published work and the published work of his research team, he was a valuable advisor all these years of testing and brainstorming, helping me to solve all the raised problems and difficulties.

Furthermore, I would like to thank Prof. Dimitrios Yfantis, who as a member of the advisory committee was always willing to consult and advise me in order to overcome problems. I really appreciate the thorough discussions that we had during the implementation of this research, giving me a different dimension in the general topic of research and the way that this shall be approached.

Moreover, I would like to thank the members of the PhD Dissertation Committee Prof. Giorgos Batis, Prof. Stefania-Haido Karagianni, Prof. Dimitra Dimotikali and Lec. Antonis Karantonis, all educational personnel in the School of Chemical Engineering of NTUA, for the study of my dissertation and the important comments that they provided me in order to improve the scientific subject of this document.

As the following pages demonstrate, the energy source and the stimulation manner are of fundamental importance in order to achieve the best possible results from an active testing scenario. So in this point, I would like to specially thank the excitation sources of this dissertation, Dr. Nico Avdelidis, Engineer NTUA, and Dr. Clemente Ibarra-Castanedo, Post Doctoral Researcher in CVSL Laboratory of Université Laval. Nico is one of the basic contributors for the implementation of this thesis and without his valuable information and advices, this work would not have been conducted. Additionally, our common involvement to other research activities beyond the infrared, produced a collaborative relation

and a friendship which based on the know how experience that Nico has and the common will power was able to overcome several problems and produce solutions. On the other hand, Clemente was always willing to share any information and advice, while he also actively supported the experimental phase of this dissertation thesis. As a result, he can be considered not only figuratively but literally as well, as the excitation source of this thesis. Similarly to Prof. Maldague, his published research work was a valuable advisor for this dissertation, and helped me in solving several uncertainties, created during its implementation.

Special thanks are also attributed to my colleague and mainly friend Dr. Eleni Cheilakou. I have to mention that a promise written at the respective preface of her dissertation was kept more than the expected. Apologies if I put her in further troubles but as a Latin dictum says "*scripta manent*". Nevertheless I promise that in the very near future, I will reinstate these balances and I hope that we will continue our pleasant and creative collaboration. Additionally, I would also like to thank Dr. Vasiliki Dritsa for her continuous interest regarding the progress of my dissertation and the valuable information that she was always providing me, as a PhD holder.

Finally, I would like to express my thanks to my friend and colleague Dr. Stefano Sfarra, member of the Las.E.R. Laboratory of University of L'Aquila for the creative and pleasant research collaboration that we had during all these years, testing -always non destructively- different cultural heritage items. As the Cultural Heritage of both Greece and Italy are large enough, I hope that this collaboration will be continued, producing interesting research activities and testing methodologies.

Last but not least, I would like to profoundly thank my parents Giannis and Maria and my sister Chrysa for their support not only through these years, but always when I asked for their help. Special thanks are also attributed to Antonia, as she depressed the dynamic nature of her character in order to produce the calmness conditions for the difficult and demanding stage of my dissertation writing.

ABSTRACT

The subject matter of the present dissertation is the study of different active thermographic approaches, evaluating their effectiveness and reliability to operate as stand-alone inspection techniques, producing a complete characterisation of the test-piece in terms of qualitative and quantitative assessment. The motivation of this research is the fact that thermal imaging still has the potential of further development, as the quantitative assessment under thermographic investigations is a relatively recent advancement.

For the implementation of an active thermographic inspection, the test object is excited through the aid of an external energy source and the spatial- temporal variations on the surface temperature distribution are sequentially recorded through the aid of an infrared camera. Thermographic analysis is based on the identification of thermal contrasts on the investigated surface, while the produced detectability can be further enhanced by the subsequent elaboration of the acquired signal. To evaluate defects or generally detected features of interest, image processing algorithms have to be applied. These processing techniques are considered essential to handle thermographic data as they produce an enhanced visibility of the detected features, compensating a series of negative factors that affect the manipulation of raw temperature data, while the proper interpretation of the processed results can additionally provide quantitative information regarding the detected features. Alternatively, quantification can be performed through the jointly conduction of numerical and experimental studies, aiming to correlate the information acquired from both procedures and produce a quantitative evaluation.

Based on the aforesaid, the present dissertation focused on the study of different active thermographic approaches evaluating their effectiveness and reliability to initially operate as stand-alone inspection techniques and secondly -but also important- to produce a complete characterisation of the test-piece in terms of qualitative and quantitative assessment. More specifically in this research work, initially laminated Carbon Fibre Reinforced composites (CFRPs) were investigated by means of Pulsed Thermography (PT) aiming to the acquisition of qualitative (internal defects identification) and quantitative information (depth of the internal defects), while the second case study evaluated the performance of Cooling Down Thermography (CDT) to reveal the presence of hidden mosaic artefacts beneath a covering intervention procedure and provide information regarding the mosaic location, thickness and thermal properties. The selection of the testing configuration in each of the above inspection problems was conducted taking into consideration that every material response differently to the application of a heat flux and this response is related to its thermal properties. In other words, the proper inspection method was chosen to provide the best possible results, taking into account the thermal properties of the investigated material and how these interact on a heating stimulation of a specific duration and energy deposition. Finally, the quantification procedures used to acquire the

required information were based on exclusively experimental data in the former case (PT) by determining the peak slope time and the blind frequency respectively, while quantification in the latter case (CDT) was performed through the simultaneous conduction of numerical and experimental studies and the correlation of the produced results in a three steps methodology.

The present dissertation is focusing on the study of the two quantification methods stated above, evaluating the produced accuracy regarding informative parameters such us the depth of a feature, the thickness of a feature and its indirect characterisation through the estimation of its thermal properties. The general conclusion of this study is that active thermal imaging can be successfully applied for the structural integrity assessment of different materials and structures, acting as a useful tool able to provide a sufficient internal detectability and/or quantitative estimations.

ΕΚΤΕΝΗΣ ΠΕΡΙΛΗΨΗ

Το αντικείμενο της παρούσας διδακτορικής διατριβής αφορά στη διερεύνηση της αποτελεσματικότητας και της αξιοπιστίας διαφορετικών προσεγγίσεων ενεργητικού θερμογραφικού ελέγχου για τη λήψη αποτελεσμάτων σε σχέση με τον ποιοτικό έλεγχο υποεπιφανειακών περιοχών ενδιαφέροντος και την ανάκτηση πληροφοριών για τον ποσοτικό χαρακτηρισμό τους.

Τα τελευταία χρόνια, η εφαρμογή τεχνικών Μη Καταστρεπτικού Ελέγχου (ΜΚΕ) είναι ευρέως διαδεδομένη σε πολλούς τομείς των μηχανικών επιστημών όπως σε περιπτώσεις ελέγχου κτιριακών εγκαταστάσεων, στην εξέταση βιομηχανικών εγκαταστάσεων και γενικότερα μηχανολογικού και ηλεκτρολογικού εξοπλισμού, στην εξέταση της υπάρχουσας κατάστασης αλλά και των επεμβάσεων συντήρησης σε πολιτισμικά έργα, στον έλεγχο των αστοχιών στα υλικά των αεροσκαφών, κλπ. Κύριος παράγοντας για την διάδοση και την εδραίωση αυτών των τεχνικών ελέγχου, είναι το βασικό πλεονέκτημα τους να επιτρέπουν την εξέταση της φυσικής κατάστασης ενός αντικειμένου, χωρίς να επηρεάζεται η μελλοντική χρησιμότητά του. Με άλλα λόγια, ο γενικός όρος του "Μη Καταστρεπτικού Ελέγχου" αναφέρεται στην εφαρμογή τεχνολογιών, οι οποίες χωρίς να τροποποιούν την κατάσταση του υπό εξέταση στόχου, μπορούν ταυτοχρόνως να καθορίσουν την απουσία ή παρουσία συνθηκών ή/και ασυνεχειών, οι οποίες έχουν επίδραση στην λειτουργικότητά του.

Ανάμεσα στις τεχνικές αυτές, ο θερμογραφικός μη καταστρεπτικός έλεγχος –συχνά αποκαλούμενος και ως Υπέρυθρη Θερμογραφία- είναι ένας γρήγορα εξελισσόμενος τομέας τόσο σε επιστημονικό όσο και σε πρακτικό επίπεδο αφού βρίσκει εφαρμογή σε ένα μεγάλο εύρος επιθεωρήσεων. Η αρχή της Θερμογραφίας Υπερύθρου βασίζεται στην καταγραφή της υπέρυθρης ακτινοβολίας που εκπέμπεται από την επιφάνεια ενός σώματος, η ανάλυση της οποίας μπορεί να παρέχει πληροφορίες για τον εντοπισμό επιφανειακών ή/και υποεπιφανειακών "*θερμικών ανομοιογενειών*", οδηγώντας ταυτόχρονα στην ανάκτηση πληροφοριών για την εσωτερική κατάσταση του υπό εξέταση υλικού. Κατά τα πρώτα χρόνια εφαρμογής της, η θερμογραφία υπερύθρου χρησιμοποιούνταν αποκλειστικά ως μια συμπληρωματική μέθοδος υποστήριξης ευρέως χρησιμοποιούμενων ΜΚΕ τεχνικών, όπως η υπερηχοσκόπηση και η ραδιογραφία, αφού θεωρούνταν ως μια τεχνική η οποία μπορεί να παρέχει χαμηλής ανάλυσης ποιοτικά αποτελέσματα. Επιπρόσθετα, ένας λόγος που περιόριζε τις δυνατότητες της θερμογραφίας ήταν η έλλειψη εξειδικευμένων τεχνικών επεξεργασίας θερμογραφικών δεδομένων για την ανάλυση του ανακτώμενου σήματος. Ωστόσο, χάρη στις πρόσφατες εξελίξεις στην τεχνολογία κατασκευής θερμικών καμερών και την ανάπτυξη τεχνικών επεξεργασίας θερμογραφικού σήματος, η παγκόσμια ερευνητική κοινότητα έχει εστιάσει το ενδιαφέρον της στην εξέλιξη της τεχνικής αυτής για την αυτόνομη εφαρμογή της σε πολλές περιπτώσεις επιθεωρήσεων και ελέγχου.

Η εκτέλεση ενός θερμογραφικού ελέγχου μπορεί να περιγραφεί από τα ακόλουθα βασικά βήματα: το υπό εξέταση σώμα διεγείρεται θερμικά με τη χρήση μιας εξωτερικής πηγής ενέργειας (ενεργητική προσέγγιση) και κατά τη διάχυση της θερμότητας στο εσωτερικό του, η θερμοκρασιακή κατανομή

στην επιφάνεια του και η μεταβολή της στο χρόνο, καταγράφονται μέσω μιας θερμικής κάμερας. Η καταγραφή αυτή μπορεί να αποτυπωθεί και να οπτικοποιηθεί σε ένα μόνιτορ, ενώ η ερμηνεία και η ανάλυση των αποτελεσμάτων βασίζεται στον εντοπισμό θερμοκρασιακών διαφορών στην υπό εξέταση επιφάνεια, οι οποίες αποδίδονται στην παρουσία "*θερμικών ανομοιογενειών*" στο εσωτερικό του υλικού επηρεάζοντας τον ρυθμό διάχυσης της θερμότητας στις συγκεκριμένες περιοχές. Πρόσφατες εξελίξεις στην ανάλυση θερμογραφικών δεδομένων, επιτρέπουν την παρακολούθηση του φαινομένου αυτού, μελετώντας διαφορετικές πληροφοριακές παραμέτρους από αυτή της μεταβολής της επιφανειακής θερμοκρασίας (π.χ. πρώτη χρονική και δεύτερη χρονική παράγωγος της μεταβολής της θερμοκρασίας, φάση του ανακλώμενου από την επιφάνεια θερμικού κύματος κ.α.) παρέχοντας ενισχυμένη ευαισθησία ανίχνευσης. Το τελευταίο βήμα προκειμένου να ολοκληρωθεί η παραπάνω διαδικασία ελέγχου είναι η ανάκτηση ποσοτικών πληροφοριών κυρίως για τη θέση (βάθος), τις πλευρικές διαστάσεις και τις θερμικές ιδιότητες των ανιχνεύσιμων "*θερμικών ανομοιογενειών*". Βέβαια, παρόλο που οι βασικές αρχές της θερμογραφίας υπερύθρου είναι εκτενώς τεκμηριωμένες στην βιβλιογραφία, η μελέτη για την εφαρμογή της τεχνικής αυτής με στόχο τον ποσοτικό χαρακτηρισμό του υπό εξέταση αντικειμένου είναι περιορισμένη. Πιο συγκεκριμένα, μέχρι πρόσφατα η τεχνική της θερμογραφίας υπερύθρου επέτρεπε τον εντοπισμό και την οπτικοποίηση εσωτερικών φθορών και ατελειών αλλά περιορισμένες ποσοτικές πληροφορίες μπορούσαν να ανακτηθούν με την παραπάνω διαδικασία.

Βάσει της παραπάνω περιγραφής, το κίνητρο για την εκπόνηση της συγκεκριμένης ερευνητικής μελέτης, είναι ότι ο θερμογραφικός έλεγχος εξακολουθεί να έχει τη δυνατότητα περαιτέρω εξέλιξης, προκειμένου να ανταποκριθεί στις απαιτήσεις των άλλων ΜΚΕ τεχνικών που χρησιμοποιούνται συνήθως σε επιτόπου επιθεωρήσεις. Ως εκ τούτου σκοπός της παρούσας διδακτορικής διατριβής είναι η μελέτη δύο διαφορετικών ενεργητικών θερμογραφικών τεχνικών, διερευνώντας την αποτελεσματικότητα και την αξιοπιστία τους ως αυτόνομες τεχνικές ελέγχου, οι οποίες να μπορούν να παρέχουν έναν ολοκληρωμένο χαρακτηρισμό του υπό εξέταση αντικειμένου μέσω της ποιοτικής και ποσοτικής αποτίμησης του. Συγκεκριμένα, πολύστρωτα σύνθετα υλικά ενισχυμένα με ανθρακονήματα (CFRPs), εξετάστηκαν με την τεχνική της Παλμικής Θερμογραφίας (Pulsed Thermography) για τη λήψη ποιοτικών πληροφοριών (ανίχνευση εσωτερικών φθορών) και ποσοτικών πληροφοριών (βάθος εσωτερικών φθορών) αντίστοιχα. Στη συνέχεια ο ενεργητικός θερμογραφικός έλεγχος εφαρμόστηκε με την τεχνική της σταδιακής πτώσης της θερμοκρασίας (Cooling-Down Thermography) για την ανίχνευση επικαλυμμένων με επίχρισμα ψηφιδωτών και την ανάκτηση ποσοτικών πληροφοριών όσον αφορά τη θέση της ψηφοθετημένης επιφάνειας (πάχος κάλυψης), το πάχος του στρώματος των ψηφίδων και τον έμμεσο χαρακτηρισμό του υλικού κατασκευής αυτών, μέσω της εκτίμησης των θερμικών ιδιοτήτων τους. Η επιλογή των παραπάνω ενεργητικών τεχνικών εξέτασης πραγματοποιήθηκε λαμβάνοντας υπόψη ότι κάθε υλικό ανταποκρίνεται διαφορετικά στην εφαρμογή ενός θερμικού παλμού ανάλογα με τις θερμικές ιδιότητές του. Έτσι, η κατάλληλη θερμογραφική τεχνική επιλέχθηκε για να προσεγγίσει το αντίστοιχο πρόβλημα ελέγχου, ανάλογα με τον τρόπο ανταπόκρισης του υπό εξέταση υλικού σε μια διαδικασία θερμικής διέγερσης προκαθορισμένης

χρονικής διάρκειας και έντασης αλλά και ανάλογα με το βάθος ανίχνευσης. Η Παλμική Θερμογραφία επιλέχθηκε, αφού είναι η πιο ευρέως διαδεδομένη τεχνική θερμογραφικού ελέγχου λόγω των χαρακτηριστικών πλεονεκτημάτων της γρήγορης και εύκολης εφαρμογής της. Από την άλλη πλευρά, ο ενεργητικός θερμογραφικός έλεγχος με την τεχνική της σταδιακής πτώσης της θερμοκρασίας έχει ως κύρια χαρακτηριστικά την εφαρμογή ενός θερμικού παλμού μεγάλης διάρκειας ενώ παράλληλα απαιτούνται μεγάλοι χρόνοι παρακολούθησης της σταδιακής ψύξης της υπό εξέτασης επιφάνειας. Αρχικά αυτά τα δυο χαρακτηριστικά μπορεί να εκτιμηθούν ως μειονεκτήματα της μεθόδου, αλλά η τεχνική αυτή χρησιμοποιείται σε περιπτώσεις ενδιαφέροντος πολιτικού μηχανικού, που απαιτείται μια αποτελεσματική διαδικασία θέρμανσης και καταγραφής λόγω των μη ικανοποιητικών ως προς τη διάχυση της θερμότητας ιδιοτήτων που χαρακτηρίζουν τα δομικά υλικά και λόγω της ανίχνευσης σε βάθος που συνήθως απαιτείται σε τέτοιες εφαρμογές. Τέλος, η ποσοτική προσέγγιση πραγματοποιήθηκε μέσω αποκλειστικά πειραματικών αποτελεσμάτων στην πρώτη περίπτωση, ενώ η ανάκτηση ποσοτικών πληροφοριών στην δεύτερη περίπτωση περιελάμβανε την παράλληλη διεξαγωγή υπολογιστικών και πειραματικών διερευνήσεων, με στόχο τη συσχέτιση των ανακτώμενων αποτελεσμάτων μέσω μια μεθοδολογίας τριών βημάτων.

Όπως αναφέρθηκε και παραπάνω, ο κύριος στόχος της μελέτης αυτής ήταν η αποτίμηση της αξιοπιστίας διαφορετικών τεχνικών ενεργητικού θερμογραφικού ελέγχου έτσι ώστε να ενισχυθούν οι δυνατότητες τους μέσω της εκτέλεσης του όχι και τόσο καλά τεκμηριωμένου βήματος της ποσοτικής προσέγγισης. Όσον αφορά την εφαρμογή της παλμικής θερμογραφίας για την εξέταση σύνθετων υλικών, σκοπός ήταν η διερεύνηση της αξιοπιστίας της τεχνικής αυτής για την ποιοτική (εντοπισμός) και ποσοτική αποτίμηση της φθοράς από την παρακολούθηση πληροφοριακών παραμέτρων προερχόμενες αποκλειστικά από πειραματικές μετρήσεις, η εφαρμογή των οποίων σε αναλυτικές μαθηματικές σχέσεις μπορούσε να παρέχει ποσοτικές εκτιμήσεις. Προκειμένου να πραγματοποιηθεί η παραπάνω διερεύνηση, αρχικά καθορίστηκαν μια σειρά συγκεκριμένων βημάτων-στόχων, που είναι τα εξής:

- *Καθορισμός των περιορισμών και δυνατοτήτων της Παλμικής Θερμογραφίας για την ανάκτηση ποιοτικών πληροφοριών κατά την εξέταση σύνθετων υλικών ενισχυμένα με ανθρακονήματα.*

Προκειμένου να επιτευχθεί αυτός ο στόχος, η ανιχνευσιμότητα της φθοράς αποτιμήθηκε μετά την εφαρμογή εξελιγμένων τεχνικών επεξεργασίας θερμογραφικών δεδομένων για τη διαχείριση του ανακτώμενου σήματος. Η αποτελεσματικότητα των τεχνικών αυτών διερευνήθηκε μέσω οπτικών παρατηρήσεων από τις ακατέργαστες και επεξεργασμένες ακολουθίες θερμογραφικών εικόνων και μέσω υπολογισμών της αναλογίας σήματος-θορύβου (Signal-to-Noise ratio). Η παραπάνω επιμέρους διερεύνηση οδήγησε στον καθορισμό των δυνατοτήτων και των περιορισμών των τεχνικών επεξεργασίας θερμογραφικού σήματος, ενώ η αποτελεσματική εφαρμογή τους σε παλμικές θερμογραφικές επιθεωρήσεις σύνθετων υλικών αποτιμήθηκε ως συνάρτηση του βάθους

ανίχνευσης, των πλευρικών διαστάσεων της ανιχνεύσιμης αστοχίας και της επιφανειακής γεωμετρίας του υπό εξέτασης αντικειμένου.

- *Καθορισμός των περιορισμών και δυνατοτήτων της Παλμικής Θερμογραφίας για την ανάκτηση ποσοτικών πληροφοριών κατά την εξέταση σύνθετων υλικών ενισχυμένα με ανθρακονήματα.*

Προκειμένου να επιτευχτεί αυτός ο στόχος, δύο διαφορετικές μέθοδοι ποσοτικοποίησης εξετάστηκαν μελετώντας τη λήψη αποτελεσμάτων από ένα εύρος βαθών στα οποία προσομοιωμένες αποκολλήσεις είχαν τοποθετηθεί στα υπό εξέταση σύνθετα δείγματα. Η πρώτη τεχνική ποσοτικοποίησης βασίστηκε στην λήψη πληροφοριών από μη επεξεργασμένα θερμοκρασιακά δεδομένα, ενώ η δεύτερη τεχνική χρησιμοποίησε πληροφορίες μετά την εφαρμογή εξελιγμένων τεχνικών επεξεργασίας θερμογραφικών δεδομένων και πιο συγκεκριμένα μετά την ανάλυση μέσω της Παλμικής Θερμογραφίας Φάσης (Pulsed Phase Thermography). Η αποτίμηση των αποτελεσμάτων βάθους από τις παραπάνω μεθόδους, έγινε λαμβάνοντας υπόψη το σφάλμα πρόβλεψης, ενώ η απόκλιση του καταγράφηκε σε σχέση με το πραγματικό βάθος αξιολογήθηκε λαμβάνοντας υπόψη τις προδιαγραφές των υπό εξέταση δειγμάτων, τις πειραματικές παραμέτρους κάτω από τις οποίες διεξήχθη η έρευνα όπως επίσης και τις παραμέτρους που επιλέχθηκαν για την ανάλυση των πειραματικών δεδομένων. Η παραπάνω επιμέρους μελέτη οδήγησε στον καθορισμό των καταλλήλων παραμέτρων πειραματικής εκτέλεσης και επεξεργασίας, προκειμένου να επιτευχθεί η ακριβέστερη εκτίμηση βάθους.

Όσον αφορά την εφαρμογή ενεργητικού θερμογραφικού ελέγχου με την τεχνική της σταδιακής πτώσης της θερμοκρασίας για την αποκάλυψη επικαλυμμένων ψηφιδωτών, ο βασικός στόχος ήταν η διερεύνηση συσχέτισης αποτελεσμάτων μοντελοποίησης και πειραματικής εξέτασης, καθιστώντας ικανό τον ποσοτικό χαρακτηρισμό των επικαλυμμένων ψηφοθετημένων επιφανειών. Προκειμένου να πραγματοποιηθεί η παραπάνω μελέτη, αρχικά καθορίστηκαν μια σειρά συγκεκριμένων βημάτων-στόχων, και είναι τα εξής:

- *Θεωρητική αποτίμηση του ενεργητικού θερμογραφικού ελέγχου με την τεχνική της σταδιακής πτώσης της θερμοκρασίας σε σχέση με το συγκεκριμένο πρόβλημα ελέγχου.*

Προκειμένου να επιτευχθεί αυτός ο στόχος, χρησιμοποιήθηκε ένα υπολογιστικό πρόγραμμα προσομοιώσεων για την περιγραφή του πραγματικού προβλήματος ελέγχου. Μέσω διαφορετικών μοντελοποιήσεων, διερευνήθηκε η ακρίβεια της περιγραφής των φαινομένων διάχυσης της θερμότητας διαμέσου των διαφορετικών διαστρωματώσεων του επικαλυμμένου ψηφιδωτού, όταν αυτό υπόκειται σε ένα θερμικό παλμό μεγάλης διάρκειας. Επιπρόσθετα, υπολογιστικές μελέτες πραγματοποιηθήκαν για την διερεύνηση της επίδρασης της διαφοροποίησης συγκεκριμένων χαρακτηριστικών όπως το πάχος της επικάλυψης, το πάχος του ψηφοθετημένου στρώματος και οι θερμικές ιδιότητες του επικαλυμμένου ψηφιδωτού στη διάχυση της θερμότητας. Η μελέτη αυτή έγινε παρακολουθώντας πληροφοριακά χαρακτηριστικά όπως ο χρόνος εμφάνισης της μέγιστης

επιφανειακής θερμοκρασιακής διαφοράς μεταξύ μιας περιοχής με και χωρίς ψηφοθετημένο υπόστρωμα. Η παραπάνω επιμέρους διερεύνηση οδήγησε στην κατανόηση της θερμικής συμπεριφοράς επικαλυμμένων ψηφιδωτών και στην συσχέτιση της (μέσω της παρακολούθησης του χρόνου μέγιστης θερμοκρασιακής διαφοράς) ως συνάρτηση των χαρακτηριστικών του υπό εξέταση ψηφιδωτού (πάχος κάλυψης, πάχος στρώματος ψηφίδων, θερμικές ιδιότητες ψηφίδων).

- *Πειραματική διερεύνηση για την αποτελεσματικότητα του ενεργητικού θερμογραφικού ελέγχου με την τεχνική της σταδιακής πτώσης της θερμοκρασίας για την αποκάλυψη υποεπιφανειακών ψηφοθετημένων στρωμάτων σε ένα περιβάλλον επικάλυψης.*

Προκειμένου να επιτευχθεί αυτός ο στόχος και βάση των αποτελεσμάτων που προέκυψαν από τις προσομοιώσεις, πραγματοποιήθηκαν πειραματικές μετρήσεις για την αξιολόγηση την ανιχνευσιμότητας των επικαλυμμένων ψηφίδων. Η μελέτη αυτή έγινε καταγράφοντας το φαινόμενο σταδιακής ψύξης από την επιφάνεια του καλυμμένου ψηφιδωτού και από την επιφάνεια μιας περιοχής αναφοράς (χωρίς ψηφοθετημένο υπόστρωμα), αντίστοιχα. Η παραπάνω επιμέρους μελέτη οδήγησε στην κατανόηση της θερμικής συμπεριφοράς των επικαλυμμένων ψηφιδωτών μετά από μια διαδικασία θερμικής διέγερσης και τη συσχέτιση της θερμικής ανταπόκρισης αυτών με τις διαφορετικές διαστρωματώσεις από τις οποίες αποτελούνταν.

- *Ανάπτυξη μιας διαδικασίας ποσοτικής προσέγγισης, καθιστώντας ικανό τον ποσοτικό χαρακτηρισμό επικαλυμμένων ψηφιδωτών.*

Μετά την αποκάλυψη των υποεπιφανειακών ψηφιδωτών στρωμάτων, ποσοτικές πληροφορίες σε σχέση με την θέση, το πάχος και τις θερμικές ιδιότητες του ψηφιδωτού, ανακτήθηκαν συσχετίζοντας πειραματικά αποτελέσματα και αποτελέσματα μοντελοποίησης. Συγκεκριμένα, δημιουργώντας το αντίστοιχο πρόβλημα αντιστροφής (Inverse Problem), ήταν δυνατή η παρακολούθηση των διαφοροποιήσεων της πληροφοριακής παραμέτρου (χρόνος μέγιστης θερμοκρασιακής διαφοράς) ως συνάρτηση του υπό διερεύνηση παράγοντα (πάχος κάλυψης, πάχος ψηφίδων και θερμικές ιδιότητες ψηφίδων). Η επιμέρους μελέτη οδήγησε στον ποσοτικό χαρακτηρισμό των επικαλυμμένων ψηφιδωτών.

Βάσει της παραπάνω περιγραφής, η παρούσα διδακτορική διατριβή έχει οργανωθεί σε 7 κεφάλαια.

Το πρώτο κεφάλαιο, παρουσιάζει την υπάρχουσα κατάσταση όσον αφορά την εφαρμογή της Θερμογραφίας Υπερύθρου ως τεχνική Μη Καταστρεπτικού Ελέγχου, ενώ παρουσιάζονται αναλυτικά το κίνητρο για την εκπόνηση της παρούσας διδακτορικής διατριβής και οριοθετούνται οι στόχοι της. Τέλος το εισαγωγικό αυτό κεφάλαιο κλείνει με μια σύντομη περιγραφή της δομής της εργασίας.

Στο δεύτερο κεφάλαιο, γίνεται μια εισαγωγή στις θεμελιώδεις αρχές της Θερμογραφίας Υπερύθρου. Συγκεκριμένα, πραγματοποιείται μια επισκόπηση στις βασικές αρχές της υπέρυθρης ακτινοβολίας, στις φασματικές ιδιότητες τόσο του μέλανος σώματος όσο και των γκρίζων σωμάτων, ενώ παρουσιάζονται και οι βασικοί τρόποι μετάδοσης της θερμότητας και οι θερμοφυσικές ιδιότητες που πρέπει να

λαμβάνονται υπόψη για την ερμηνεία των αποτελεσμάτων κατά τη θερμογραφική εξέταση των υλικών. Εν συνεχεία ακολουθεί μια σύντομη περιγραφή των δύο βασικών τεχνικών θερμογραφικού ελέγχου, αυτής της παθητικής και της ενεργητικής προσέγγισης αντίστοιχα, εστιάζοντας στις βασικές αρχές εκτέλεσής τους, τα βασικά πλεονεκτήματα-περιορισμούς και συνήθεις εφαρμογές στην εξέταση υλικών και κατασκευών. Τέλος, το κεφάλαιο αυτό κλείνει με την σύντομη παρουσίαση κάποιων σημαντικών πρακτικών παραγόντων που πρέπει να λαμβάνονται υπόψη και να αξιολογούνται πριν την εκτέλεση ενός θερμογραφικού ελέγχου.

Το **τρίτο κεφάλαιο** εστιάζει στο θέμα της ενεργητικής θερμογραφίας υπερύθρου, η οποία είναι η κατηγορία από την οποία επιλέχθηκαν οι κατάλληλες προσεγγίσεις για την εκτέλεση της παρούσας ερευνητικής μελέτης. Συγκεκριμένα, παρουσιάζονται οι θεωρητικές αρχές και η πειραματική διαδικασία των πιο διαδεδομένων ενεργητικών θερμογραφικών τεχνικών, ενώ παράλληλα γίνεται και μια βιβλιογραφική ανασκόπηση στις εφαρμογές της κάθε μεθόδου στον τομέα των μη καταστρεπτικών ελέγχων. Αρχικά, αναλύεται η *Παλμική Θερμογραφία (Pulsed Thermography)* αφού είναι η πιο διαδεδομένη τεχνική ελέγχου λόγω της γρήγορης και εύκολης εφαρμογής της, ενώ ακολουθεί η περιγραφή της *Συγχρονισμένης Θερμογραφίας (Lock-in or Modulated Thermography)* η οποία προκειμένου να διεγείρει θερμικά το υπό εξέταση σώμα χρησιμοποιεί περιοδικά θερμικά κύματα αντί του απότομου θερμικού παλμού που εφαρμόζεται στην παλμική θερμογραφία. Μια ακόμη θερμογραφική τεχνική ενεργητικού ελέγχου είναι αυτή της *Θερμογραφίας Βηματικής Θέρμανσης (Step Heating Thermography)* της οποίας η πειραματική διαδικασία είναι όμοια με αυτήν της Παλμικής Θερμογραφίας, αλλά η παρακολούθηση και καταγραφή της μεταβολής της θερμοκρασίας στην υπό εξέταση επιφάνεια γίνεται κατά το στάδιο θερμικής διέγερσης και όχι κατά το στάδιο ψύξης, όπως στην παλμική θερμογραφία. Ακολουθεί μια αναφορά σε ενεργητικές τεχνικές οι οποίες βασίζονται στην εφαρμογή ενός θερμικού παλμού μεγάλης χρονικής διάρκειας, οι οποίες όπως αναφέρθηκε και παραπάνω χαρακτηρίζονται επίσης και από μεγάλους χρόνους καταγραφής του φαινομένου. Τέλος το κεφάλαιο αυτό κλείνει με μια σύντομη αναφορά σε ενεργητικές τεχνικές όπως η *Θερμογραφία Δονήσεων (Vibrothermography)* και η *Θερμογραφία Δινορρευμάτων (Eddy Current Thermography)* των οποίων οι αρχή λειτουργίας βασίζεται στην διέγερση του υπό εξέταση αντικειμένου με τη χρήση μηχανικών και ηλεκτρομαγνητικών πηγών ενέργειας αντίστοιχα και με την παρουσίαση της *Θερμογραφίας Γραμμικής Σάρωσης (Line-Scan Thermography)* η οποία βασίζεται στις θεωρητικές αρχές των παραπάνω μεθόδων αλλά η βασική διαφορά της είναι η πειραματική εκτέλεση, αφού κατά την εφαρμογή της η πηγή θερμικής διέγερσης και η θερμική κάμερα κινούνται παράλληλα στην επιφάνεια εξέτασης με μια προκαθορισμένη ταχύτητα και σε μια προκαθορισμένη απόσταση μεταξύ τους.

Μετά την εκτενή παρουσίαση των ενεργητικών προσεγγίσεων θερμογραφικού ελέγχου, **το τέταρτο κεφάλαιο** επικεντρώνεται στην βιβλιογραφική επισκόπηση των εξελιγμένων τεχνικών επεξεργασίας θερμογραφικού σήματος, οι οποίες χρησιμοποιούνται για την ανάκτηση ποιοτικών ή/και ποσοτικών πληροφοριών. Συγκριμένα, στο κεφάλαιο αυτό, αναλύονται οι θεωρητικές αρχές εξελιγμένων τεχνικών

επεξεργασίας θερμογραφικού σήματος όπως αυτές που βασίζονται στην παρακολούθηση των θερμοκρασιακών διαφορών (*Thermal Contrast-based Techniques*), της *Θερμογραφικής Ανασύνθεσης Σήματος (Thermographic Signal Reconstruction)*, της *Θερμογραφίας Κυρίων Συνιστωσών (Principal Component Thermography)* και της *Παλμικής Θερμογραφίας Φάσης (Pulsed Phase Thermography)*. Το βασικό πλεονέκτημα των παραπάνω τεχνικών είναι η ενίσχυση της ανιχνευσιμότητας και η βελτίωση της ποιοτικής διαχείρισης των αποτελεσμάτων, παρέχοντας οπτικές πληροφορίες που μπορεί να μην είναι ορατές κατά την διαχείριση και ανάλυση ακατέργαστων θερμοκρασιακών δεδομένων. Ο δεύτερος στόχος της εφαρμογής τέτοιων τεχνικών επεξεργασίας είναι η προετοιμασία των δεδομένων προκειμένου να ανακτηθούν ποσοτικές πληροφορίες. Ως εκ τούτου, το δεύτερο μέρος αυτού του κεφαλαίου παρουσιάζει κάποιες μεθόδους ποσοτικοποίησης, οι οποίες βασίζονται στην μελέτη διάχυσης της θερμότητας χρησιμοποιώντας πληροφοριακές παραμέτρους διαφορετικές από αυτήν της επιφανειακής θερμοκρασίας και την μεταβολή της στο χρόνο. Αυτές οι μέθοδοι σχετίζονται με την ποσοτική θερμογραφία υπερύθρου και η ανάκτηση πληροφοριών βάθους βασίζονται αποκλειστικά σε πειραματικά δεδομένα μέσα από τα οποία είναι εφικτός ο εντοπισμός ενός χαρακτηριστικού σημείου στο οποίο ένα συγκεκριμένο φαινόμενο λαμβάνει χώρα και σχετίζεται με τη σειρά του με την ανίχνευση της εσωτερικής φθοράς-αστοχίας. Επίσης μια διαφορετική προσέγγιση ποσοτικών εκτιμήσεων, μπορεί να εκτελεστεί χρησιμοποιώντας μεθόδους αντιστροφής, οι οποίες μπορούν να δώσουν ποσοτικές πληροφορίες, συσχετίζοντας αποτελέσματα από πειραματικές μετρήσεις και υπολογισμούς μοντελοποίησης. Μετά την εκτενή αναφορά τεχνικών για την ενίσχυση των αποτελεσμάτων ποιοτικού ελέγχου και την ποσοτική εκτίμηση του βάθους, το κεφάλαιο αυτό κλείνει με την παρουσίαση της μεθόδου εκτίμησης των πλευρικών διαστάσεων της φθοράς μέσω *του υπολογισμού του εύρους στο μισό της μεγίστης τιμής του (Full width at half maximum- FWHM).*

Στο **πέμπτο κεφάλαιο**, διερευνάται η εφαρμογή και η αποτελεσματικότητα της Παλμικής Θερμογραφίας στην ποιοτική και ποσοτική αποτίμηση της φθοράς σε σύνθετα υλικά ενισχυμένα με ανθρακονήματα. Για το σκοπό αυτό, χρησιμοποιήθηκαν τρεις σύνθετες επιφάνειες με τα ίδια χαρακτηριστικά φθοράς αλλά με διαφορετική επιφανειακή γεωμετρία, και διεξήχθησαν δυο επιμέρους μελέτες στοχεύοντας στον εντοπισμό της εσωτερικών προσομοιωμένων αστοχιών και την εκτίμηση του βάθους στο οποίο αυτές βρίσκονται. Η αποτελεσματικότητα του παλμικού θερμογραφικού ελέγχου στην ανιχνευσιμότητα της φθοράς, αποτιμήθηκε αρχικά βασιζόμενη σε οπτικές παρατηρήσεις μετά την εφαρμογή εξελιγμένων τεχνικών επεξεργασίας θερμογραφικού σήματος, εξετάζοντας παράγοντες όπως η ελαχιστοποίηση της επίδρασης της μη ομοιόμορφης εφαρμογής της θερμικής διέγερσης, η μείωση του ανεπιθύμητου θορύβου και η ενίσχυση της ανίχνευσης των εσωτερικών ατελειών. Παράλληλα, πραγματοποιήθηκαν μετρήσεις για τον υπολογισμό της αναλογίας σήματος/ θορύβου (Signal-to-Noise Ratio), τόσο για την επιβεβαίωση των οπτικών συμπερασμάτων όσο και για την ποσοτικοποίηση της παραγόμενης ποιότητας εικόνας πριν και μετά την επεξεργασία του ανακτώμενου σήματος. Η συγκριτική μελέτη των τεχνικών εξελιγμένης επεξεργασίας θερμογραφικών δεδομένων οδήγησε στον προσδιορισμό των παραμέτρων για την επιλογή της καταλληλότερης τεχνικής

επεξεργασίας ανάλογα με τις απαιτήσεις της επιθεώρησης και το βάθος ανίχνευσης. Στο δεύτερο μέρος της μελέτης αυτής, διερευνάται η αποτελεσματικότητα της μεθόδου για τη λήψη ποσοτικών πληροφοριών, όσον αφορά στην προσέγγιση του βάθους στο οποίο εντοπίστηκαν οι χαρακτηριστικές προσομοιωμένες φθορές μέσω της παραπάνω ποιοτικής επιθεώρησης. Συγκεκριμένα, η ποσοτική ανάλυση πραγματοποιήθηκε παρακολουθώντας το φαινόμενο διάχυσης της θερμότητας τόσο στο χώρο των χρόνων (θερμοκρασιακά δεδομένα) όσο και στο χώρο των συχνοτήτων (δεδομένα φάσης) αποσκοπώντας στον προσδιορισμό των πληροφοριακών παραμέτρων του χρόνου εμφάνισης της μέγιστης κλίσης της θερμοκρασιακής διαφοράς (Thermal Contrast Peak Slope Time) και της τυφλής συχνότητας (Blind Frequency), αντίστοιχα. Οι μέθοδοι αυτές διαχειρίζονται δεδομένα από διαφορετικές τεχνικές επεξεργασίας θερμογραφικού σήματος όμως απαιτούν την χρήση μιας περιοχής αναφοράς για την παρακολούθηση της αντίστοιχης εξέλιξης της διαφοράς έντασης μεταξύ τυφλού σήματος και σήματος ενδιαφέροντος. Έτσι, μέσω της εφαρμογής διαφορετικών μεθόδων ποσοτικοποίησης έγινε μια συγκριτική μελέτη για τη λήψη πληροφοριών του βάθους από τη διαχείριση θερμογραφικών δεδομένων σε διαφορετικά πεδία ανάλυσης και ταυτόχρονα αποτιμήθηκε ο βαθμός επίδρασης της επιλογής μιας περιοχής αναφοράς για την ακριβή εκτίμηση του βάθους. Μέσω της συγκεκριμένης μελέτης, ανακτήθηκαν αποτελέσματα σε σχέση με τα όρια ανιχνευσιμότητας της Παλμικής Θερμογραφίας και την ακρίβεια στην εκτίμηση του βάθους ως συνάρτηση των πειραματικών παραμέτρων διεξαγωγής της έρευνας και των χαρακτηριστικών των υπό εξέταση δειγμάτων.

Στο έκτο κεφάλαιο, διερευνάται η καταλληλότητα και η αποτελεσματικότητα του ενεργητικού θερμογραφικού ελέγχου για την αποκάλυψη επικαλυμμένων με επίχρισμα ψηφιδωτών και τον ποσοτικό χαρακτηρισμό τους, μετά την εφαρμογή μιας διαδικασίας θερμικής διέγερσης μεγάλης διάρκειας. Μέσω της εκτέλεσης παραμετρικών μελετών μοντελοποίησης και διαφοροποιώντας είτε γεωμετρικά χαρακτηριστικά (πάχος κάλυψης, πάχος ψηφίδων) είτε τις θερμικές ιδιότητες του ψηφοθετημένου υποστρώματος, εξετάστηκε η χρονική εξέλιξη της μεταβολής της θερμοκρασιακής κατανομής στην επιφάνεια πάνω από το επικαλυμμένο ψηφιδωτό και στην επιφάνεια αναφοράς. Η παραπάνω μελέτη οδήγησε επίσης στην χρονική παρακολούθηση της μεταβολής της αντίστοιχης θερμοκρασιακής διαφοράς και στον εντοπισμό του χρονικού σημείου εμφάνισης της μέγιστης τιμής της. Παράλληλα με τις μελέτες μοντελοποίησης, πειραματικές μετρήσεις έλαβαν χώρα εξετάζοντας τη θερμική συμπεριφορά των επικαλυμμένων ψηφιδωτών μέσω της ίδιας πληροφοριακής παραμέτρου που χρησιμοποιήθηκε για την ανάκτηση πληροφοριών από την μοντελοποίηση. Από την παραπάνω διερεύνηση (θεωρητική και πειραματική) πραγματοποιήθηκε ο ποσοτικός χαρακτηρισμός των επικαλυμμένων ψηφιδωτών μέσω της συσχέτισης αποτελεσμάτων μοντελοποίησης και πειραματικών αποτελεσμάτων. Συγκεκριμένα, οι ανακτώμενες παρατηρήσεις από τις παραμετρικές μελέτες μοντελοποίησης αρχικά μετατράπηκαν σε πληροφορία, δημιουργώντας το αντίστοιχο πρόβλημα αντιστροφής, το οποίο έδωσε τη δυνατότητα παρακολούθησης της μεταβολής του χρόνου εμφάνισης της μέγιστης θερμοκρασιακής διαφοράς (εξαρτημένη μεταβλητή) ως συνάρτηση της μεταβολής της υπό διερεύνηση παραμέτρου (ανεξάρτητη μεταβλητή). Η συσχέτιση των πειραματικών

αποτελεσμάτων παρακολούθησης του χρόνου στο παραπάνω πρόβλημα αντιστροφής, οδήγησε στη μέτρηση της υπό διερεύνησης παραμέτρου και στην εκτίμηση του πάχους κάλυψης, του πάχους των ψηφίδων και τον έμμεσο χαρακτηρισμό των επικαλυμμένων ψηφοθετημένων στρωμάτων μέσω του προσδιορισμού των θερμικών ιδιοτήτων τους.

Τα επιμέρους συμπεράσματα και προτάσεις παρατίθενται στο τέλος κάθε κεφαλαίου, και στο **έβδομο κεφάλαιο,** παρουσιάζονται τα γενικά συμπεράσματα καθώς και προτάσεις για την συνέχιση της έρευνας και την περαιτέρω εξέλιξη της τεχνικής.

Στη συνέχεια παρατίθενται τα σημαντικότερα αποτελέσματα και συμπεράσματα της διδακτορικής διατριβής.

- Τα αποτελέσματα που προέκυψαν από τη διερεύνηση της αποτελεσματικότητας διαφορετικών προσεγγίσεων ενεργητικού θερμογραφικού ελέγχου, έδειξαν ότι η τεχνική αυτή μπορεί να εφαρμοστεί επιτυχώς σε περιπτώσεις αποτίμησης της δομικής ακεραιότητας υλικών ή /και κατασκευών, παρέχοντας ικανοποιητική ανιχνευσιμότητα των υποεπιφανειακών περιοχών ενδιαφέροντος και εκτιμήσεις για τον ποσοτικό χαρακτηρισμό τους. Η επιλογή της καταλληλότερης τεχνικής ελέγχου είτε αυτή αφορά στην ποιοτική ή στην ποσοτική διερεύνηση, πρέπει να προσαρμόζεται ανάλογα με τις θερμικές ιδιότητες του υπό εξέταση υλικού και το επιθυμητό βάθος ανίχνευσης, ενώ χαρακτηριστικά όπως η συχνότητα δειγματοληψίας και η χωρική και χρονική διακριτική ικανότητα του θερμογραφικού εξοπλισμού πρέπει επίσης να λαμβάνονται υπόψη.
- Τα αποτελέσματα που προέκυψαν από τον ποιοτικό έλεγχο μέσω διαφορετικών ενεργητικών τεχνικών, έδειξαν ότι το ανακτώμενο μη επεξεργασμένο σήμα μπορεί να παρέχει το σύνολο των απαραίτητων πληροφοριών για τον εντοπισμό υποεπιφανειακών περιοχών ενδιαφέροντος. Βέβαια, ο ποιοτικός χαρακτηρισμός από απλά θερμοκρασιακά δεδομένα, μπορεί να οδηγήσει σε παρερμηνεία ή στην απώλεια πληροφοριών όταν πρέπει να εξεταστούν μικρές ή/και βαθύτερες φθορές. Επιπρόσθετα, η παρερμηνεία ή απώλεια πληροφοριών μπορεί να ενισχυθεί από μια διαδικασία μη ομοιόμορφης θέρμανσης, η οποία μπορεί να επηρεαστεί από τα γεωμετρικά χαρακτηριστικά της υπό εξέταση επιφανείας. Τα αποτελέσματα που προέκυψαν από τη διαχείριση του ανακτώμενου σήματος μετά την εφαρμογή εξελιγμένων τεχνικών επεξεργασίας θερμογραφικών δεδομένων (Θερμογραφική Ανασύνθεση Σήματος- TSR, Παλμική Θερμογραφία Φάσης –PPT, Θερμογραφία Κυρίων Συνιστωσών-PCT), έδειξαν ότι οι τεχνικές αυτές μπορούν να ενισχύσουν την ανάκτηση ποιοτικών πληροφοριών, εξαλείφοντας ή μειώνοντας αισθητά την αρνητική επίδραση των παραπάνω παραγόντων. Η εξέταση εφαρμογής εξελιγμένων τεχνικών επεξεργασίας θερμογραφικών δεδομένων οδήγησε στον καθορισμό των δυνατοτήτων των τεχνικών αυτών, ενώ η αποτελεσματική εφαρμογή τους σε θερμογραφικούς ελέγχους αποτιμήθηκε ως συνάρτηση των χαρακτηριστικών όπως: το βάθος της φθοράς, οι πλευρικές της διαστάσεις και η επιφανειακή γεωμετρία του υπό εξέταση αντικειμένου. Από τη διερεύνηση αυτή, καθορίστηκαν οι παράμετροι που πρέπει να

λαμβάνονται υπόψη για την καταλληλότερη επιλογή τεχνικών επεξεργασίας θερμογραφικού σήματος και η βελτιστοποίηση εφαρμογής τους ανάλογα με τις απαιτήσεις του ελέγχου και το βάθος ανίχνευσης.

- Όσον αφορά στην ποσοτική διερεύνηση με τεχνικές ενεργητικού θερμογραφικού ελέγχου, τα αποτελέσματα της παρούσας ερευνητικής μελέτης έδειξαν ότι οι μέθοδοι ποσοτικοποίησης μπορούν να παρέχουν ικανοποιητικές εκτιμήσεις είτε εντοπίζοντας πληροφοριακές παραμέτρους από πειραματικά δεδομένα (Κεφ. 5) ή συσχετίζοντας πειραματικά και υπολογιστικά αποτελέσματα (Κεφ. 6). Όταν στόχος του θερμογραφικού ελέγχου είναι ο ποσοτικός χαρακτηρισμός, αντίθετα με τον ποιοτικό έλεγχο, η διαδικασία θερμικής διέγερσης και τα γεωμετρικά χαρακτηριστικά της υπό εξέτασης επιφανείας έχουν από μικρή ως αμελητέα επίδραση στην ανάκτηση ποσοτικών πληροφοριών. Αντίθετα, η ανάκτηση ποσοτικών πληροφοριών και η ακρίβεια της μέτρησης εξαρτώνται από την σωστή επιλογή των πειραματικών παραμέτρων και των παραμέτρων ανάλυσης. Τα αποτελέσματα που προέκυψαν από τη διερεύνηση και εφαρμογή διαφορετικών μεθόδων ποσοτικοποίησης οδήγησαν στον καθορισμό των κατάλληλων πειραματικών παραμέτρων και παραμέτρων ανάλυσης, προκειμένου να επιτευχθεί η ακριβέστερη ποσοτική εκτίμηση.

TABLE OF CONTENTS

Chapter 1

Introduction

1.1 Background description

In the recent years, Non Destructive Testing & Evaluation (NDT&E) techniques have been widely used in different engineering disciplines (i.e. aerospace, civil, mechanical etc.), due to their outstanding advantage of being able to determine the physical condition of an object without affecting its future usefulness [1,2]. In other words, the general term of Non Destructive Testing (NDT) refers to the implementation of inspection technologies, which can provide information without altering the test-piece in any way, and simultaneously determine the absence or presence of conditions and/or discontinuities, that may have an impact on its serviceability. The list of NDT techniques used for inspection purposes is large and continuously grows as research activities effort to find new ways of applying physics and other sciences in order to develop new NDT methods. The most common NDT techniques that are widely used in nowadays are visual inspection, penetrant testing, magnetic particles testing, eddy current testing, radiography, ultrasound testing and acoustic emission [3-6]. All these techniques have a great impact on many industrial fields, as they can be applied for the quality control of a product during its design, manufacturing and maintenance stages, while several NDT applications find also use for the structural integrity assessment of various constructions.

Among the different nondestructive techniques, Thermographic Non Destructive Testing (TNDT), also often briefly called *Thermography* is a very rapidly evolving sector in science as well as in industrial and other fields, owing to the enormous progress recently made in microsystems technologies of IR detector design, electronics and computer science. The basic principle of infrared thermography is to capture the thermal radiation emitted by the surface of a material, which can be then analysed, providing information regarding the existence of surface and/or subsurface thermal resistances and consequently understand material's internal configuration. In the early years, Infrared Thermography was exclusively used as a supplementary technique to support primary inspection techniques such as radiography and ultrasonic testing. At that time, it was considered to be a purely qualitative technique with limited data capture (resolution and frame rate) in addition to the lack of dedicated signal processing tools for the correspondent analysis. However, in the recent years due to the advancements in infrared cameras technology and data processing codes, effort is being driven to the application of thermal imaging as a stand-alone inspection technique.

1.2 Problem statement, research motivation and objectives

Until now thermographic systems allowed defects to be detected and visualised, but reduced quantitative information was available from standard thermal imaging methods. Figure 1.1 describes the actual status for the implementation of an active thermographic inspection, where the steps are as follow: the test object is excited through the aid of an external energy source; variations on the surface temperature distribution are recorded through the aid of an infrared camera, which can be then be

visualised on a monitor. Thermographic analysis is based on the identification of thermal contrasts on the investigated surface owned to the presence of "*thermal heterogeneities*", while the produced detectability through the above described steps can be further enhanced by the subsequent elaboration of the acquired signal. The last step of this status is the providing of quantitative information regarding the location (depth), size and thermal properties characterisation of the detected features.

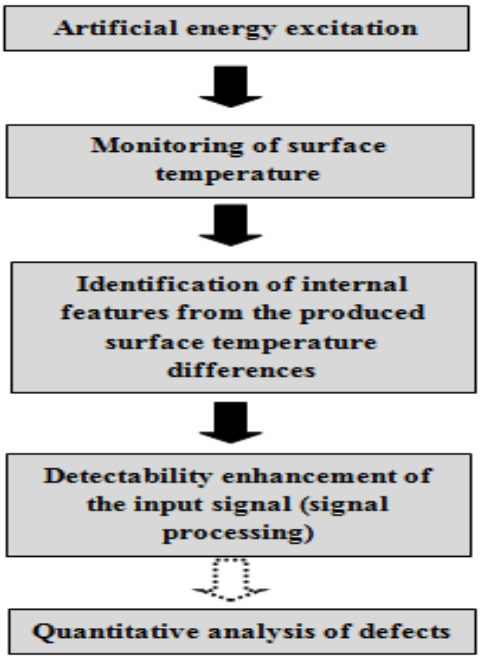

Fig. 1.1: *Schematic representation of an active thermographic survey.*

Taking into consideration the above mentioned, the main motivation behind this research study was the fact that thermal imaging still has the potential of further development in order to meet the requirements of other NDT techniques, commonly used on field level inspections. Even that the basic operational principles of Infrared Thermography are well published [7], limited work has concentrated on the application of this technique in order to provide a complete characterisation of the inspected target, including quantitative information retrieval [8]. Thus, the present dissertation focused on the study of different active thermographic approaches evaluating their effectiveness and reliability to initially operate as stand-alone inspection techniques and secondly -but also important- to produce a complete characterisation of the test-piece in terms of qualitative and quantitative assessment. More specifically in this research work, initially laminated Carbon Fibre Reinforced composites (CFRPs) were investigated by means of Pulsed Thermography (PT) aiming to the acquisition of qualitative (internal defects identification) and quantitative information (depth of the internal defects), while the second case study evaluated the performance of Cooling Down Thermography (CDT) to reveal the presence of hidden mosaic artefacts beneath a covering intervention procedure and provide information regarding the mosaic location, thickness and thermal properties. The selection of the testing configuration in each of the above inspection problems was conducted taking into consideration that every material response differently to the application of a heat flux and this response is related to its

thermal properties. In other words, the proper inspection method was chosen to provide the best possible results, taking into account the thermal properties of the investigated material and how these interact on a heating stimulation of a specific duration and energy deposition. PT was selected as it is the most commonly applied thermographic technique due to its advantageous characteristics of fast and easy deployment. On the other hand, the main characteristics of CDT (also referred as Square Pulsed Thermography) are the long excitation and observation times. These two characteristics may initially estimated as disadvantageous, however this technique is widely used in civil engineering inspections where sufficient heating and monitoring times are required, due to the low thermal properties that building materials generally possess and due to the fact that a deeper probing usually is required. Finally, the quantification procedures used to acquire the required information were based on exclusively experimental data in the former case (PT), while quantification in the latter case (CDT) was performed through the simultaneous conduction of numerical and experimental studies and the correlation of the produced results in a three steps methodology.

As stated above the main objective of this study was to evaluate the reliability of different active thermographic techniques in order to enhance their inspection capabilities through the implementation of the not well defined quantitative analysis step. As regards, the pulsed thermographic testing of composite materials, the scope was to establish the adequacy of this inspection procedure, enabling the qualitative and quantitative defect assessment through experimental observations and through the retrieval of informative parameters which were used in order to solve analytical formulas, producing the quantitative estimations. In order to achieve this, a series of specific steps was initially determined, and can be stated as:

- *Define the limitations and capabilities of optical Pulsed Thermography for qualitative information retrieval on CFRP composites.*

  In order to achieve this objective, detectability was evaluated selecting representative processing algorithms from a large body of pulsed thermography routines. These algorithms were applied to handle raw temperature data and analyse the acquired thermographic sequences. The effectiveness of each algorithm on defect detectability enhancement was ascertained, though visual observations from the processed imaging outputs and through Signal-to-Noise (SNR) computations. This resulted to the determination of the capabilities and limitations of each processing technique, while their effective application on pulsed thermographic inspections was evaluated as a function of the inspection depth, defect lateral dimensions and surface geometry of the inspected sample.

- *Define the limitations and capabilities of optical Pulsed Thermography for quantitative information retrieval on CFRP composites.*

  In order to achieve this objective, two different depth quantification procedures were studied inspecting a range of depths in which simulated delaminations were inserted into the CFRP specimens. The first quantification method used information from raw temperature data, while the second one used information from the above discussed signal processing implementations and in

particular from pulsed phase thermographic data. The depth results produced from the two different quantification procedures were compared in terms of error production, and the divergences observed from the actual depth were estimated taking into consideration the specification of the investigated samples, the experimental parameters selected to conduct this study and the parameters selected to analyse the data. This resulted to the definition of the proper experimental and analysis parameters which are producing the best possible result.

As regards, the Cooling down thermographic inspection of plastered mosaics, the main objective was to correlate numerical simulations and experimental testing, enabling the quantitative characterisation of the hidden aesthetic artefacts. In order to achieve this, a series of specific steps were initially determined and can be stated as:

- *Theoretical assessment of cooling down thermographic technique related to the inspection problem.*

  In order to achieve this objective a simulation computer programme was used, modelling the actual inspection problem. Through several simulations, the adequacy of describing the heat transfer phenomena occurred into the plastered mosaics regime when subjected to a long pulsed heating, was evaluated. Additionally numerical studies were performed, studying the effect of specific parameters variations (i.e. covering thickness, mosaic thickness and mosaic thermophysical properties) on informative characteristics such as the time of maximum thermal contrast occurrence between a mosaic-free and a mosaic-consisted area. This resulted to the correlation of the informative parameters variability as a function of the features of interest characteristics, permitting for modelling to act as a complementary tool to retrieve information regarding the influence of mosaics depth, thickness and thermal properties variations on the acquired thermal results.

- *Investigation of the feasibility of cooling down thermography to reveal hidden mosaic artefacts beneath a covering intervention.*

  In order to achieve this objective and based on the understanding achieved from numerical modelling, experimental measurements were conducted to evaluate the seeing-through condition produced on the covered mosaic panels. This was performed by studying the temperature variations observed on the surface of a mosaic-consisted and mosaic-free area respectively. This resulted to the understanding of the thermal response produced after a stimulation process on the plastered mosaics.

- *Development of a quantitative procedure enabling the characterisation of plastered mosaics.*

  Once the hidden mosaic layers were qualitatively detected by cooling down thermographic testing, quantitative information in terms of mosaic parameters (e.g. location, thickness, nature) were acquired through the correlation of numerical and experimental results and by solving the inverse problem (parameter estimation). This resulted to the hidden mosaic characterisation through the constant established between the simulation and experimental results.

1.3 Thesis outline

The present dissertation thesis is organised in 7 chapters, including the present one. In **Chapter 2**, an introduction into the topic of Infrared Thermography is presented, including the principles of infrared radiation, the spectral characteristics that govern both a blackbody and the real bodies as well as the heat transfer modes along with the thermophysical properties, which should be taken under consideration when performing thermographic inspections. Additionally, an introduction on the two main thermographic approaches, this of passive and active thermography is provided, highlighting their operational principles, common applications and the main advantages and limitations that each technique possesses. Finally, this chapter is concluded with a brief presentation of some crucial practical remarks that should be taken into account, in order to obtain the best possible results when performing thermal imaging surveys.

Chapter 3 deepens to the topic of active infrared thermography, which was the main category from which techniques were selected to implement this research study. Thus, an overview of the theoretical principles and the experimental configurations of the most commonly used active thermographic approaches along with some of their applications in the field of NDT&E are presented. Initially, Pulsed Thermography (PT) is discussed, as it is the most common applied active thermographic technique due to its simplicity and rapid implementation, while the description of Lock-in Thermography (LT) is following, which uses periodic heating instead of the pulsed heating applied in PT. Another active thermographic configuration is this of Step Heating Thermography (SHT), which experimental procedure is very similar with that of PT; however the monitoring of the heating up phase is of prime interest in such types of inspections. Additionally, a presentation of long excitation based active configurations whose main difference from PT and SHT is the long excitation and observation times is discussed and finally, this chapter is closing with a brief description of other forms of active thermal imaging such as Vibrothermography (VT) and Eddy Current Thermography (ECT) which involve mechanical and electromagnetic excitation respectively, and the active configuration of Line-Scan Thermography (LST), where the heating source and the camera are moved along the area of inspection with a predefined speed and in fixed distance between them.

After the detailed discussion regarding the state-of-the-art active infrared approaches, **Chapter 4** provides an overview of the signal processing techniques that have been proposed and are used for the qualitative and quantitative assessment of active thermographic data. More specifically, this overview presents the theoretical principles of thermal-contrast based techniques, derivatives reconstruction processing, principal component analysis and pulsed phase thermography. These techniques are widely used, as they produce an improved qualitative interpretation of active thermographic results. The second objective of advanced signal processing techniques is to prepare the data in order to be manipulated properly and provide quantitative information regarding the detected features of interest. As a result, the second part of this chapter is dedicated to the discussion on some quantification

methods, which are based on the heat diffusion study in different processing domains. These methods are related to quantitative infrared thermography based on exclusively experimental methods, aiming to the determination of the point in which a specific phenomenon occurs, associated with the detection of a hidden feature. On the other hand, a different approach for quantitative purposes can be implemented as well by involving inverse techniques which can provide quantitative information through the correlation of numerical and experimental results and by solving inverse problems. Finally, this chapter is concluded with the presentation of a quantitative approach to determine the lateral dimensions of a detected feature, which is based on the study of intensity variations onto a line profile using the statistical analysis of Full Width at Half Maximum (FWHM).

The next chapter, **Chapter 5**, is dedicated to the implementation of PT with flash excitation in order to establish its suitability for qualitative and quantitative defect assessment on CFRP laminates. In order to implement this study, three CFRP panels having the same defects description and thickness but with a different shape are initially assessed by applying different signal processing routines on the acquired thermal data. The effectiveness of the above processing routines is evaluated in a qualitative manner, comparing the visual outputs and the information retrieval in terms of defect detectability enhancement and noise reduction. Simultaneously, the produced defect detectability is evaluated in a quantitative basis through Signal-to-Noise Ratio (SNR) computations, quantifying the image quality and the intensity contrast created between the defective and sound areas. This comparative study of various algorithms on factors such as robustness to noise, qualitative information retrieval, and optimum defect detection, resulted to the parameters setting for the most efficient algorithm selection according to the user's needs. The second part of this study is dedicated to depth retrieval procedures based on experimental data. More specifically, investigations regarding the quantitative depth information recovery are performed in the temporal and frequency domains respectively, identifying the informative parameters of temperature contrast peak slope time and of blind frequency. These analytical methods for depth prediction require the need for a sound area determination and thus a comparison is performed regarding the influence degree of the sound area selection in depth prediction accuracy either working with raw temperature or phase data. Through the above study, results are extracted regarding the detection limits of pulsed excitation testing and the depth estimations accuracy of the detected defects below the surface.

Finally, **Chapter 6** investigates the reliability and suitability of active thermography based on long pulsed excitation heating in order to test multilayered structures and identify hidden mosaic artefacts beneath layers of plaster. Moreover, the combination and comparison of results from experimental testing and numerical simulations is studied, with the goal to quantitatively characterise the subsurface mosaic layers. For this reason, fabricated plastered panels consist of different tesserae materials and simulating different wall mosaics covering procedures, are tested aiming to identify their sub surfaces, and retrieve quantitative information about the covering layer thickness, the mosaic layer thickness and the mosaic thermophysical properties determination. Initially in order to acquire information about the

effect of specific parameters variations on informative characteristics such as temperature decay and thermal contrast evolution, a computer program is involved modelling transient thermographic problems on the predefined samples (models). Through numerical simulations, the temporal changes of the surface temperature distribution over a reference and over an area of interest are calculated after varying geometrical parameters and after varying the thermophysical properties of the mosaic artefact. Along with the numerical simulations, experimental measurements are performed by externally heating the specimens' surface. Through the above study, results are extracted by the correlation of numerical and experimental results and by solving the inverse problem (parameter estimation). This procedure was able to interpret the measured physical quantities of maximum thermal contrast and of the relative time of this maximum occurrence as a function of the investigated parameters, permitting their quantitative estimation.

Conclusions and recommendations are made at the end of each chapter and they are brought together in **Chapter 7** along with some future perspectives for the continuation of this research.

1.4 References

[1] P.J. Shull (2002). *Nondestructive Evaluation, Theory, Techniques and Application.* Marcel Dekker Inc., New York, USA.

[2] C.J. Hellier (2003). *Handbook of Nondestructive Evaluation.* McGraw-Hill, New York, USA.

[3] *The Nondestructive Testing Handbooks,* 2nd ed., American Society for Nondestructive Testing, Columbus, OH: Vol. 1, *Leak Testing,* McMaster, R. C. (ed.); Vol. 2, *Liquid Penetrant Testing,* McMaster, R. C. (ed.); Vol. 3, *Radiography and Radiation Testing,* Bryant, L. E. (ed.); Vol. 4, *Electromagnetic Testing,* Mester, M. L. (ed.); Vol. 5, *Acoustic Emission,* Miller, R. K. (ed.); Vol. 6, *Magnetic Particle Testing,* Schmidt, J. T. and Skeie, K. (eds.); Vol. 7, *Ultrasonic Testing,* Birks, A. S. and Green, R. E. (eds.); Vol. 8, *Visual and Optical Testing,* Allgaier, M. W. and Ness S. (eds.); Vol. 9, *Special Nondestructive Testing Methods,* Stanley, R. K. (ed.); Vol. 10, *Nondestructive Testing Overview,* Ness, S. and Cherlock, C. N. (eds).

[4] B. F. Larson (2002). *Study of the Factors Affecting the Sensitivity of Liquid Penetrant Inspections: Review of Literature Published from 1970 to 1998.* FAA Technical Report Number DOT/FAA/AR-01/95, Office of Aviation Research, Washington, DC.

[5] J. Krautkramer, H. Krautkramer (1995). *Ultrasonic Testing of Materials.* 4th ed., Springer-Verlag, New York.

[6] R.A. Quinn (1980). *Industrial Radiology—Theory and Practice.* Eastman Kodak, Rochester, NY.

[7] X.P.V. Maldague (2002). *Introduction to NDT by Active Infrared Thermography.* Materials Evaluation, Vol. 60 (9), pp. 1060-1073.

[8] C. Ibarra-Castanendo, M. Genest, P. Servais, X.P.V. Maldague, A. Bendada (2007). *Qualitative and quantitative assessment of aerospace structures by pulsed thermography.* Nondestructive Testing and Evaluation, Vol. 22(2-3), pp. 199-215.

Chapter 2

Fundamentals of Infrared Thermography

2.1 Introduction

Among the different non-destructive testing techniques that are in use nowadays, Infrared Thermography (IRT) stands as an attractive tool for non-contact inspections [1], correctly characterised as a technique able to *"see the unseen".* As the name implies, it uses the distribution *(suffix-graphy)* of surface temperature *(prefix thermo-)* to assess the investigated structure and to reveal information of what is under the surface [2].

Measurements through IRT are based on the monitoring of the thermal radiation emitted from the surface of a body with the aid of an infrared camera, resulting to a thermal image that maps the surface temperature distribution over the area of inspection. By image analysis and elaboration, it is possible to acquire information about the condition of the structure, as well as the presence of hidden features beneath the surface of the object under test. In general terms, IRT can be deployed in two different experimental modes, mainly according to the application in which is involved. As a result, this technique can be divided in two basic approaches, this of passive and this of active thermography respectively. Passive Thermography is based on the monitoring of the thermal radiation emitted by the surface of the test body under natural conditions, while in Active Thermography in order to study the condition of the structure, infrared images have to be recorded during and /or after the application of a thermal stimulation. In nowadays, different active thermographic approaches have been developed mainly according to the excitation sources used and the way that the object under inspection is being stimulated [3]. Nevertheless, in both cases (passive and active) the resulting thermal patterns, known as thermograms or thermal images, are used to diagnose and evaluate the condition of the test target.

Aim of this chapter is to provide an introduction to the topic of IRT starting with some historical notes about the discovery of infrared radiation and the development of infrared imaging technology. Thereafter, an introduction on the nature of infrared radiation is presented along with the fundamental principles and spectral characteristics that govern the behaviour of a blackbody (ideal body) and a real body in thermal radiation emittance. A brief review of heat transfer modes is then discussed and a review on the thermophysical properties that should be taken under consideration when performing thermographic inspections is presented. After the basic characteristics that describe the response of a material in heat transfer, the two main thermographic approaches (passive and active) are presented including operating principles, advantages, limitations and some of their main applications in Non-Destructive Testing & Evaluation (NDT&E) field. Finally, the chapter is completed with a brief presentation of some crucial practical remarks that should be taken into account, in order to obtain the best possible results when performing thermal imaging surveys.

2.2 Development of infrared technology

The existence of the infrared portion of the electromagnetic spectrum was accidentally discovered around 1800 by *Sir William Herschel (1738-1822),* while searching for new optical filters to reduce the

brightness of sun's image in telescopes during solar observations [4,5]. By testing different samples of colored glass, inserted in the telescopes, Herschel observed that some of the colored classes passed very little of the sun's heat while others passed so much heat that he risked eye damage after only a few seconds of observation. As a result, he was convinced of the necessity to set up a systematic experiment with the objective of finding a single material that would give the desired reduction in brightness and the maximum reduction of heat. He began the experiment by actually repeating Newton's prism experiment [6], but looking for the heating effect rather than the visual distribution of intensity in the spectrum. In particular, after black painting the bulb of a sensitive mercury-in-glass thermometer, he measured the temperatures along the visible portion of spectrum from violet to red. As the blackened thermometer was moved slowly along the colors of the spectrum, the temperature readings showed a steady increase from the violet end to the red end (Figure 2.1). This observation was not entirely unexpected, since the Italian researcher *Marsilio Landriani (1746-1815)*, in a similar experiment in *1777*, had observed much of the same effect [7]. However, Herschel was the first who noted that the temperature was still elevated beyond the red band where no radiation was visible. Moving the thermometer into the "dark region" beyond the red end of the spectrum, he confirmed that the heating continued to increase. When Herschel revealed his discovery, he referred to this new portion of the electromagnetic spectrum as the "*thermometrical spectrum*". The radiation itself, he sometimes referred to as "*dark heat"* and *"invisible rays"* [2]. The term "*infrared*" (beyond the red) began to appear in print 75 years later, and it is still unclear who should receive credit as the originator.

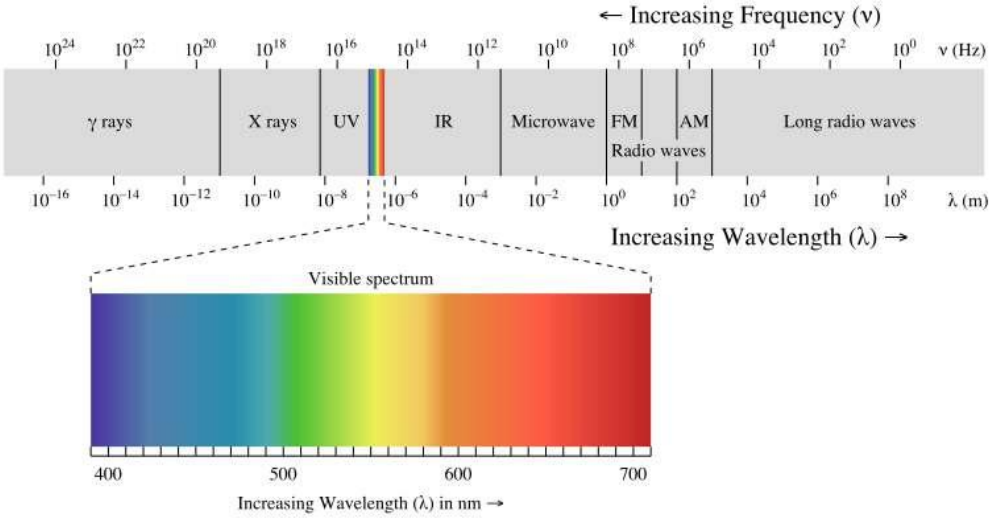

Fig. 2.1: *Visible portion of the electromagnetic spectrum*

Mercury Thermometers, as radiation detectors, remained unchallenged until 1829, the year when *Leopoldo Nobili (1784-1835)* inverted the thermocouple (based on the thermoelectric effect discovered in 1821 by *Thomas Seebeck (1770-1831)*, known as *Seebeck Effect*) [8-10]. The thermocouple was capable of detecting the heat from a person standing three meters away. Infrared technology was further developed in 1833, when *Macedonio Melloni* developed the first thermopile by connecting several thermocouples in series. The new device was at least 40 times as sensitive as the mercury thermometers

for detecting heat radiation, as it was capable to detect heat radiation from a person ten meters away [2].

The first infrared picture was produced by *Sir John Herschel (1792-1871)* -son of William Herschel- in 1840 using an evaporograph. *Sir John Herschel* continued research trying to discover methods in order to make visible the infrared radiation. Based upon the differential evaporation of a thin film of oil, exposed to a heat pattern focused upon it; the thermal image could be seen by reflected light where the interference effects of the oil film made the image visible to the eye. Sir John Herschel also managed to record a primitive thermal image on paper (formed by the differential evaporation), which he called it a *"thermograph"* [11].

The improvement of infrared detector sensitivity progressed after the breakthrough invention of the bolometer in 1880 by *Samuel P. Langley (1834-1906)* [8-10]. A bolometer is a thermal detector, comprised from a thin blackened strip of platinum connected in one arm of a Wheatstone bridge circuit. When thermal radiation was focused on the platinum strip, its electrical conductivity was changing, caused of the impinging heat, something that could be detected by the response of a sensitive galvanometer. This instrument is said to have been able to detect the heat from a cow at a distance of 400 meters.

Further improvement on thermal radiation theory was performed in 1900 by the German Physicist *Max Planck (1858-1947)* who was able to describe the spectral distribution of the radiation from a blackbody (Eq. 2.3) Max Planck's radiation theory accelerates the progress in infrared and thermal imaging technologies in a rapid manner. Another reason which led to the rapid development of infrared technology was the advent of two world wars, where huge research activity had been done aiming to develop infrared detectors capable of converting infrared radiation into visual image enabling to 'see in the dark'.

Until the end of 1920s, the developed imaging systems were based on the operation principle of bolometer, however the development of two new infrared detectors, this of image converter and this of photon detector, changed the above established condition. At first, the image converter received the greatest attention by the military, due to the fact that it enabled an observer to literally see in the dark. However, the sensitivity of the image converter was limited in the near infrared wavelength and the most interesting military targets (i.e. enemy soldiers) had to be illuminated by infrared beams. Since this involved the risk of giving away the observer's position to a similarly equipped enemy observer, it is understandable that military interest in the image converter eventually faded. With the advent of the Second World War, research was focused on the development of photon detectors which had greater sensitivity than the image converter and do not require an external infrared beam to operate. The success of photon detectors was huge, and the military services had classified this research as a top secret. As a result, the photon detectors developed during the two world wars passed to civilian applications in the mid of 1950s.

The first photon detectors made of lead sulfide (PbS) and developed between 1930 and 1944, were operating to infrared wavelengths between 1.3 and 3μm, characterised by enhanced sensitivity and

improved response time. The fact that photon detectors operation was not based on heating of a sensitive surface to produce an output signal related to the target temperature as in the case of thermal detector, enable this imaging system to produce a faster response compared with the bolometers and thermopiles available previously. Beginning in the late of 1940's and continuing into the 1950's, a wide variety of new materials were developed for IR sensing. Lead selenide (PbSe), lead telluride (PbTe), and indium antimonide (InSb) extended the spectral range beyond that of PbS, providing sensitivity in the 3-5μm medium infrared wavelengths (MWIR). Mercury tallium telluride (HgTeCd) followed in the 1960s, extending the spectral range and providing sensitivity in the 8-14 μm long infrared wavelengths (LWIR).

In the 1960s and 1970s, the first infrared cameras became commercially available. These devices were using pyroelectric tube technology [2,12]. In early 1980s, a small revolution occurred in the IR community with the development of the first focal play array (FPA) infrared camera [2,12]. FPAs are similar in structure to solid-state CCD (change-coupled devices) video cameras but their main difference is that they are sensitive in infrared radiation [2]. FPA technology, by having more than one row of detectors, offers several advantages such as higher spatial resolution and less noise on the acquired result [13]. In nowadays, FPA cameras are manufactured based on two types of infrared detectors: photonic cooled detectors or uncooled microbolometers.

In the past, infrared thermography was not mature or reliable enough to be employed in practical engineering applications. However, due to the huge development of infrared sensing technology, this situation has changed and more engineers have begun to use and accept infrared thermography as a reliable non-destructive testing tool. In nowadays, IRT is widely applied in research and development as well as in a variety of fields such as nondestructive testing, condition monitoring and predictive maintenance, buildings and infrastructures inspections, industrial, medical applications, etc. The main advantage of IRT over classical NDT techniques resides in the possibility of inspecting large areas in a fast and safe manner without needing to have access in both sides of the component under inspection.

2.3 The nature of infrared radiation

In physics, visible light, ultraviolet radiation, IR radiation, and so on, can be described as waves and in particular electromagnetic waves [2,8,12]. All matter regardless of its state or composition, continuously emits electromagnetic (EM) radiation, which can be considered as the most important process responsible for energy transfer in the atmosphere [14]. Waves are periodic disturbances that keep their shape while progressing in space as a function of time. Their spatial periodicity is called *wavelength* λ (given in meters, micrometers, nanometers, etc.), their transient periodicity is called *period of oscillation T* (in seconds), while their reciprocity is the *frequency f= 1/T* (in *Hz*). Both are connected via the speed of propagation *c* of the wave in vacuum by:

$$c = f \cdot \lambda \qquad \text{(Eq. 2.1)}$$

The amount of energy of radiated energy by a photon *E*, i.e. a particle measure, can be directly related to the corresponding wavelength λ, or frequency *f* of a wave, through the following relationship:

$$E = hf = \frac{hc}{\lambda} \qquad \text{(Eq. 2.2)}$$

where h= 6.6256 x10^{-34} [J·s] is the universal (or Planck's) contrast, and c=2.9979 x 10^8 [m/s] is the speed of light. As can be seen from the above formula, the amount of photon energy *E* transferred through electromagnetic radiation is inversely proportional to the particular wavelength of the EM wave. Therefore, hence EM waves at different λ or *f* are basically the same kind of physical "objects", the difference among them is the amount of photon energy *E*, related to each particular wavelength or frequency (i.e. electromagnetic radiation).

Figure 2.2, gives an overview of EM waves, ordered according to their wavelength or frequency. As can be seen from the above figure, the electromagnetic spectrum consists of a variety of different waves. Starting from the left of the figure, Gamma (γ) rays and x-rays –the most energetic forms according to Equation 2.2- have the highest frequencies and are located at the shortest wavelengths (between 10^{-14} and 10^{-18} m). Gamma (γ) rays and x-rays are well known for their medical, security and nondestructive testing applications [15]. The visible portion of the electromagnetic spectrum covers a small range within this spectrum with wavelengths from 0.38 to approximately 0.74 μm. The adjacent to the visible spectral region is called infrared and finds numerous applications in the imaging NDT&E [1]. On the other hand, wavelengths ranging from1 mm to several hundred meters, right part of the figure, are transparent to the atmosphere, so they are mostly used for data transmission, e.g. radio, TV, mobile, phones, etc. Recently, new sensing developments in the frequency range from 0.1 to 10 THz have led to the newly defined terahertz radiation [16], which overlaps part of the IR and microwaves ranges.

The most important process for infrared imaging is the so-called thermal radiation. In any particular measurement with an infrared camera, the object under inspection emits radiation into the direction of the camera which can be detected and measured. The term thermal radiation implies that all substances at a temperature T > 0 K (-273.15 ^{0}C) emit electromagnetic radiation due to molecular and atomic agitation associated with the internal energy of the material. The amount of radiation and its distribution as a function of wavelength depends on temperature and material properties [15,17,18].

The thermal radiation band is enclosed between 0.1 and 1000 μm of the electromagnetic spectrum, highlighted in Figure 2.2. This portion of EM spectrum can be divided into three spectral bands: the ultraviolet (UV) spectrum, the visible band and the infrared (IR). The infrared region of the electromagnetic spectrum (0.74-1000 μm), in which infrared imaging finds use, can be further discriminated into five parts summarized in the down right side of Figure 2.2: Near Infrared (NIR) from 0.74 to 1 μm, Short Wavelength Infrared (SWIR) from 1 to 3μm, Medium Wavelength Infrared (MWIR) from 3 to 5 μm, Long Wavelength Infrared (LWIR) from 8-14 μm, and Very Long Wavelength Infrared (VLWIR) from 14 to 1000 μm. Although this subdivision is somehow arbitrary

and varies from one source to another, it is based on the atmosphere high transmissivity "windows", i.e. the wavelength regions where atmosphere interferes the less with the incoming IR radiation. Band between 5 to 8 μm is called low atmospheric transmittance window as the radiation suffers from the highest attenuation in this region as can be seen from Figure 2.2. For IR imaging, three particular ranges of IR spectrum are used which are the Near Infrared, Mid Wave Infrared and Long Wave Infrared. Commercial cameras for infrared imaging are operating in these three ranges.

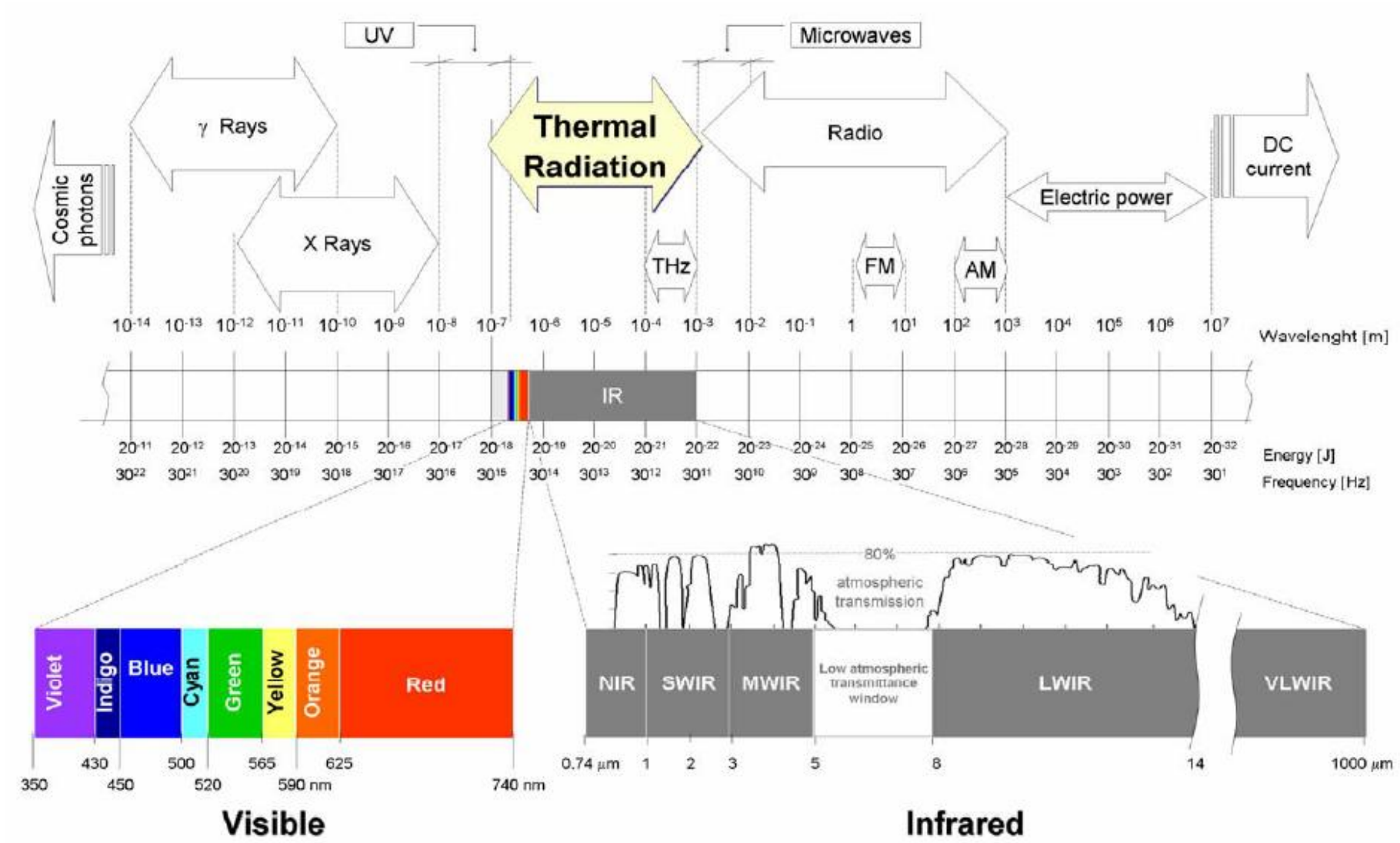

Fig. 2.2: *The electromagnetic spectrum [19]*

2.4 Fundamental principles of infrared radiation

2.4.1 Blackbody radiation

When considering the total radiant flux that is incident on the surface of a real object, this can be distinguished in three different outcomes. Some fraction of this total radiant energy is absorbed, some is reflected and some is transmitted through the object. In 1860, *Gustav Robert Kirchhoff (1824-1887)* defined the concept of *blackbody,* as an object which absorbs all radiation that impinges on it, regardless of direction and wavelength [20]. In other words, blackbody can be defined as an ideal emitter and an ideal absorber that neither reflects nor transmits the incident radiation. It is perfectly diffuses and radiates at all wavelengths and temperatures, and its spectral radiant exitance is the maximum possible compared with that of any actual thermal source at the same temperature. Therefore, all radiation leaving a blackbody is emitted by its surface and no surface can emit more energy than a blackbody.

A blackbody is a basic concept in physics and its definition as well as the laws of blackbody radiation are of importance in order to understand the absorption and emission processes occurred on the surfaces of real objects. Although closely approximated by some surfaces, it is important to note that no surface has precisely the properties of a blackbody. The visualization of a blackbody can be described by considering a cavity from an opaque material with a small entrance aperture, whose inner surface is of uniform temperature as shown in Figure 2.3. The radiant flux entering this hole from the outside will be trapped within the cavity regardless of the material and the surface characteristics of its wall sides. Repeated internal reflections occur until all the fluxes are absorbed by the walls.

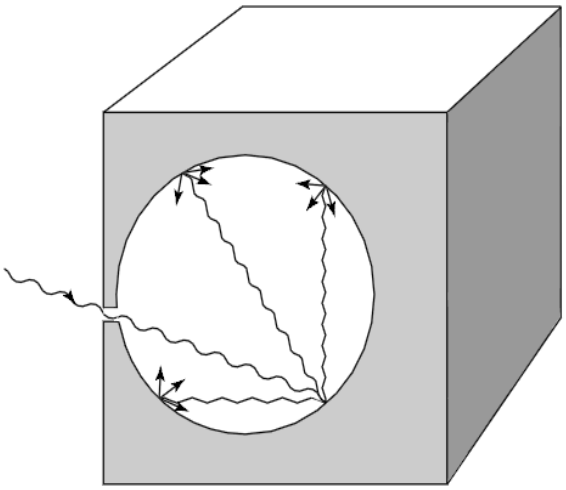

Fig 2.3: *Schematic representation of a blackbody* [14]

In general, the blackbody definition is a useful tool in studying thermal radiation and electromagnetic energy transfer in all wavelength bands. Being a perfect radiation absorber, the blackbody is used as a standard with which the radiative properties of actual bodies may be compared. In the followings, three fundamental laws are presented that govern blackbody behaviour in radiation.

In 1901, *Max Planck (1858-1947)* found an expression by which was able to describe the spectral distribution of the radiation intensity from a blackbody [21]. The spectral emissive power of a blackbody, known as *Planck Distribution Law,* can be expressed by the following formula [20]:

$$E_{\lambda,b}(\lambda, T) = \frac{C_1}{\lambda^5(e^{C_2/\lambda T} - 1)} \qquad \text{(Eq. 2.3)}$$

where $E_{\lambda,b}$ [W/m^2 μm] is the blackbody spectral radiant emittance at wavelength λ [μm] and temperature T [K], $C_1 = 2\pi hc = 3.742\ x\ 10^8$ [W μm^4/m^2] is the first radiation constant, and $C_2 = hc/k = 1.439\ x10^4$ [μm K] is the second radiation constant, with c= 2.998 x10^8 [m/s] being the velocity of light in vacuum, h= 6.626 x10^{-34} [J s] and k =1.381 x10^{-23} [J/K] the universal Planck and Boltzmann constants respectively.

Figure 2.4 depicts the graphic representation of a series of blackbody spectra for various temperatures following Eq. 2.3. Planck Distribution formula, when plotted for various temperatures, produces a family of curves and by following any particular Planck curve, interesting observations can be retrieved. In particular, emitted radiation varies continuously with the wavelength and the total amount of energy increases with increasing temperature. In particular, the spectral emissive power is zero for λ =0, then increases rapidly to a maximum at a wavelength λ_{max} and after passing it, approaches zero again at very long wavelengths. The higher the temperature, the shorter the wavelength at which the maximum peak occurs, indicating that at shorter wavelengths more radiation is appeared to be emitted.

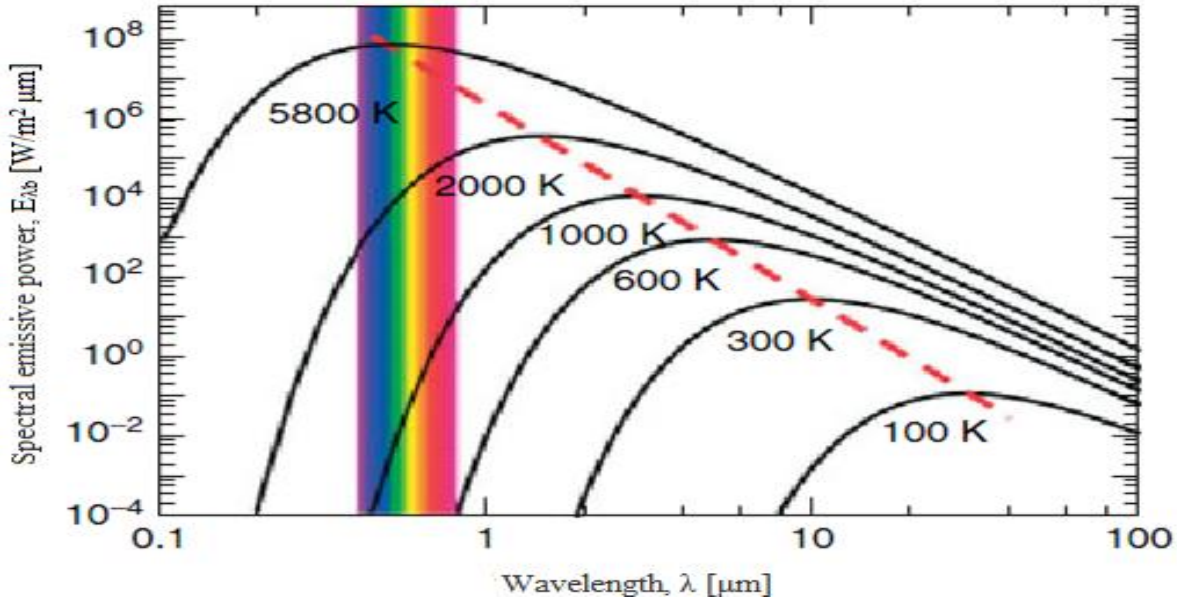

Fig. 2.4: *Blackbody spectral radiant emittance according to Planck's law, plotted for various absolute temperatures. The dotted line represents the points of maximum radiant emittance at each temperature as described by Wien's Displacement law. [18]*

By differentiating Plank's Law (Eq. 2.3) with respect to wavelength λ and setting the result equal to zero, *Wien's Displacement Law* is obtained, which states that the wavelength of the maximum intensity of blackbody radiation is inversely proportional to the temperature. Graphically, this is represented in Figure 2.4 marked as a straight red dotted line. In 1893, *Wilhelm Wien (1864-1928)* by measuring the spectral distributions for a blackbody at different temperatures *T*, he found that the peak energy was proportional to their corresponding wavelength λ [μm] for varying temperatures, and that is [20]:

$$\lambda_{max} = \frac{C_3}{T} \qquad \text{(Eq. 2.4)}$$

where C_3 = 2897.8 [μm K] is the third radiation constant. Wien's law expresses mathematically, the common observation that colors vary from red to orange or yellow as the temperature of the thermal radiator increases. The wavelength of the color is the same as the calculated wavelength λ_{max}. For blackbodies at 300, 1000 and 6000 K, maximum emission occurs around 10, 3 and 0.5μm respectively. The first case resembles environmental radiation, the second, for example, a hot plate from an electric stove, and the third case, the apparent average temperature of the outer layers of sun. The sun (approx. 6000 K) radiates energy mostly in the yellow portion of the visible spectra, peaking at about 0.5 μm. At room temperature (300 K) the peak of the radiant emittance lies at 9.7 μm, in the infrared portion of the electromagnetic spectrum.

In 1879, *Josef Stefan (1835-1893)* experimentally determined a simple expression relating radiant emission from a surface to its temperature. The resulting expression, known as *Stefan-Boltzmann Law* can be obtained by integrating Planck's Law over the entire spectrum ($0 < \lambda < \infty$) and states that the total flux density E_b [W/m^2] emitted by a blackbody is proportional to the fourth power of its absolute temperature *T* [20]:

$$E_b = \sigma T^4 \qquad \text{(Eq. 2.5)}$$

where σ = 5.6697 x 10^{-8} [W/m^2 K^4] is the Stefan-Boltzmann constant, which depends on C_1 and C_2 values. Graphically, E_b represents the area below the Planck curve for a particular temperature on Figure 2.5.

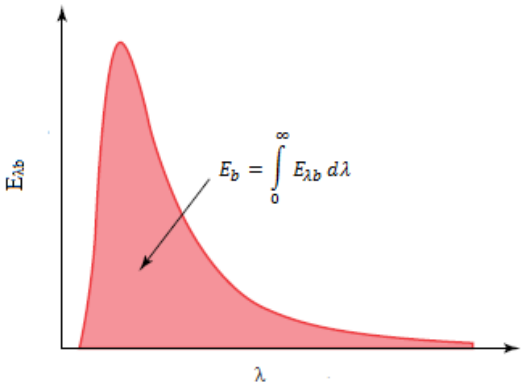

Fig 2.5: *Visualisation of Stefan-Boltzmann's Law[18].*

As presented above, Planck's law gives the intensity radiated by a blackbody as a function of wavelength, and it is an important tool to estimate spectral distribution for a blackbody, which corresponds to the theoretical maximum possible emission from any real object. On the other hand, Stefan-Boltzmann's law gives the total flux integrated over all wavelengths. However, since in thermographic NDT&E schemes, the infrared camera captures radiation only from a limited band of the electromagnetic spectrum, Plank's law rather than Stefan-Boltzmann law has to be applied [22].

2.4.2 Characteristics of real bodies in thermal radiation

The preceding three fundamental laws have been defined to describe the ideal behaviour of the blackbody. Real objects almost never comply with the above described laws even if they may approach the blackbody behaviour in certain spectral bands and conditions. Real surfaces absorb only a part of the incident radiant flux, with another part reflected and another part transmitted. Thus, various

radiative properties for real bodies have been defined to describe their radiative behaviour with respect to a standard which is the radiative performance of the blackbody. The radiative behaviour of real bodies depends on many factors such as [2,17]: the composition, surface quality and geometry, temperature, wavelength of the radiation and angle at which the radiation is emitted.

As stated above, when incident radiation flux hits the surface of a real object, three processes can be occurred which prevent a real object from acting as a blackbody. In particular at a given wavelength λ, a fraction of the incident radiation may be absorbed, a fraction may be reflected and a fraction may be transmitted. By following the law of energy conservation, these properties are linked together considering the flux exchange on a real surface for which [20]:

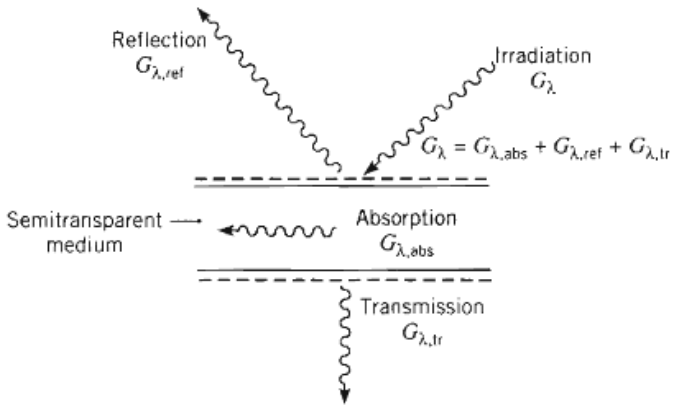

Fig. 2.6: *Absorption, transmission and reflection processes associated with a semitransparent medium.*

$$G_\lambda = G_{\lambda,abs} + G_{\lambda,ref} + G_{\lambda,tr} \qquad \text{(Eq. 2.6)}$$

where G_λ represents the irradiation energy and $G_{abs}, G_{refl},$ and G_{tr} represent the radiant fluxes of absorption, reflection, and transmission, respectively. For an opaque medium G_{tr} is equal to zero while for a perfect mirror G_{abs} and G_{tr} are equal to zero.

In order to describe the emission of thermal radiation from the surface of a real object, the term ***emissivity (ε)*** has been introduced as a fundamental radiative property of real bodies. As stated above, in the case of real objects, blackbody emission is an idealization and no real surface can emit the maximum thermal radiation at a given temperature, as blackbody does. Contrary, the real emission of thermal radiation from the surface of any object can however be easily computed by multiplying the blackbody radiation with a dimensionless quantity, this of emissivity *ε,* that describes the influence of the object under investigation in thermal radiation emittance. In other words, the emissivity of an object can be defined as the ratio of the amount of radiation actually emitted from the surface *E* to that emitted from a blackbody E_b at the same temperature, wavelength and direction and mathematically this can be expressed [20]:

$$\varepsilon(\lambda, T) = \frac{E(T)}{E_b(T)} \qquad \text{(Eq. 2.7)}$$

From the definition of emissivity, it is clear that $0 \leq \varepsilon \leq 1$. According to the spectral emissivity value, four types of radiation sources can be distinguished, and these are [21, 23]: a blackbody (perfect radiator) for which $\varepsilon(\lambda, T) = \varepsilon = 1$; a gray body for which $\varepsilon(\lambda, T) = \varepsilon =$ constant < 1; a white body (perfect reflector) for which $\varepsilon(\lambda, T) = \varepsilon = 0$; and a selective radiator, for which $\varepsilon(\lambda, T)$ varies with λ.

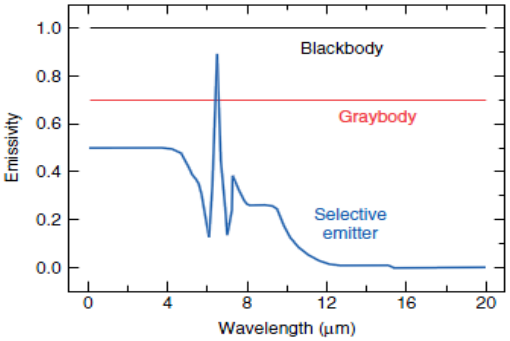

Fig.2.7:*Emissivities of blackbodies, gray bodies and selective emitters [18]*

As a material property the emissive ability of a body depends on several factors such as [18]: its temperature, its physical and chemical composition, its geometrical structure and surface roughness. Additionally, emissivity depends on the wavelength to which the emitted radiation corresponds and the angle at which the radiation is emitted. In IR imaging, this property is essential as accurate temperature measurements with IRT require precise knowledge of this quantity. For this reason, several sets of emissivity values for different materials can be found in the literature [2,24,25], while several research methodologies and procedures have been proposed in order to determine and measure the emissivity value of different materials and /or under different conditions [26-28].

On the other hand, ***Absorptivity (α)*** measures the fraction of the absorbed energy by a surface and can be defined as the ratio of the spectral radiant energy absorbed by an object to that incident upon it. For a blackbody $\alpha = 1$ whilst for a white body $\alpha = 0$. For real surfaces, absorptivity ranges between 0 and 1. As in the case of emissivity, absorptivity depends on the direction and wavelength, but it is practically unaffected by surface temperature. In a similar manner, ***Reflectivity (ρ),*** measures the fraction of the incident radiation reflected by a real surface and can be defined as the ratio of the spectral radiant energy reflected by an object to that incidents upon it. Surfaces may be characterised as diffuse or specular, according to the manner in which they reflect radiation [20]. Diffuse reflection occurs regardless of the direction of the incident radiation and the intensity of the reflected radiation is independent of the reflection angle. In contrast, if the angle of reflection is equal to that of the incident radiation then specular radiation is occurred. Last, ***Transmissivity (τ)*** measures the fraction of transmitted radiation after passing through a participating medium and can be defined as the ratio of spectral radiant energy transmitted through an object to that incident upon it. Taking into consideration the above definitions[1], Eq. 2.6 can be re-written by considering the sum of the factors that characterise the behaviour of a real object in incident thermal radiation and can be expressed as:

$$a_\lambda + \rho_\lambda + \tau_\lambda = 1 \qquad \text{(Eq. 2.8)}$$

[1] Emissivity, Absorptivity and Reflectivity are properties of ideal materials. Real materials may have defects, surface irregularities and may contain layers of different materials so are characterised by emittance, absorptance and reflectance. However, the infrared community has indiscriminately adapted the suffix (-vity) to characterise real materials properties as well [25].

while for an opaque material without transmission, the preceding relationship is simplified to:

$$a_\lambda + \rho_\lambda = 1 \quad \text{(Eq. 2.9)}$$

The relation between the abilities of emitting and absorbing the electromagnetic energy by any physical body can be described by *Kirchhoff's Law*. In other words, the general form of Kirchhoff's Law provides a link between the absorption and emission processes and thus between the spectral emissivity and spectral absorptivity at a specific temperature and wavelength [17,21], and that is:

$$\varepsilon_\lambda = \alpha_\lambda \quad \text{(Eq. 2.10)}$$

A medium with absorptivity α_λ absorbs α_λ times the blackbody radiant intensity E_λ and therefore emits ε_λ times the blackbody radiant intensity. For a blackbody, absorption is maximum in all wavelengths and so is emission thus we have:

$$\varepsilon_\lambda = \alpha_\lambda = 1 \quad \text{(Eq. 2.11)}$$

On the other hand, a gray body is characterised by incomplete absorption and emission and may be described by:

$$\varepsilon_\lambda = \alpha_\lambda < 1 \quad \text{(Eq. 2.12)}$$

The validity of Eq. 2.10 is restricted to blackbody emission. Nevertheless, it is still applicable for the case of diffuse surfaces, which are independent of the direction distribution of the emitted radiation [20].

2.5 Heat transfer mechanisms and thermophysical properties of materials

The above presented spectral properties and characteristics define the magnitude of the energy emitted from the surface of a body. Additionally, another crucial parameter, which affects this emission rate and shall be taken into account –mainly in transient thermal regimes- is the heat transfer phenomena occurred into the solid bulk. More specifically, whenever there exists a temperature difference in a medium or between two media, heat transfer occurs and this heat energy is always moved from the medium with the higher temperature to the medium with the lower temperature. In other words, heat transfer can be defined as energy in transit, due to the presence of a temperature difference [20]. The three different modes of heat transfer are these of conduction, convection and radiation, and regardless the way that this is taking place, it is performed until thermodynamic equilibrium is reached. However, in the case of radiation, this can be occurred as well in a thermal equilibrium environment. The monitoring of heat transfer phenomena can be performed by studying the temperature distribution in a solid which is dependent on its three coordinates *x, y ,z* and on time *t*, expressed by the function *T(x,y,z,t).*

When dealing with transient thermal problems and the inspection by means of IRT, conduction is the most important heat transfer mode as this mechanism defines the amount of heat reached and finally emitted by the surface of the solid. In particular, conduction heat transfer is described as the transfer of heat from the more energetic to the less energetic particles within a body due to interactions between

them [20]. Different materials conduct heat at different rates and these rates are related to their thermal properties, with the most important being this of thermal conductivity. As a result, the radiation emitted by the surface of a body is directly related to its surface spectral properties; however it is in an indirect manner related to its thermal and physical properties as well. In particular, there are three basic properties which lay the foundation of any conduction analysis of a material and these are the thermal conductivity k, the specific heat c_p, and the mass density ρ [20]. Density ρ [kg/m^3] is a measure of mass per unit volume and the specific heat, c_p [J/kg K], represents the amount of heat required to increase the temperature of a substance unit quantity by one unit. The product of density and specific heat ($\rho \cdot c_p$) is indicating the ability of the material to store thermal energy, which is known as heat capacity. On the other hand, thermal conductivity k [W/m ^{o}C] is a property that indicates the transfer rate by conduction for a specific material. As higher is the thermal conductivity of a material the greater is the heat transfer rate by conduction into its bulk. Additionally, the above three thermophysical properties can be combined into the property of thermal diffusivity α [m^2/s] which measures the material's ability to conduct heat in relation to its capacity to store it and can be expressed as:

$$\alpha = \frac{k}{\rho c_p} \qquad \text{(Eq. 2.13)}$$

More diffusive materials respond faster to thermal changes, i.e. they reach thermal equilibrium before less diffusive materials. On the other hand, the above thermophysical properties can also be combined to the material property of thermal effusivity e [Ws$^{1/2}$ m^{-2}K^{-1}] which measures the material ability to exchange heat with its surroundings, i.e. how it reacts to temperature variations. It is calculated as the square root of the product of the thermal conductivity, density, and specific heat [29] and is expressed as:

$$e = \sqrt{k\rho c} \qquad \text{(Eq. 2.14)}$$

The knowledge of the influence of a tested material's thermophysical properties and the understanding of heat transfer problems are very important in TNDT, as they can provide the operator information about observed phenomena such as abnormal temperature patterns detected on the surface by the aid of an infrared camera.

2.6 IRT as an NDT&E technique

The simplicity of thermal imaging implementation, establishes IRT as a promising technique among the several NDT inspection methods existing in nowadays, which can be further used as a stand-alone technique in many situations. For instance, IRT can be satisfactorily applied for the maintaining and monitoring of the integrity condition of materials and structures, as it is able to detect various types of surface and subsurface defects such as voids, delaminations, cracks, inclusions and other anomalies. Due to its non-contact nature, IRT has minimal access requirements and provides several advantages such as the rapid and full-field inspection of large areas, personnel protection as infrared radiation is not

harmful, and its application in cases where other established NDT techniques cannot provide efficient results (e.g. the detection of thermal leakages). The basic concept of IR imaging is to detect spatial variations in the measured surface temperature. In such a way, anomalies in the surface temperature distribution reveal the presence of defects, which can be interpreted, in two-dimensional images, displaying these variations in a range of different colors. In the following subsections, the two basic infrared thermographic approaches are presented along with some applications in which they can be deployed to.

2.6.1 Passive Thermography

Passive Thermography serves as an inspection technique and a diagnostic tool, which measures the heat flux, generated from the surface of the test object under natural conditions [30]. As discussed above, the measurement of the radiant heat pattern emitted by a body can determine regions or points of increased or reduced heat emission, which can further indicate the presence of an internal imperfection. In other words, passive thermographic inspection aims to the detection of subsurface and/or surface features, owing to temperature differences (ΔT) observed on the investigated surface during the monitoring with an IR camera. This technique is commonly used in applications where the features of interest are naturally at a higher or lower temperature than the background and in applications where temperature is an essential parameter in order to assess the condition or the proper operation of a component. The recording of abnormal temperature profiles can reveal a potential problem, as key term in several procedures is the temperature shift with respect to a reference. In general terms of inspection, a temperature difference value - often referred to as *delta-T* (ΔT) or *hot spot* - of a few degrees ($> 3^{o}$C) can be characterised as suspicious, while higher values indicate strong evidence of abnormal behaviour [2].

Advantage of passive thermography includes its ability to early detect potential problems with the benefit of reducing repair and operational costs in several types of installations. In addition, the minimal need for surface treatment prior testing as no interaction or physical contact is required between the investigated surface and the measuring equipment as well as the fact that information recovery can be performed in real time and/or during normal operation of the test object, provides the advantage that systems under passive thermal inspection rarely may require to be shut down. Contrary, in many instances, it is necessary for systems to be fully operational in order to produce the optimum thermal environment for testing [31,32]. However, environmental conditions play an important role especially on outdoor passive thermographic surveys. For instance, high winds can reduce the effectiveness of outdoor surveys due to surface temperature shear effect or similarly rain may lead to surface cooling, thus masking thermal effects from features below the surface [30]. Moreover, the accuracy of temperature measurements is limited when the inspected surfaces are consisted of various types of materials with different emissivity values [33] and if there are no naturally occurring thermal contrasts, passive thermography will not provide efficient results.

Applications of passive thermal imaging are numerous and widespread in use. In general context of constructions, passive thermography is commonly used as a diagnostic tool for predictive maintenance of buildings [34-40]. More specifically, through passive infrared inspections, it is possible to detect where and how energy is leaking from the building's envelope and collect information for clarifying its operating conditions. As a result, passive thermography in buildings -commonly referred as building thermography- is an NDT technique able to detect problems before physical symptoms appear. Some of its applications in buildings diagnostics include the reveal of defective insulation and air leaks, the inspection of windows and the identification heat leakage, detection of moisture accumulation, the information retrieval for the location of hidden objects inside the structure (i.e. pipes, ventilation ducts and anchors), and the examination of heating systems performance and condition (i.e. effectiveness, insulation defects, blockage in pipes). The aforementioned problems-irregularities can be easily detected as they alter locally the overall thermal conductivity of the element. Moreover, through alterations in the thermal inertia characteristics of building elements, temperature differences on the surface of the investigated materials can reveal the presence of hidden materials (Figure 2.8) or moisture in the infrastructure.

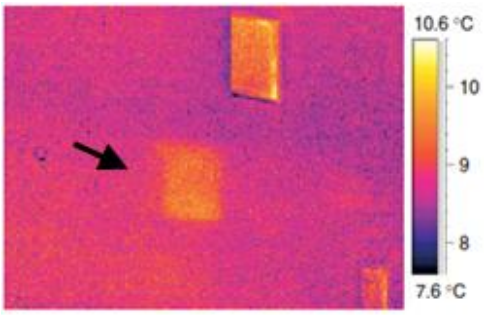

Fig. 2.8: *Passive Thermographic inspection of a building facade. The black narrow indicates a hidden window closed within the masonry and covered with plaster [18].*

In terms of industrial processes and electromechanical installations, passive thermal method is applied for predictive maintenance and condition monitoring in order to detect abnormal temperatures, which are indicating a potential problem that must be fixed [32]. Passive Thermography is very effective in locating problems in electrical installations before they became debilitating to a process [41]. If a part of a circuit has higher resistance than the rest of the circuit, it will have to dissipate the extra energy it obtains, through Ohm's law. Many mechanical systems can be monitored from the above method, as elevated temperatures and overheating on different components of a mechanical installation, can be easily detected by an IR camera [42].

On the other hand, medicine is recognised as one of the first non military applications of IRT, and nowadays passive thermal imaging is increasingly becoming acceptable by physicians as a supplementary diagnostic and monitoring tool for various diseases [43-45]. This is based on the fact that diseases as well as injuries lead to changes in skin surface temperature, which can be recorded by an infrared device. Last, several applications of passive thermography have been proposed and are more obvious to the general public. Many research and rescue missions utilize passive thermography to locate lost people in the darkness. The automobile and marine industries have also begun to install IR systems, being marketed as night vision. In general, the utilization of passive thermography is providing mainly qualitative results (i.e. a thermal image of temperature distributions on the surface of the test object) since the goal is simply to identify anomalies and inhomogeneities. However, if thermal modeling is

available, some investigations can provide quantitative measurements as well [46,47].

2.6.2 Active Thermography

In contrast to passive approach, Active Thermography requires an external energy source to stimulate the object under inspection and to produce a thermal contrast between the features of interest and the background. This approach is applied to conditions where the test object is normally in a thermal equilibrium and no natural temperature differences are presented or –if they are presented- they may not be sufficiently strong, for the identification of internal inhomogeneities beneath the investigated surface [48,49]. Defect detection principle in active thermography is based on the heating -cooling is also possible [21] - of the test object's surface. The process of the thermal front travelling inside the sample provides a transient temperature gradient inside the structure and when it meets an inhomogeneous area, the different thermal properties accelerate or impede the heat propagation into the material bulk, resulting to surface temperature modifications detected by the IR camera. Figure 2.9 gives a brief overview of active thermal imaging concept for the identification of internal features. This procedure can be applied in two different modes: this of reflection and this of transmission [2]. The reflection mode (Figure 2.9) is best suited to detect defects close to the heated surface, while the transmission mode is better suited for the detection of deeper defects as it is implemented by accommodating the excitation source and the camera on the opposite sides of the inspected component. However, the use of transmission mode is generally limited as in many instances there is no access to both sides of a component and in general active inspection in reflection mode can provide results of higher resolution than these obtained in transmission mode.

Active thermographic testing scenarios are presenting, similarly to the passive inspection, the advantages of non-invasive inspections, secure inspection environment and since the resulting output is of visual nature, this can lead to immediate interpretation of the thermal response [51]. However, difficulties in achieving a sufficiently uniform stimulation over a large inspection region can be an important issue when dealing with active IR and defect detectability is strongly related to the depth and size of the defect, reducing the potential of this technique to limited thickness inspections [2].

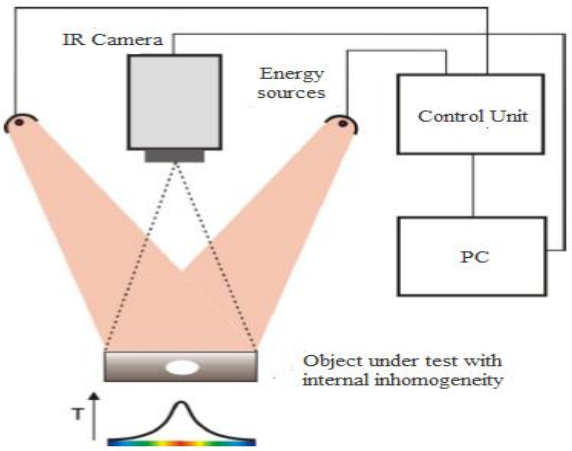

Fig. 2.9: *Schematic setup of active thermography using optical lamps. A sample with a subsurface defect is heated by absorbing visible light and surface temperature distribution is recorded using an IR camera as a function of time.*

As regards the thermal excitation procedure, practically any energy source can be used to stimulate the specimen being inspected. Means of external stimulation may include flash lamps, heat lamps, forced hot or cold air, electromagnetic induction and ultrasonic energy. As illustrated in Figure 2.10, a

four group division can be devised according to the most widespread excitation forms. In optical excitation, energy is delivered to the surface by means of optical devices such as photographic flashes (for pulsed heat stimulation) or halogen lamps (for periodic heating). Optical energy stimulates the defects externally, where energy is delivered to the surface of the test object as the light is transformed into heat. Thermal waves propagate by conduction through the specimen until they reach a discontinuity that either slows down or speeds up the waves propagation (depending on the thermal properties of both the test object and the discontinuity), resulting to a hot or cold spot on the surface of the specimen. In mechanical excitation, the energy is injected into the sample by means of mechanical oscillations, using for instance a sonic or an ultrasonic transducer. Mechanical excitation heats up the defects internally, as the mechanical oscillations injected into the sample spread in all directions dissipating their energy at the discontinuities in the form of heat, which travels to the surface by conduction. Last, in electromagnetic excitation, Eddy currents are externally induced to electro-conductive materials through electromagnetic coils, and heat is produced internally from the circulation of these currents into the material. A further classification in active thermographic scenarios derives from the manner that the test object is being stimulated. Basically two modes have been adapted, this of pulsed and lock-in (modulated) excitation [52,53], with the term step heating can also be found in literature, mainly referring to a long pulse excitation [54]. As a result, active thermographic testing either in reflection or transmission mode, can be characterised by the type of the energy source used to produce the thermal contrasts as well as by the regime of stimulation, which could be either a transitory (i.e. pulsed and step heating functions) or a steady regime (i.e. modulated function). The selection of the most well suited simulation regime and source type are mainly depended on the application.

Regardless the stimulation source used and the way that the test object is being excited, the basic operational principle in all active thermographic inspections is the sequential monitoring of the thermal response of the surface with respect to time, during and /or after the application of a heating excitation. The sequential output, mainly deployed in a digital format, can provide information regarding the spatial and temporal surface temperature variations and each pixel, composing the thermal image, can be analysed qualitatively and /or quantitatively through signal processing algorithms. In particular, acquired thermal images can be processed using different techniques with the most common in use include time domain and frequency domain analysis, respectively. Image processing is commonly used firstly to improve the visual appearance of the images through the reduction of noise and secondly to acquire quantitative and/or enhanced information regarding the detected features of interest. These processing techniques can be applied to any thermographic sequence, as they are independent from the energy source used and the stimulation procedure and a detailed presentation of the most common of these techniques applied in active thermographic data analysis will be discussed in the following chapters.

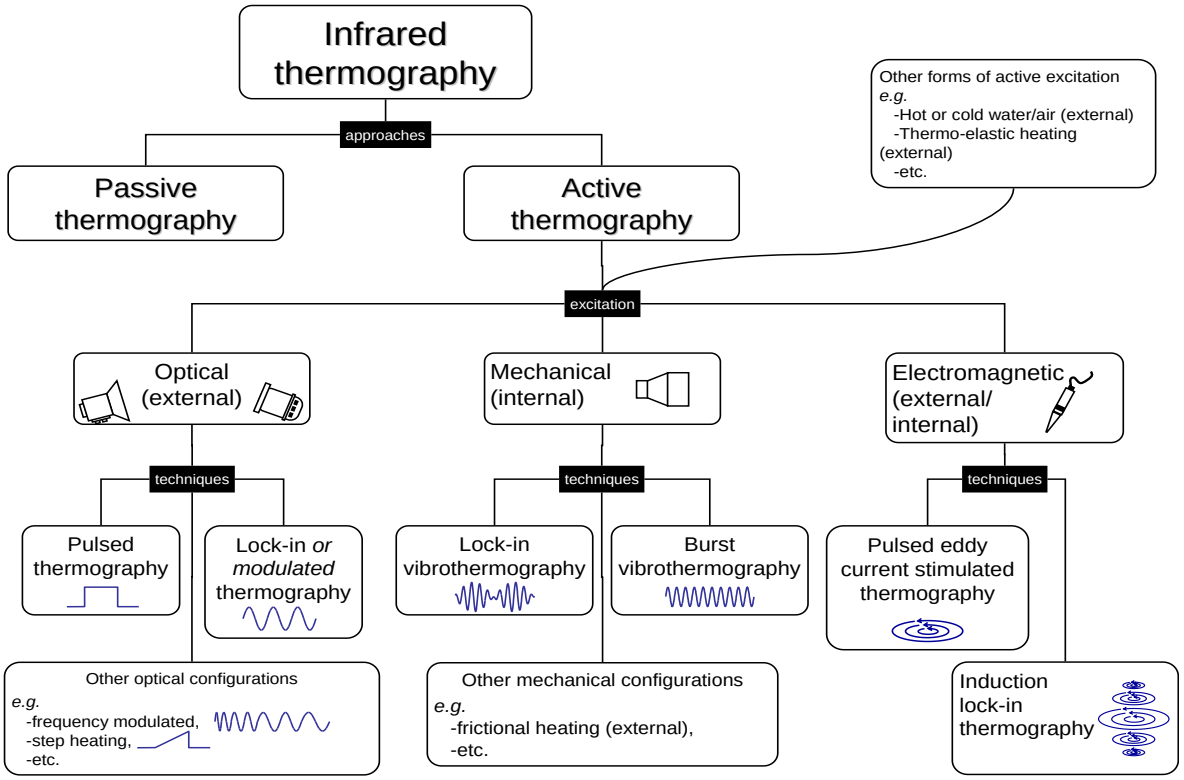

Fig. 2.10: *Passive and Active infrared thermographic approaches [55].*

2.7 Practical considerations in infrared thermographic measurements

In thermographic measurements either in the passive or active configuration, the radiant energy leaves the target surface, passes through a transmitting medium (usually following an atmospheric path) and reaches the measuring equipment. Therefore, in order to explain properly and obtain a reliable thermographic result from the inspected surface, the aforementioned sets of characteristics need to be considered prior the inspection. Moreover as Infrared Thermography is applied in several fields, each particular application presents specific characteristics and requirements, which entail a specific choice of infrared system, test procedure and data analysis. In the previous sections of this chapter a review of how the characteristics of the target's surface and its thermal properties influence the thermal radiation emittance, was presented. The behaviour of real bodies in heat emission is strictly related to their spectral and thermal properties while as the transmitting medium, is usually air, this characteristic can be largely ignored for short distances up to a few meters [56]. The last characteristic, which is of great importance and need to be considered, is the choice of the imaging system, as it depends on a number of variables including its performance, the temperatures of the test object to be measured and the necessary measurement accuracy.

The performance of an infrared system is generally characterised by three factors and these are its thermal sensitivity, spatial resolution and temporal resolution [22]. The sensitivity is generally expressed as the *noise-equivalent temperature difference (NEDT)* and this index indicates the temperature resolution (temperature sensitivity), quantifying the minimum detectable temperature

difference appearing on the target surface. The smaller the index number, the better is the thermal resolution. Some recently developed IR thermographic systems are able to detect temperature differences of less than 20 mK at ambient temperature. The spatial resolution is an essential factor as well for the imaging equipment performance as this index describes the capability of a system to measure the surface temperature of small objects. The spatial resolution establishes the relationship between target size and its temperature reading, and a high image resolution in a measurement system is crucial for performing accurate quantitative analysis. Modern systems are able to produce images composed of several tens of thousands of pixels. For some specific inspections with active thermal imaging, *temporal resolution* can be an important parameter for data acquisition and interpretation. The *temporal resolution* represents the rate at which a complete image is adapted, usually expressed in frames per second (Hz). Particularly, in materials where heat propagates very quickly and the entire sample may return to a near -equilibrium state within a very short time, data acquisition shall be occurred during this early time interval so that the interaction of heat transfer with the defect will appear in the thermal image (or the temperature-time curve). Fortunately, the state-of-the-art IR focal plane array (FPA) cameras typically operate at frame rates higher than 60 Hz and the entire image is acquired in less than 15 ms.

Aside from the equipment characteristics and material's properties that should be taken into account prior the test implementation, the interpretation of results is another crucial parameter for the proper information recovery during an infrared thermographic survey. As a result, thermography applications are often require the utilization of extensive diagnostic software for data analysis and thermal images display and the interpretation of results through the aforementioned diagnostic software can be done in several manners according to the desirable output. The most common approach to display thermographic data is the two-dimensional (2D) map, where each element (pixel) gives the intensity (e.g. temperature) of a point on the target's surface. One-dimensional (1D) profiles can be also used in a spatial or temporal profile. Spatial profiles are useful to highlight geometrical features, while 1D temporal profiles give useful information about the defect depth. It is also possible to represent data as three-dimensional (3D) views, in which x and y coordinates correspond to the pixel location, and z coordinate is the intensity value. In general terms of thermographic data interpretation, data is commonly represented as thermograms, i.e. a map of the thermal patterns on the specimen surface, although other representations have been proposed as well [2, 57], such as maxigrams (maps of maximum thermal contrast), timegrams (maps of the time of maximum thermal contrast), and diffusivity maps.

2.8 References

[1] X.P.V. Maldague, (1993). *Nondestructive Evaluation of Materials by Infrared Thermography*. Springer-Verlag, London.

[2] X. Maldague (2001). *Theory and Practice of Infrared Technology for Non Destructive Testing.* John-Wiley & Sons, New York, USA.

[3] X.P.V. Maldague (2002). *Introduction to NDT by Active Infrared Thermography*. Materials Evaluation, Vol. 60 (9), pp. 1060-1073.

[4] Infrared Processing and Analysis Center. *Discovery of the Infrared.* E-resource: http://coolcosmos.ipac.caltech.edu/cosmic_classroom/ir_tutorial/discovery.html

[5] D.S. Prakash Rao (2008). *Infrared Thermography and its application in civil engineering*. In Indian Concrete Journal, Vol. 82(3), pp. 41-50

[6] I. Newton. *Opticks (Great Mind Series).* Published by Prometheus Books, 2003.

[7] ThermaCAM Researcher, User's manual, Flir Systems, Danderyd, Sweden, 2005.

[8] G. Gaussorgues, S. Chomet (1994). *Infrared Thermography*. Chapman & Hall, Cambridge, UK.

[9] H. Kaplan (2007). *Practical Applications of Infrared Thermal Sensing and Imaging Equipment*. 3rd Edition, SPIE- The Society of of Photo-Optical Instrumentation Engineers Publishing, Washington, USA.

[10] D.P. Dewitt, G.D. Nutter (1988). *Theory and Practice of Radiation Thermometry*. John Wiley &Sons, New York, USA.

[11] R.A. Thomas (1999). *Thermography monitoring handbook.* Machine and Systems Condition Monitoring Series, Coxmoor Publishing Company, Oxford, UK.

[12] H.M. Runciman (1999). *Chapter 35: Thermal Imaging.* In J.G. Webster (Ed.): Measurement Instrumentation & Sensors Handbook, CRC Press LLC & Springer-Verlag, Florida, USA.

[13] M.E. Couture (2001). *Challenges in IR optics*. In B. F. Andresen, G. F. Fulop, M. Strojnik (Eds.): Proc. of SPIE- The International Society for Optical Engineering, Infrared Technology &Applications XXVII, Vol. 4369, Orlando, USA, 2001, pp. 649-661.

[14] K. N. Liou (2002). *An Introduction to Atmospheric Radiation.* 2nd Edition, International Geophysics Series, Vol. 84, Elsevier Science, California, USA.

[15] P.J. Shull (2002). *Non Destructive Evaluation, Theory, Techniques and Applications.* Marcel Dekker Inc, New York, USA.

[16] P. H. Siegel (2002). *Terahertz Technology.* IEEE Transaction on Microwave Theory and Techniques, Vol. 50 (3), pp. 910- 28.

[17] R. Siegel, J. Howell (1992). *Thermal Radiation Heat Transfer.* 4rd Edition, Hemisphere Publishing Corporation, Taylor & Francis Group, Washington, USA.

[18] V. Vollmer, K.P. Mollmann (2010). *Infrared Thermal Imaging. Fundamentals, Research and*

Applications. John Wiley &Sons, New York, USA.

[19] C. Ibarra-Castanedo (2005). *Quantitative subsurface defect evaluation by pulsed phase thermography: depth retrieval with the phase.* Ph. D. thesis, Université Laval, [access online: http://www.theses.ulaval.ca/2005/23016/23016.pdf].

[20] F.P. Incropera, D.P. DeWitt, T.L. Berqman, A.S. Lavine (2006). *Fundamentals of Heat and Mass Transfer.* 6th Edition, John Wiley &Sons, New York, USA.

[21] M. Planck (1959). *The Theory of Heat Radiation.* Dover Publications, New York, USA.

[22] G.M Carlomagno, G. Cardone (2010). *Infrared Thermography for convective heat transfer measurements.* In J. of Experiments in Fluids, Vol.49 (10), pp.1887-1218.

[23] R.D. Hudson (1969). *Infrared System Engineering*. John Wiley & Sons Inc, USA.

[24] W.L. Wolfe, G.J. Zissis (Eds.) (1993). *The Infrared Handbook.* 4th printing, Environmental Research Institute of Michigan, Infrared Information and Analysis Center, Office of Naval Research, Washington.

[25] G.C. Host (2000). *Common Sense Approach to thermal Imaging.* JCD Publishing & SPIE Optical Engineering Press, Florida, USA.

[26] ASTM E1933-97, *Standard Test Methods for Measuring and Compensating for Emissivity Using Infrared Imaging Radiometers*, American Society for Testing and Materials, Pennsylvania, USA, 1997.

[27] A. Moropoulou, N.P. Avdelidis, M. Koui, I. Tzevelekos (2000). *Determination of emissivity for building materials using infrared Thermography.* Journal of Thermology International, Vol. 10 (3), pp. 115-118.

[28] S.J. Marshall (1984). *The infrared emittance of semi-transparent materials measured at cold temperatures*. In G.J. Burrer (Ed.): Proc. of SPIE- The International Society for Optical Engineering, Thermosense VI, Vol. 0446, Orlando, Florida,1984, pp. 188-192.

[29] P. Bison, E. Grinzato (2008). *Building materials characterisation by using IR thermography for efficient heating systems.* In V.P. Vavilov, D.D. Burleigh (Eds.): Proc. of SPIE- The International Society for Optical Engineering, Thermosense XXX, Vol. 6939, Orlando, Florida,2008, art. no69390Y.

[30] D.J. Titman, (2001). *Applications of Thermography in Non-Destructive Testing of Structures.* NDT&E International, Vol. 34, pp.149-154.

[31] R.J. Lewak (1994). *Infrared techniques in the nuclear power industry.* In X.P.V. Maldague (ed.): Infrared Methodology and Technology, International Advances in Nondestructive Testing, Monograph Series, Gordon and Breach, New York, Chap. 9, pp. 319-366.

[32] V. Vavilov, V. Demin (2002). *Infrared Thermographic Inspections of Operating Smokestacks.* Infrared Physics & Technology, Vol. 43 (3-5), pp. 229-232.

[33] D.A. Artis, W.H. Carnahan (1982). *Survey of emissivity variability in Thermography of urban*

areas. In J. of Remote Sensing of Environment, Vol. 12, pp. 313-329.

[34] S. Ljungberg (1994). *Infrared Techniques in Buildings and Structures: Operation and Maintenance.* In X.P.V. Maldague (Ed.): Infrared Methodology and Technology, International Advances in Nondestructive Testing, Monograph Series, Gordon and Breach, New York, Chap. 6, pp. 211-252.

[35] C.A. Balaras, A.A. Argiriou (2002). *Infrared Thermography for Buildings Diagnostics.* Energy and Buildings, Vol. 34, pp. 171-183.

[36] Z. Li, W. Yao, S. Lee, C. Lee, Z. Yang (2000). *Application of Infrared Thermography Technique in Building Finish Evaluation*. Journal of Nondestructive Evaluation, Vol. 19(1), pp. 11-19.

[37] E. Grinzato, C. Bressan, S. Marinetti, P.G. Bison, C. Bonacina (2002). *Monitoring of the Scrovegni Chapel by IR Thermography: Giotto at Infrared.* Infrared Physics & Technology, Vol. 43, pp. 165-169.

[38] E. Grinzato, F. Peron, M. Strada (1999). *Moisture Monitoring of Historical Buildings by Long Period Temperature Measurements.* Proc. of SPIE- The International Society of Optical Engineering, Thermosense XXI, D.H. Lemieux, J. R. Snell (Eds.),Vol. 3700, pp. 471- 482.

[39] N.P. Avdelidis, T. Kauppinen (2008). *Thermography as a tool for building applications and diagnostics.* In V.P. Vavilov, D.D. Bureigh (Eds.): Proc. of SPIE- The International Society of Optical Engineering, Thermosense XXX, Orlando, FL, Vol. 6939, pp. U1-5.

[40] D. Paoletti, D. Ambrosisni, S. Sfarra, F. Bisegna (2013). *Preventive thermographic diagnosis of historical buildings for consolidation.* In J. of Cultural Heritage, Vol. 14 (2), pp. 116-121.

[41] T.L. Hurtley (1994). *Infrared Techniques for electric utilities.* In X.P.V. Maldague (ed.) Infrared Methodology and Technology, International Advances in Nondestructive Testing, Monograph Series, Chap. 8, pp. 265-317, Gordon and Breach, New York

[42] Lu Shi-Gi, Y. Li, Y. Qian (2011). *Research on the applications of infrared technique in the diagnosis and prediction of diesel engine exhaust fault.* Journal of Thermal Science, Vol. 20(2), pp.189-194.

[43] B.B. Lahiri, S. Bagavathiappan, T. Jayakumar, J. Philip (2012). *Medical applications of infrared thermography: A review.* Infrared Physics &Technology, Vol. 55, pp. 221-235.

[44] K. Roback (2010). *An overview of temperature monitoring devices for early detection of diabetic foot disorders*. Expert Rev. Med. Devices, Vol. 7(5), pp. 711-8.

[45] M. Bharara, J.E. Cobb, D.J. Claremont (2006). *Thermography and thermometry in the assessment of diabetic neuropathic foot: a case for furthering the role of thermal techniques.* International J. Lower Extremity Wounds, Vol. 5(4), pp. 250-60.

[46] Q. Li, E. Liasi, D. Simon, R. Du, J. Bujas-Dimitrijevic, A. Chen (1999). *Heating of industrial sewing machine needles: FEA model and verification using IR radiometry.* In D.H. Lemieux, J.

R. Snell (Eds.): Proc. of SPIE- The International Society of Optical Engineering, Thermosense XXI, Orlando, FL, Vol. 3700, pp. 347- 357.

[47] M.H.A. Larbi Youcef, V. Feuillet, L. Ibos, Y. Candau, P. Balcon, A. Filloux (2012). *In situ quantitative diagnosis of insulated building walls using passive infrared thermography.* In Proc. of 11th International Conference on Quantitative Infrared Thermography-(QIRT11), Napoli, Italy, (CDROM).

[48] S.M. Shepard (1997). *Introduction to Active Thermography for Nondestructive Evaluation.* Anti Corrosion Methods and Materials, Vol. 44(4), pp. 236-239.

[49] N.P. Avdelidis, C. Ibarra-Castanedo, X. Maldague, Z.P. Marioli-Riga, D.P. Almond (2004*). A Thermographic Comparison for the Assessment of Composite Patches.* Infrared Physics & Technology, Vol. 45(4), pp. 291-299.

[50] N.P. Avdelidis, C. Ibarra-Castanedo, P. Theodorakeas, A. Bendada, E. Saarimaki, T. Kauppinen, M. Koui, X.P.V. Maldague (2010). *NDT characterisation of carbon-fibre and glass-fibre composites using non-invasive imaging techniques.* In X.P.V. Maldague (Ed.): Proc. of the 10th Quantitative Infrared Thermography Conference (QIRT10), Quebec City, Canada, pp. 703-710.

[51] X.P.V. Maldague (2000). *Applications of Infrared Thermography in Non Destructive Evaluation.* In P. Rastogi (Ed.): Trends in Optical Nondestructive Testing, Elsevier Publishing, city, pp. 591-609.

[52] G. Carlomagno, C. Meola, (2002). *Comparison between thermographic techniques for frescoes NDT.* NDT&E International Vol. 35 (8), pp. 559–565.

[53] C. Ibarra-Castanedo, J.M. Piau, S. Guilbert, N.P. Avdelidis, M. Genest, A. Bendada, X.P.V. Maldague (2009). *Comparative study of active thermography techniques for the nondestructive evaluation of honeycomb structures.* J. Research in Nondestructive Evaluation, Vol. 20 (1), pp. 1-31.

[54] Nondestructive Testing Handbook, Third Edition, Vol.3, Infrared and Thermal Testing, Chap. 15, ASNT, (2001), pp. 495-496.

[55] C. Ibarra-Castanedo, M. Genest, J.M. Piau, S. Guibert, A. Bendada, X.P.V. Maldague (2007). *Active Infrared Thermography Techniques For the Nondestructive Testing of Materials.* In C. H. Chen (Ed.): Ultrasonics and Advanced Methods for Nondestructive Testing and Materials Characterisation, World Scientific Publishing, City, Chap. 14, pp. 325-348.

[56] P. Zayicek, H. Kaplan (1999). *Infrared Thermography Field Application Guide.* EPRI, Paolo Alto, CA: 1999. Report TR-107142.

[57] Y.A. Plotnikov, W.P. Winfree (1999). *Temporal treatment of a thermal response for defect depth estimation.* In D.O. Thompson, D.E. Chimenti (Eds.): Review of Progress in Quantitative Nondestructive Evaluation, Vol. 19, pp. 587-594

Chapter 3

Active Infrared Thermographic Techniques

3.1 Introduction

When IRT has to be deployed for the evaluation of materials or components that are thermally static (all points are at ambient temperature), it is necessary to generate a flow of thermal energy such that the thermophysical and structural properties of the test object can be made to enhance or impede this flow. When this is done effectively, the analysis of the acquired thermal images can indicate the variations of these properties. In other words, active IRT by involving the introduction of a systematic and controlled amount of heat to the material under test and by monitoring the surface temperature evolution or decay with respect to time, is able to search for abnormalities in the thermal patterns, which can indicate "*defective zones*" or more generally "*areas of interest*", in accordance to established accept/reject criteria. The basis of all active thermographic approaches is the thermal excitation of the material under investigation and practically, as mentioned in the previous chapter, any kind of energy source can be used for this purpose. As a result, several types of thermal excitation procedures can be involved in active thermographic scenarios, including energy delivery mechanisms based on conduction, convection, thermal radiation, electromagnetic radiation, mechanical vibrations etc. For instance, thermal stimulation can be performed with ice, snow or the injection of hot/cold air. However, these configurations do not allow automation or repeatability and for this reason heating sources are generally used which, according to the nature of stimulation, can be further divided in the categories of optical, mechanical, induction and microwave stimulation. In addition, regardless of the heating source, stimulation can be applied under different excitation conditions as it will be presented next.

Based on the above mentioned and the way that the tested target is being stimulated, the aim of this chapter is to provide an overview of the theoretical principles and the experimental configurations of the most common in use active thermographic approaches along with some of their applications in the field of NDT&E. Initially, Pulsed Thermography (PT) is presented, as it is the most commonly used active thermographic technique due to its simplicity and rapid implementation. The description of Lock-in Thermography (LT) is following, which uses periodic heating instead of the pulsed heating, applied in Pulsed thermography, and can act as a useful tool in a variety of applications, providing straightforward quantitative information. Another active thermographic configuration is this of Step Heating Thermography (SHT) which experimental procedure is very similar with that of pulsed thermography; however the monitoring of the heating up phase is of prime interest in such types of inspections. Additionally, a presentation of long excitation based active configurations whose main difference from Pulsed and Step heating Thermography is the long excitation and observation times is discussed. Finally, the chapter is ending with a brief description of other forms of active thermal imaging such as Vibrothermography (VT) and Eddy Current Thermography (ECT) which involve mechanical and electromagnetic excitation respectively, and the active configuration of Line-Scan Thermography (LST), where the heating source and the camera are moved along the area of inspection with a predefined speed and in fixed distance between them.

3.2 Pulsed Thermography (PT)

PT -also known as Flash Thermography when working with optical flash devices- is one of the most common forms of active thermography [1], as it can be involved in a variety of applications. PT can be defined as a technique where energy is applied to the specimen using a pulsed excitation by a quick burst of heat energy. The pulsed duration can vary depending of the material thickness and its thermal properties (i.e. thermal conductivity, thermal diffusivity) and it can be a matter of few milliseconds for high conductivity materials such as metals, while for low conductivity materials such as plastics and polymer laminates, the pulsed duration can be matter of few seconds [1]. The excitation source can heat up or cool the object under investigation with respect to the surrounding environment, since the important point in all active thermographic schemes is the propagation of a thermal wave into the material. When working with optical devices, the delivery of a brief amount of energy on the surface of the test target results to the sudden surface temperature increase (in the case of warm excitation) from the initial thermal perturbation, which subsequently decreases as the thermal wave penetrates into the bulk material. Data acquisition in pulsed thermographic investigation consists of the recording of IR images' sequence as a function of time after the pulsed excitation occurrence. The presence of any subsurface defect or discontinuity alters the diffusion rate so that when observing the surface temperature, defects appear as surface regions of different temperatures. In particular, as time elapses defective zones will appear at higher or lower temperature on the surface with respect to non defective regions, depending on the thermal properties of both the material and the defect and the amount of energy deposited on the surface.

The initial temperature increase in PT configuration is of a few degrees, which is no long enough to cause damage to the material under inspection. As a result, the stimulation in PT preserves the non-destructive character of this technique; however this is limiting its detectability strength [2,3]. Major attractions of the technique are its fast and simple implementation as the inspection only depends on the thermal stimulation pulse, and no physical contact with the material being inspected is required. However, results can be easily affected by a variety of factors [2,4,5] such as environmental reflections, surface emissivity variations, non-uniform heating and surface geometry variations. Nevertheless, the effects of the aforementioned problems can be reduced by using advanced signal processing algorithms which have been especially developed to process pulsed thermographic data and to enhance the detectability by improving the signal-to-noise ratio of the acquired results [6]. In other words, defect enhancement techniques have to be applied in order to produce a successful thermographic inspection when working with pulsed thermographic data.

3.2.1 Theoretical aspects in Pulsed Thermography

The basis of PT can be best understood by considering the underlying physical process of incident heat pulse interaction with a subsurface defect. Immediately after illumination by a spatially uniform

light pulse, the material will absorb some of the incident energy and the thermal response of a semi-infinite, opaque solid body can be described by the Fourier's law of heat diffusion or heat diffusion equation [7]:

$$\nabla^2 T - \frac{1}{\alpha}\frac{\partial T}{\partial t} = 0 \qquad \text{(Eq. 3.1)}$$

where ∇ is the the 3D del operator (in the 3D Cartesian coordinate system is given by: $\nabla = i \cdot \partial/\partial x + j \cdot \partial/\partial y + k \cdot \vartheta/\vartheta z$), $T = T(x, y, z, t)$ is the time-dependent temperature of the sample and $\alpha = k/\rho c_p$ [m^2/s] its thermal diffusivity, with k [W/mK] the thermal conductivity, ρ [kg/m^3] the mass density, and c_p [J/kg K] the specific heat under constant pressure. From the above equation, it can be observed that in the absence of any subsurface discontinuity, the surface temperature decay depends on the thermal diffusivity of the bulk material. However, when an insulting subsurface defect or discontinuity obstructs the flow of heat into the sample, the temperature decay is retarded and the surface region above the defect cools at a slower rate compared to the defect-free regions, resulting in a localized temperature difference ΔT (thermal contrast). Thus the monitoring of temperature-time signal contains information about the thermal properties of the material being inspected and can further identify the presence of any subsurface defects or discontinuities.

The 1D solution of the Fourier equation for the propagation of a *Dirac* heat pulse (an ideal waveform defined as an intense unit-area pulse of so brief duration that no measuring equipment is capable to distinguishing it from even shorter pulses [8]) in a semi-infinite homogeneous and isotropic solid by conduction has the form [7] :

$$T(z,t) = T_0 + \frac{Q}{e\sqrt{\pi t}} \exp\left(-\frac{z^2}{4\alpha t}\right) \qquad \text{(Eq. 3.2)}$$

where Q [J/m^2] is the energy absorbed by the surface, T_0 [K] the initial temperature and $e = (k\rho c_p)^{1/2}$ [$Ws^{1/2}\ m^{-2}K^{-1}$] the material thermal effusivity. A *Dirac* heat pulse is composed of periodic waves at all frequencies and amplitudes. However, it is not possible to reproduce such a waveform. In practice, a heat pulse provided by a powerful source such as photographic flashes has approximately a square shape [9] and in this case, the signal is composed of periodic waves at several frequencies. The shorter is the pulse, the broader the range of frequencies. At the surface (z=0 mm), Equation 3.2 can be written as follow [7]:

$$T(0,t) = T_0 + \frac{Q}{e\sqrt{\pi t}} \qquad \text{(Eq. 3.3)}$$

Although Equation 3.3 is only an approximation of the complex 3D diffusion problem described by Fourier's law (Eq. 3.1), many of the PT processing techniques are based on this simplification to perform qualitative and quantitative analysis. According to the above simplification, after the thermal excitation the temperature rise ΔT at a given point of the sample surface diminishes with time t, due to the heat diffusion into the sample, according to the expression [7]:

$$\Delta T(t) = \frac{Q}{e\sqrt{\pi t}} \quad \text{(Eq. 3.4)}$$

In pulsed thermographic inspections, deeper defects will be observed later due to the longer time taken for the thermal wave to reach them and. The time taken for the thermal wave to be reflected back to the surface is inversely proportional to the thermal diffusivity of the material and directly proportional to the square of the defect depth [10,11], which can be expressed by Equation 3.5. In addition, the loss of contrast is proportional to the cube of the depth of the defect [12] and is determined by Equation3.6.

$$t \approx \frac{z^2}{a} \quad \text{(Eq. 3.5)}$$

$$c \approx \frac{1}{z^3} \quad \text{(Eq.3.6)}$$

where *t* is the observation time, *z* is the depth of the defect, *a* is the thermal diffusivity of the material and *c* the loss of contrast. The above two relations show the limitation of PT. In particular, due to the fact that in PT the heat energy of the spreading thermal front disperses in all directions through the test specimen, the resulting thermal effects of internal discontinuities appear with weak contrast and only shallow defects are clearly observed. An empirical rule of thumb states that *the radius of the smallest detectable discontinuity should be at least one to two times larger than its depth under the surface* [2,13].

3.2.2 Pulsed thermographic experimental procedure and data analysis

As discussed above, PT is based on the thermal stimulation of the inspected sample and the analysis of its thermal response. The inspection usually includes three phases which are presented in Figure 3.1 and these are:

- *Thermal Excitation*

The first step in order to perform a PT investigation is to apply a spatially-uniform external thermal flux of energy for a short period of time which will cause a sudden increase of temperature in the surface of the test object. The duration of pulsed excitation as discussed above, can last from a few milliseconds to a few seconds with respect to the thickness and the thermal properties of the sample under investigation (Figure 3.1a).

- *Observation of thermal response and data acquisition*

The thermal pulse, which is delivered on the surface in the first phase, propagates through the material via conduction. During the propagation of the excited pulse, the IR camera scans the front surface, recording a sequence of thermal images and representing the thermal distribution of the surface as a function of time. Essential parameters that shall be taken into consideration in any PT measurement are the required amount of external energy in order to achieve a satisfactory thermal excitation of the sample, the total observation time of the cooling phase and the number of thermal images to be acquired

in the thermographic sequence (defined by the acquisition frame rate). A synchronization control unit is usually needed to control the time between the launch of the thermal pulse and the recording of the thermographic sequence. Data is stored as a 3D matrix as can be seen in Figure 3.1b, where the acquired frames in the thermographic sequence are characterised by a Δt time interval. In PT two methods of observation are possible: thermal reflection and thermal transmission modes (Figure 3.1a). In the thermal reflection method both the heat source and the infrared camera are placed on the same side, towards the front surface of the inspected sample. Contrary, in the transmission mode, the infrared camera is placed on the opposite side to the heat source. Each method of observation has its advantages and disadvantages. The reflective observation method is a single side inspection and provides high resolution but only shallow defects can be revealed. The transmission mode, on the other hand, needs accessibility to the rear side and has lateral resolution lower than this in reflection method. Nevertheless, transmission mode allows the detection of shallow as well as deep defects but does not provide defect depth information.

- *Data analysis*

After data acquisition and storage, the thermographic sequence can be analyzed in order to retrieve qualitative and quantitative information such as the defect location and shape. In brief, the analysis of temporal data can be explained as follow: hidden defects change locally the thermal properties of the material and as the thermal wave propagates into the material bulk, the surface cooling rates in defect and defect-free areas are not uniform. The presence of an internal defect or irregularity having a thermal resistance greater than the bulk material causes the reflection of the heat waves back to the surface and a local thermal contrast is observed on the acquired thermal images with respect to the surrounding sound area. The time-dependence of the temperature of a defective and a defect-free pixel is schematically plotted in Figure 3.1c. As can be seen from the representative plot, when monitoring the surface temperature, inhomogeneities show up as areas of different temperature (Pixel 2) with respect to the homogeneous part of the sample (Pixel 1). As a result, the produced thermal contrast indicates the presence of subsurface defects.

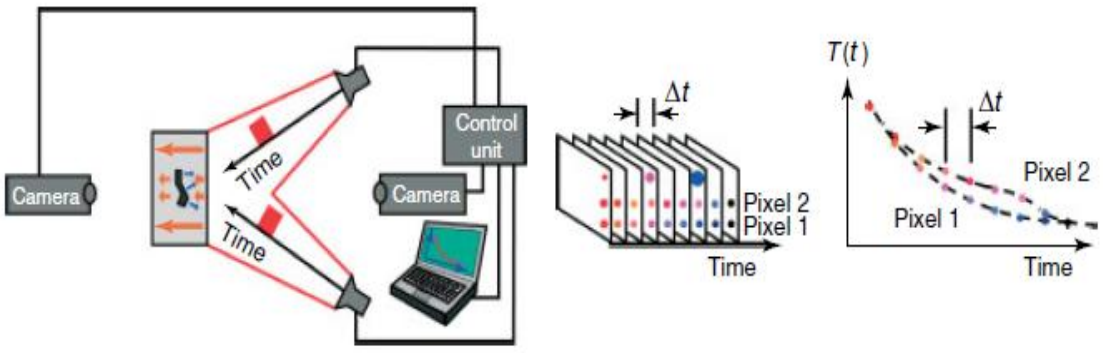

(a) *(b)* *(c)*

Fig. 3.1: *Principle and experimental arrangement of pulsed thermography (a) experimental procedure (b) data acquisition and (c) data analysis. Images are recorded at time intervals Δt and temperature plots of single pixels as a function of time can reveal the differences in the cooling rates due to anomalies [14].*

3.2.3 Applications of Pulsed Thermography in NDT&E

PT can be used in a variety of inspection processes as the potential of this technique to perform depth-resolved inspections in short measuring times has exploited its use in several industrial sectors. Furthermore, new application fields for PT are constantly emerging, thanks to the advancements in the technology of IR cameras manufacturing and pulsed signal processing algorithms development. Some of the applications of PT include the control inspection of aerospace structural components [15-20], the inspection of turbine blades [21-23] and the evaluation of adhesion integrity on plastic welded joints [24]. Several studies have been performed involving PT technique for the assessment and defect characterisation in a variety of composite materials and structures such as fibre reinforced polymers and metals [25-27] or honeycomb structures [4], as well as for the evaluation performance of bonded composite joints and patches [28,29]. PT has also been proposed for moisture detection and integrity inspection of building materials [30-32], as well as for the investigation of art objects and historic artefacts [33-35]. Additionally, several research works used PT for the characterization of defects such as cracks, delaminations and impact damage [36-40], as well as for corrosion monitoring in metallic components [41]. Lastly, methodologies based on pulsed heating and monitoring of the surface temperature decay have been proposed to estimate the thermal properties of various materials [42-44] such as thermal diffusivity, thermal effusivity heat capacity and thermal conductivity or to investigate physical characteristics such as porosity which can further provide information about the bond integrity of the structure [45,46].

3.3 Lock-in Thermography (LT)

LT [47] can be considered as the development of photothermal radiometry [48] in which a modulated laser source is used to periodically illuminate point-wise the object's surface by injecting thermal waves into the specimen. In photothermal imaging, the thermal response is recorded using an infrared detector and decomposed by a lock-in amplifier in order to obtain phase and amplitude information for the modulation at each point of inspection [47]. Consequently, photothermal imaging as a point by point inspection technique requires long acquisition times (e.g. in the case of deep defects detection where low frequencies shall be involved or in a large sample inspection) and as mentioned above, additional to the investigation equipment, hardware is also needed in order to extract the phase and amplitude of the thermal response. The advantage of LT compared with photothermal radiometry is as follow [49,50]: the laser beam is replaced with one or several modulated heating sources (i.e. halogen lamps) which are covering the entire sample surface instead of only one point, and the infrared detector is replaced with an infrared camera capable of monitoring large surfaces. Moreover, in LT with the use of software capable to retrieve mathematically the amplitude and phase of the thermal response, no extra hardware (lock-in amplifier) is required as in the case of photothermal imaging. As a result, LT dramatically

simplifies and speeds up the acquisition process for imaging NDT applications compared with photothermal radiometry.

In terms of experimental setup, LT, also known as modulated thermography [51], is very similar with PT; however in this case the thermal excitation is delivered to the specimen surface in the form of periodic waves, contrary to the pulse energy applied in the case of pulsed excitation. In the majority of the cases, sinusoidal waves are typically used as input providing the advantage of preserving the frequency and the shape of the response. The main advantage of this technique is that quantitative information for the location of an internal area of interest can be achieved straightforward, as a direct relationship between the diffusion length of the thermal wave and the inspection frequency exists, providing depth retrieval estimations through amplitude and phase data without further processing.

The energy required to perform an LT experiment is generally less than in other active techniques, which might be valuable if a low power source is to be used or if special care has to be given to the investigated specimen such as for the inspection of cultural heritage objects [52]. However an inspection with LT covering a large number of depths requires longer times than other approaches such as PT, since many different modulation frequencies have to be applied for each depth inspection. For instance, the acquisition time required for a modulation cycle of 1 Hz is at least 1 s while 0,1 Hz requires at least 10 s and so on [2]. The long acquisition times in combination with the fact that dynamic equilibrium must be established before reaching a permanent regime and starting a new measurement, are making LT a time consuming inspection procedure. Additionally, the availability of heat flux modulation frequencies may not be sufficient low in order to acquire information and detect deeper defects [52].

3.3.1 Theoretical aspects in Lock-in Thermography

Heat diffusion from periodical transfer of energy through a solid semi-infinite body results in a time-dependent thermal wave which in one dimension (through the 1D solution of the Fourier's heat diffusion law for a periodic thermal wave) is given by [53]:

$$T(z,t) = T_0 exp\left(-\frac{z}{\mu}\right) expi\left(\omega t - \frac{z}{\mu}\right) = A(z) expi(\omega t - \varphi(z)) \qquad \text{(Eq. 3.7)}$$

where T_0 [^{0}C] is the initial change in temperature produced by the heat source, $\omega=2\pi f$ [rad/s] is the modulation frequency, f [Hz] is the wave frequency, $A(z)$ is the thermal amplitude, $\varphi(z)$ is the phase shift of the thermal wave travelling inside the material and μ [m] is the thermal diffusion length, which is dependent from the thermal diffusivity α and the wave frequency f [53]:

$$\mu = \sqrt{\frac{2 \cdot \alpha}{\omega}} = \sqrt{\frac{\alpha}{\pi \cdot f}} \qquad \text{(Eq. 3.8)}$$

Equation 3.8 states that the thermal waves propagate deeper in more diffusive materials but information about deeper features is available at lower frequencies as the observed frequency-

dependent behaviour is a direct consequence of the inverse relationship existing between the diffusion length and the modulation frequency. Consequently, thermal waves of lower frequency flow into the material deeper than high frequency waves, however their penetration speed is lower as it is dependent on the modulation frequency [54].

3.3.2 Lock-in thermographic experimental procedure and data analysis

The experimental setup of LT is depicted in Figure 3.2. Two lamps are shown although it is possible to use several lamps mounted on a frame to increase the uniformity of excitation and further increase the amount of energy delivered to the surface. The lamps send periodic waves (sinusoids for example) at a given modulation frequency ω, for at least one cycle, which depends on the specimen thermal properties and the defect depth (Eq. 3.8).

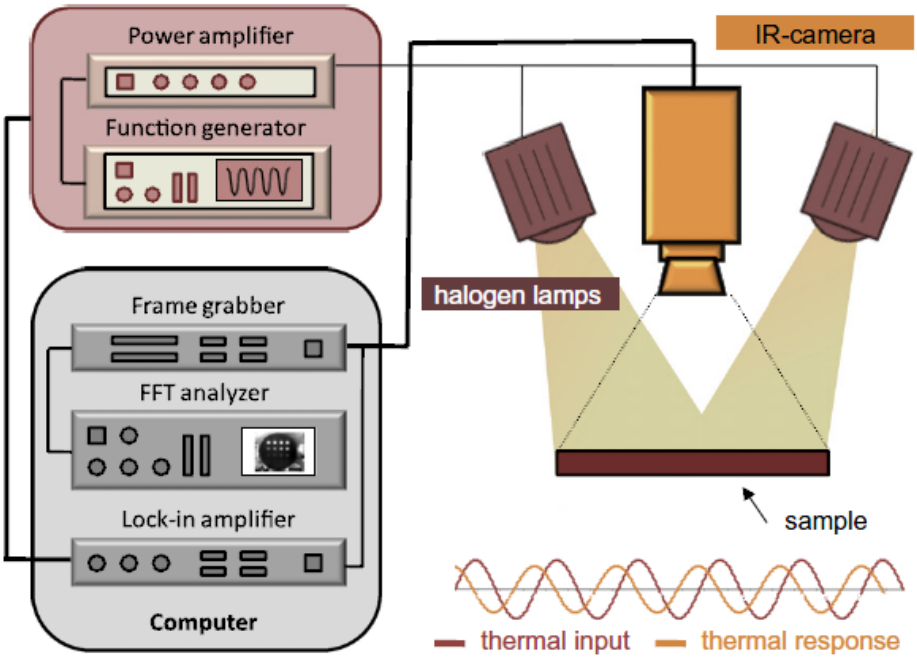

Fig. 3.2: *Experimental setup of lock-in thermography, working with optical devices as excitation source [55]*

Optical waves propagate by radiation through the air and when reach the specimen surface, energy is absorbed penetrating into the material as thermal waves. The incident wave is described by a position and a time-temperature modulation which is used as a reference in order to measure changes in the amplitude and phase of the reflected thermal wave. In particular, as the thermal wave penetrates into the material bulk, at the location of internal interfaces it is reflected back to the surface. The reflected thermal wave interferes with the incident wave, generating a measurable temperature modulation at the surface of the component which can be detected

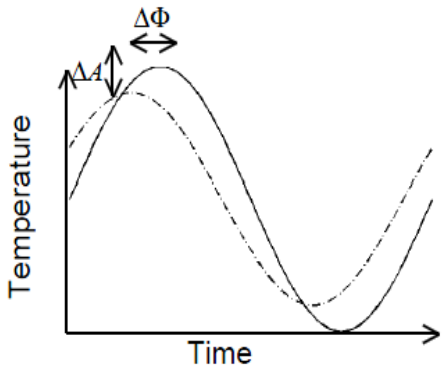

Fig. 3.3: *Computation of phase and amplitude shifts between the incident and reflected wave.*

with the aid of an infrared camera. In other words, the main objective with LT is the measurement of the produced changes in the amplitude and phase of the response signal at the surface due to internal defects. In practice, different methods [49,56,57] are used to compute phase and amplitude shifts between the incident and the response signal. As discussed above, both the amplitude and phase images can be used for the purpose of defect detection, however various studies have shown that the phase data is relatively undisturbed by problems associated with non-uniform heating and emissivity variations contrary to amplitude data [51-53].

In the case of sinusoidal excitation, amplitude and phase images can be retrieved by knowing the coordinates of four equidistant points in the reference and in the response signal respectively, following the equations [58]:

$$A = \sqrt{(S_1 - S_3)^2 - (S_2 - S_4)^2} \qquad \text{(Eq. 3.9)}$$

$$\varphi = tan^{-1}\left(\frac{S_1 - S_3}{S_2 - S_4}\right) \qquad \text{(Eq. 3.10)}$$

where S_i is the photothermal signal of a point taken at time t_i. This procedure is known as four points algorithm [49,58] and is illustrated in Figure 3.4.

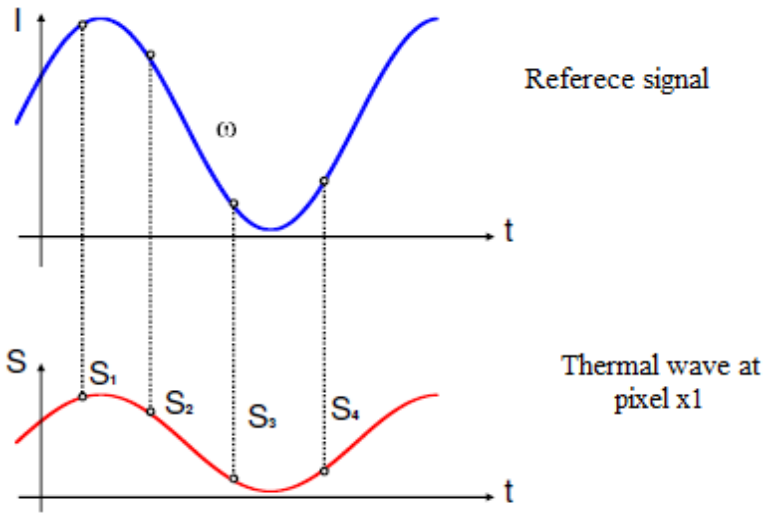

Fig. 3.4: *Four-point algorithm principle for the computation of amplitude and phase images in the presence of sinusoidal excitation: Modulation of illumination I (top), and reconstruction of thermal wave signal S at pixel.*

The sinusoidal input is represented on the top of Figure 3.4, while the response signal is depicted at the bottom. Input and output have the same shape when sinusoids are used; however there is only a change in amplitude and phase that can be calculated from Equations 3.9 and 3.10. The four-point method is fast in order to calculate the phase and amplitude shifts, however it is only valid for sinusoidal stimulation and is affected by noise. In practice, the signal can be de-noised in part by averaging several images instead of a single one and/or by increasing the number of modulation frequencies to be used [49,58].

Another way to extract amplitude and phase information from the LT data is based on the Fourier transform. Image sequences are analyzed pixel by pixel and the time dependent thermographic sequence is transformed pixel-wise using the discrete Fourier transform which was initially proposed for pulsed thermographic data [56] (see Chapter 4). Thereby, the signal is decomposed into real and imaginary parts which are used to estimate the amplitude and phase. A detailed description of this technique is presented in the following chapter.

The amplitude and phase information acquired in the frequency domain through LT can provide quantitative evaluations in a straightforward manner. In particular, Equation 3.8 demonstrates the direct relationship between the depth of a defect and the thermal diffusion length μ, as the depth can be correlated with the diffusion length in which the thermal properties of the defect are making this variation obvious. Through research studies, it has been observed that when working with amplitude data, the maximum detectable depth is equal to μ [59], while when working with the phase the maximum detectable depth is approximately1.8μ [60-64]. Thus it is preferable to show results in terms of phase angle, since it provides deeper probing capabilities.

In general, for a correct non-destructive evaluation using LT approach, it is necessary to select the heat flux frequency in a range appropriate for inspection of the object through its entire thickness. Tests should start at with quite high frequency value to investigate the surface layer; then the frequency value must be decreased to investigate deeper layers, after which the frequency must be further reduced; this procedure shall go on until the entire thickness of the specimen is investigated or the minimum available frequency value is set. Information about the thermal diffusivity and the thickness of the investigated object are considered essential for appropriate selection of wave frequencies and a correct non-destructive evaluation by means of LT [55].

3.3.3 Applications of Lock-in Thermography in NDT&E

Applications of LT are numerous and in different fields, as its experimental implementation is simple and straightforward. The approach has been used to acquire information about the fibre orientation and detect the position of local inhomogeneities in the interior of fibre reinforced composites [65], to detect delaminations or hidden subsurface features in multilayered structures[49,66,67], to measure the thickness of ceramic coatings [68,69], and inspect aircraft components in order to reveal internal defects [70,71]. In addition it has been used for the evaluation of different materials such as metals [60], polymers [72,73] and composites [74], as well as for the evaluation of different assembling ways such as adhesively bonded and welded joints [75]. Several studies have been produced, presenting the effectiveness of LT as a functional diagnostic technique in solar cells inspections and electrical installations control [76,77]. Lastly, LT has been used for the assessment of cultural heritage objects [52] acquiring information not only about possible common defects (i.e. detachments, cracks), but as well as for material composition and previous restoration interventions.

3.4 Step Heating Thermography (SHT)

SHT [78] is an inspection technique, which is based on the monitoring of the specimen's surface temperature variation as a function of time, during the application of a heating pulse. More specifically, in SHT the surface temperature rise of the sample is monitored with respect to time while the sample is continuously heated at low power usually from several seconds to a few minutes [2]. This technique, also referred as Time-Resolved Infrared Radiometry (TRIR) [79], differs from pulsed excited configuration in that the thermal behaviour of the specimen surface is of prime interest during the transient heating phase [80], contrary to PT where the temperature decay is of interest as the sample cools down. As a result, the utilization of low intensity heat sources in step heating procedure allows a longer heating period enabling deeper defects detection without damaging the investigated specimen. The typical experimental setup for SHT consists of a heat source and an infrared camera as in the case of PT inspection. However, the beginning of the heating procedure is triggered with respect to the acquisition of IR images, which are recorded sequentially. As in all active thermographic techniques, in the case of step heating thermography, the variation in the surface temperature with time depends on the heat diffusion inside the structure, which is affected by the existence of embedded features. Although from the experimental point of view SHT is different than PT, both procedures provide thermal signals that contain exactly the same information [81]. As a result, the choice to apply either the pulsed or the step heating approach will thus depend on the applications, and more specifically, on the time scale of the phenomena of interest. Slow phenomena are better investigated under step heating stimulation, while fast phenomena are better monitored with pulsed thermography.

Specific advantages of this technique include the ability to determine either defect depth or material's thermal characteristics from a single test without the need for a calibration measurement made on a defect-free region of the specimen [82]. Moreover, by applying heating of low energy, the time varying temperature change on the surface of the specimen can be maintained at a high level throughout the measurement process and simultaneously the parallel nature of the detection process (excitation and monitoring) allows large areas to be studied in a single test.

3.4.1 Theoretical aspects in Step Heating Thermography

Figure 3.5 presents a section of a material with an internal inclusion of different thermal properties. As can be seen from the schematic, if the thickness of the material is equal to L along the direction parallel to the radiation then the front-face of the defect is located at depth L_1. The thermal properties of bulk material and defect are described by thermal effussivity, which is constant throughout the volume of the two phases and if $e_0 \neq e_1$ then the temperature T_0 measured over the defect-free region will differ from temperature T_1 measured over the area of the defect. The surface temperature rise at any time for the one dimensional heat transfer in a two layers structure (Figure 3.5) is given by [83]:

$$T(t) = C_c\sqrt{t}\left\{1 + \sum_{n=1}^{\infty} 2(-\Gamma)^n \left[exp\left(-\frac{n^2L^2}{a_o t_0}\right) - \frac{nL\sqrt{\pi}}{\sqrt{a_o t}} erfc\left(\frac{nL}{\sqrt{a_o t}}\right)\right]\right\} \qquad \text{(Eq. 3.11)}$$

where T is the surface temperature, t is the time, α is the thermal diffusivity, C_c is a contrast term related to energy absorption [84], L is the top layer thickness (corresponds to L_1 in the schematic), and finally Γ is the mismatch factor between the two layers. The mismatch factor is a dimensionless unit which thermally characterises a set of two materials and is defined as [84]:

$$\Gamma = \frac{e_1 - e_o}{e_1 + e_o} \qquad \text{(Eq. 3.12)}$$

with e [$Ws^{1/2}$ $m^{-2}K^{-1}$] being the thermal effusivity given by $e = \sqrt{c \cdot \rho \cdot k}$ and subscripts 0 and 1 corresponding to defect-free and defective layer respectively. Mismatch factor Γ, as stated above, is a dimensionless unit and varies in a constant range of -1 up to 1. Its value gives information of how much two materials differ in thermal sense and if its absolute value is close to 1, it indicates a good ability to draw a distinction between a defect and a defect-free area by analyzing the temperature gradient on the surface of the inspected material. Additionally, if $\Gamma \neq 0$ then sign of Γ indicates which material is thermal insulator in relation to the second. In Table 3.1 an explanation of the meaning of thermal mismatch factor in TNDT is presented through some characteristics values.

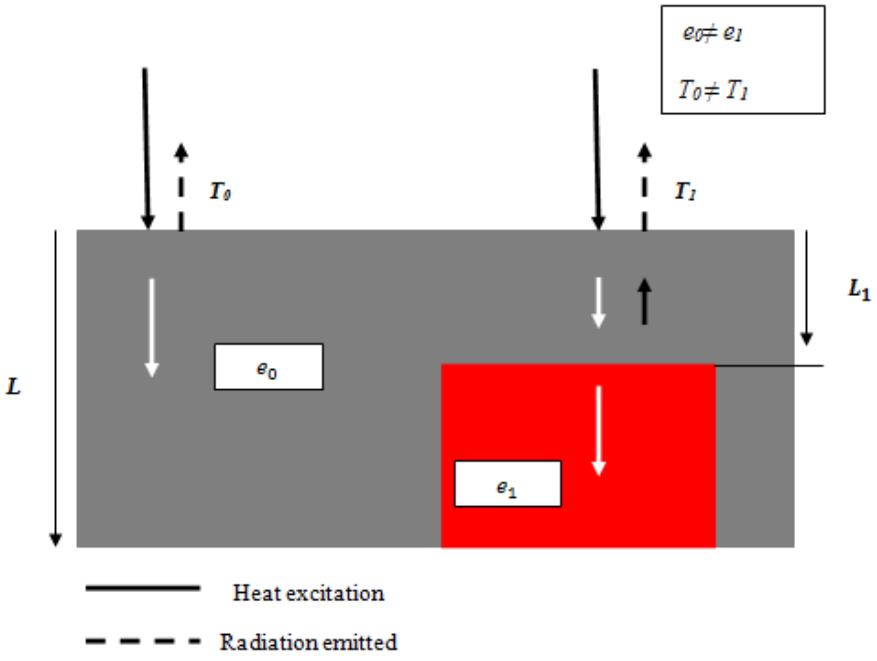

***Fig. 3.5**: Heat Transfer of in homogenous and inhomogeneous body.*

Table 3.1: *Thermal mismatch factor Γ and its meaning in TNDT*

Value of mismatch factor Γ	***Defect in relation with the bulk material***	***Temperature rise of the surface of material with defect related with the defect free area***	***Detectability of defect by IR thermography***
-1	Good thermo insulator	faster	high
-0.1	Weak thermo insulator	Slightly faster	low
0	The same	The same	Impossible
0.1	Weak thermo insulator	Slightly slower	low
1	Good thermo insulator	slower	high

3.4.2 Step heating experimental procedure and data analysis

As stated above, the temperature increase during the application of a step heating pulse is monitored through the sequential acquisition of thermal images in a predefined time interval. According to Equation 3.11, the surface temperature increases linearly with respect to the square root of time in the case of a homogeneous material (Γ=0) [84]. However, in the case of a two layers structure (i.e. embedded defect) the surface temperature exhibit the same linear behaviour at early times as the thermal wave penetrates in the first layer, however when the heating front reaches the substrate (of different thermal properties), the rate of temperature may increase or decrease as it deflects from the linear behaviour to the square root of time. The value of time when the deflection occurs is an important parameter in SHT and referred as *transit time* t_T which can be defined as the square root of time when the temperature plot departs from linearity. The thermal transit time is not affected by the mismatch factor, however the changes in temperature excursion below the linear case can indicate positive values of Γ and represents cases where the subsurface has higher thermal effusivity than the surface layer and vise versa [2]. Data processing in step heating approach includes the determination of the thermal transit time t_T through normalized temperature and the correspondent normalized temporal data [2,84].

3.4.3 Applications of Step Heating Thermography in NDT&E

The simplicity of the required equipment and testing procedures makes SHT an attractive inspection method for in-field applications. It is an effective method for determining physical parameters of coatings such as thickness and thermal diffusivity and characterizing the degree of coating disbanding [78,85,86]. In addition, SHT has been used to characterise damage in composites [87-90], detect vertical cracks in a range of materials and characterise heat sink efficiency in microelectronic devices [91]. Lastly, the use of the approach has also been reported in order to evaluate and distinguish different types of surface crusts in arid and sub arid soils [92]. Although at the moment mainly optical excitation has been used in step heating, there is no limitation to the use of other excitation forms.

3.5 Long excitation based techniques

Long based excitation testing is an active thermographic concept able to provide qualitative and quantitative thermal scanning of various structures and elements. Its basic characteristic is the submission of the investigated sample to a long square pulse heating procedure through a continuous heating pulse that may last from several seconds up to several minutes [93,94]. The experimental procedure and data acquisition is very similar with that of PT, as the temperature decay is monitored using an infrared camera after the application of the long pulse heating; nonetheless the heating up phase can also be recorded as well [95], similarly to the step heating approach. However as can be understood, the main differences of this configuration contrary to the traditional PT and/or SHT are the long duration of the heating excitation and the long observation time of the temperature decay and/or evolution. In this kind of inspections different heating units can be used including radiant and fan heaters or systems with multiple halogen lamps, while the heating procedure can be done dynamically by moving the heating source under computer control or manually in order to obtain a nearly homogeneous initial temperature distribution. This technique can be usefully applied in specific applications where the long thermal excitation cannot create further damage to the sample (i.e. structural evaluation in civil engineering) and locate deeper defects in low diffusivity materials, that cannot be detected with other infrared imaging techniques [96,97].

The basic principle of long heating techniques such as cooling down thermography [96] and long square pulsed thermography [98, 99] is to bring the sample under inspection in a moderate uniform temperature and then place it in an ambient with a lower temperature. In ambient temperature, the sample starts loosing heat from its surface by irradiation while inside the sample, the temperature gradient between the surface and the deeper regions produces a conductive heat flow to the surface that is altered by the presence of internal defects. The monitoring of the surface temperature decay can thereby reveal deep internal defects. This technique however is less flexible than other nondestructive imaging approaches as its main disadvantage is the long time in order to complete a single experiment.

In long pulsed heating techniques, the most common detection procedure involves the use of the so called "*reference point*" selected by the operator from a presumably sound area and the performance of temperature computations in a differential mode as presented in Figure 3.6. In other words, the detection with long pulsed thermography is based on the identification of maximum temperature contrasts along with their correspondent observation times which can be determined

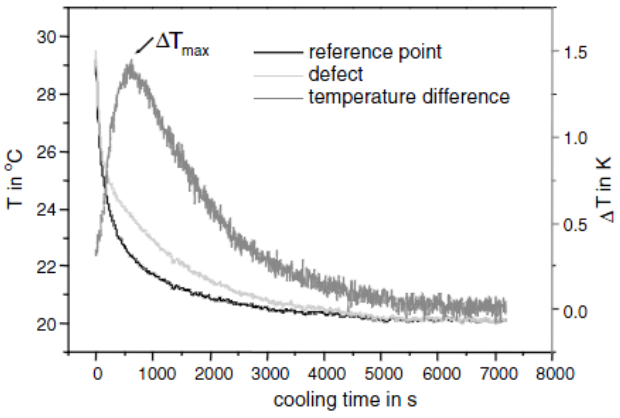

Fig. 3.6: *Transient curves above a sound area and a defect and the representative difference curve with a maximum temperature deference ΔT_{max} [100].*

from the IR images. After determining experimentally the values of ΔT_{max} and t_{max}, through particular inverse procedures information regarding the depth and the size of the features can be retrieve combing numerical calculations and experimental results [100,101]. Recently a new approach for quantitative long square pulse thermography demonstrates the processing of temporal data in the frequency domain in order to extract quantitative depth information without the aid of numerical stimulations [102].

As discussed above, long excitation-based techniques find numerous applications especially for civil engineering inspections. In particular, this type of inspection can be assessed for the investigation of masonry structures [97,103] for the characterization of masonry structure beneath plaster, the detection of voids, delaminations and subsurface and/or surface cracks. In addition, investigations under long excitation heating have been reported for the assessment of the structures with carbon fibre reinforced plastics (CFRPs) for reinforcing concrete structures [104], and on honeycomb aerospace components [105].

3.6 Other forms of Active Thermography

As presented above, the most important heating functions in active thermography are these of an instantaneous pulse excitation, the step heating function, modulated heating and square pulse heating function. Based on these excitation modes it is obvious that the way of thermal stimulation defines the name of the thermographic concept, highlighting the mode of excitation as an important characteristic in all active infrared thermographic concepts. The above classification according to the way that the test object is being stimulated, derives from the fundamental principle that the information obtained in each thermographic procedure are strongly related by the heating process, governing each concept. A second classification derives from the type of the excitation source used (i.e. optical, mechanical, induction etc.) which also defines its name, highlighting the excitation type as another important characteristic of active thermography. Following this principle, apart from optical excitation, mechanical excitation is a very common stimulation process which involves sonic or ultrasonic waves and refers to Vibrothermography or eddy currents induction which refers to Eddy Current Thermography. In following subsections, brief descriptions of the theoretical and experimental aspects of the aforementioned approaches along with a brief presentation of the line scan heating function are discussed.

3.6.1 Vibrothermography (VT)

VT was first introduced as an inspection method in the late 1970's as it was observed that cracks or delaminations in a solid material, after the excitation with high energy-low frequency ultrasound, were generating heat which could be detectable with the aid of an infrared camera [106,107]. Despite the promising start, this technique remained dormant until recently, when techniques known as ultrasound thermography [108], or thermosonic testing [109] were introduced. Significant improvements in IR camera performance made it possible to detect small cracks using low excitation energies or short

duration pulses of high energy. As a result, there has been considerable renewed interest in implementing VT as a nondestructive crack detection method [110].

In contrast to the classical thermographic setup, where the energy is delivered to the surface of the sample externally through a heat source (e.g. optical devices), in VT the sample is mechanically excited by sonic or ultrasonic waves. This active technique utilizes mechanical waves to internally stimulate hidden defects without heating the surface as in optically excited methods. The excitation is carried out by coupling an ultrasonic transducer to the sample surface, generating mechanical waves, which are traveling in all directions in the material interior. Due to the direct conversion from mechanical to thermal energy, heat is released by friction precisely at the locations of defective zones such as cracks and delaminations [107]. In other words, mechanical excitation acts as a selective inner heat source diffusing inside the material and VT can locate defective areas by detecting temperature variations at the surface.

In VT, two basic configurations can be considered as analogues to optical excitation methods. Lock-in VT is analogue to optical Lock-in approach; while the second technique Burst VT is analogue to optical pulsed thermographic configuration. In the case of lock-in VT [111,112], the ultrasonic wave used to excite the structure is amplitude modulated at a low frequency resulting to periodical heat generation. The main advantage of this method is that a relatively low excitation power is used. However, by applying a single-frequency amplitude modulated excitation to the sample it is possible that the frequency does not match for the application and for this reason frequency modulated VT has also been introduced in the field of TNDT [113], where a range of ultrasonic frequencies is used in a single experiment. In comparison to modulated excitation, the second technique Burst VT [114,115] uses short oscillation bursts in order to internally excite the sample under inspection. This configuration aims to reduce the testing times as the vibration is applied for a very short time (normally less than 1 s) with the aim of producing a quantity of heat at the defect, which can be detected in the form of surface temperature rise by the IR camera. The heating up is followed by a cooling down period, which is recorded similarly to the case of optical PT. The brief pulse of mechanical energy in burst VT ranges in the frequencies of 15 to 50 KHz and the energy delivered to sample is typically in the range of 500-3000 Joules [116]. The experimental setup for burst and modulated VT are illustrated in Figure 3.7.

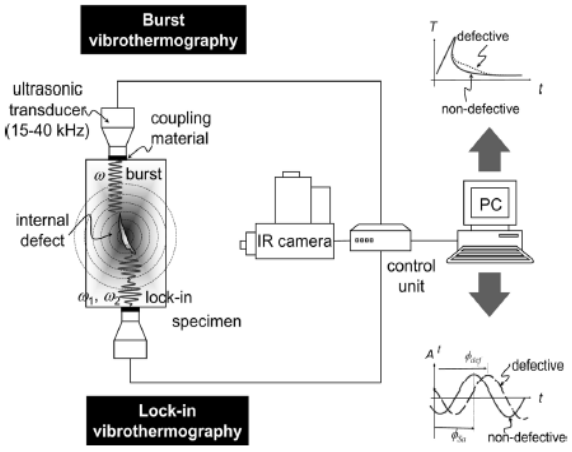

Fig. 3.7: *Schematic setup of the experimental arrangement in Vibrothermography. Inspection can be carried out in either burst or lock-in mode [4].*

Ultrasonic excitation is ideal for NDT imaging as the defect detection is independent from its orientation inside the specimen, and both internal and open surface defects can be detected. However, both brust and modulated VT require attention to some experimental parameters [116]. Although the amplitude, frequency and duration of the mechanical excitation are factors that affect the internal defects stimulation (and detectability), these factors are less critical than some other details of the experimental setup which can undermine the detection process. In particular, when applying vibrothermal NDT, special attention should be carried out in the pressure and the contact area between the horn and the specimen and the duration of the stimulation. The longer the transducer operates at the surface; the most heat is released in the contact surface, increasing the probability of damaging the area. In addition, mechanical energy from the horn should be transferred to the inspected material as efficiently as possible. For this reason, the insertion of a coupling material between the transducer and the sample is strongly recommended as a bad or no coupling implies poor ultrasound transmission and creates unwanted heat near the ultrasound injection point, especially when testing has to be performed in surfaces with irregularities. Once all these factors are correctly addressed, inspection is extremely fast and results provide good defect contrast which can result in an increased detectability of small cracks, which may be undetectable using other thermographic method [116]. In general, no temporal post-processing is required in VT if the testing has been performed in the proper experimental conditions. However, advanced signal processing can be applied as well [117,118].

The ability to rapidly detect defects over large areas and the ability to detect small cracks that are undetectable using other NDE techniques has increased the interest for VT inspections in several industrial sectors. One of the initial applications of VT was the detection of internal delaminations in composite materials [119]. However recent advances in infrared technology exploited vibrothermal imaging as an inspection tool for cracks and fatigue damage detection in both isotropic and composite structures [108,115, 120-122].

3.6.2 Eddy Current Thermography (ECT)

ECT, also known as thermo-inductive inspection [123] or induction thermography [124] is a technique that combines eddy current excitation and thermographic imaging [125,126]. In particular, the stimulation process is based on the electromagnetic excitation of conducting materials by inducing eddy currents from electromagnetic coils, which are converted to heat through ohmic heating, according to Joule's Law. As a result, the influence of heat diffusion into the material can be monitored through the recording of the temperature transients on the surface of the material by an IR camera. Defects such as cracks, voids or delaminations which are within the range of the eddy current distribution disturb the current flow and thus change the temperature distribution, while defects which do not directly interact with the induced current flow may interact with the propagated heat into the material (as in the case of traditional heat lamps techniques). Thus, ECT has the advantage that both direct heating and diffuse heating can contribute to defect detection.

From the experimental point of view, eddy current thermography involves the application of a high frequency (typically 50-500 kHz) electromagnetic wave to the material under inspection. The inductive heating can be applied in two different ways: in a pulse mode [123,124,127] where the electromagnetic coil is switched on for a short time (typically from some ms to a few s) or in modulated mode by a harmonic signal [128]. Compared to optical stimulation, inductive heating has the advantage that the energy is generated directly inside the material, in a thin skin below the surface. Therefore, surface properties like the absorption coefficient do not have an influence on the generated heat. The depth of the heated zone, the so called "*penetration depth*" of the eddy current is depending on material parameters like the magnetic permeability and the electrical conductivity and it can be further varied by the frequency of the inductive excitation. The penetration depth of current flows is much larger than the heated depth through optical stimulation, where the light is absorbed in a much thinner subsurface layer [129]. In addition there is no requirement of surface preparation or cleaning before the testing and no coupling medium is needed unlike mechanical excitation-based techniques.

Applications of ECT find use for the detection of surface and subsurface cracks of different shape and directions in conductive materials [130,131,132] such as metallic materials. Pulsed configuration has also been applied for the evaluation of Rolling Contact Fatigue in rail track heads [133] and early detection of corrosion, especially under coatings [134], while the combination of periodic heating and phase sensate detection has been used in the characterization of coating adhesion [135] as well as for. Lastly, applications of this technique have been reported for the inspection of composites and aerospace components [136].

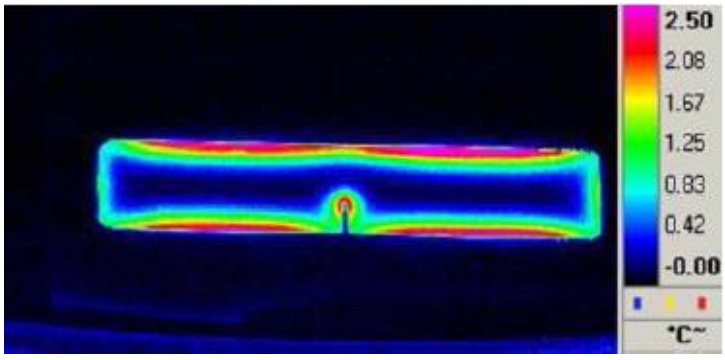

Fig. 3.8: *IR image of a steel sheet with an artificial crack after short time heated with an induction coil [123]*

3.6.3 Line-Scan Thermography (LST)

LST is an inspection technique in which the specimen can be moved under the line heat source and the monitoring device which are fixed in a stationary position or alternatively the source and the imaging equipment can be moved at a contrast velocity and in a predefined distance over the stationary specimen [137]. The principle behind LST is based on the fact that heat diffusion takes some time to dissipate throughout a material and the temperature at a particular point on the test panel will reach a maximum some time after the line source has passed [138]. In order to perform a line scan inspection and to account the heat diffusion through the material, the thermal detection apparatus is suited at a predefined distance away from the line heating source, as can be seen from Figure 3.9. The optimum distance of the detector is determined by the thermal diffusivity of the test material and the scanning velocity. If the detector is too far from the line source then too much cooling of the test sample will occur and the accuracy in the detection of internal abnormalities will be diminished. On the other hand, if the detector is too close to the line source then adequate heat diffusion will not occur and hence once again accuracy in the detection will also be diminished.

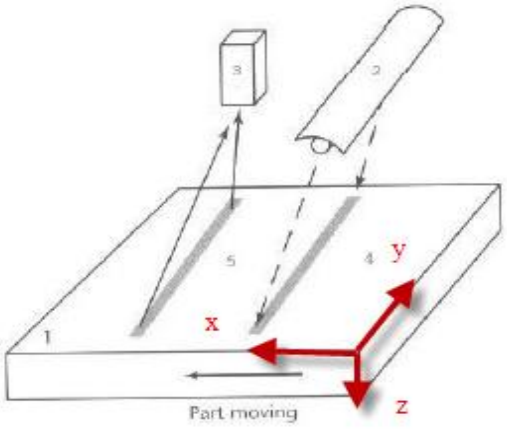

Fig. 3.9: *Line-scan thermographic configuration with 1. Inspected surface, 2. Line source, 3.infrared camera, 4. Surface temperature profile and 5. Observation area.(modified by 139]*

As stated above in LST inspections, a heat flow is generated in the lateral direction of line source movement (y-direction) coupled in addition to the heat flow in the surface-normal direction (z direction). This distinguishes LST from other non destructive inspection techniques, where the heat flow in the z-direction is mainly studied. Changes in scanning speed also affect the amount of heat absorbed by the test piece. An increase in scan velocity decreases the heat flux to the sample, and therefore the temperature change due to a defect is diminished. One advantage of LST is that it is giving the ability for visualisation of defects that would otherwise be transparent in the lateral orientation.

LST as an inspection procedure is very well suited for high output moving investigations such as in the manufacturing industry where measurements may require continuity and repeatability. As a result, recent advantages in the approach involve the use of linear robotic scanners which could be use to efficiently transport the imager and the heating source across large areas of an inspection material [140]. However, a drawback of this technique is its application only to flat surfaces, limiting its capabilities to inspect non planar test pieces.

3.7. References

[1] P.O. Moore ed., X. Maldague technical ed., (2001). *Infrared and Thermal Testing, Nondestructive Testing Handbook, Vol. 3*. 3rd Edition. Colombus, Ohio, American Society for Nondestructive Testing.

[2] X. Maldague (2001). *Theory and Practice of Infrared Technology for Non Destructive Testing.* John-Wiley & Sons, New York.

[3] D.P. Almond, S.G. Pickering (2012). *An analytical study of pulsed thermography defect detection limit.* Journal of Applied Physics, Vol. 111 (9), Art. no 093510.

[4] C. Ibarra-Castanedo, J.M. Piau, S. Guilbert, N.P. Avdelidis, M. Genest, A. Bendada, X.P.V. Maldague (2009). *Comparative study of active thermography techniques for the nondestructive evaluation of honeycomb structure.* J. Research in Nondestructive Evaluation, Vol. 20 (1), pp. 1-31.

[5] C. Ibarra-Castanedo, N.P. Avdelidis, E.G. Grinzato,P.G. Bison, S. Marinetti, L. Chen, M. Genest, X. Maldague (2006). *Quantitative inspection of non-planar composite specimens by pulsed phase thermography.* J. QIRT, Vol. 3(1), pp. 25-40.

[6] P. Albendea, F.G. Madruga, A. Cobo, J.M. Lopez-Higuera (2010). *Signal to noise ratio (SNR) comparison for pulsed thermographic data processing methods applied to welding defect detection.* In X.P.V. Maldague (ed.): Proc. of 10th International Conference on Quantitative Infrared Thermography-QIRT10, Quebec City, Canada, pp. 375-382

[7] H.S. Carslaw, J.C. Jaeger (1988). *Conduction of heat in solids.* 2nd Edition, Clarendon Press, Oxford.

[8] R. Bracewell (1965). *The Fourier Transform and its Applications.* McGraw-Hill, Toronto, Canada.

[9] X. Maldague, A. Ziadi, M. Klein (2004). *Double pulse infrared thermography.* NDT&E International, Vol. 37 (7), pp. 559-564.

[10] X.P.V. Maldague, (1993). *Nondestructive Evaluation of Materials by Infrared Thermography.* Springer-Verlag, London, UK.

[11] P. Cielo, X. Maldague, A.A. Deom, R. Lewak (1987). *Thermographic nondestructive evaluation of industrial materials and structures.* Materials Evaluation, Vol. 45(4), pp. 452-460.

[12] J. Allport, J. McHugh (1988). *Quantitative evaluation of transient video thermography*. In D.O. Thomphon, D.E. Chimenti (Eds.): Review of Progress in Quantitative Nondestructive Evaluation, AIP Conference Proceedings, Plenus Press, New York, Vol. 7, pp. 253-262.

[13] V.P. Vavilov, R. Taylor (1982). *Theoretical and practical aspects of the thermal nondestructive testing of boned structures.* In R.S. Sharpe (ed.): Research Techniques in Nondestructive Testing, Vol. 5, pp. 238-279.

[14] V. Vollmer, K.P. Mollmann (2010). *Infrared Thermal Imaging. Fundamentals, Research and Applications.* John Wiley &Sons, New York.

[15] N.P. Avdelidis, D.P. Almond (2004). *Through skin sensing assessment of aircraft structures using pulsed thermography* NDT&E International, Vol.37(5), pp 353-359.

[16] C. Ibarra-Castanendo, M. Genest, P. Servais, X.P.V. Maldague, A. Bendada (2007). *Qualitative and quantitative assessment of aerospace structures by pulsed thermography.* Nondestructive Testing and Evaluation, Vol. 22(2-3), pp. 199-215.

[17] N.P. Avdelidis, B.C. Hawtin, D.P. Almond (2003). *Transient thermography in the assessment of defects of aircraft composites.* NDT&E International, Vol. 36(6), pp. 433-439.

[18] L.D. Favro, T. Ahmed, X. Han, L. Wang, P.K. Kuo, R.L. Thomas (1996). *Thermal wave imaging of disbanding and corrosion on aircraft.* In D.O. Thompson, D.E. Chimenti (eds.): Review of Progress in Quantitative Nondestructive Evaluation, Vol. 15B, pp. 1747-1753, Plenum Press, New York.

[19] N.P. Avdelidis, D.P. Almond, Z.P. Marioli-Riga, A. Dobbinson, B.C. Hawtin (2006). *Pulsed thermography: philosophy, qualitative and quantitative analysis on aircraft materials and applications.* In X. Maldague ed.: Proc. of Vth International Workshop Advances in Signal Processing for Non Destructive Evaluation of Materials, Quebec City, Canada, pp. 171-179.

[20] N.P. Avdelidis, D.P. Almond (2004). *Transient thermography as a through skin imaging technique for aircraft assembly: modeling and experimental results.* J. Infrared Physics and Technology, Vol. 45(2), pp. 103-114.

[21] B.B. Chaudhry, H. Holmes, S.M. Shepard, T. Ahmed (2002). *Thermographic quality assurance of turbine engine components.* In Proc. of 2002 International Joint Power Generation Conference (IJPGC2002), Scottsdale, Arizona, USA

[22] V. Carl, E. Becker, A. Sperling (1998). *Thermography Inspection system for gas Turbine Blades.* In Proc. of 7th European Conference on Nondestructive Testing-ECNDT98, 26-29 May, 1998, Copenhagen.[access online: http://www.ndt.net/article/ecndt98/408.htm]

[23] N. Tao, Z. Zeng, L. Feng, X. Li, Y. Li, C. Zhang (2011). *The application of pulsed thermography in the inspection of wind turbine blades.* In J.J. Puschell, J. Chu, H. Gong, J. Lu (eds.): Proc. of SPIE – The International Society for Optical Engineering, Symposium on Photoelectronic Detection and Imaging 2011: Advances in Infrared Imaging and Applications Vol. 8193, Art. no 819319.

[24] M. Omar, M. Hassan, K. Donohue, K. Saito, R. Alloo (2006). *Infrared thermography for inspecting the adhesion integrity of plastic welded joints.* NDT&E International, Vol. 39(1), pp.1-7.

[25] M.F. De Moura, J.P.M. Goncalves (2004). *Modeling the interaction between matrix cracking and - 59 -ibrothermogr in carbon-epoxy laminates under low velocity impact.* Composites

Science and Technology, Vol. 64(7-8), pp. 1021-1027

[26] N.P. Avdelidis, D.P. Almond, A Dobbinson, B.C. Hawtin, C. Ibarra-Castanedo, X. Maldague (2004). *Aircraft composites assessment by means of transient thermal NDT*. Progress in Aerospace Science, Vol. 40, pp.143-162.

[27] C. Ibarra-Castanedo, N.P. Avdelidis, E.G. Grinzato, P.G. Bison, S. Marinetti, C.C. Plescanu, A. Bendada, X.P.V. Maldague (2011). *Delamination detection and impact damage assessment of GLARE by active thermography.* In Int. J. of Materials and Product Technology, Vol.41 (1-4), pp.5 – 16

[28] J.A. Schroeder, T. Ahmed, B. Chaudhry, S. Shepard (2002). *Non destructive testing of structural composites and adhesively bonded composite joints: pulsed thermography.* Composites: Part A, Vol. 33, pp. 1511-1517.

[29] N.P. Avdelidis, C. Ibarra-Castanedo, X. Maldague, Z.P. Marioli-Riga, D.P. Almond (2004*). A Thermographic Comparison study for the Assessment of Composite Patches.* Infrared Physics & Technology, Vol. 45(4), pp. 291-299.

[30] G. Carlomagno, C. Meola, (2002). *Comparison between thermographic techniques for frescoes NDT*. NDT&E International Vol. 35 (8), pp. 559–565.

[31] E. Grinzato, P.G. Bison, S. Marinetti (2002). *Monitoring of Ancient Buildings by the Thermal Method*. Journal of Cultural Heritage, Vol. 3, pp. 21-29.

[32] E. Rosina, N. Ludwig (1999). *Optical thermographic procedures for moisture analysis in building materials.* In J. Lammasniemi, H. Wiggenhauser, G. Busse, B.G. Batchelor, W. Poelzleitner, G. Dobmann (Eds.): Proc. of SPIE- The International Society for Optical Engineering, Diagnostic Imaging Technologies and Industrial Applications, , Vol. 3827, pp.22-33.

[33] F. Mercuri, U. Zammit, N. Orazi, S. Paoloni, M. Marinelli, F. Scudieri (2011*). Active infrared thermography applied to the investigation of art and historic artefacts.* Journal of Thermal Analysis and Calorimetry, Vol. 104 (2), pp. 475-485.

[34] N.P. Avdelidis, M. Koui, C. Ibarra-Castanedo, X. Maldague (2007). *Thermographic studies of plastered mosaics*. J. Infrared Physics and Technology, Vol. 49, pp. 254-256.

[35] K. Blessley, C. Young, J. Nunn, J. Coddington, S. Shepard (2010). *The feasibility of flash thermography for the examination and conservation of works of art.* In J. of Studies in Conservation, Vol. 55, pp. 107-120.

[36] A.R. Hamzah, P. Delpech, M.B. Saintey, D.P. Almond (1996). *An Experimental investigation of defect sizing by Transient Thermography*. In J. Insight, Vol. 38(3), pp.167-171

[37] R.E. Martin, A.L. Gyekenyesi (2002). *Pulsed thermography of ceramic matrix composites.* In A.L. Gyekenysi, S.M. Shepard, D. R. Huston, A.E. Aktan, P.J. Shull (Eds.): Proc. of SPIE-The International Society for Optical Engineering, Nondestructive Evaluation and Health

Monitoring of Aerospace Materials and Civil Infrastructures, San Diego, CA , Vol. 4704, pp. 82-92.

[38] S. Marinetti, P.G. Bison, E. Grinzato, G. Manduchi (1997). *Automatic Procedure for thermal NDE of delaminations in CFRP by neural networks.* In D.O. Thomphon, D.E. Chimenti (eds.): Review of Progress in Quantitative Nondestructive Evaluation, Vol. 16, pp. 773-780.

[39] M. Genest (2012). *Pulsed thermography image processing for damage growth monitoring.* In D.O. Thomphon, D.E. Chimenti (eds.): Review of Progress in Quantitative Nondestructive Evaluation, AIP Conference Proceedings, Plenus Press, New York, Vol. 31, pp. 721-728.

[40] R.J. Ball, D.P. Almond (1998). *The detection and measurement of impact damage in thick carbon fibre reinforced laminates by transient thermography.* In NDT&E International, Vol. 31(3), pp. 165-173.

[41] J.O. Taylor, H.M. Dupont (1998). *Inspection of metallic thermal protection systems for the X-33 launch vehicle using pulsed infrared thermography.* In J.R. Snell, R.N. Wurzbach (Eds.): Proc. SPIE- The International Society for Optical Engineering, Thermosense XX, Orlando, Florida, Vol. 3361, pp. 301-310.

[42] W.J. Parker, R.J. Jenkins, C.P. Butler, G.L. Abbot (1961). *Flash method of determining thermal diffusivity, heat capacity and thermal conductivity.* J. Applied Physics, Vol. 32(9), pp. 1679-1684.

[43] P. Bison, A. Bortolin, G. Cadelano, G. Ferrarini, E. Grinzato (2012). *Comparison of some thermographic techniques applied to thermal properties characterization of porous materials.* In Proc. of the 11th Quantitative Infrared Thermography Conference (QIRT12), Naples, Italy, (CDROM).

[44] P. Bison, E. Grinzato (2008). *Building materials characterization by using IR thermography for efficient heating systems.* In V.P. Vavilov, D.D. Burleigh (Eds.): Proc. of SPIE- The International Society for Optical Engineering, Thermosense XXX, Vol. 6939, Orlando, Florida,2008, art. no69390Y.

[45] G. Mayr, G. Hendofer (2010). *Porosity determination by pulsed thermography in reflection mode.* In X.P.V. Maldague (Ed.): In Proc. of the 10th Quantitative Infrared Thermography Conference (QIRT10), Quebec City, Canada, pp. 933-940

[46] A. Ciliberto, G. Canaccini, O. Salvetti, M. Chimenti, L. Azzarelli, P.G. Bison, S. Marinetti, A. Freda, E. Grinzato (2002). *Porosity detection in composite aeronautical structures.* Infrared Physics & Technology, Vol. 43, pp. 139-143.

[47] G. Busse (2001). *Techniques of infrared thermography: Part 4. Lockin thermography.* In P.O. Moore (ed.) X. Maldague (Tech. ed.): Nondestructive Handbook, Infrared and Thermal Testing, Vol. 3, 3rd edition, Colombus, Ohio, ASTN Press, 2001.

[48] P.E. Nordal, S.O. Kanstand (1979). *Photothermal Radiometry.* In J. Phisica Scripta, Vol. 20,

pp. 659-662.

[49] D. Wu, G. Busse (1998). *Lock-in thermography for nondestructive evaluation of materials*. Revue Générale de Thermique, Vol. 37(8), pp. 693-703.

[50] D. Wu, R. Steegmueller, W. Karpen, G. Busse (1995). *Characterazation of CFRP with lock-in thermography.* In D.O. Thompson, D. Chimenti (Eds.): Review of Progress in Quantitative NDT, Plenus Press, New York, Vol. 14, pp. 439-446.

[51] G. Giorleo, C. Meloa (2002). *Comparison between pulsed and modulated thermography in glass- epoxy laminates.* NDT&E International, Vol. 35(5), pp.287-292.

[52] G.M. Carlomagno, C. Meola (2002). *Comparison between thermographic techniques for frescoes NDT.* NDT&E International, Vol. 35(8), pp.559-565.

[53] C. Meloa, G.M. Carlomagno (2004). *Recent advances in the use of infrared thermography.* In J. of Measurement Science and Technology, Vol. 15, pp. R27-58.

[54] L.D. Favro, X. Han (1998). *Thermal wave Materials Characterisation and Thermal Wave Imaging*. In G. Birnbaum, B.A. Auld (eds.): Section 7 of Topics on Nondestructive Evaluation, Sensing for Materials Characterisation, Processing and Manufacturing, ASTN TONES, Vol. I, pp. 399-415.

[55] R. Montanini (2010). *Quantitative determination of subsurface defects in a reference specimen made of Plexiglas by means of lock-in and pulse phase infrared thermography.* In Infrared Physics and Technology, Vol. 53, pp. 363-371.

[56] X.P. Maldague, S. Marinetti (1996). *Pulsed Phase Infrared Thermography.* Journal of Applied Physics, Vol. 79(5), pp.2694-2698.

[57] J.C. Krapez (1998). *Compared performances of four algorithms used for modulated thermography.* In D. Balageas, G. Busse, G.M. Carlomagno (Eds.): Proc. of Quantitative Infrared Thermography Conference (QIRT'98), Lodz, Poland, pp.148-153.

[58] G. Busse, D. Wu, W. Karpen (1992). *Thermal wave imaging with phase sensitive modulated thermography*. Journal of Applied Physics, Vol. 71 (8), pp. 3962-3965.

[59] G. Busse, A. Rosencwaig (1980). *Subsurface imaging with Photoacoustics.* Appl. Phys. Lett., Vol. 36(10), pp.815-816.

[60] G. Busse (1979). *Optoacoustic phase angle measurement for probing a metal.* Appl. Phys. Lett. Vol. 35,pp. 759-760

[61] R.L. Thomas, J.J. Pouch, H.Y. Wong, L.D. Favro, P.K. Kuo, A. Rosencwaig (1980). *Subsurface flaw detection in metals by photoacoustic microscopy.* J. Appl. Phys. Vol. 51(2), pp. 1152-1156.

[62] A. Letho, J. Jaarinrn, T. Tiusanen, M. Jokinen, M. Luukkala (1981*). Magnitude and phase in thermal wave imaging.* Electronic Letters, Vol. 17(11), pp. 415-418.

[63] A. Rosencwaig, G. Busse (1980). *High resolution photoacoustic thermal wave microscopy.* In

Applied Physics Letters, Vol. 36, pp. 725-727.

[64] G. Busse (1982). *Optoacoustic and photothermal material inspection techniques.* Applied Optics, Vol. 21(1), pp. 107-110.

[65] W. Karpen, R. Steegmuller, G. Busse (1994). *Depth profiling of orientation in laminates with lock-in thermography.* In D. Balageas, G. Busse, G.M. Carlomagno (eds.): Proc. of Quantitative Infrared Thermography Conference (QIRT'94), Sorrento, Italy, pp.281-286.

[66] C. Meola, G.M. Carlomagno, G. Giorleo (2004). *The use of infrared thermography for materials characterization.* J. Mater. Process. Technol. Vol. 155-156, pp. 1132-1137.

[67] D. Wu (1994). Lock-in Thermography for defect characterization in veneered wood. In D. Balageas, G. Busse, G.M. Carlomagno (eds.): Proc. of Quantitative Infrared Thermography Conference (QIRT'94), Sorrento, Italy, pp.298-302.

[68] D. Wu, J. Rantala, W. Karpen, G. Zenzinger, B. Schonbach, W. Rippel, R. Steegmuller, L. Diener, G. Busse (1996). *Applications of lockin thermography methods.* In D.O. Thomphon, D.E. Chimenti (eds.): Review of Progress in Quantitative Nondestructive Evaluation, AIP Conference Proceedings, Plenus Press, New York, pp. 511-519.

[69] D. Verge, G. Busse (1989). *Remote inspection of coatings with wave radiometry.* Infrared Physics, Vol. 29(2-4), pp. 839-845.

[70] C. Meola, G. M. Carlomagno, A. Squillace, A. Vitiello (2006). *Non-destructive evaluation of aerospace materials with lock-in thermography.* Engineering Failure Analysis, Vol. 13(3), pp. 380-388

[71] D. Wu, A. Salerno, U. Malter, R. Aoki, R. Kochendorfer, P.K. Kachele, K. Woithe, K. Pfister, G. Busse (1996). *Inspection of aircraft structural components using lock-in thermography.* In D. Balageas, G. Busse, G.M. Carlomagno (eds.): Proc. of Quantitative Infrared Thermography Conference (QIRT'96), Stuttgart, Germany, pp.251-256.

[72] G. Busse, P. Eyerer (1983). *Thermal wave remote and nondestructive inspection of polymers.* Applied Physics Letters, Vol. 43(4), pp. 355-357.

[73] G. Busse (1994). *Nondestructive evaluation of polymer materials.* NDT&E International, Vol. 27(5), pp.253-262.

[74] C. Meloa, G.M. Carlomagno, A. Squillace, L. Giorleo (2002). *Non-destructive control of industrial materials by means of lock-in thermography.* Measurement Science and Technology, Vol. 13(10), pp. 1583-1590.

[75] C. Meloa, G.M. Carlomagno, A. Squillace, L. Giorleo (2004). *The use of infrared thermography for nondestructive evaluation of joints.* Infrared Physics & Technology, Vol. 46, pp. 93-99.

[76] O. Breitenstein, W. Warta, Langenkamp (2003). *Lock-in Thermography- Basics and Use for evaluating Electronic Devices and Materials.* 2nd edition, Springer Series in Microelectronics.

[77] O. Breitenstein, J.P. Rakotoniaina, M.H. Al Rifai (2003). *Quantitative evaluation of shunts in solar cells by Lock-in Thermography*. Progress in Photovoltaics: Research and Applications, Vol. 11, pp. 515-526.

[78] J.W. Machlachlan-Spicer, W.D. Kerns, L.C. Aamodt, J.C. Murphy (1989). *Measurement of coating physical properties and detection of coating disbands by time resolved Infrared radiometry.* J. Nondestructive Evaluation, Vol. 8(2), pp.107-120.

[79] J.W. Maclachlan-Spicer, L.C. Aamodt, J.C. Murphy (1991). *Application of time resolved infrared radiometry (TRIR) to identify structural damage in composite materials.* Advanced NDE Technology Program. Ames Laboratory, Iowa, USA, pp. 11-28

[80] R. Osianer, J.W. Machlachlan-Spicer (1998). *Time-resolved infrared radiometry with step heating, a review.* Revue Generale de Thermique, Vol. 3, pp. 680-682.

[81] J.W. Maclachlan-Spicer, J.C. Murphy, L.C. Aamodt (1989*). Characterisation of ceramic coatings by advanced nondestructive evaluation methods.* In proc. of 12th Annual Conference on Composites and Advanced Ceramic Materials: Ceramic Engineering and Science Proceedings, Vol. 9 (9-10).

[82] J.W. Maclachlan-Spicer, W.D. Kerns, L.C. Aamodt, R. Osiander, J.C. Murphy (1993). *Time-resolved infrared radiometry (TRIR) using a focalplane array for characterization of hidden corrosion.* In L.R. Allen (Ed.): Proc. of SPIE- The International Society for Optical Engineering, Thermosense XV, Orlando, Florida, Vol. 1933, pp. 148-159.

[83] J.C. Murphy, L.C. Aamodt, J.W. Maclachlan-Spicer (1992). *Principles of photothermal detection in solids.* In A. Mandelis (ed.), Principles & Perspectives of Photothermal & Photoacoustic Phenomena. Elsevier Science Publising, New York, pp. 41-94.

[84] R. Osiander, J.W. Maclachlan-Spicer, J.C. Murphy (1996). *Analysis methods for full-field time resolved infrared radiometry.* In D.D. Burleigh, J.W. Spicer (Eds.): Proc. of SPIE- The International Society for Optical Engineering, Thermosense XVIII, Orlando, Florida, Vol. 2766, pp. 218-227.

[85] J.W. Maclachlan-Spicer, W.D. Kerns, L.C. Aamodt, J.C. Murphy (1991). *Time-resolved infrared radiometry (TRIR) of multilayer organic coatings using surface and subsurface heating.* In G.S. Baird (Ed.): Proc. of SPIE- The International Society for Optical Engineering, Thermosense XIII, Orlando, Florida, Vol. 1467, pp. 311-321.

[86] L.C. Aamodt, J.W. Maclachlan-Spicer, J.C. Murphy (1990). *Analysis of characteristic thermal transit times for time resolved infrared radiometry studies of multilayered coatings.* In J. Applied Physics, Vol. 68(12). pp.6087-6098.

[87] J.W. Machlachlan-Spicer, W.D. Kerns, L.C. Aamodt, J.C. Murphy (1992). *Time resolved infrared radiometry for characterization of impact damage in composite materials.* In D.O. Thomphon, D.E. Chimenti (eds.), Review of Progress in Quantitative Nondestructive

Evaluation, Vol. 11, Plenus Press, New York.

[88] J.W. Machlachlan-Spicer, W.D. Kerns, L.C. Aamodt, J.C. Murphy (1992). *Source patterning in time resolved infrared thermography of composite structures.* In J.K. Eklund (Ed.): Proc. of SPIE- The International Society for Optical Engineering, Thermosense XIV, Orlando, Florida, Vol. 1682, pp. 311-321.

[89] A.A. Badghaish, D.C. Fleming (2008). *Quantitative characterization of resistive defects in thick composites using step heating thermography.* In V.P. Vavilov, D.D. Burleigh (Eds.): Proc. of SPIE- The International Society for Optical Engineering, Thermosense XXX, Orlando, Florida, Vol. 6939, pp.693916-1 -12.

[90] A.A. Badghaish, D.C. Fleming (2008). *Non-destructive inspection of composites using step heating thermography.* In J. of Composite Materials. Vol. 42(13), pp. 1337-1357.

[91] J.W. Machlachlan-Spicer, M.G. Bevan, W.D. Kerns, H.S. Feldmesser (1993). *Thermal characterization of heat sink adhesive systems for spacecraft electronics by time-resolved infrared radiometry.* In J. Electronic Packaging, Vol. 115(1), pp.101-105.

[92] A.S. Soliman, M.E. Abdel Rahman, R.J. Heck (2010). *Comparing time-resolved infrared thermography and X-ray computed tomography in distinguishing soil surface crusts.* In J. Geoderma, Vol. 158, pp. 101-109.

[93] C. Maierhofer, M. Rollig (2009). *Application of active thermography to the detection of safety relevant defects in civil engineering structures.* In Proc. of SENSOR+TEST Conference 2009: 11th International Conference on Infrared Sensors and Systems, Nurnberg, Germany, pp. 215-220.

[94] V. Vavilov, T. Kauppinen, E. Grinzato (1997). *Thermal characterization of defects in building envelopes using long square pulsed and slow thermal wave techniques.* Research in Nondestructive Evaluation, Vol. 9, pp. 181-200.

[95] A. Tavukcuoglu, S. Akerven, E. Grinzato (2010). *In situ examination of structural cracks at historic masonry structures by quantitative infrared thermography and ultrasound testing.* In J. of Modern Optics, Vol. 57(18), pp. 1779-1789.

[96] S. Danesi, A. Salerno, D. Wu, G. Busse (1998). *Cooling down thermography: principle and results for NDE.* In J.R. Snell, R.N. Wurzbach (eds.): Proc. of SPIE- The International Society for Optical Engineering, Thermosense XX, Vol. 3361, pp. 266-274.

[97] E. Cheilakou, N.P. Avdelidis, C. Ibarra – Castanedo, M. Koui, A. Bendada X.P. Maldague (2010). *Non destructive study of plastered mosaics with the use of active thermography.* In R. B. Dinwiddie, M. Safai (Eds.): Proc. of SPIE- The International Society for Optical Engineering, Thermosense XXXII, Vol. 7661, art. no.76610F

[98] C. Maierhofer, M. Rollig (2009). *Active thermography for the characterization of surfaces and interfaces of historic masonry structures.* In Proc. of Non-Destructive Testing In Civil

Engineering Conference- NDTCE'09, Nantes, France, June 30th-July 3rd 2009, CD-ROM.

[99] R. Arndt (2008). *Square pulsed thermography in the frequency domain.* In V.P. Vavilov, D.D. Burleigh (eds.): Proc. of SPIE- The International Society for Optical Engineering, Thermosense XXX, Orlando, FL, Vol. 6939, art. no. 69390X.

[100] C. Maierhofer, H. Wiggenhauserr, A. Brink, M. Rollig (2008). *Quantitative numerical analysis of transient IR-experiments in buildings.* Infrared Physics & Technology, Vol. 46(1-2), pp. 173-180.

[101] C. Maierhofer, A. Brink, M. Rollig, H. Wiggenhauser (2005). *Quantitative impulse thermography as a non-destructive method in civil engineering- Experimental results and numerical simulations.* In J. of Construction and Building Materials, Vol. 19, pp. 731-737.

[102] R.W. Arndt (2010). *Square pulse thermography in frequency domain as an adaption of pulsed phase thermography for qualitative and quantitative applications in cultural heritage and civil engineering.* Infrared Physics & Technology, Vol.53, pp. 246-253.

[103] C. Maierhofer, M. Rollig, R. Krankenhagen (2010). *Integration of active thermography into the assessment of cultural heritage buildings.* Journal of Modern Optics, Vol. 57(18), pp. 1790-1802.

[104] C. Maierhofer, A. Brink, M. Rollig, H. Wiggenhauser (2002). *Transient thermography for structural investigation of concrete and composites in the near surface region.* In Infrared Physics & Technology, Vol. 43(1-2), pp. 271-278.

[105] S. Sfarra, A. Bendada, A. Paoletti, D. Paoletti, D. Ambrosisni, C. Ibarra-Castanedo, X. Maldague (2010). *Square pulsed thermography and digital speckle photography: Non-destructive testing techniques applied to the defects detection in aerospace materials.* In Proc. of the 2nd International Symposium on NDT in Aerospace, Hamburg, Germany, art. no. p3, (CDROM).

[106] E.G. Henneke, K.L. Reinfsnider, W.W. Stinchcomb (1979). *Thermography, an NDI method for damage detection.* Journal of Metals, Vol. 31 (9), pp. 11-15.

[107] R.B. Mignogna, R.E. Green, J.E. Duke, E.G. Henneke, K.L. Reinfsnider (1981). *Thermographic investigation of high power ultrasonic heating in materials.* Ultrasonics, Vol.7, pp. 159-163.

[108] A. Dillenz, T. Zweschper, G. Busse (2001). *Defect selective imaging of aerospace structures with elastic-wave-activated thermography.* In A.E. Rozlosnik, R.B. Dinwiddie (Eds.): Proc. of SPIE- The International Society for Optical Engineering, Thermosense XXIII, Orlando, Florida, Vol. 4360, pp.580-586.

[109] L.D. Favro, X. Han, Z. Ouyang, G. Sun, H. Sui, R.L. Thomas (2000). *Infrared imaging of defects heated by a sonic pulse.* Rev. of Sci. Instr., Vol. 71(6), pp. 2418-2421.

[110] M. Morbidini, P. Cawley, T. Barden, D. Almond, P. Duffour (2006). *Prediction of the*

thermosonic signal from fatigue cracks in metals using vibration damping measurements. Journal of Applied Physics 100, 104905.

[111] J. Randala, D. Wu, G. Busse (1996). *Amplitude-modulated lock-in - 67 -ibrothermography for NDE of polymers and composites.* Research in Nondestructive Evaluation, Vol. 7(4), pp. 215-228.

[112] J. Randala, D. Wu, G. Busse (1998). *NDT of polymer materials using lock-in thermography with water coupled ultrasonic excitation.* In NDT&E International, Vol. 31(1), pp. 43-49.

[113] T. Zwescper, G. Riegert, A. Dillenz, G. Busse (2003). *Frequency modulated elastic wave thermography.* In K. Elliot Cramer, X.P. Maldague (Eds.): Proc. of SPIE- The International Society for Optical Engineering, Thermosense XXV, Vol. 5073, pp. 386-391.

[114] L.D. Favro, X. Han, O.Y. Zhong, G. Sun, R.L. Thomas (2011). *Sonic IR imaging of delaminations and disbands in composites.* In J. of Physics D: Applied Physics, Vol. 44, art. no. 034013.

[115] T. Zwescper, G. Riegert, A. Dillenz, G. Busse (2003). *Ultrasound Burst phase thermography (UBT) for applications in the automotive industry.* In D.O. Thomson, D.E. Chimenti (eds.): Review of Quantitative Nondestructive Evaluation, AIP Conference Proceedings, Plenus Press, New York, Vol.22, pp. 531-536.

[116] S.M. Shepard, T. Ahmed, J.R. Lhota (2004). *Experimental considerations in Vibrothermography.* In Proc. SPIE- The International Society for Optical Engineering, ThermosenseXXVI, Orlando, Florida,Eds. D.D. Burleigh, K.E. Cramer, G.R. Peacock, Vol. 5405, pp. 332-335

[117] C. Ibarra-Castanedo, M. Genest. S. Guibert, J.M. Piau, X. Maldague, A. Bendada (2007). *Inspection of aerospace materials by pulsed thermography, lock-in thermography and Vibrothermography: A comparative study.* In K.M. Knettel, V.P. Vavilov, J.J. Miles (eds.): Proc. of SPIE- The International Society for Optical Engineering, Thermosense XXIX, Vol. 6541, art. no. 654116.

[118] S.D. Holland (2011). *Thermographic signal reconstruction for - 67 -ibrothermography.* Infrared Physics & Technology, Vol. 54(6), pp. 503-511.

[119] K.L. Reinfsnider, E.G. Henneke, W.W. Stinchcomb (1980). *The mechanics of Vibrothermography.* In W.W. Stinchcomb (Ed.): The Mechanics of Nondestructive Testing, Plenum Press, New York, pp. 249-276.

[120] A. Dillenz,, T. Zweschper, G. Busse (2001). *Progress in ultrasound phase thermography.* In A.E. Rozlosnik, R.B. Dinwiddie (eds.): Proc. of SPIE- The International Society for Optical Engineering, Thermosense XXIII, Vol. 4360, pp. 574-579.

[121] J. Renshaw, S.D. Holland, R.B. Thompson (2008). *Measurement of crack opening stresses and crack closure stress profiles from heat generation in vibrating cracks.* J. Applied Physics

Letters, Vol. 93, pp. 081914.1-3.

[122] L.D. Favro, R.L. Thomas, X. Han, Z. Ouyang, G. Newaz, D. Gentile (2001). *Sonic infrared imaging of fatigue cracks.* In International J. of Fatigue, Vol. 23, pp. 471-476

[123] B. Oswald-Tranta (2007). *Thermo-inductive crack detection.* Nondestructive Testing and Evaluation, Vol. 22 (2-3), pp. 137-153.

[124] U. Netzelmann, G. Walle (2008). *Induction Thermography as a tool for reliable detection of surface defects in forged components.* In Proc. of the 17th World Conference on Nondestructive Testing, Shangai, China, (CDROM).

[125] G. Zenzinger, J. Bamberg, M. Dumm, P. Nutz (2005). *Crack detection using eddytherm.* In Review of Progress in QNDE 24, Eds. D.O. Thompson, D.E. Chimenti, AIP Conference Proceedings, Vol. 760, pp. 1646-1653.

[126] N. Tsopelas, N.J. Siakavellas (2009). *Improvements in electromagnetic-thermal non-destructive inspection by data processing.* NDT&E International, Vol. 42(5), pp.477-486.

[127] I.Z. Abidin, G.Y. Tian, J. Wilson, S. Yang, D. Almond (2010). *Quantitative evaluation of angular defects by pulsed eddy current thermography.* NDT&E International, Vol. 43, pp. 537-546.

[128] G. Riegert, T. Zweschper, G. Busse (2004). *Lock-in thermography with eddy-current excitation.* J. Quantitative Infrared Thermography (QIRT), Vol. 1(1), pp. 21-32.

[129] D.P. Almond, P.M. Patel (1996). Photothermal Science and Technique, Chapman &Hall: London.

[130] N. Tsopelas, N.J. Siakavellas (2006). *Electromagnetic-thermal NDT in thin conducting plates.* NDT&E International, Vol. 39 (5), pp. 391-399.

[131] B. Oswald-Tranta (2004). *Thermo-Inductive investigations of magnetic materials for surface cracks.* Quantitative Infrared Thermography (QIRT), Vol. 1(1) pp. 33-46.

[132] G. Walle, U. Netzelmann (2006). *Thermographic crack detection in ferritic steel components using inductive heating.* In Proc. of ECNDT 2006, Berlin, Germany, art. no. Tu 4.8.5.

[133] D. Hesse, P. Cawley (2006). *Excitation of surface wave modes in rails and their Application for defect detection.* In D.O. Thomphon, D.E. Chimenti (eds.): Review of Progress in Quantitative Nondestructive Evaluation, AIP Conference Proceedings, Plenus Press, New York, Vol. 820, pp. 1593-1600.

[134] G.Y. Tian, Y. He, L. Cheng, P. Jackson (2012). *Pulsed eddy current thermography for corrosion characterization.* International J. of Applied Electromagnetics and Mechanics, Vol. 39 (1-4), pp. 269-276.

[135] G.L. Fitzpatrick, D.K. Thome, R.L. Skaugset, E.Y.C. Shih (1993). The present status of magneto-optic eddy current imaging technology. In D.O. Thomson, D.E. Chimenti (Eds.): Review of Progress in Quantitative Nondestructive Evaluation, American Institute of Physics.

Vol. 12, Plenum Press, New York, pp. 617-624.

[136] L. Cheng, G. Y. Tian (2011). *Surface crack detection for carbon fiber reinforced plastic (CFRP) materials using pulsed eddy current thermography*. In J. IEEE Sensors, Vol. 11(12), pp. 3261–3268.

[137] J. Varis, M. Onsanen, J. Rantala, M. Luukkala (1995). *Observations on image formation in the line scanning thermal imaging method.* In D.O. Thomphon, D.E. Chimenti (eds.): Review of Progress in Quantitative Nondestructive Evaluation, AIP Conference Proceedings, Plenus Press, New York, Vol. 14, pp. 447-452.

[138] J. Varis, J. Rantala, J. Hartikainen (1994). *A numerical study on temperature distribution of line heated anisotropic carbon fiber composites.* In J. Research in Nondestructive Evaluation, Vol. 6 (2), pp.69-83.

[139] J. Varis, J. Rantala,J. Hartikainen, R. Lehtiniemi,, M. Luukkala (1995). *A numerical study on temperature distribution of line heated anisotropic carbon fiber composites*. In D.O. Thomphon, D.E. Chimenti (eds.): Review of Progress in Quantitative Nondestructive Evaluation, AIP Conference Proceedings, Plenus Press, New York, Vol. 14, p. 1341-1345.

[140] Cramer, K.E., R. Jacobstein, T. Reilly (2001). *Boiler tube corrosion characterization with a scanning thermal line.* In A.E. Rozlosnik, R.B. Dinwiddie (Eds.): Proc. of SPIE- The International Society for Optical Engineering, Thermosense XXIII, Vol. 4360, Orlando, 2001, pp. 594-605.

Chapter 4

Thermal Image Processing and Quantitative Data Analysis

4.1 Introduction

Regardless the mode of active infrared thermographic testing, the inspected sample has to be excited through the application of heat and the transient state of heat diffusion can then be studied through the sequential recording of thermal images and the monitoring of the surface temperature changes for specified time duration. The information recovery in such types of investigations can be performed in two different modes, this of qualitative and this of quantitative data analysis, respectively. Qualitative inspections involve collecting thermal images and searching for any sign of non-uniformity in the thermal patterns, as the presence of inhomogeneities -characterised by different thermal properties with respect to the sound material- affects the surface temperature mapping and permits their visual detection through its colorful representation. Obviously, large and near the surface defects are immediately noticeable from the raw IR images. However, in order to detect smaller defects within the target, efficient enhancement methods of the heat diffusion signature into the inspected sample have to be applied. The aforementioned along with the increasing demand for a more accurate evaluation of the observed anomalies, as the fact that qualitative inspection relies on the training and experience of the operator, led the research community to propose and develop signal processing algorithms, capable of enhancing the obtained output and evaluating the features of interest through quantitative manners. For this reason, a great variety of signal processing techniques has been developed, providing promising interpretation of the final output and enhancing the contrast and quality of the recorded thermal data.

Taking into account the aforementioned, aim of this chapter is to provide an overview of the signal processing techniques that have been proposed and are used for the qualitative and quantitative assessment of active thermographic data. As stated above, the main objective of advanced signal processing algorithms is to initially improve the visual appearance of the acquired raw thermal images. However in some instances, before actually processing the data, a preprocessing procedure is required as imaging hardware limitations may result in "*useless pixels*" generation, affecting the final output. After a brief presentation of the most common signal preprocessing routines, a detailed description of the most common in use signal processing and analysis techniques is following, presenting the theoretical principles of thermal-contrast based techniques, derivatives reconstruction processing, principal component analysis and pulsed phase thermography. The above techniques are widely used, as they produce an improved qualitative interpretation of active thermographic results, enhancing the defect detectability and geometry and reducing the negative influence of noise. Along with the enhanced visual interpretation produced, the second objective of advanced signal processing techniques is to prepare the data in order to be manipulated properly and provide quantitative information regarding the detected features of interest. As a result, the second part of this chapter is dedicated to the discussion on some quantitative analysis methods, which are based on the heat diffusion study in different processing domains. In general, quantitative estimations are mainly refer to the information retrieval about the location and the size of a feature of interest and the procedures followed in order to acquire these information are based on the determination of the point in which a specific phenomenon

occurs, associated with the detection of this hidden feature. The above described, are related to quantitative infrared thermography based on experimental methods, which can provide information in a straightforward manner, as the experimental results are solving numerical formulas. On the other hand, a different approach for quantitative purposes can be implemented as well by involving inverse techniques which can provide quantitative information through the correlation of numerical and experimental results and by solving inverse problems. Finally, this chapter is concluded with the presentation of a quantitative approach to determine the lateral dimensions of a feature detected, which is based on the study of intensity variations in a line profile using the statistical analysis called Full Width at Half Maximum (FWHM) and can be applied on the experimental results regardless the domain in which the processing is performed.

4.2 Preprocessing techniques for IR thermographic data

As stated above, before the actual thermographic data processing and analysis, a preprocessing procedure shall be initially performed in some instances. In other words, it is sometimes necessary to rectify some problems related mainly to the acquisition system and/or the experimental conditions, before processing the signal to retrieve potential information about the target inspected. The most common problems that can be observed on raw unprocessed thermographic data are listed in Table 4.1.

Table 4.1: *Common problems of raw thermal data [1,2]*

Problem	***Description***
Fixed Pattern Noise (FPN)	Fixed pattern noise (FPN) is the result of the different responses produced from the individual detectors of an array to the incoming radiation and it is a common problem characterising the focal plane arrays infrared devices. The fixed pattern noise can be eliminated by capturing an image from a blackbody, which can be later subtracted from the images of the thermographic sequence. Both thermographic sequence and blackbody image are captured by the same testing configuration.
Bad Pixels	Bad Pixel can be defined as an anomalous pixel in the image frame that behaves differently from the rest of the pixel array and it can be either a dead or a hot pixel. A dead pixel in the image frame remains black while a hot pixel is permanently bright. As they do not provide any useful information and only contribute to image contrast deterioration, the non-uniformity correction can be carried out by replacing them with an average value of neighboring pixels.
Vignetting	Vignetting is another source of noise on thermograms which causes the darkening of image corners with respect to the image center due to limited exposure. Vignetting depends on both pixel location and temperature difference with respect to the ambient. In order to reduce the effect of vignetting, a calibration procedure has been proposed utilizing a linear function of each individual sensor [3].
Temperature Calibration	The temperature calibration of thermal camera is carried out using a polynomial transformation function. In the process of temperature calibration, a reference heat source is selected whose temperature can be varied in steps. These

	temperature variations from heat source are captured with the thermal camera as a reference sequence of images. These reference images are averaged and fit into the polynomial function used to calibrate the thermal camera. Once all the images acquired are curve fitted into the polynomial function, the calibration of camera is complete and can now be used for image acquisition.
Noise filtering	Noise filtering is the most common preprocessing technique used on the acquired thermal images. Median or Gaussian filtering can be used to filter noise from the captured images resulting to images with a better contrast between sound and defective areas.

4.3 Signal processing of thermographic data

The main reason for the establishment of advanced signal processing algorithms as a treatment tool over raw thermal data is its difficulty to be handled and analysed as various parameters (i.e. emissivity and reflectivity variations, non-uniform heating, surface geometrical variations, and spatial resolution of the infrared equipment) may affect internal features detectability [4]. For this reason as discussed earlier, image processing is commonly used for two purposes: firstly to improve the visual appearance of the images and secondly to prepare data for the retrieval of quantitative information regarding the inspected features. In the following pages, the most common in use advanced signal processing algorithms are presented with the majority of them based on the processing of image data on a pixel by pixel basis. These processing techniques even if they have been developed and are most commonly applied for the treatment of PT data, there is no limitation to be implemented in other forms of transient or stationary active infrared thermographic concepts.

4.3.1 Thermal contrast processing techniques

The development of thermal contrast techniques derives from the fundamental principle of IRT, which is the detection of surface temperature differences produced over defective and non-defective zones. Calculating thermal contrasts is a basic operation in thermographic schemes and despite its simplicity; it is the origin of many PT processing algorithms. Particularly, this technique is based on the determination of the point/area to be analysed with respect to a reference point/area which has to be preselected and is considered as the surface point/ area where no subsurface defect is presented beneath it. In most of the cases, reference area is a background in the thermal image, which can be clearly distinguished from the defective ones. In order to retrieve images that represent the mapping of the produced temperature differences over the area of inspection, different thermal contrast definitions (i.e. absolute contrast, running contrast, normalized contrast and standard contrast) can be used [5,6], but as can be understood, they all share the need for specifying a reference area within the field of view.

The *absolute contrast* $C_a(t)$ extracts the absolute difference of temperatures between the point of interest and the reference point, and it is defined as [5]:

$$C_a(t) = T_d(t) - T_{Sa}(t) \quad \text{(Eq. 4.1)}$$

where *t* is the time, $T_d(t)$ is the temperature in the point of interest (i.e. defective area) at time *t* and $T_{Sa}(t)$ is the temperature in the reference point. The absolute contrast calculation is a simple and efficient method for defect visualization and at a particular *t* if $C_a(t) = 0$ no defect can be detected. However, the main disadvantage of this procedure is that considerable variations on the results can be observed when changing the location of the sound pixel on the thermal image [7]. On the other hand, the *running contrast* $C_r(t)$ can be obtained by the absolute contrast normalized with respect to the cooling process over the reference point and it is less affected by surface optical properties variations, defined as [5]:

$$C_r(t) = \frac{C_a(t)}{T_{sa}(t)} \quad \text{(Eq. 4.2)}$$

The *normalized contrast* $C_n(t)$ is computed with respect to the value of temperature at the instant time t_m when the excess of temperature is maximal. Normalisation can also be calculated, involving other temperature values such as at the end of the inspection procedure and the normalized contrast is defined as [5]:

$$C_n(t) = \frac{T_d(t)}{T_d(t_m)} - \frac{T_{Sa}(t)}{T_{Sa}(t_m)} \quad \text{(Eq. 4.3)}$$

A different definition of thermal contrast is this of *standard contrast* $C_s(t)$, which can be defined as [5]:

$$C_s(t) = \frac{T_d(t) - T_d(t_0)}{T_{Sa}(t) - T_{Sa}(t_0)} \quad \text{(Eq. 4.4)}$$

with t_0 being a specific time point before the application of heat on the inspected area.

The mapping of temperature differences through thermal contrasts can be performed either on a single thermogram or on all the thermograms composing the sequence of images. In general, the advantage of working with thermal contrasts instead of temperature data derives from the fact that the mapping of thermal contrasts is producing increased sensitivity of the detected variations and thus an enhanced defect visibility and image quality [5]. However, the main limitation of these methods is the fact that in order to produce such image types, the use of the temperature over a sound area is required and its determination is a critical issue. More specifically, in many cases only assumptions can be made as it may not be known in advance where the defects are, if present at all. Furthermore as stated above, considerable variations on the results can be observed either by the effect of non-uniform heating on the surface of the target, or by changing the location of the reference point over the background area.

4.3.2 Differential Absolute Contrast (DAC)

Taking into consideration the above limitations of classical thermal contrast based techniques, an alternative method, this of DAC [8,9], has been developed to perform a more convenient computation of the sound area temperature. This technique is based on Eq. 4.1 of the classical thermal contrast approach, however its main differentiation relies on the fact that instead of looking for a non-defective area somewhere in the thermogram, its temperature at time *t* is computed locally assuming that in the

first few images all points behave as a sound area with no defects beneath them [8]. In other words, the basic step in order to use DAC algorithm, is to define *t'* as a given time value between the instant when the pulse is occurred and the precise moment when the first defective spot appears, producing a thermal contrast over the field of view. At times earlier than *t'*, there is no indication for the existence of a defect, and the local temperature decay over a sound area and over a defective area have exactly the same behaviour.

In order to calculate the absolute thermal contrast through differential absolute contrast technique, the 1D solution of the Fourier heat diffusion equation is used (Eq. 3.4). Taking the thermogram obtained at time *t'*, when no defect has become visible the temperature of the sound area can be obtained from:

$$T_{Sa}(t') = T(t') \quad \text{(Eq. 4.5)}$$

From Equation 3.4 the value *Q/e* can be solved to obtain through:

$$\frac{Q}{e} = \sqrt{\pi t'} \cdot T(t') \quad \text{(Eq. 4.6)}$$

By substituting the value *Q/e* in Equation 4.2 with Equation 4.6, the defect –free can be expressed as:

$$T_{Sa}(t) = \sqrt{\frac{t'}{t}} \cdot T(t') \quad \text{(Eq. 4.7)}$$

And by the combination of Equation 4.7 with the definition of absolute contrast (Eq. 4.1), The DAC thermal contrast is given by [8]:

$$\Delta T_{DAC} = T(t) - \sqrt{\frac{t'}{t}} \cdot T(t') \quad \text{(Eq. 4.8)}$$

In comparison with the classical thermal contrast based algorithms, the DAC method can provide efficient results as the determination of the sound area at early times is practically unaffected from the unwanted effect of non-uniform heating even for the case of anisotropic materials [10]. The only requirement of DAC algorithm is the proper definition of *t'*. This procedure can be performed manually, however Interpolated Differential Absolute Contrast algorithm [11] has also been proposed as a procedure to remove the manual selection of *t'*, expunging the result of incorrect time value estimation. In addition, as the accuracy of DAC model decreases for longer times (the 1D solution of Fourier diffusion equation collapses), a DAC method by using quadrupole theory [12] through a modified DAC algorithm [9,13] has been proposed which can be valid for later times inspections as well.

4.3.3 Thermographic Signal Reconstruction (TSR)

As presented above, interpretation of thermal data has typically been based on the analysis of amplitude variations in the temperature contrast of each pixel with respect to a defect-free reference point. TSR [14-18] offers an alternative to the thermal contrast-based methods in time domain processing by using polynomial interpolation which allows increasing the spatial and temporal resolution of the acquired results, while reducing the amount of data to be manipulated. TSR algorithm

is based on the assumption that the temperature profiles for non-defective areas follow the decay curve given by the one dimensional solution of the Fourier diffusion equation (Eq. 3.4). However, if this rewritten and transformed in the logarithmic notation, it can be expressed as [14]:

$$\ln(\Delta T) = \ln(\frac{Q}{e}) - \frac{1}{2}\ln(\pi t) \quad \text{(Eq. 4.9)}$$

Equation 4.9 demonstrates that the surface temperature decay for a homogeneous solid material after the application of a heat pulse, can be described by a linear function with a -1/2 slope, when this is studied in the logarithmic scale. Additionally, this also depends from an offset term that is a function of the input energy and the material thermal effusivity and from a second term that depends only on time. The above linear behaviour is graphically presented in the plot of Figure 4.1 (blue line). However, as the heat flux penetrates into the material bulk and encounters a subsurface inhomogeneity, a deviation from linearity occurs as Figure 4.1 also illustrates (red line). The above discussed, are highlighting that the logarithmic behaviour of surface temperature decay exhibits a remarkable consistency, as with the pixels corresponding to a defect-free area are following a linear behaviour, while the pixels corresponding to an internal defect are departing from linear signature at a specific time point without however displaying sudden deviations from the expected linear behaviour. As a result, when working with temperature-time data in the logarithmic scale, this enables defect detection in a more accurate manner compared with the study of the raw temperature-time data over sound and defective areas.

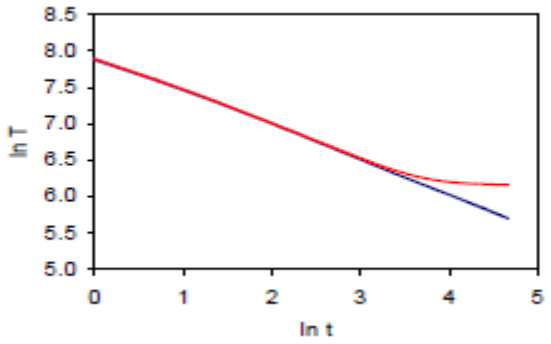

Fig. 4.1: *Logarithmic time decay of the surface temperature. Temperature decay is linear with slope of -0.5 until the heat flow is obstructed by a subsurface defect [6].*

Based on the above observations, a procedure has been proposed [14] which can approximate the logarithmic time-dependence of each experimental temperature pixel through a function of polynomial fitting by an *m*-degree polynomial of the form:

$$ln\big(T(t)\big) = a_0 + a_1\, ln(t) + \, a_2[ln(t)]^2 + \ldots + a_m[ln(t)]^m \quad \text{(Eq. 4.10)}$$

Typically, *m* is set to an order of 4 or 5, as experimental tests [14-16] proved that this value of polynomial degree preserves the essential thermal response, while rejecting non-thermal noise contributions. Higher orders of polynomial degrees have also been proposed when working with non-homogeneous and anisotropic materials in order to fit the experimental results at later times [19]. Once the time evolution of each pixel has been approximated by Eq. 4.10, the original temperature data can be reconstructed in order to produce the synthetic temperature, as follows [14]:

$$T(t) = exp[a_0 + a_1\, ln(t) + \, a_2[ln(t)]^2 + \ldots + a_m[ln(t)]^m] \quad \text{(Eq. 4.11)}$$

Compared to conventional processing of raw thermographic data, the processing of synthetic data (reconstructed time-dependent sequence of Eq. 4.11) provides significant advantages [17] such as noise reduction since synthetic *T(t)* reproduces the true thermal behaviour of the signal suppressing high frequency noise, and data compression as the time evolution of a pixel can be reconstructed (from which the name of the method follows) by using only the *m+1(m+1<N)* coefficient images.

Another advantage of synthetic data reconstruction through TSR method is the calculation of time-derivative images. In time-derivative analysis, each pixel time history is differentiated using the following expression [18]:

$$\frac{d\,ln(T)}{d\,ln(t)} = \sum_{n=0}^{N} m a_m\, ln(t)^{m-1} \qquad \text{(Eq. 4.12)}$$

Even that first, second or higher order derivative images can be created, in practice only the first and second time-derivative images are used [20]. The first and second time-derivatives actually provide information on the rate of temperature variation. These measurements are analogous to the relations of position, velocity and acceleration in mechanics. The raw thermogram corresponds to the surface temperature of the inspected object (position). The first time derivative gives information on the cooling rate of the surface (velocity), while the second time derivative provides information on the deceleration or acceleration of the cooling rate (analogous to acceleration in mechanics). In other words, time derivative images are considering the temperature change instead of temperature amplitude, resulting to increased sensitivity of small temperature changes compared to the information obtained from the raw thermal images [21]. In addition, problems such as non-uniform heating, emissivity variations, environmental reflections and surface geometry have a low impact on derivative data and thus these images are remarkably free of noise [18]. Last, derivative images are producing a significant reduction of diffusion blurring as a consequence of the fact that derivative analysis provides earlier detection of the features of interest [22]. In other words, features often appear earlier in derivative images than in the correspondent raw images, and this capability (to detect defects at early times) compensates the effect of lateral heat diffusion presented at later images in the sequence as time elapses.

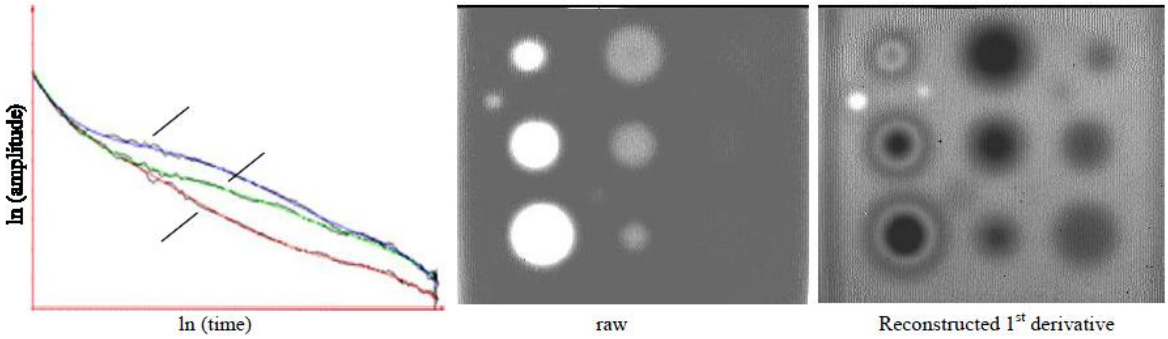

(a) (b) (c)

Fig. 4.2: *a) Logarithmic temperature time plots for a background point (red line), shallow (green line) and deep (blue line) In the reconstructed 1st derivative image, the sensitivity of the deeper holes and of the smaller holes is significantly better than in raw image result [16].*

As can be seen from the above result (Figure 4.2), in time derivative analysis, the indication of defects will appear darker in the derivative images and then lighter with respect to the intact region because the heat trapped above the defect slows down the cooling rate on the surface.

4.3.4 Principal Component Thermography (PCT)

PCT [23,24] also known as Principal Component Analysis (PCA) [25], is an orthogonal linear transformation that transforms the thermogram sequence into a new coordinate system. The idea behind PCT is to remove possible correlation in the data by creating a new uncorrelated dataset called principal components. PCT has been applied in the thermal NDT for data reduction and flaw contrast enhancement [26,27]. The approach is based on the application of singular value decomposition (SVD) in order to decompose the thermograms sequence into its principal components.

The first step of PCA algorithm is to reshape the three-dimensional thermographic sequence into a two-dimensional array where the columns and rows contain the spatial and temporal information respectively. Thus the original thermographic sequence $T(x,y,t)$ becomes $A\ (N,M)$ where $N=Nx\ X\ Ny$ and $M= Nt$, with Nx and Ny being the number of pixels per row and column of the IR camera and Nt the number of thermal images in the thermographic sequence. The two dimensional array A is then adjusted by subtracting the mean along the time dimension, and decomposed into eigenvectors and eigenvalues. The SVD of an MN matrix $A\ (M>N)$ can be calculated, as can be seen from Eq. 4.13 [23]:

$$A = USV^T \qquad \text{(Eq. 4.13)}$$

where U is an MN orthogonal matrix, S being a diagonal NN matrix (with singular values of A present in the diagonal), V^T is the transpose of an NN orthogonal matrix (characteristic time). This operation is represented in Figure 4.3. The use of SVD in PCT is performing data reduction in such a manner that a set of compact orthogonal statistical representation of the spatial and temporal variations, also known as empirical orthogonal functions (EOFs) are obtained [23-25]. These variations are related to contrasts associated with underlying material defects [23]. Since the spatial and temporal variations in the thermographic sequence are progressing relatively slowly, the principal temporal variations of the dataset are usually contained within the first few eigenvectors. As a result, the principal temporal variations of the dataset are usually contained within the first few EOF images. In particular in PCA, the first EOF represents the most characteristic variability of the data; the second EOF contains the second most important variability, and so on. Typically, a 1000 thermogram sequence can be replaced by 10 or less EOFs [19].

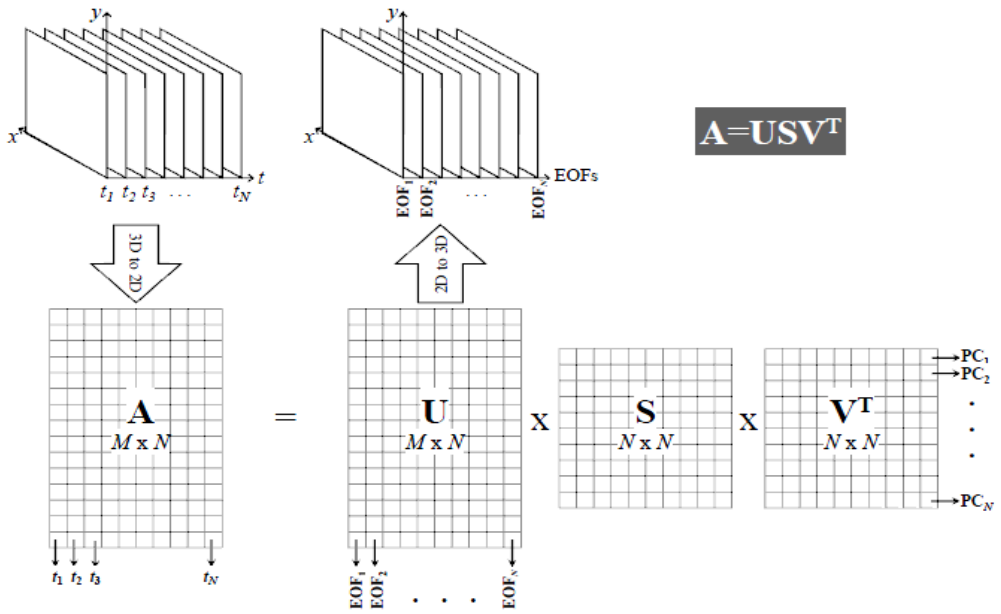

Fig. 4.3: *Schematic representation of SVD as applied to thermographic data in principal component analysis.*

4.3.5 Pulsed Phase Thermography (PPT)

PPT [28-31] is a processing technique which is based on the combination of pulsed and lock-in thermographic approaches, implementing the Fourier transformation in order to map the temporal function of temperature variation into a function in the frequency domain. In LT a heat flux of a single frequency is delivered into the specimen and analysed in a steady regime, while in pulsed configuration the responses from a range of frequencies are incorporated to a single transient signal. PPT uses the experimental procedure of PT and the data analysis of Lock-in approach (frequency domain processing) and as a result, in addition to the temporal information gained by PT, the analysis by PPT technique, further provides phase and amplitude information. Moreover, the pulsed mode of heating used in PPT (in this case thermal excitation is composed of periodic waves at several frequencies) enables the technique to simultaneously study a range of different depths from a single experiment, contrary to lock-in approach where in order to study a depth range, a range of different modulation frequencies shall be used in order to perform a complete depth investigation. The main advantages of PPT derive from the properties of phase data [28-31] which produces enhanced detectability of defects, minimization of surface characteristics (i.e. geometrical variations), reduction of non-uniform heating influence, and enhanced resolution of hidden features geometry. The above advantages have also been reported to different studies, investigating various types of materials [33-37].

In PPT procedure, after the sequential recording of thermal data at a fixed sampling frequency, mathematical tools such as the one-dimensional Discrete Fourier Transform (DFT) can be used in order to transform data in the frequency spectrum, following the expression [38]:

$$F_n = \Delta t \sum_{k=0}^{N-1} T(k\Delta t) exp^{(-j2\pi nk/N)} = Re_n + Im_n \qquad \text{(Eq. 4.14)}$$

where *j* is the imaginary number ($j^2 = -1$), *n* designates the frequency increment ($n = 0, 1, \ldots N$), Δt is the sampling time interval, and *Re* and *Im* are the real and the imaginary parts of the transform, respectively. Once the data has been converted into the Fourier domain, real and imaginary parts of the complex transform are used to estimate the amplitude (A), and the phase (ϕ) through [28]:

$$A_n = \sqrt{Re_n^2 + Im_n^2} \qquad \text{and} \qquad \varphi = tan^{-1}\left(\frac{Im_n}{Re_n}\right) \qquad \text{(Eq. 4.15)}$$

The DFT can be used with any waveform (e.g. transient pulse), however this procedure requires lengthy computations. Fortunately, the fast Fourier transform (FFT) algorithm [39] has been proposed and can be applied as well in order to obtain phase and amplitude information, with the advantage of greatly reducing the computation time. After its proposition for PT data treatment [28], this algorithm has been widely adapted as a useful tool for Fourier transformations when working with thermographic data and its application was further extended for the data analysis of other active thermographic techniques such as L and VT [40,41].

Figure 4.4 shows the 3D transformation of time-dependent thermal data to 3D frequency-dependent phase data sequence through Equation 4.15. The phase profiles for a defective (red) and a sound area (blue) are illustrated in Figure 4.4d, which as can be seen are anti-symmetric, providing the same information in both sides of the frequency spectrum. As a result, from the acquired sequence of *N* thermographs, there are *N/2* useful frequency components [42]. This observation leads to the conclusion that sampling a continuous temperature signal *T(t)* with a time rate t_s, limits the frequency domain to a maximum frequency of $f = (2t_s)^{-1}$ in the phase data sequence. From the aforesaid, it can be understood that the frequency resolution (frame rate of acquisition) and the total acquisition time, when performing PPT investigations are crucial parameters and should be determined prior the experimental procedure, by taking into consideration the thermal properties of the material (high conductivity materials require high sampling frequencies and short acquisition times) and the depth of the features of interest (larger depths require low sampling frequencies and longer acquisition times) to avoid loss of information [30]. Thus, the time-frequency duality of the Fourier transform plays an important role in the selection of the aforementioned experimental parameters and for this reason, in order to characterise a wide range of defects in different depths from a single experiment, a four step interactive methodology has been proposed when working with PPT [31].

As discussed above, the phase in thermographic NDT is of prime interest due to its specific advantages in image interpretation and hidden features detectability. Nevertheless, noise content in phase data can be considerable, especially at high frequencies which may require a de-noising step. However, the combination of PPT and TSR has proven to be very attractive for this matter, reducing the noise from the output signal, by reconstructing the thermographic data into synthetic data, and

processing the coefficient images with PPT algorithm [32]. In addition, this combination is suitable when the capabilities of the processing unit are limited, as a reduced amount of data has to be manipulated.

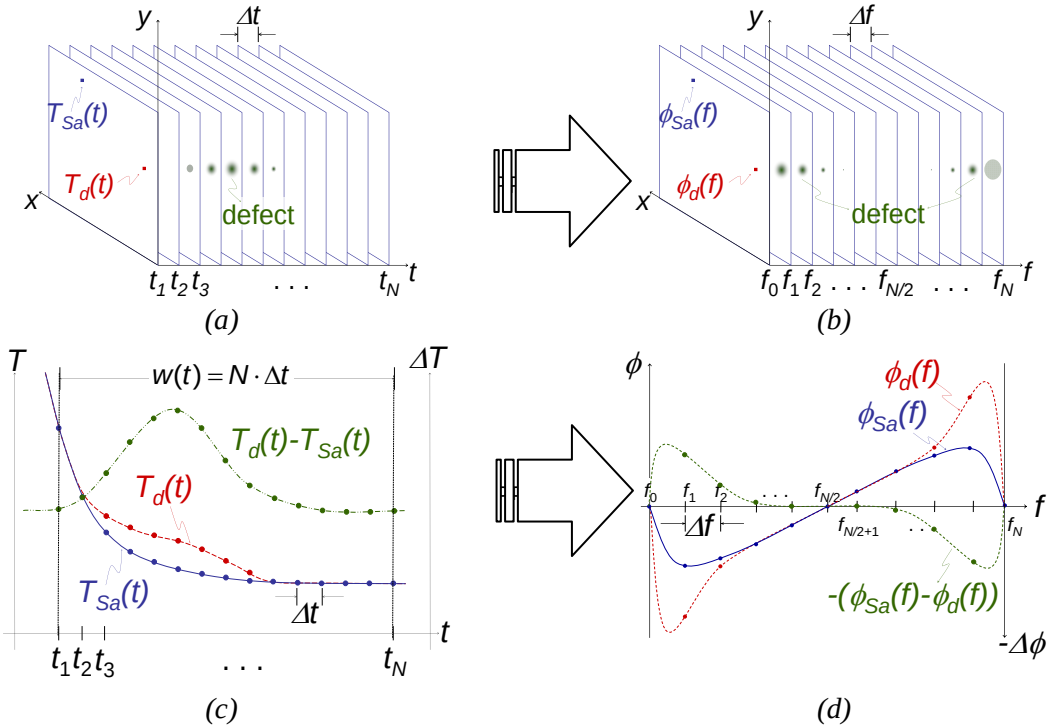

Fig.4.4: *Schematic representation of Pulsed Phase Thermography with (a) the thermogram 3D matrix depicting the appearance and disappearance of a defect through time, (b) the phasegram 3D matrix showing the defect visibility in the frequency spectrum, (c) the thermal profiles for a non defective pixel (-T_{sa}), a defective pixel (--T_d) and the difference between them (T_d -T_{Sa}), and (d) the phase profiles for a non defective pixel (-ϕ_{sa}), a defective pixel (--ϕ_d) and the difference between them (φ_d -φ_{Sa}). [43].*

4.4 Quantitative analysis of infrared thermographic data

As presented above, different processing techniques have been developed for the interpretation of infrared thermographic data, aiming to defect detectability enhancement and noise reduction on the final output result. Regardless the domain where the thermal data is processed, different procedures have also been proposed for quantitative characterisation of defects, which are based either on exclusively analytical methods [5,44] or inverse methods implementing numerical calculations and experimental measurements [5,45]. Quantitative characterisation of defects includes mainly depth information retrieval and the estimation of defect's lateral dimension, while studies have also investigated the determination of the thermal properties either of the material inspected or of the hidden feature detected. The procedures based on experiential observations can somehow produce results in a straightforward manner, as these are used in order to solve analytical formulas. By involving inverse techniques, the quantitative characterisation of features of interest requires the establishment of a numerical model taking into account many parameters, although among these parameters often only one parameter is of interest (i.e. depth) and can be estimated by correlating numerical and experimental

results. In the followings, a review of some analytical quantitative methods in different domains is presented based on the signal processing algorithms described above.

4.4.1 Quantitative depth estimation in time domain

For quantitative depth prediction, the most widely used algorithms utilize temporal characteristics of the thermal response received from the excited surface. In particular, these methods relate the defect depth with a characteristic time value, which is associated with the appearance of the hidden defect as a temperature difference on the surface of the inspected sample. According to the thermal phenomenon studied (i.e. temperature evolution of the thermal response or thermal contrast evolution between this characteristic response and a sound area), different procedures have been proposed for quantitative depth estimations. The most common method involves the *Peak Contrast Time (PCT)* which is the time point when the maximum thermal contrast between a defective and a preselected reference point occurs. The reference is normally a point chosen manually from the sound area, while the averaging temperature over a non defective zone can also be used in order to reduce the negative effect of non uniform heating. However, as the peak contrast occurs relatively lately, when the 3D conduction heat transfer has a great influence, different methods have also been proposed involving earlier determinations of a characteristic time point such as the *Peak Slope Time (PST)* and the *Logarithmic Peak Second Derivative Time (LSDT)*, providing greater accuracy on the acquired results and illuminating the negative effects of lateral heat diffusion around the defective area. A brief description of the theoretical analysis of these depth prediction methods is discussed in the following subsections.

The idea behind the determination of the aforementioned time points is based on the fact that when studying the heat diffusion after the application of a thermal pulse on the surface, the time taken for the thermal wave to be reflected back to the surface is inversely proportional to the thermal diffusivity of the material and directly proportional to the square of its depth [5, 46,47]. As a result, the specific characteristic time when the defect becomes obvious on the surface has certain relation with the defect depth and this can be expressed as [48]:

$$t_{SCT} = \frac{L^2}{ba} \qquad \text{(Eq. 4.16)}$$

where t_{SCT} is the specific characteristic time, α is the thermal diffusivity of the inspected material, L is the depth of defect and b is a proportionality coefficient related with the particular procedure used and the defined characteristic time determined.

4.4.1.1 Peak Thermal Contrast Time method

As stated above, traditionally the temporal analysis of PT data involved the maximum contrast to identify the depth of a defect, taking the peak time of this maximum thermal contrast occurrence. When pulsed thermal energy is applied, the specimen surface is instantaneously heated to a high temperature. Heat conduction takes place from the heated surface to the interior of the sample, leading to a continuous decrease of the surface temperature. The decay of the surface temperature with time for a

semi-infinitive isotropic solid is described from the formula $T(t) = Q/e\sqrt{\pi t}$ (Eq. 3.3), while in the presence of a subsurface defect or a structural difference, the one dimensional solution of heat diffusion is given by [49]:

$$T(t) = \frac{Q}{e\sqrt{\pi t}}\left[1 + 2\sum_{n=1}^{\infty} R^n \exp\left(-\frac{n^2 L^2}{\alpha t}\right)\right] \quad \text{(Eq. 4.17)}$$

where is L the defect depth and R is the thermal wave reflection coefficient between the two media and n defines the number of internal thermal wave reverberations. The thermal contrast can be obtained by subtracting Eq. 3.3 from Eq. 4.16, and if setting $w = L^2/\alpha$ and $A = Q/e\sqrt{\pi}$, this can be expressed as:

$$\Delta T = 2At^{(-1/2)}\sum_{n=1}^{\infty} R^n \exp\left(-\frac{n^2 w}{t}\right) \quad \text{(Eq. 4.18)}$$

The first derivative of the thermal contrast can be expressed as:

$$\Delta T' = 2At^{(-3/2)}\sum_{n=1}^{\infty} R^n \exp\left(-\frac{n^2 w}{t}\right)\left(\frac{n^2 w}{t} - \frac{1}{2}\right) \quad \text{(Eq. 4.19)}$$

and the peak contrast time corresponds to the time that Eq. 4.19 equals to zero. The solution of the above equation reveals that the time of maximum thermal contrast is approximately proportional to the square of the defect depth, however experimental and numerical studies have shown that the proportionality coefficient b depends on defect size and the mismatch factor of defect-material interface [50-53]. The smaller the defect size, the lower the maximum contrast and the shorter the peak contrast time [51]. More specifically, the maximum contrast occurs lately, at a time when lateral heat transfer takes importance and introduces discrepancies between the reality and the results of the models used which is 1D for sake of rapidity due to the enormous number of information to process.

4.4.1.2 Peak Slope Time method

In order to suppress the effects of 3D heat transfer, early detection approaches have been proposed as well. More specifically, one of the earliest time points on a temperature time evolution curve, which is used for defect depth estimations, is the moment when the temperature signal above the inspected point diverges from the reference signal. Usually as raw thermal data contains noise, establishing of a threshold level is required to identify this point on the temperature-time curve [54]. In terms of thermal contrast curves, the corresponding time when the signal diverges from the reference signal, can be defined as the time when the thermal contrast crosses a specified threshold level, which can be determined as the point when the thermal contrast differs to zero. This characteristic time value has the advantage of depth prediction in early times, thus possible effects produced from lateral heat diffusion in the area of the defect are particularly removed. However, the determination of this value requires a sampling rate high enough in order to accurately capture the initial time when the temperature in the defective zone diverse from the reference temperature and it does not provide accurate results for shallow defects characterisation [55]. Another early time point is the moment when the contrast curve

has the peak slope [56,57]. This parameter can be easily found as it corresponds to the peak of the 1st derivative of the thermal contrast and is commonly referred as *Peak slope time method.* The exact relationship between depth and peak slope time can be determined by solving for this specific time value in Eq. 4.19 or equivalently by identifying the time when the second derivative of the thermal contrast equals to zero. This parameter is essential for defect depth estimation as experimental and numerical studies have shown that results are unaffected from the size of the defect [58,59]. In this method, the time (t_s) at which the peak in the slope contrast occurs, was found to be related with the defect depth L_d in a sample of thickness L and of thermal diffusivity α according to [58]:

$$t_s = \frac{3.64 L_d^2}{\pi^2 a} \qquad \text{(Eq. 4.20)}$$

The proportionality coefficient equal to 3.64 was found to be valid regardless the type of the material when $L_d/L \leq 0.5$, while for deeper defects ($L_d/L > 0.5$) this proportionality coefficient was found to vary as presented in Figure 4.5.

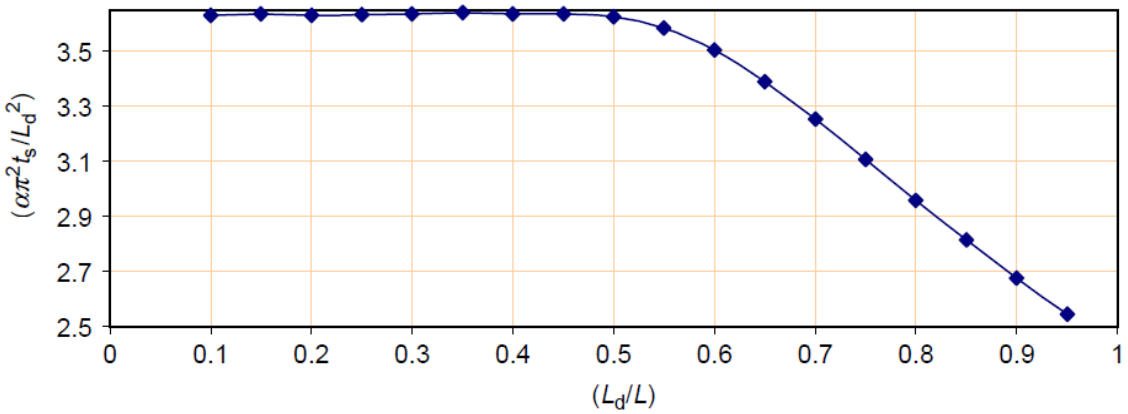

Fig.4.5: *Variation of proportionality constant with respect to defect's depth –sample's thickness ratio [58].*

4.4.1.3 Logarithmic Peak Second-Derivative method

Unlike to the situation in the temperature contrast methods, where the selection of a reference point is required, a method has been proposed to determine defect depth directly from the temperature decay for each individual surface point. Such a procedure involves the use of *Logarithmic Peak Second-Derivative Time* (*LPSD),* which is a reference free depth prediction method and provides an important decrease of noisy data influence [60]. In the logarithmic 2nd derivative method, quantities are calculated directly from the temperature decay as the specific characteristic time in LPSD corresponds to the peak time in the 2nd derivative plot of the surface temperature versus logarithmic time. The time when the peak occurs can be used to determine the defect depth. This method can be directly analysed by Eq. 4.17, as the second derivative in the logarithmic notation, can be expressed as [57]:

$$\frac{d^2(\ln T)}{\mathrm{d}(lnt)^2} = \frac{t}{T}\frac{dT}{dt} - \frac{t^2}{T^2}\left(\frac{dT}{dt}\right)^2 + \frac{t^2}{T^2}\frac{d^2T}{dt^2} \qquad \text{(Eq. 4.21)}$$

where

$$\frac{dT}{dt} = -\frac{1}{2}At^{(-3/2)} + 2At^{(-3/2)}\sum_{n=1}^{\infty} R^n \exp\left(-\frac{n^2 w}{t}\right)\left(\frac{n^2 w}{t} - \frac{1}{2}\right) \quad \text{(Eq. 4.22)}$$

and

$$\frac{d^2T}{dt^2} = \frac{3}{4}At^{(-5/2)} + 2At^{(-5/2)}\sum_{n=1}^{\infty} R^n \exp\left(-\frac{n^2 w}{t}\right)\left[\left(-\frac{n^2 w}{t}\right)^2 - \frac{3n^2 w}{t} + \frac{3}{4}\right] \quad \text{(Eq. 4.23)}$$

when Eq. 4.23 is solved by a numerical method, the peak second derivative time can be defined as:

$$t_{LSDT} = \frac{\pi L^2}{\pi^2 \alpha} \quad \text{(Eq. 4.24)}$$

By comparing Eq. 420 and 4.24, it can be observed that the peak second derivative time occurs slightly earlier than the peak slope time and as can be understood a method based on an early characteristic time is more likely to capture the peak defect signal before it is affected by 3D conduction, which could lead to more accurate depth determination. Additionally, the capability to derive defect depth directly from the temperature data for each individual surface point represents a significant advantage for automation in thermographic data processing.

4.4.2 Quantitative depth estimation in frequency domain

As discussed above the phase data is of prime interest in thermographic imaging, as additionally to the enhanced detectability that it provides, a depth prediction approach analogous to the early detection through the thermal contrast curve has been developed [30,43]. This approach consists of identifying the depth of the defect from the frequency for which the phase contrast between defective and sound areas crosses the zero contrast line [3]. This technique relies on the thermal diffusion length, i.e.$\mu = (\alpha/\pi f)^{1/2}$, in a manner similar to LT, as the depth of the defect can be estimated from a relationship of the form [43]:

$$z = C_1 \cdot \mu = C_1\sqrt{\frac{a}{\pi f_b}} \quad \text{(Eq. 4.25)}$$

where C_1 is a correlation constant and f_b [Hz] is the so called *blind frequency*, defined as the limiting frequency at which a defect located at a particular depth presents enough (phase or amplitude) contrast to be detected on the frequency spectrum. The above described, are illustrated in Figure 4.6, where the depth determination procedure using phase data is schematically presented. The phase profiles for two defects at different depths (φz_1, φz_2), and for a sound area (φz_{sa}), are shown at the bottom part of the graph, while the corresponding phase contrasts ($\Delta\varphi z_1$, $\Delta\varphi z_2$) calculated from the phase profiles as: $\Delta\varphi = \varphi_d - \varphi_{Sa}$, where φ_d is the phase of a defective pixel and φ_{Sa} is the phase for a non-defective pixel. For clarity, phase profiles have been drawn on the positive area of the diagram while phase contrasts have been drawn on the respective negative area. Defects are visible when $\Delta\varphi>0$, from $f=0Hz$ to the blind frequency f_b, which is lower for deeper defects ($f_{bz1}>f_{bz2}$). Phase profiles for defective

pixels merge with the phase profiles of a sound area into a straight line for frequencies higher than the corresponding blind frequencies ($f>f_b$). Consequently, shallow defects have a larger frequency range of visibility than deeper ones. In the above presented result, the absolute phase contrast definition was used for the determination of the blind frequency (similarly to the absolute thermal contrast definition in temporal data treatment).

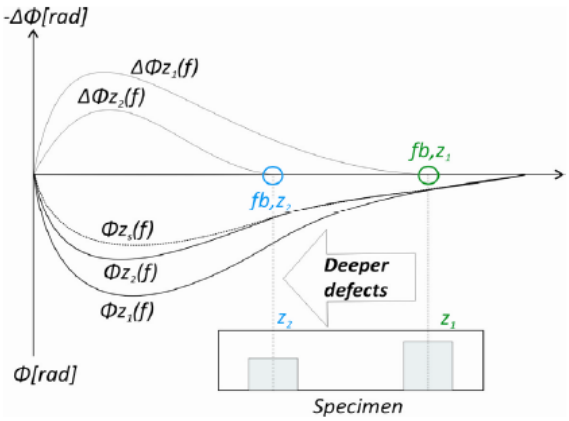

Fig. 4.6: *Schematic representation of phase retrieval procedure for the determination of defect depth in Pulsed phase thermography [43].*

Thus, depth retrieval from phase needs the sound area for phase difference calculation and the problem of a priori knowledge of the defect location or the non-uniform heating can produce an extra error on depth prediction. However a procedure that uses the DAC method in phase data has been proposed to overcome this difficulty [62]. Moreover, automatic determination of blind frequency can be done as well, without the need of a sound area definition though an automated depth retrieval algorithm which estimates the curve slope of a non defective pixel by least squares regression and iteratively locate the frequency value (i.e. the blind frequency), at which the slope of a defective pixel diverges from the typical linear behaviour of a non-defective pixel [63].

From the above described procedures, in order to perform depth measurement only the blind frequency and the correlation coefficient have to be determined. Conventional experimental C_1 values when using the phase in lock-in experiments range from 1.5 to 2 [64] with a value of $C_1 = 1.82$ [65] typically adapted in experimental studies [66]. PPT results agree with this value range either for homogeneous or composite materials [31,43]. Thus, when the value of proportionality coefficient is known, the PPT inversion problem is reduced to the estimation of the blind frequency. In any other case, in order to validate the depth results, the accuracy of the correlation coefficient value used in Equation 4.27 should be evaluated through numerical or graphical measures between the variables of z and μ after the determination of the blind frequency [43].

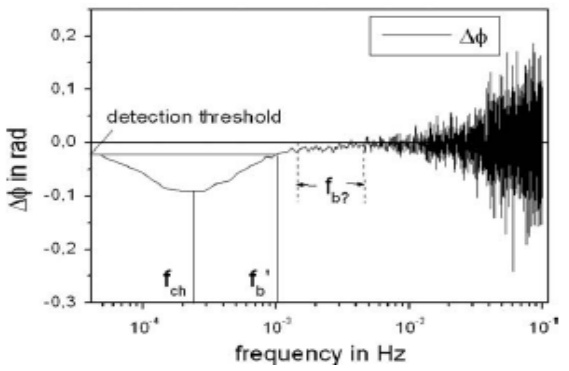

Fig. 4.7: *Determination of characteristic frequency in phase data acquired after a long square heating excitation process [67].*

Recently the use of PPT algorithm has been proposed to be implemented in long square pulse heating methods in order to retrieve quantitative information about the depth of a defect. The quantitative approach of SPT in the frequency domain makes use of the fact, that a broad signal in time domain when transformed in the frequency domain has a clearly defined peak in the frequency

spectra (Figure 4.7). This method makes thereby use of the frequency in which the first exterma of phase- or amplitude contrast- is presented and is referred as *characteristic frequency* f_{ch} and not of the blind frequency as in the classical pulsed thermography. From the above mentioned considering a correction factor k_c, similarly as in the "short" pulsed classical PPT, the depth of the defect can be deduced by [67]:

$$z = k_c \sqrt{\frac{a}{\pi f_{ch}}} \qquad \text{(Eq. 4.26)}$$

This quantitative method involving PPT technique in square pulsed heating was developed since the blind frequency was not quantifiable from data acquired after long heating.

4.4.3 Defect size extraction

The above presented procedures can be used in order to predict the defect depth in active thermal scenarios. All the developed procedures are based on the identification of signal amplitude variations between a defective and a defect-free area, regardless the domain in which the analysis is performed. Another important informative parameter for defect characterisation is the definition of its lateral dimensions. After thermal stimulation in transient thermography the cooling rates of the surface upon a sound area and a defective area are different. This difference allows detecting the dimensions of a subsurface defect based on the heat flaw perturbations caused by the defect as the thermal wave travels into the tested material bulk. In particular the lateral dimensions of a defect may be determined by measuring e.g. raw thermal data using the FWHM approach [68-71] along a line profile that bisects the area of interest (defective zone). A line profile finds the informative parameter (i.e. temperature, phase, amplitude) of each pixel along the length of the line. Figure 4.8 depicts this analysis procedure schematically.

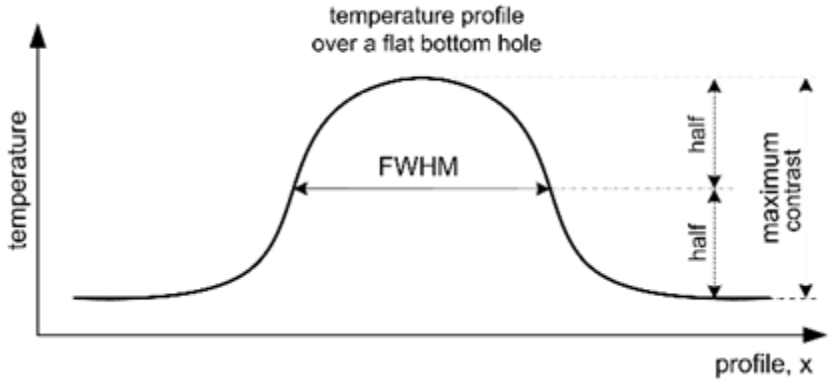

Fig. 4.8: *Radiance profile over a defective area.*

The profile in x-axis is assumed to cross the center of the defect and once the defect dimensions have been estimated in pixels units and taking into consideration the imaging equipment- sample distance and camera's lens parameters, the pixels can be converted in physical units through the IFOV parameter of the camera. From numerical modeling and experimental results, it has been found that the FWHM

approach is a very promising technique in order to determine the lateral dimensions of a defect in thermographic data and the best correlation with the real dimensions is observed at early times. As the time passes FWHM approach provides narrower results due to shrinkage effect phenomenon [72]. Thus, the best possible results concerning the size of a detected defect are attained at particularly short transient times, even if the clearest images (with the higher contrast) are acquired at longer periods [73].

4.5 References

[1] C. Ibarra-Castanedo, A. Bendada, X. Maldague (2007). *Thermographic Image Processing for NDT*. In Proc. of IV Conferencia Panamericana de END, Buenos Aires, Argentina, 2007.

[2] C. Ibarra-Castanedo, D. Gonzalez, M. Klein, M. Pilla, S. Vallerand, X. Maldague (2004). *Infrared image processing and data analysis.* Infrared Physics & Technology, Vol. 46(1-2), pp. 75-83.

[3] S. Marinetti, X. Maldague, M. Prystay (1997). *Calibration procedure for Focal Plane Array Cameras and noise equivalent material loss for quantitative thermographic NDT.* Materials Evaluation, Vol. 55 (3), pp. 407-412.

[4] X.P.V. Maldague, (1993). *Nondestructive Evaluation of Materials by Infrared Thermography*. Springer-Verlag, London.

[5] X. Maldague (2001). *Theory and Practice of Infrared Technology for Non Destructive Testing.* John-Wiley & Sons, New York.

[6] J.C. Krapez (2001). *Thermal Contrasts in Pulsed Thermography*. In P.O. Moore ed., X. Maldague technical ed.: Infrared and Thermal Testing, Nondestructive Testing Handbook, Vol. 3. 3rd Edition. Colombus, Ohio, American Society for Nondestructive Testing.

[7] C. Ibarra-Castanedo, H. Benitez, X. Maldague, A. Bendada(2007). *Review of thermal-contrast-based signal processing techniques for the nondestructive testing and evaluation of materials by infrared thermography*. In Proc. of International Workshop on Imaging NDE, Chennai, India, April 25-28 2007.

[8] M. Pilla, M. Klein, X. Maldague, A. Salerno (2002). *New Absolute Contrast for pulsed thermography*. In D. Balageas, G. Busse, G. Carlomagno (eds.): Proc. of Quantitative Infrared Thermography Conference (QIRT02), Dubronvik, Croatia, pp.53-58.

[9] H. Benitez, C. Ibarra-Castanedo, A. Bendada, X. Maldague, H. Loaiza, E. Caicedo (2008). *Definition of a new thermal contrast and pulse correction for defect quantification in pulsed thermography*. Infrared Physics & Technology, Vol. 51, pp. 160-167.

[10] C. Ibarra-Castanedo, A. Bendada, X. Maldague (2005). *Image and signal processing techniques in pulsed thermography*. In GESTS International Transactions on Computer Science and Engineering. Vol.22 (1), pp. 89-100.

[11] D. Gonzalez, C. Ibarra-Castanedo, M. Pilla, M. Klein, J. Lopez-Higuera, X. Maldague (2004). *Automatic interpolated differentiated absolute contrast algorithm for the analysis of pulsed thermographic sequences.* In D. Balageas, J. Buchlin, G. Carlomagno, G. Busse (eds.): Proc. of Quantitative Infrared Thermography 7, QIRT7, Brussels, Belgium, pp. H.16.1-H16.6

[12] D. Maillet, S. Andre, J. Batsale, A. Degiovanni, C. Moyne (2000). *Thermal quadrupoles: solving the heat equation through integral transforms.* John Wiley & Sons, West Sussex, England.

[13] H. Benitez, C. Ibarra-Castanedo, A. Bendada, X. Maldague, H. Loaiza, E. Caicedo (2006). *Modified Differential Absolute Contrast Using thermal quadrupoles for the nondestructive testing of finite thickness specimens by Infrared Thermography.* In Proc. of Canadian Conference on Electrical and Computer Engineering (CCECE2006), Ottawa, Canada, (CDROM).

[14] S.M. Shepard (2001). *Advances in Pulsed Thermography.* In A.E. Rozlosnik, R.B. Dinwiddie (eds.): Proc. of SPIE- The International Society for Optical Engineering, Thermosense XXIII, Vol. 4360, pp. 511-516.

[15] S.M. Shepard, T. Ahmed, B.A. Rubadeux, D. Wang, J.R. Lhota (2001). *Synthetic processing of pulsed thermographic data for inspection of turbine components.* Insight, Vol. 43(9), pp.587-589.

[16] S.M. Shepard, J.R. Lhota, B.A. Rubadeux, T. Ahmed, D. Wang (2002). *Enhancement and reconstruction of thermographic NDT data.* In X.P.V. Maldague, A.E. Rozlosnik (eds.): Proc. of SPIE- The International Society for Optical Engineering, Thermosense XXIV, Vol. 4710, pp. 531-535.

[17] S.M. Shepard (2003). *Temporal noise compression and analysis of thermographic image data sequences*, US Patent 6516084.

[18] S.M. Shepard, J.R. Lhota, A. Rubadeux, D. Wang, T. Ahmed (2003). *Reconstruction and Enhancement of active thermographic image sequences*. Optical Engineering, SPIE Publishing, Vol. 42, pp. 1337-1342.

[19] C. Ibarra-Castanedo, J.M. Piau, S. Guilbert, N.P. Avdelidis, M. Genest, A. Bendada, X.P. Maldague (2009). *Comparative study of Active Thermography Techniques for the Nondestructive Evaluation of Honeycomb Structures.* Research in Nondestructive Evaluation, Vol. 20 (1), pp. 1-31.

[20] S.M. Shepard (2007) *Flash Thermography of aerospace composites.* In Proc. of IV Conferencia Panamericana de END, Buenos Aires, Brazil (CDROM).

[21] R.E. Martin, A.L. Gyekenysi, S.M. Shepard (2003). *Interpreting the Results of Pulsed Thermography Data*. Materials Evaluation, Vol. 61 (5), pp. 611-616.

[22] S.M. Shepard, J.R. Lhota, B.A. Rubadeux, D. Wang, T Ahmed (2003). *Materials characterisation using reconstructed thermographic data.* In D.O. Thompson, D.E. Chimenti (eds.): Review of Progress in Quantitative Nondestructive Evaluation, American Institute of Physics, Vol. 22, pp. 1270-1276.

[23] N. Rajic (2002). *Principal component thermography for flaw contrast enhancement and flaw depth characterisation in composites structures.* Composite Structures, Vol. 58 (4), pp.521-528.

[24] N. Rajic (2002). *Principal component thermography.* Technical Report TR1298, Aeronautical

and Maritime Research Laboratory, Defense Science & Technology Organisation, Victoria, Australia.

[25] S. Marinetti, E Grinzato, P.G. Bison, E. Bossi, M. Chimenti, G. Pieri, O. Salvatti (2004). *Statistical analysis of IR thermographic sequences by PCA.* Infrared Physics and Technology, Vol. 46, pp. 85-91.

[26] J.N. Zalameda, P.A. Howell, W.P. Winfree (2005). *Compression techniques for improved algorithm computational performance.* In G.R. Peacock, D.D. Burleigh, J.J. Miles (eds.): Proc. of SPIE- The International Society for Optical Engineering, Thermosense XXVII, Vol. 5782, pp. 399-406.

[27] K.E. Cramer, W.P. Winfree (2006). *The application of Principal Component Analysis Using fixed Eigenvectors to Infrared thermographic inspection of the space shuttle thermal protection system.* In Proc. of 9th International Conference on Quantitative Infrared Thermography (QIRT 08), Krakow, Poland.

[28] X.P.V. Maldague, S. Marinetti (1996). *Pulse Phase Infrared Thermography.* Journal of Applied Physics, Vol. 79(5), pp. 2694-2698.

[29] X. Maldague, J.P. Countier (1997). *Review of Pulse phase infrared thermography*. In Proc. of 4th International Workshop on Advanced Infrared technology and Applications (AITA), Firenze, Italy September 15-16, 1997, Vol. 53(1), pp. 271-286.

[30] C. Ibarra-Castanedo, X. Maldague (2004). *Pulsed Phase Thermography Reviewed.* QIRT Journal, Vol. 1(1), pp. 47-70.

[31] C. Ibarra-Castanedo, X.P.V. Maldague (2005). *Interactive methodology for Optimized Defect charectization by quantitative pulsed phase thermography.* Research in Nondestructive Evaluation, Vol. 16(4), pp.175-193.

[32] X. Maldague, F. Galmiche, A. Ziadi (2002). *Advances in pulsed phase thermography.* Infrared Physics & Technology, Vol. 43, pp. 175-181.

[33] C. Ibarra–Castanedo, M. Genest, P. Servais, X.P.V. Maldague, A. Bendada (2007). *Qualitative and quantitative assessment of aerospace structures by pulsed thermography.* Nondestructive Testing and Evaluation, Vol. 22(2-3), pp. 199-215.

[34] N.P. Avdelidis, C. Ibarra-Castanedo, X. Maldague, Z.P. Marioli-Riga, D.P. Almond (2004). *A thermographic comparison study for the assessment of composite patches.* Infrared Physics & Technology, Vol. 45(4), pp. 291-299.

[35] R. Montanini (2010). *Quantitative determination of subsurface defects in a reference specimen made of Plexiglas by means of lock-in and pulse phase infrared thermography.* Infrared Physics & Technology, Vol.53, pp.363-371.

[36] F. Mercuri, U. Zammit, N. Orazi, S. Paoloni, M. Marinelli, F. Scudieri (2011). *Active infrared thermography applied to the investigation of art and historic artefacts.* Journal of Thermal

Analysis and Calorimetry, Vol. 104 (2), pp. 475-485.

[37] N.P. Avdelidis, M. Koui, C. Ibarra-Castanedo, X. Maldague (2007). *Thermographic studies of plastered mosaics.* Infrared Physics &Technology, Vol. 49(3), pp. 254-256.

[38] R. Bracewell (1965). *The Fourier Transform and its Applications.* McGraw-Hill, New York, USA.

[39] J.W. Cooley, J.W. Tukey (1965). *An algorithm for the machine calculation of complex Fourier series.* In Mathematics of Computation J., Vol. 19(90), pp. 297-301.

[40] A. Dillenz, T. Zweschper, G. Busse (2001). *Progress in ultrasound phase thermography*. In A.E. Rozlosnik, R.B. Dinwiddie (eds.): Proc. of SPIE- The International Society for Optical Engineering, Thermosense XXIII, Vol. 4360, pp. 230-238, Orlando, Florida, USA.

[41] A. Dillenz, T. Zweschper, G. Busse (2002). *Brust phase angle thermography with elastic waves.* In X.P. Maldague, A.E. Rozlosnik, R.B. Dinwiddie (eds.): Proc. of SPIE- The International Society for Optical Engineering, Thermosense XXIV, Vol. 4710, pp. 572-577, Orlando, Florida, USA.

[42] S. Marinetti, Y.A. Plotnikov, W.P. Winfree, A. Braggiotti (1999). *Pulsed Phase thermography for defect detection and visualization.* In D.D. Burleigh, J.M. Spicer (eds.): Proc. of SPIE- The International Society for Optical Engineering, Thermosense XVIII, Vol. 3586, pp. 230-238.

[43] C. Ibarra-Castanedo (2005). *Quantitative subsurface defect evaluation by pulsed phase thermography: depth retrieval with the phase.* Ph. D. thesis, Université Laval, [available online: http://www.theses.ulaval.ca/2005/23016/23016.pdf].

[44] P.H. James, C.S. Welch, W.P. Winfree (1989). *A numerical grid generation scheme for thermal simulation in laminated structures.* In D.O. Thompson, D.E. Chimenti (Eds.): Review of Progress in Quantitative Nondestructive Evaluation, Plenum Press, New York, Vol. 8A, pp. 801–809.

[45] J.C. Krapez, P. Cielo (1991). *Thermographic nondestructive evaluation: data inversion procedures part I: 1D analysis.* In Research in Nondestructive Evaluation, Vol. 3(2), pp. 81-100.

[46] S.K. Lau, D.P. Almond, P.M. Patel (1991). *Transient Thermal wave techniques for the evaluation of surface coatings.* Journal of Physics D:Applied Physics, Vol. 24 (3), pp. 428–436

[47] D.P. Almond, S.K. Lau (1994). *Defect sizing by transient thermography I: an analytical treatment*. Journal of Physics D: Applied Physics, Vol. 27 (5), pp.1063-1069.

[48] Z. Zeng, C. Li, N. Tao, L. Feng, C. Zhang (2012). *Depth prediction of non-air interface defect using pulsed thermography*. NDT&E International, Vol. 48, pp. 39-45.

[49] D. Almond, P. Patel (1996). *Photothermal science and techniques.* 1st Edition, Chapman & Hall, London, UK.

[50] L.D. Favro, H.J. Jin, Y.X. Wang, T. Ahmed, X. Wang (1991). *IR thermal wave tomographic studies of structural composites, review of progress in quantitative nondestructive evaluation.*

Proc. of the 18th Annual Review, Vol. 11A, Branswick, Me, July 28-August 2, 1991, pp. 447-451.

[51] X. Han, L.D. Favro, P.K. Kuo, R.L. Thomas (1995). *Early-time pulse-echo thermal wave imaging.* In D.O. Thompson, D.E. Chimenti (eds.): Review of Progress in Quantitative Nondestructive Evaluation, Vol. 15, pp. 519-524.

[52] S.K. Lau, D.P. Almond, J.M. Milne (1991). *A quantitative analysis of pulsed video thermography*. NDT&E International, Vol. 24(4), pp.195-202.

[53] J.C. Krapez, F. Lepoutre, D. Balageas (1994). *Early Detection of thermal contrast in pulsed stimulated thermography.* Journal de Physique IV, Vol. 4, C7.47-C7.50.

[54] J.C. Krapez, D. Balageas, A. Deom, F. Lepoutre (1994). *Early Detection by stimulated infrared thermo-graphy. Comparison with ultrasonics and holo/shearo-graphy.* In X.P.V. Maldague (Ed.): Advances in Signal Processing for NDE of Materials, NATO ASI Series E, Kluwer Academic Publishers, Vol. 262, pp. 303-321.

[55] Y.A. Plotnikov, W.P. Winfree (1999). *Temporal treatment of a thermal response for defect depth estimation.* In D.O. Thompson, D.E. Chimenti (eds.): Review of Progress in Quantitative Nondestructive Evaluation, Vol. 19, pp. 587-594

[56] L.D. Favro, X. Han, P.K. Kuo, R.L. Thomas (1996). *Imaging the early time behaviour of reflected thermal wave pulses.* In D.D. Burleigh, J.M. Spicer (eds.): Proc. of SPIE- The International Society for Optical Engineering, Thermosense XVIII, Vol. 2473, pp. 162-166.

[57] J.G. Sun (2006). *Analysis of pulsed thermography methods for defect depth prediction.* J. Heat Transfer, Vol. 128 (4), pp.329-338.

[58] H.I. Ringermacher, R.J. Archacki, W.A. Veronesi (1998). *Nondestructive testing: Transient Depth Thermography*, US Patent No. 5711603.

[59] C. Deemer, J.G. Sun, W.A. Ellingson, S. Short (1999). *Front-flash thermal imaging characterisation of continuous fiber ceramic composites.* In E. Ustundag, G. Fischman (Eds.): Proc. of 23rd Annual Conference on Composites, Advanced Ceramics, Materials, and Structures: A: Ceramic Engineering and Science, Vol. 20(3), pp. 317-324.

[60] S.M. Shepard, J.R. Lhota, A. Rubadeux, D. Wang, T. Ahmed (2003). *Reconstruction and Enhancement of active thermographic image sequences*. Optical Engineering, Vol. 42, pp. 1337-1342.

[61] C. Ibarra-Castanedo, N.P. Avdelidis, E.G. Grinzato, S. Marinetti, L. Chen, M. Genest, X. Maldague (2006). *Quantitative inspection of non-planar composite specimens by pulsed phase thermography*. QIRT Journal, Vol. 3(1), pp. 25-40.

[62] M. Susa, H. Benitez, C. Ibarra-Castanedo, H. Loaiza, A. Bendada, X. Maldague (2006). *Phase contrast using differentiated absolute contrast method.* In Proc. of 8th International Conference on Quantitative Infrared Thermography (QIRT06), Padova, Italy, pp. 1-10.

[63] C. Ibarra-Castanedo, D. Gonzalez, X. Maldague (2004). *Automatic algorithm for quantitative pulsed phase thermography calculations.* In Proc of the 16th WCNTD- World Conference on Nondestructive Testing [CD ROM], Montreal, Quebec, August 30-Sempember 3, 2004.

[64] G. Busse (1979). *Optoacoustic phase angle measurement for probing a metal.* Applied Physics Letters. Vol. 35(759),pp. 759-760

[65] R.L. Thomas, J.J. Pouch, H.Y. Wong, L.D. Favro, P.K. Kuo (1980). *Subsurface flaw detection in metals by photoacustic microscopy.* J. of Applied Physics, Vol. 51(2), pp. 1152-1156.

[66] C. Meloa, G.M. Carlomagno (2004). *Recent advances in the use of infrared thermography.* In J. of Measurement Science and Technology, Vol. 15, pp. R27-58.

[67] R.W. Arndt (2010). *Square pulse thermography in the frequency domain as adaption of pulsed phase thermography for qualitative and quantitative applications in cultural heritage and civil engineering.* Infrared Physics and Technology, Vol. 53, pp. 246-253.

[68] M.B. Saintey, D.P. Almond, S.K. Lau (1994). *Defect sizing by transient thermography. I: A numerical treatment.* J. Physics D: Applied Physics, Vol. 27, pp. 1063-1069.

[69] M.B. Saintey, D.P. Almond (1995). *Defect sizing by transient thermography. II: A numerical treatment.* J. Physics D: Applied Physics, Vol. 28, pp. 2539-2546.

[70] N.P. Avdelidis, D.C. Hawtin, D.P. Almond (2003). *Transient Thermography in the assessment of defects of aircraft composites.* In NDT&E International, Vol. 36, pp. 433-439.

[71] Y.A. Plotnikov, W.P. Winfree (1998). *Advanced image processing for defect visualization in infrared thermography.* In J.R. Snell, R.N. Wurzbach (eds.): Proc. of SPIE- The International Society for Optical Engineering, Thermosense XX, Orlando, FL, Vol. 3361, pp. 331-338.

[72] A.R. Hamzah, P. Delpech, M.B. Saintey, D.P. Almond (1996). *Experimental investigations of defect sizing by transient thermography*. Insight, Vol. 38 (3), pp. 167-171.

[73] N.P. Avdelidis, D.P. Almond (2004). *Transient thermography as a through skin imaging technique for aircraft assembly: modeling and experimental results.* J. Infrared Physics and Technology, Vol. 45(2), pp. 103-114.

Chapter 5

Pulsed Thermographic Inspection of CFRP Composites

5.1 Introduction

A composite material can be defined as a material containing two or more distinct phases combined in such a way that it results to a product with enhanced properties compared to these of the individual components if used separately. In nowadays, advanced composites related to fibre-reinforced materials from an epoxy resin (or other) matrix combined with carbon, glass, and Kevlar or similar aramid fibres, are widely used in industrial applications. Composites such as Carbon Fibre Reinforced Plastics (CFRPs), Glass Fibre Reinforced Plastics (GFRPs), and metal aluminium laminates (i.e. Glass Fibre Reinforced Aluminium- GLARE) have become increasingly popular among conventional well studied engineering materials, as they possess high strength to weight ratios along with enhanced design potential. In addition their higher stiffness, superior corrosion resistance and improved fatigue performance have exploited their use on several operating structures. Nevertheless, contrary to the advantages that these materials have, the integrity of such components can be impaired in several ways during fabrication, assembly and on-life stages from various types of defects which affect their performance.

The industrial interest, especially in the aeronautical and transport in general fields, has been oriented towards the use of fibre-reinforced materials due to their above mentioned advantages. In the same time, there has been an increasing demand for safety, which in turn, involves an increasing demand for quality. As a result, the wide use of these materials has created the need for the development and implementation of rapid and of field level non-destructive inspections both for quality assurance during the manufacturing process as well as for long-term condition monitoring of in-field performance. These methods must provide inspectors with the ability not only to detect defects, but also the means to quantify these defects for continuous monitoring and comparison. For this reason, a large amount of work has been carried out and focused on the development of rapid and with large area inspection capabilities methods able to detect damage by suitable Non-Destructive Testing and Evaluation (NDT&E) techniques [1-5].

Pulsed thermography with flash excitation possesses the advantage of a very rapid implemented inspection technique as a sequence of thermal images can be acquired in a few seconds, while the detection of subsurface features can be greatly enhanced by the subsequent analysis of these images through various signal processing algorithms. As a result, main aim of this study is to examine the effectiveness of pulsed thermography (flash method) and to establish its suitability for qualitative and quantitative defect assessment on CFRP laminates. This type of composite materials was selected to be investigated as well, as these materials are the most common in use in specific construction demands, when lightweight structures of high strengths and stiffness are required. For this reason, three carbon/epoxy (CFRP) laminates with different geometries, consisted of simulated delaminations (Teflon insertions between the plies) of different sizes and depths were examined under laboratory conditions using photothermal pulsed thermography. By comparing various algorithms on factors such

as robustness to noise, quantitative information retrieval, and optimum defect detection, the most efficient algorithm may be chosen according to the user's needs.

Based on the aforesaid, after a brief introduction about composites' characteristics, manufacturing procedures and the common defect modes appeared in these structures, the experimental work description is following, which is divided in two main parts. In particular, initially the three CFRP panels, having the same defects description and thickness but with a different shape (planar, trapezoid and curved) were assessed by applying different signal processing routines on the acquired thermal data (i.e. Thermographic Signal Reconstruction, Pulsed Phase Thermography and Principal Component Thermography). The effectiveness of the above processing routines was initially evaluated in a qualitative manner, comparing the visual outputs and the information retrieval in terms of defect detectability enhancement and noise reduction. Simultaneously, the produced defect detectability was evaluated in a quantitative basis through Signal-to-Noise Ratio (SNR) computations, quantifying the image quality and the intensity contrast created between the insertion area and the adjacent background area of the composite panel. The comparative SNR study aimed to the providing of information regarding the capabilities of the processing algorithms and the influence of size and depth on the detectable contrast. The second part of this study is dedicated to depth retrieval procedures based on experimental data. More specifically, investigations regarding the quantitative depth information recovery were performed in the temporal and frequency domains respectively, identifying the temperature contrast peak slope time and the blind frequency. These analytical methods for depth prediction require the need for a sound area determination and thus a comparison was performed regarding the influence degree of the sound area selection in depth prediction accuracy either working with raw temperature or phase data. Additionally, the above described depth retrieval procedure was implemented considering as a reference the average intensity measured from the entire surface. The effectiveness of this procedure was also investigated, as in such manner, depth measurements can be implemented eliminating potential negative impacts from the random selection of a sound area from the background.

Concluding, the overall objective of this study was to investigate the potential of pulsed thermography to characterise detected defects in carbon fibre reinforced materials (CFRPs), commonly used in the aerospace industry. Especially, a major goal was to use pulsed thermographic data analysis in order to provide the following information about the defected areas:

- Detection limits through pulsed excitation testing.
- Evaluation of data analysis algorithms for defect detectability enhancement.
- Depth estimations of the detected defect below the surface

5.2 Fibre reinforced composites

The main characteristic of fibre reinforced composites is the combination of fibres within a matrix usually of a plastic or a resin material. The primary function of the fibres is to carry load, while the matrix serves as a binder that holds, protects and transfers stress between the fibres. In the most common design, this of laminate or laminae structures, a ply is formed that can be combined with other plies and can be shaped to form the final product. Each ply is usually rotated by a determined angle with respect to adjacent plies in order to improve the composite material strength [6].

The fibres are the principal constituent in FRPs, as they occupy the largest volume fraction in a composite structure and share the major portion of the load acting on it. The most common fibre types used in reinforced composites are of carbon (CFRPs), glass (GFRPs), and aramid. Proper selection of the type, amount and orientation is essential since it influences characteristics such as tensile, comprehensive strength and modulus, fatigue strength as well as its electrical and thermal conductivity. In other words, the type and quantity of reinforcement determines the final properties of the composite. In fibre reinforced composites, the fibres can be placed in the interior structure in a discontinuous or continuous mode [7], while the latter products are used in applications where high strength and stiffness along with light weight are required, contrary to the discontinuous fibre composites where the strength and stiffness are less important.

The second component in a reinforced composite is the matrix. The role of the matrix is to provide a continuous phase in the composite structure and the most common materials used for matrices manufacturing are of polymer, metal or ceramic [8]. Polymers have low strength and stiffness, metals have intermediate strength and stiffness but high ductility and ceramics have high strength and stiffness but are brittle. The matrix in a fibre reinforced composite performs several critical functions including maintaining the fibres in the proper orientation and spacing, transferring stress between the fibres, providing a barrier against an adverse environment and protect the surface of the fibres from mechanical abrasion. In polymer and metal matrix composites, a strong bond between the fibres and the matrix shall be formed as the matrix transforms loads to the fibres through shear loading in their interface. In ceramic composites, the objective is often to increase the toughness rather than stiffness and strength. Therefore, a low interfacial strength bond is desirable. The matrix provides lateral support against the possibility of fibres buckling under compression loading, thus influencing the compression strength of the material. The polymeric matrices are the most common in use as they can be easily processed and offer good mechanical properties. This kind of matrix is divided into two major categories [8]. These of thermoplastics, which can subdivided in polyamides, thermoplastic polyesters and polypropylene. And these of thermosets which can be further subdivided in polyesters, vinyl-esters, epoxies, phenolics.

The physical and mechanical properties of composites are dependent on the properties, geometry and concentration of both the reinforcement (fibres) and the matrix. By increasing the volume content of

reinforcement, this can increase the strength and stiffness of a composite to a point [9]. However, there is a practical limit of 70% volume of reinforcement that can be added to form a fibre composite. Higher percentages of fibres volume can lead to fibres entanglement as not enough matrix material exists to support the fibres effectively and keep them separated. Similarly, the geometry of individual reinforcement and their arrangement within the matrix can affect the performance of a composite. Thus, there are many factors that have to be considered when designing reinforced composite materials. The type of reinforcement and matrix, the geometrical arrangement and volume fraction of each constituent, the anticipated mechanical loads, the operating environment etc, must all be taken under account [10].

The advantages and the benefits offered by FRP composites vary depending on the choice of the resin, fibres and process of manufacturing [11]. However, fibre reinforced materials include in general, weigh reduction, higher strength to weigh ratio due to high specific strength (strength/density) and specific modulus (modulus/density), low maintenance requirements, high resistance to corrosive environments and a great variability in shape design. Applications include aerospace, transportation, construction, marine industry and more recently infrastructure. Among the different application fields, construction and transportation are being the wider in use fields.

5.2.1 Manufacturing processes of CFRP composites

The largest portion of FRP composites is fabricated by placing layer upon layer according to the designer's requirements in terms of ply profile and fibre orientation. As a result, the most common fibre-reinforced structures are laminates [12]. In particular, when there is a single ply or a lay-up in which all of the layers or plies stacked in the same orientation, the lay-up is called a lamina. When the plies are stacked at various angles, the lay-up is called laminate. Continuous fibre composites are normally laminated in which the individual layers, plies or laminae are orientated in directions that will enhance the strength in the primary load direction. Unidirectional laminae i.e. in the 0^o direction are extremely strong and stiff in the 0^o direction, while are very weak in the 90^o direction and the load must be carried by the much weaker polymeric matrix. Due to the fact that fibres orientation directly impacts the mechanical properties of the structure, the layers are oriented in the main load carrying direction; however in common practice it is usually necessary to balance load carrying capability in a number of different directions, such as 0^o, 45^o, -45^o and 90^o directions and this can be performed by stacking unidirectional plies in different directions.

Successful incorporation of fibres within a resin can be obtained via a wide range of methods, including wet lay-up, spray-up, prepreg lay-up and liquid moulding. Nevertheless, the underlying principle for composites fabrication is generally the same. A thermosetting resin, which may be either in liquid- solid state, is combined with an array of reinforcing fibres and by the application of heat and/or pressure combination, is converted to a rigid mass as the resin polymerises. In the case of thermoplastic composites, the fibres are combined with a polymer, which is already polymerised, so that the final fabrication is a forming process only.

The most common fabrication method for CFRP laminates is the prepreg technique [13,14]. A prepreg is a thin sheet of fibres traditionally pre-impregnated with a slightly cross linked resin to hold the fibres in place. In order to produce a laminated structure, process involves some form of moulding in which the component is laid-up in a desire fibres orientation. After layup is complete, resin is applied to the dry plies in order to produce the final output product. Parts are then placed in a vacuum and cured in an autoclave under high pressures at an elevated temperature. This process produces structures of low porosity, less than 1% and high mechanical integrity delivering CFRPs that are commonly used in the aerospace industry [6].

5.2.2 Damage modes in fibre-reinforced composites

As stated above, defects can inadvertently be produced in composite materials either during the manufacturing and assembly processes or in the course of the normal service- life of the component. Several damage mechanisms are encountered during service such as matrix cracking, desbonding of the matrix-fibre interface, delaminations[1], and fibre breakout. Damage accumulation, either localized or distributed throughout the volume of the composite, leads to the degradation of the composite material mechanical properties [10]. In addition, failures created during the manufacturing process are of great importance as well. Common flaws of this kind are micro-cracks in the matrix due to residual stresses, undesired inclusions, resin rich areas and voids, pores of blister due to air entrapment. Besides propagating damage modes, extreme environmental conditions also may cause material degradation. Thus, large temperature spans and moisture absorption could be considered as passive modes of damage. The main types of defects that can be encountered in fibre-reinforced composites during manufacturing/ assembly processes and in life service are [15,16]:

- *Inclusions:* A physical or mechanical discontinuity accidentally included in the material during manufacturing. Often caused by inadequately cleaned moulds, airborne dirt particles, inadequate mixing components. Inclusions usually consist of solid foreign materials and often cause structural stresses in a noticeably different manner to the parent material.
- *Fibre Debonding:* The present defect is the result of cracks running parallel to the fibres and can occur because of poor consolidation or inclusions. Fibre debonds occur when the interfacial strength between a fibre and the matrix is low. Cracks then propagate at the interface of the resin and the fibre or in very close proximity to the interface. Debonds may occur at any time during the life of the structure.
- *Fibre breakout:* Due to cutting or excessive fibre curvature at sharp corners. Can also result from impact effects and environmental degradation. This is a critical defect as fibres are designed to carry most of the load.

[1] in the case of laminated composites

- *Fibre misalignment:* Distortion, which is especially prevalent in low fibre volume fraction materials.
- *Incorrect stacking sequence:* Resulting in incorrect mechanical properties of the final product.
- *Voidage (porosity):* Can occur during the mixing of the resin and can include air, solvents or contaminants. Voids also appear during the lay-up process when air is trapped between the prepreg sheets. Rollers are usually used to remove bubbles which can produce delaminations or areas of weakness within the matrix. Can act as stress concentrations and will have an effect on some of the mechanical properties i.e. lower transverse and through-thickness tensile, flexural, shear and compression strengths. Void content is considered negligible if it is less than 1-2% [6].
- *Resin rich /starved areas:* In rich resin regions only resin is present, while poor resin regions result to the inadequate wetting out of fibre context. This type irregularity may be responsible for reducing the mechanical performance of composite materials and often occurred at the inner radius of curved material.
- *Delamination:* The separation of ply layers in a laminate. This defect can occur during manufacturing and in-service, and can have a severe detrimental effect on mechanical properties, particularly in compression. Delaminations can occur locally or can cover a large area of the laminate. In addition delaminations can be external where surface lamina become separated from the composite or internal where two adjacent lamina within the bulk composite become separated causing a voided region within the material
- *Impact damage:* One of the most common and significant modes of defect that can be occurred in FRPs materials is impact damage. These materials are susceptible to impact loading due to the fact that they are laminar systems with weak interfaces. In aircraft structures this damage can occur from dropping a tool, bird strike or runway derbis. The impact damage can cause visible damage (i.e. barely visible impact damage-BVID) and can result in particular poor performances up to 60% of the designed strength and with potentially catastrophic outcomes under compressive loading [17]. Of great concern is non-visible damage that is extremely difficult to be detected and quantified. A very common scenario is that the side of impact has a BVID and the opposite side has a significant damage. It should be note that the opposite side of the component is usually inaccessible and this is where NDT is most important. The common internal damage due to impact consists of fibre breakout, matrix deformation and cracking, fibre debonding, fibre pullout and delaminations [18,19].
- *Out of round hole:* Holes of incorrect profile caused by drill bit vibrations and movement.
- *Off axis drilled hole:* Hole drilled at an angle, not normal to the surface of the material.
- *Incorrect countersink:* Countersink drilled at incorrect angle.
- *Burned drilled holes:* Localized damage in region of drilled hole caused by frictional heating of drill bit.

From the above presented list of defects, it is clear that in many ways a composite can differ from the ideal design either due to manufacturing failures or due to unwanted in service effects. The extent to which, any of the above deviations from the ideal should be considered as a defect is a function of the indented use of the material and the significance of the deviation from the required performance. As a result, to fully maintain structures and their integrity, the defect types must be characterised in order to determine their identity, location, size as well as to set the defects acceptance criteria for manufacturing and in service stages. For this reason a number of NDT techniques have been developed as these techniques have the outstanding advantage to provide reliable and in real-time results in a variety of applications.

5.2.3 Thermal imaging and composites assessment

Among the various NDT techniques, active infrared thermography has been widely used for damage assessment in CFRP composite structures [20-23]. The most common in use active mode, this of Transient Thermography and in particular, this of photothermal pulsed thermography which compares favourably to conventional inspection technologies in terms of speed and sensitivity, while offering the advantage of contactless evaluation. Applications range from in-service maintenance of the structure to the process control during the manufacturing stages [24,25].

In the past, the practice of thermography was based almost entirely on visual assessment of the thermographic images and the evaluation of results was based on the presence of temperature contrasts between the inspected area and the background. In nowadays, each pixel in the thermal image or in the imaging sequence can be treated spatially and/or temporally as an independent entity and can be evaluated without reliance on visual assessment or prior knowledge of the physical characteristics of the sample.

Along with the thermographic technological development, in many respects, composite materials (i.e. compared with metals) are ideally suited for thermographic testing as with relatively low thermal diffusivities (i.e. compared with aluminium), the time scale at which transients associated with anomalies occurred is on the order of seconds, and are well matched to cameras frame rates. Additionally, the emissivity values of most of these structures are sufficient enough to provide results unaffected from environmental reflections.

5.3 Description of specimens

In order to evaluate the potential of pulsed thermography, experimental testing was carried out in a totally three different CFRP laminates, having fabricated defects of known characteristics. The three CFRP samples (*SP1, SP2* and *SP3*) were manufactured having the same thickness with however different shapes, evaluating the results produced when there is an angle between the normal to the surface direction and the direction of the emitted heat flow. More specifically, Specimen 1 (*SP1*) was a laminate 30cm x 30cm planar structure with a laminae orientation of $0^o/90^o$ cross ply through its

volume. This laminated coupon was consisted of ten (10) plies giving a total specimen thickness of 2 mm. As illustrated in the schematic of Figure 5.1, twenty five (25) square Teflon™ insertions of different dimensions ranging from 3 mm to 15 mm were placed between plies simulating local detached regions. These insertions were divided in five series (A-E in the schematic) placed at different depths ranging from 0.2 mm to 1mm, while each series was consisted of five square insertions of different lateral dimensions (No1 to No.5 in the schematic). Additionally, as an objective of this study was to evaluate as well the performance of pulsed thermography on complex geometry carbon/epoxy materials, Specimen 2 (*SP2*) and Specimen 3 (*SP3*) were fabricated based on the above described manufacturing specifications, having the same defects in terms of location and size but a different shape in terms of geometry compared with *SP1*. In particular, SP2 was a trapezoid structure and SP3 was a curved structure and both were inspected from their concave side, producing a probing depth from 0.2 to 1 mm. A schematic representation of these samples and their defects description are illustrated in Figure 5.2 and 5.3 respectively. Regardless the sample, the distance between each individual simulated defect was 50 mm, eliminating the possibility of thermal diffusion interaction between them which would affect the acquired results.

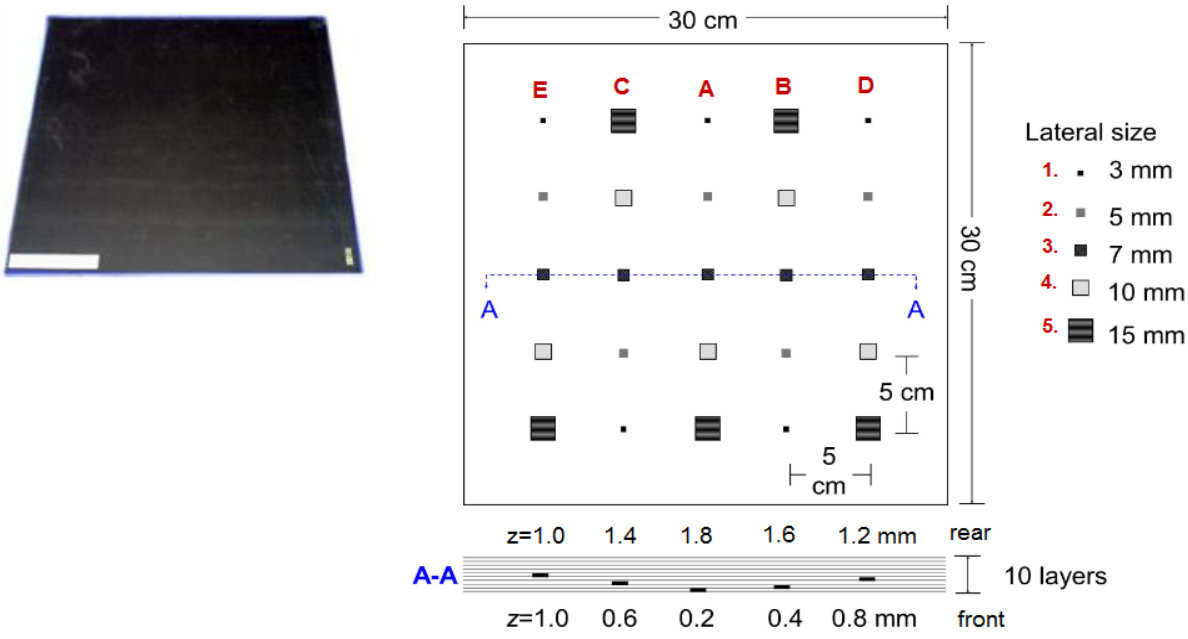

(a) *(b)*

Fig. 5.1: *Specimen 1: (a) Photograph of the sample, (b) schematic representation of defects characteristics and sample description.*

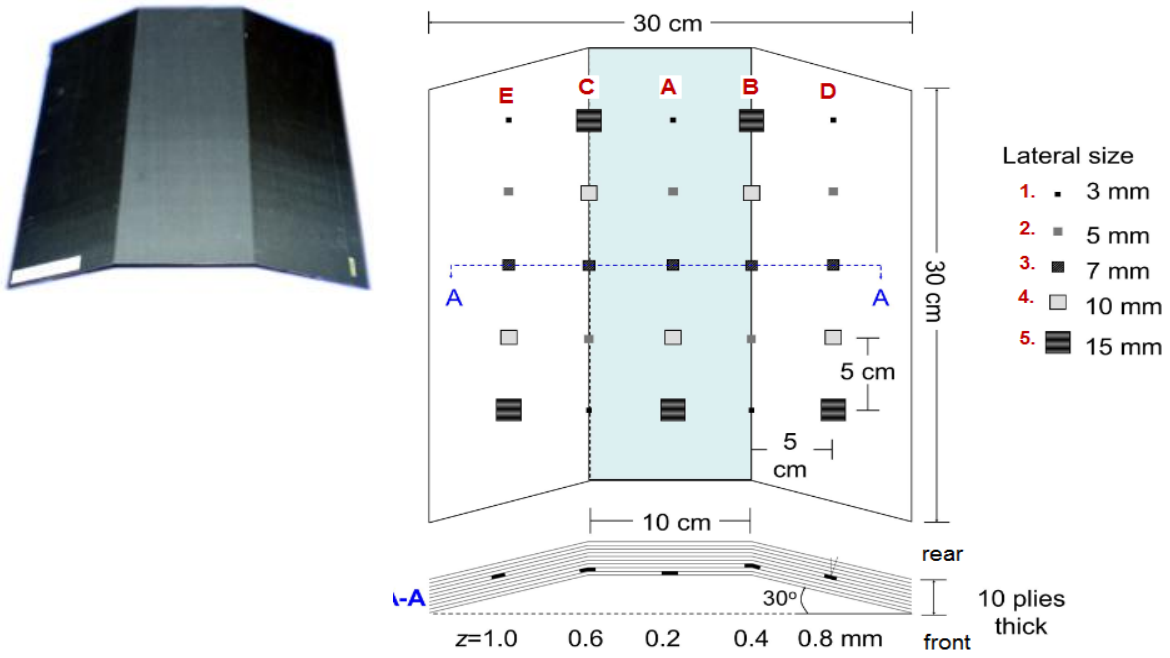

(a) *(b)*

Fig. 5.2: *Specimen 2: a) Photograph of the sample, (b) schematic representation of defects characteristics and sample description.*

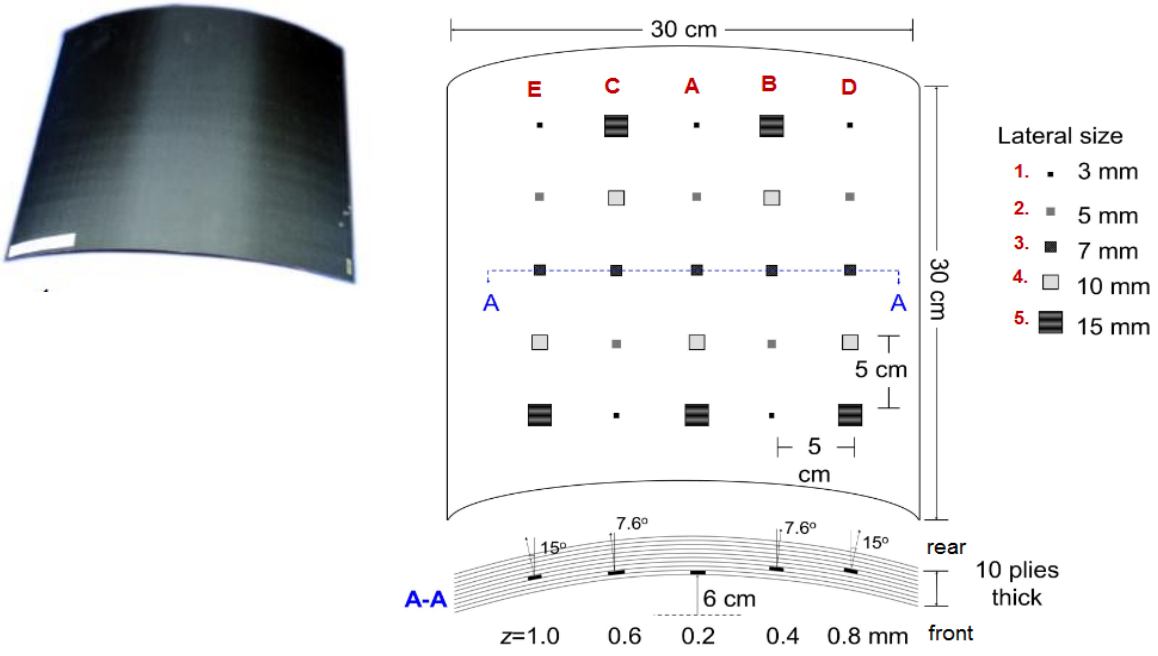

(a) *(b)*

Fig. 5.3: *Specimen 3: a) Photograph of the sample, (b) schematic representation of defects characteristics and sample description.*

5.4 Experimental procedure and data analysis

The experimental raw thermal data were acquired by using a flash thermographic system in reflection mode as shown in Figure 5.4. During test, two high energy flash lamps (Balcar FX60) were triggered at t=0 to deposit a nearly instantaneous (of a 5ms pulse duration) heat pulse on the sample's surface. The

temporal and spatial surface temperature variations after the application of the energy pulse were monitored through the aid of a high speed infrared camera, capturing a sequence of thermal images during the cooling down phase that was stored in a PC for subsequent data analysis. The camera used in this study was a mid wave (3-5 μm) device, containing a focal plane array of 320x256 pixels - infrared detectors. In order to implement the above experimental procedure, a synchronisation unit was also used controlling flash initiation, data acquisition and data storage to the PC according to the selected experimental parameters presented in Table 5.1. The three samples were inspected by depositing heat energy on their front surfaces (concave sides in the case of the complex samples) allowing of a depth investigation from 0.2 to 1 mm.

Table 5.1: *Experimental equipment and acquisition parameters for SP1, SP2 and SP3 testing*

Experimental Equipment	***Acquisition Parameters***		
Thermal stimulation: ➢ Photographic Flashes: Balcar FX 60 ➢ pulse duration: 5ms thermal pulse, ➢ deposited energy: 3.2 KJ/ flash (total energy deposited 6.4 KJ) Thermographic monitoring: Santa Barbara infrared camera, Focal Plane Array, nitrogen cooled, InSb, 320x256 pixels		***SP1***	***SP2***	***SP3***
	Sampling rate, f_s	*157 Hz*	*157 Hz*	*157Hz*
	Acquisition duration, t_{acq}	6.37 *s*	*6.7 s*	*6.8 s*
	Time interval, $\Delta t = 1/f_s$	6.3 *ms*	6.3 *ms*	*6.3ms*
	Total number of frames	*1000*	*1052*	*1076*

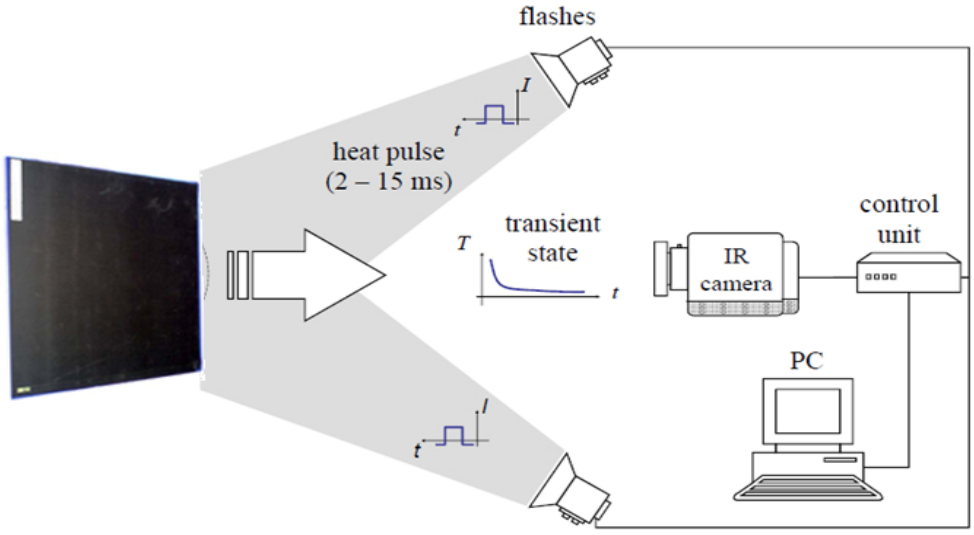

Fig. 5.4: *Schematic representation of pulsed thermographic experimental setup*

The acquired pulsed thermal data-set had a 3D format, measuring the 2D surface temperature distribution (thermal images) as a function of time *t*. Therefore, the entire data-set can be expressed as *T(x,y,t)* where *T* is the temperature on the surface position *(x,y)*. Due to the fact, that the processing algorithms used in this study are pixel-wise transformation techniques and in order to increase the data processing speed, it should be noted that before continue to data analysis phase, the recorded data were sub-sampled by a factor of 4. As a result, the parameters of the truncated *SP1* sequence were redefined

as N= 250 frames, f= 39.25 Hz, time interval Δt= 25 ms and truncation window $w(t)$= 6.37 s. Similarly as regards the two other thermographic sequences the truncated parameters were defined as following: SP2 N= 263 frames, f= 39.25 Hz, time interval Δt= 25 ms, truncation window $w(t)$= 6.7 s and SP3 N= 269 frames, f= 39.25 Hz, time interval Δt= 25 ms and truncation window $w(t)$= 6.8 s

The new sequences produced after the truncation procedure were processed in a Matlab environment, using the open source *IR View* graphical user interface, which was developed and released from Computer Vision and Systems Laboratory (CVSL) of Université Laval [26]. Additionally as stated above, the post processing algorithms used in this study in order to enhance the image quality and defect detectability of the raw thermal data were these of thermographic signal reconstruction (TSR), pulsed phase thermography (PPT) and principal component thermography (PCT).

5.5 Qualitative defect assessment

Despite the fact that pulsed thermography can provide results in a few seconds, the raw data may be affected by several parameters, incommoding the manipulation and analysis of the revealed information. The most important and most commonly appeared negative effect is this of non uniform heat deposition on the surface of the inspected sample. Figure 5.5 indicates representative thermal images from the three samples at t=1.25 s after the application of the heating pulse. As can be seen, the influence of non uniform heating was observed in all the experimental results, ascertained through the different colourful representations on the respective surface temperature maps. More specifically, the planar surface presented the strongest non uniformity on heat deposition (Figure 5.5a) with respect to the trapezoid (Figure5.5b) and curved (Figure 5.5c) panels, indicating that the produced defect detectability gradient in each case is impacted as well from the heating application and deposition on each respective surface.

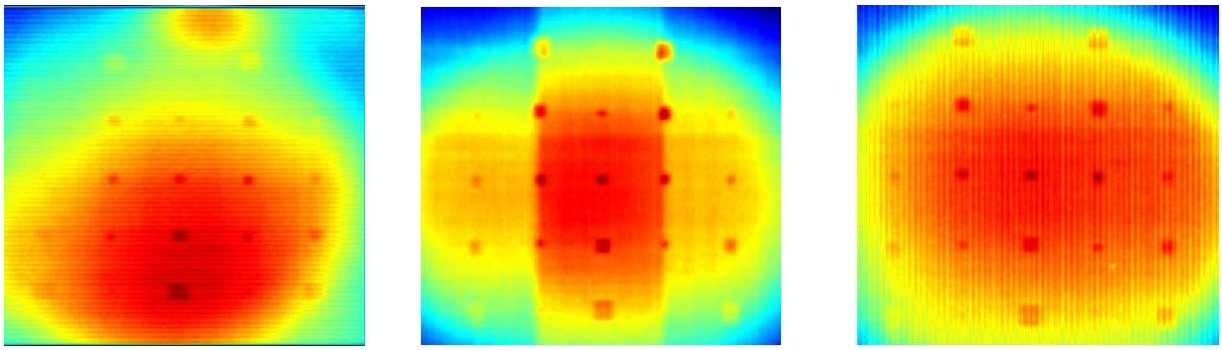

(a) *(b)* *(c)*

Fig. 5.5: *Raw thermal images of (a) SP1, (b) SP2,(c) SP3 at t=1.25 s after the application of the heating pulse.*

In the following subsections, the results (visual and SNR metric) acquired from each individual specimen investigation are presented and discussed. As stated above, the raw thermal data was processed by TSR, PPT and PCT processing techniques. The PPT analysis was performed on the raw temperature-time sequences as well as on the synthetic (reconstructed) ones, generated from TSR analysis, while observations from principal component analysis were based only on visual results, as no

SNR calculations were performed in this case. Additionally based on visual observations, the data elaboration and imaging results interpretation through the aforesaid signal processing algorithms was performed in a greyscale format, as this colour pallet was the most well suited in terms of visual appearance, enhancing the information retrieval from the imaging outputs.

5.5.1 Information retrieval from thermal data

Figure 5.6 illustrates representative thermal images in a greyscale format, acquired at different time intervals from the planar (top row), trapezoid (centre row) and curved (bottom row) sample investigations. As can be seen from the three series of imaging results regardless the sample investigated, defects nearer to the surface started producing a detectable thermal contrast earlier with respect to the contrast produced by the deeper ones, detected on later time intervals. For instance, at the minimum time intervals presented in Figure 5.6, only the three shallower defects series can be detected (A,B and C), while as time elapses the contrast of these defects is becoming weaker and some of the deeper defects are appeared. On the other hand, the comparison of the results in terms of defect detectability showed that an enhanced visibility was produced from the signal recorded by the trapezoid and curved surfaces, in which as stated above, the heating process seemed to present a stronger uniformity. In particular, the inspection on the complex geometry samples disclosed the presence of almost all the defects, as the only undetectable insertions into the trapezoid coupon were the 3mm squares located at the depths of 0.8mm and 1mm respectively, while the curved surface investigation did not reveal the 3mm insertions at the depths of 0.8 and 1 mm respectively and the deeper 5 mm square E2. Contrary, pulsed thermographic inspection of the planar surface was able to clearly identify the series located at the shallower depths (series A, B and C); while a very weak contrast was produced on the detectable defects of the D and E series. Along with the impact of the non uniform stimulation process, this slightly enhanced visibility produced for the deeper inserts on the complex geometry samples can be further attributed to the differences in terms of heat absorption due to the shape of the coupons. In other words, the edges (areas where defects series D and E are located to) on the complex geometry samples are closer to the heating source and thus the absorbed (or emitted) signal in those surface regions is stronger with respect to that on the respective regions of the planar surface. Thus stronger thermal effects in the former case were produced. However regardless the shape of the investigated CFRP, it can be generally seen that as deeper was the location of the defect and as smaller its dimension, a reduced defect resolution was produced.

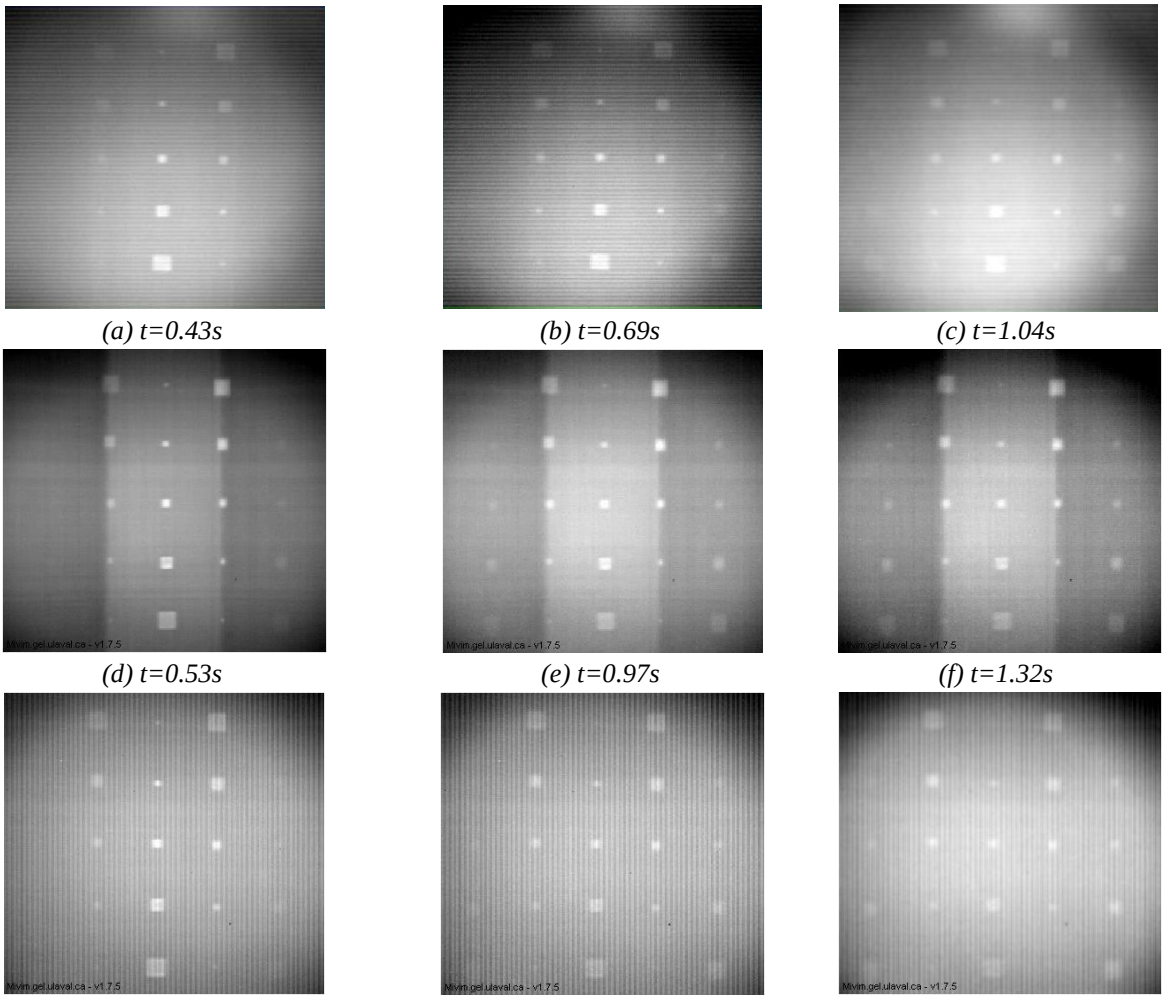

(a) t=0.43s *(b) t=0.69s* *(c) t=1.04s*

(d) t=0.53s *(e) t=0.97s* *(f) t=1.32s*

(g) t=0.53s *(h) t=1.02s* *(i) t=1.65s*

Fig. 5.6: *Raw thermal images of SP1 (top row), SP2 (centre row) and SP3 (bottom row) at different time intervals after the application of the heating pulse.*

5.5.2 Derivative analysis of thermal data (TSR)

The first processing routine applied to handle the time-history raw temperature data was this of TSR. Through the calculation of the first time and second time derivative images, defect visibility was assessed investigating the temporal variations of the cooling rate (1st derivative) and the temporal variations of the acceleration (or deceleration) of this cooling rate (2nd derivative). The derivative images were acquired after reconstructing the raw temperature data to the synthetic one, through a 4th degree polynomial fitting function. Representative first time derivative results are illustrated in Figure 5.7, while second time derivative images in Figure 5.8. Compared with the results obtained from the raw data analysis, the derivative elaboration produced an enhanced defect visibility and sensitivity for all the defects regardless their location and/or size, minimizing as well the unwanted variations created from non uniform heating. For instance some of the defects in the deeper series D and E, which were undetectable from the raw data -or if they were they produced a weak contrast- in the first and second derivative images they can be clearly observed with enhanced geometry representation. Moreover, by studying the respective times when the best contrast is produced, it is clear that derivative analysis

discloses the internal insertions at earlier times indicating the enhanced temporal sensitivity of this processing technique. On the other hand, the comparison in terms of the produced defect visibility on the three surfaces, after studying either the first or second time derivative sequences, showed that all the defects were detected on the trapezoid sample, while the planar inspection was not able to reveal defects D1 and E1 and non efficient contrast was produced for the E1 defect on the curved panel. Furthermore, additional information were produced through this analysis, as some background variations can be observed revealing the fibres orientation and the sharp geometrical changes on the trapezoid sample.

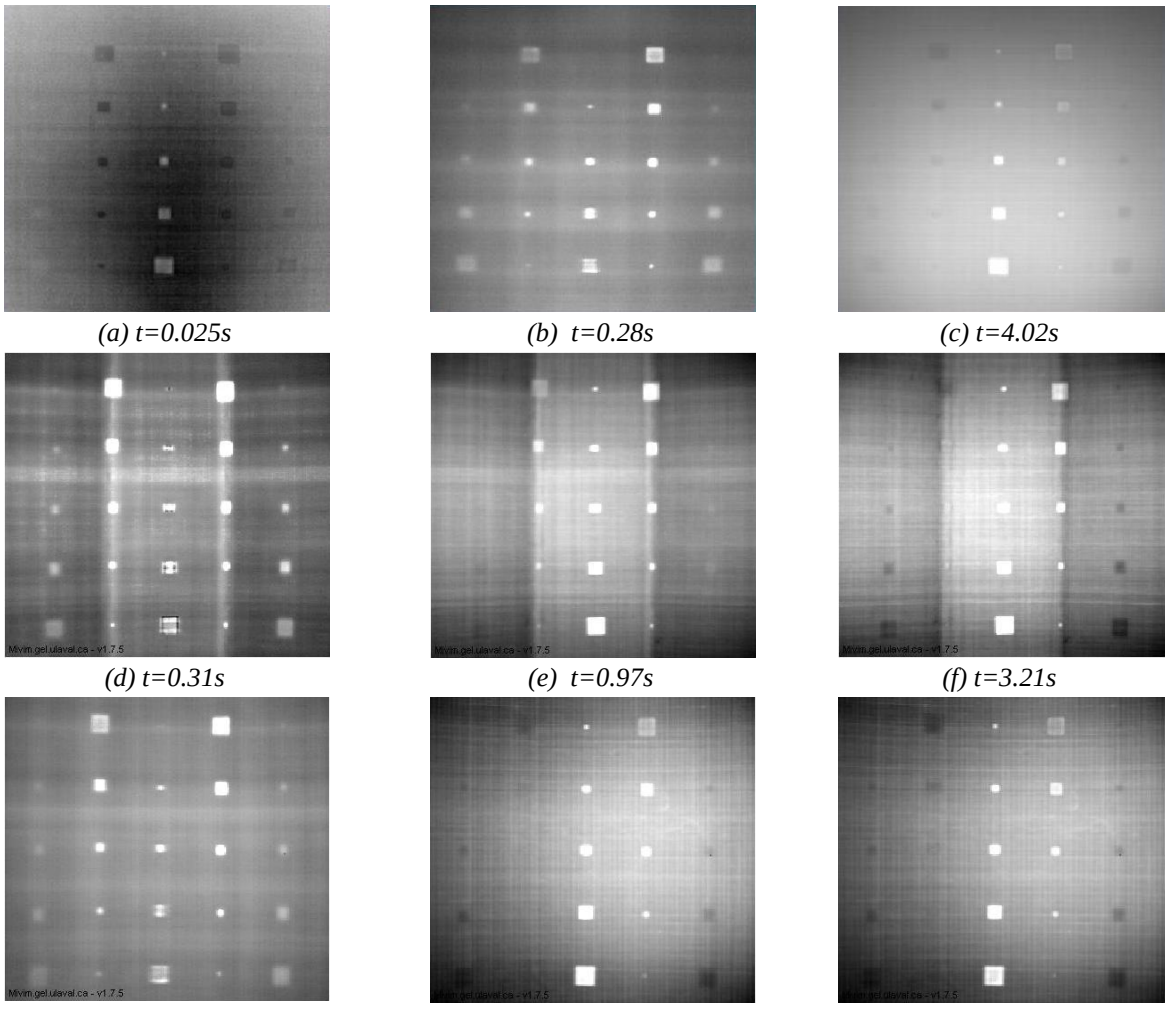

(a) t=0.025s *(b) t=0.28s* *(c) t=4.02s*

(d) t=0.31s *(e) t=0.97s* *(f) t=3.21s*

(g)t=0.33s *(h) t=1.78s* *(i) t=2.73s*

Fig. 5.7: *First time derivative images from a 4th degree polynomial fitting function acquired from the planar SP1 (top row), the trapezoid SP2 (centre row) and curved (bottom row) inspections at different time intervals.*

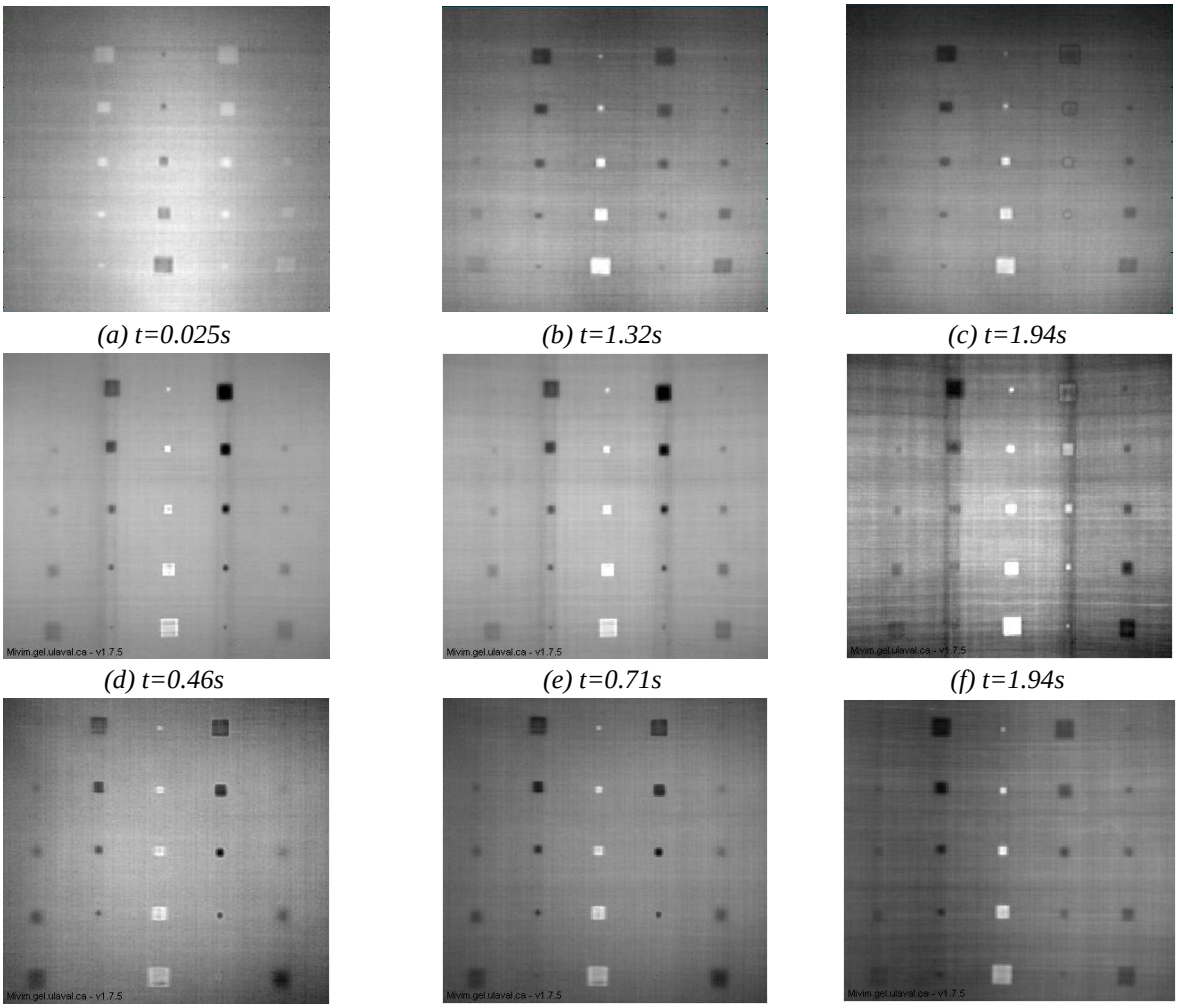

(a) t=0.025s *(b) t=1.32s* *(c) t=1.94s*

(d) t=0.46s *(e) t=0.71s* *(f) t=1.94s*

(g) t=0.41s *(h) t=0.51s* *(i) t=1.22*

Fig. 5.8: *Second time derivative images from a 4th degree polynomial fitting function acquired from planar SP1 (top raw), trapezoid SP2 (centre row) and curved SP3 (bottom row) inspections at different time intervals.*

5.5.3 Frequency domain analysis of thermal data (PPT)

The second algorithm utilized to handle the raw PT data was this of PPT. As stated above, phase information were initially retrieved from the raw temperature data, while this technique was further applied to analyse the reconstructed (synthetic) temperature -time sequences derived from the 4th degree polynomial fitting used in the TSR approach. Figure 5.9 and Figure 5.10, present indicative phasegrams at different frequencies, generated from the elaboration of raw temperature and synthetic temperature data respectively. The phase imaging results indicate that deeper defects are revealed at lower frequencies contrary to the shallowest ones which are disclosed at higher frequencies. This observation was expected as the diffusion length of the thermal wave is inversely proportional to the frequency and thus high frequencies reveal shallow defects and vice versa. As a result, at the minimum detectable frequency (Figures 5.9a and Figure 5.10a) defects located to the depth range from 0.4mm to 1mm can be seen (slight evidences of the 0.2 mm series is also appeared), while at a higher frequency (f=2.67 Hz), only the defects series nearest to the surface are visible.

As can be seen either from the raw PPT data or the synthetic PPT ones, the geometry of the sample and the heat deposition process do not influence the acquired results. This can be confirmed from the fact that the study of the respective phase images is providing exactly the same information in terms of defect visibility, regardless the shape of the target. Moreover, raw and synthetic phasegrams are very similar at lower frequencies; however the detectability at higher frequencies is much more affected by noise on the raw PPT results with respect to the respective results generated from the monitoring of the synthetic data in the frequency domain. For instance, as can be seen from Figure 5.9c, the phasegram at f=2.67 Hz reveals only the shallowest defect series, while noise starts to affect the background of image. Contrary the respective synthetic phasegram, illustrated in Figure 5.10c, is much less affected by noise, revealing in addition the second shallower defects series, thus providing more details with respect to the raw phasegram on the same frequency. As regards, the defect detectability rate in this case, this was enhanced as well compared to the respective one of the raw temperature analysis as the only undetectable defect was this of E1 in the cases of planar and curved samples inspections (all defects were appeared on the trapezoid surface).

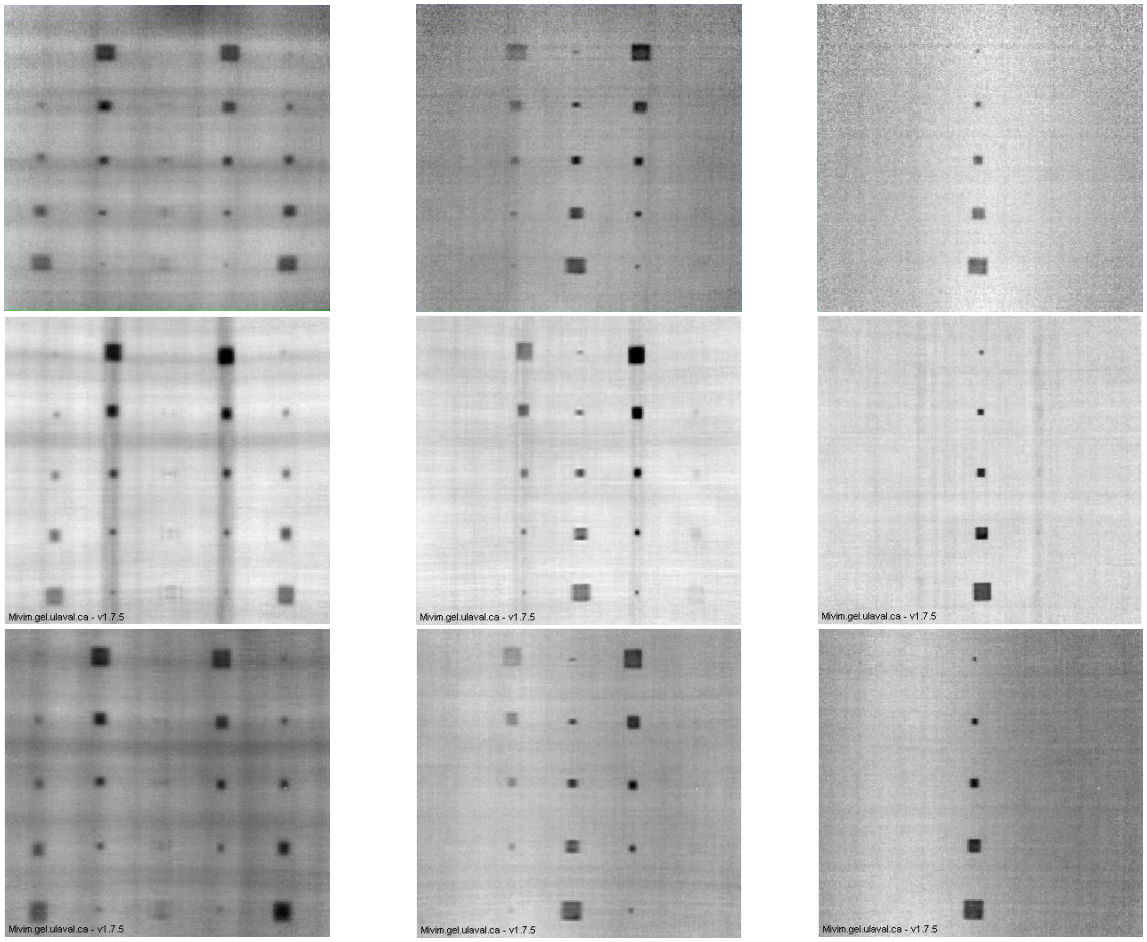

(a) f=0.16 Hz *(b) f=0.63 Hz* *(c) f=2.67Hz*

Fig. 5.9: *Phase images for SP1 (top row), SP2 (centre row) and SP3 (bottom row) at (a) f=0.16Hz, (b) f=0.63Hz and (c) f=2.67 Hz, after applying PPT on raw temperature-time data.*

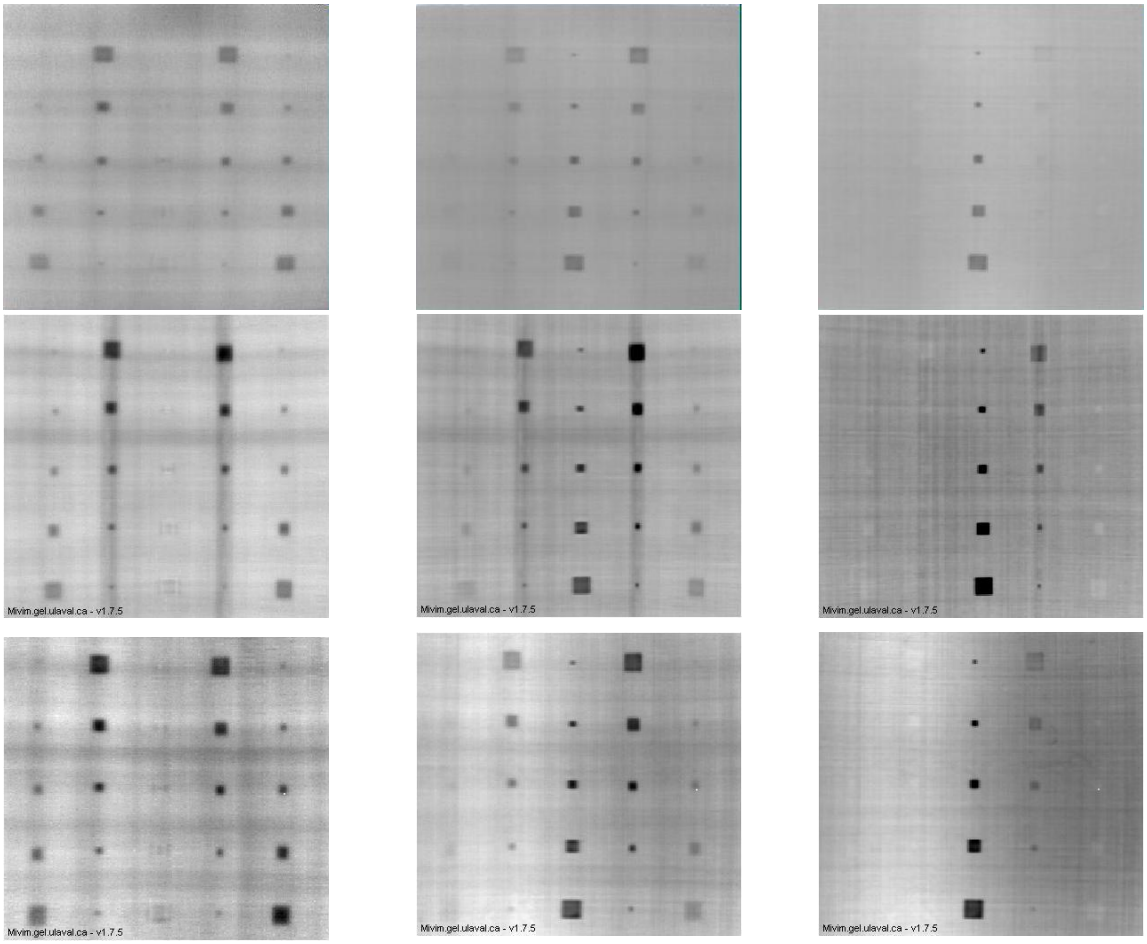

(a) f=0.16 Hz *(b) f=0.63 Hz* *(c) f=2.67Hz*

Fig. 5.10: *Synthetic phase images of SP1 (top row), SP2 (centre row) and SP3 (bottom row) at (a) f=0.16Hz, (b) f=0.63Hz and (c) f=2.67 Hz, after applying PPT on reconstructed (synthetic) temperature-time data.*

5.5.4 Principal Component Analysis (PCA) of thermal data

Similar results regarding the defect detectability enhancement were acquired after applying the principal component thermography (PCT) algorithm and reorganise the thermographic sequences to their principal components. By reorganising the time-temperature data in a transformed space where the first few images reveal the maximum spatial and temporal variances detected from the raw data, as can be seen from Figure 5.11, the EOF images highlight a specific series of defects with respect to their location in the interior of the CFRPs panels. More specifically, the second EOF (both for the planar and complex geometry inspected samples) highlights the variances created due to the shallower defects, while the third EOF is revealing additionally the two deeper series of insertions, located at the depths of 0.8mm and 1 mm respectively. The first EOF in each series of images, which describes the maximum variance detected from the raw data indicates the non uniform heating influence (the first spatial and temporal variation), which however is eliminated on the higher EOF images. Furthermore, some background variations can also be observed in this case as well due to the presence of fibres, while the sharp geometrical changes on the trapezoid panel can be perfectly seen along with the Teflon insertions on these areas. The defect detectability produced after applying PCT was similar with that produced from derivative and phase analyses respectively, with a slight however enhancement to the visible

results. In particular PCT algorithm was able to detect all the defects on the trapezoid and curved CFRPs and all the defects except the deeper and smaller E1 insertion on the planar panel.

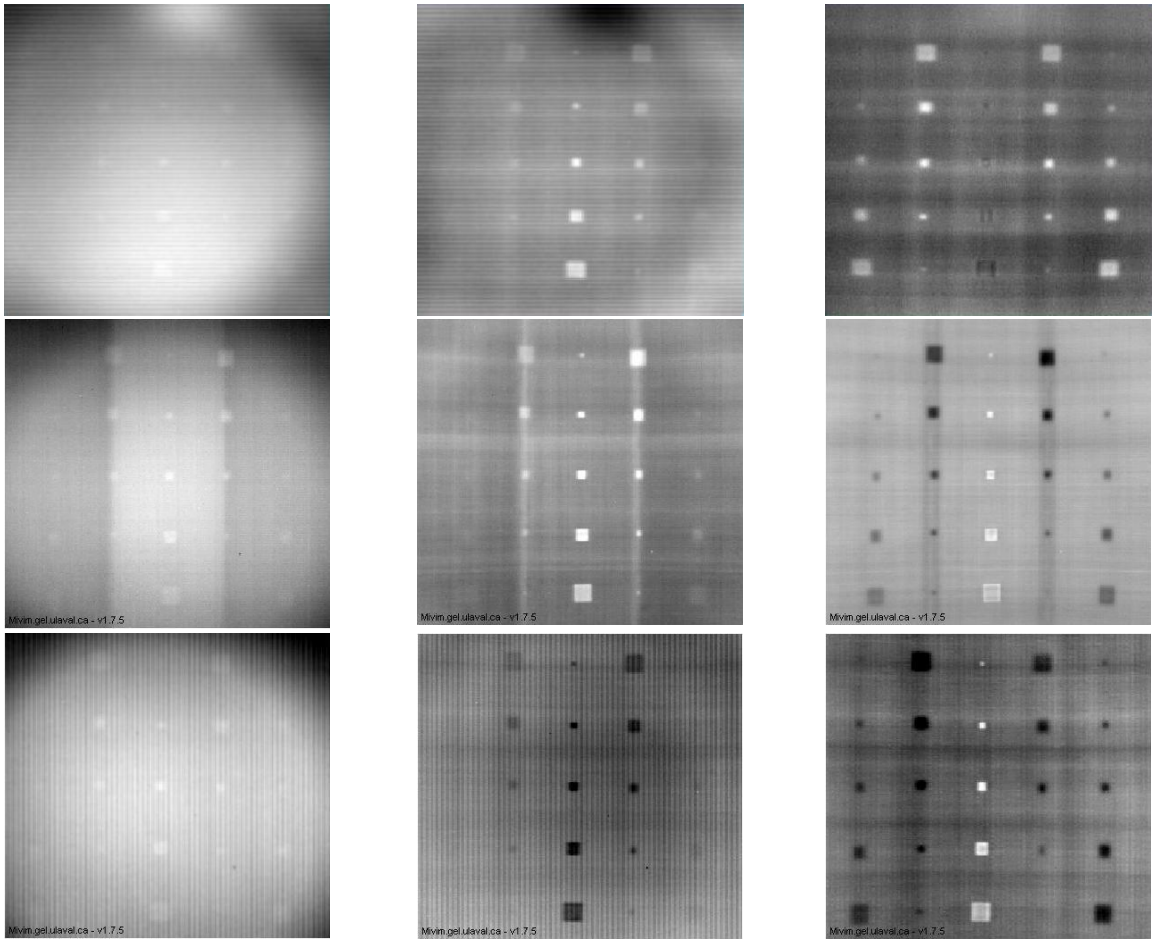

(a) EOF1 *(b) EOF 2* *(c) EOF3*

Fig. 5.11: *Empirical Orthogonal Functions after processing the raw data with PCT. The maximum variances detected are illustrated in (a) EOF1, (b) EOF2 and (c) EOF3, while the top row results are referring to sample SP1, the centre row results to sample SP2 and the bottom row results to sample SP3.*

5.5.5 Signal-to-Noise ratio calculations

Additionally to the information retrieved comparing and studying the imaging outputs, after the application of the above signal processing tools, image quality and defect contrast produced from both the temperature data and the post processed results were evaluated and compared through Signal-to-Noise (SNR) calculations. SNR metric was used in an effort to validate the visual observations and to quantitatively assess the produced defect detectability [27]. This computation was based on the definition of two areas: this of a defective and a reference area respectively. The defective area encloses the pixels in which the defect appears (this area is considered as the signal) and the reference area also called sound area is a defect-free area used to calculate the intensity contrast (this area is considered as the noise). The reference areas selected in the present study were located close to the correspondent defects, in order to ensure that the two respective regions received the same amount of heat energy and consequently minimising errors in SNR analysis due to uneven heating. SNR metric for each detectable

defect was calculated based on the expression of Eq. 5.1, where S_{def} is the intensity arithmetic mean of all the pixels inside the defective area, S_{sa} is the intensity arithmetic mean of all the pixels inside the reference area and σ_{noise} is the standard deviation of the pixels inside the reference area [28].

$$SNR = \frac{|S_{def} - S_{sa}|}{\sigma_{noise}} \quad \text{(Eq. 5.1)}$$

According to the lateral dimensions of the Teflon squares, a sound area occupying exact the same pixels as the defective one was selected next to the insertion. Regardless the processing method used to interpret the data, the exact same sound and defective regions were used as illustrated in Figure 5.12, and their dimensions were defined in terms of pixels as 4x4 for defect No 1, and 6x6, 8x8, 10x10 and 12x12 for the correspondent defects No 2, No 3, No 4 and No 5. After the definition of the respective sound and defective regions, the comparative SNR study was performed through the calculation of the maximum SNR value (best quality contrast) from the temperature and post processing analyses. Additionally, the comparison of results indicating the performance of each processing routine was implemented by using the average maximum SNR value produced from each defect series. This was performed as all the insertion series occupied the same space on the inspected specimens; the only parameter altered was the depth. A similar procedure incorporating the average maximum SNR values was also deployed in order to evaluate the impact of defect size on the produced visibility contrast. In other words, the average SNR value for defects having the same lateral dimensions was used in this case regardless the depth of the inserts.

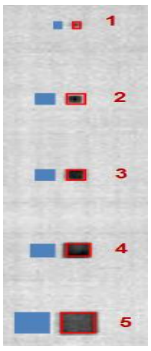

Fig. 5.12: *Definition of sound and defective areas in term of pixels occupation for SNR analysis.*

Figure 5.13 shows the comparative results from the average maximum SNR metric calculated for all the defect series, as this estimated from the raw thermographic sequences, the time derivative sequences (first and second time derivatives) and the phase data (derived either from raw or synthetic temperature data). In general as can be seen from the respective histograms, SNR increases in all cases regardless the shape of the sample and the insertion depth, after processing the raw temperature data with the aforesaid algorithms, verifying the visual observations presented above. However, by comparing the performance of the processing techniques, it can be seen that for the shallowest defects (series A), the 1st time derivate analysis and the application of PPT algorithm over synthetic temperature data produced the best signal- to-noise ratios and thus the better defect visibility. Contrary, for the deeper defects all the processing techniques turned out to be equally good or bad (i.e. defect series D and E).

The comparison of results in terms of defect depth impact on the produced detection quality indicates that regardless the processing algorithm and the specimen geometry, a higher average SNR was computed for the shallower defects, while as deeper was the location of the insert the reduced was the SNR metric and thus the produced visibility. Contrary, this observation cannot be verified from the raw

temperature data as in several instances the location and thus the energy deposition on this area seems to greatly affect the results, rather than the depth of the defect. For instance, defects series C on the trapezoid panel had a higher average SNR value with respect to the shallower defects series B. The above observation indicates that even though, some defects seemed to be visibly present on the unprocessed thermal images, the SNR calculation did not produced any meaningful result for them and vice versa.

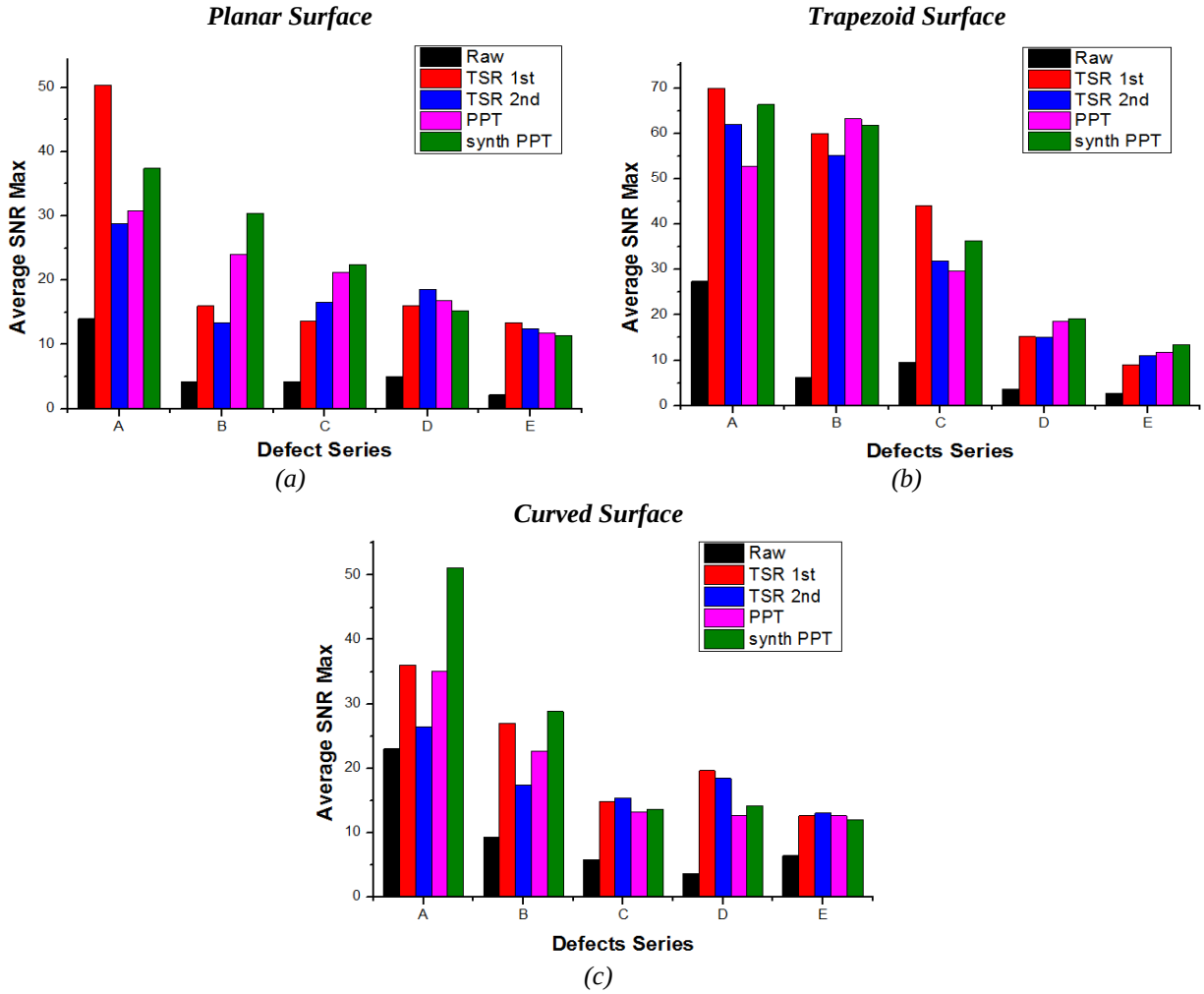

Fig. 5.13: *Comparative SNR results of the different processing methods as a function of defect depth for (a) the planar, (b) the trapezoid and (c) the curved specimens.*

Finally, a comparison between the SNR values produced after the application of PPT algorithm over raw and synthetic data respectively, is indicating that for the shallower defects located to the depths of 0.2 and 0.4 mm respectively, a better maximum SNR can be achieved when applying PPT algorithm over synthetic temperature data (similar PPT results were acquired only for the series B defects on the trapezoid sample). Contrary for the deeper inserts, it can be seen that the produced maximum SNR value is approximately equal for both the raw phase data and the synthetic one. These results are verifying the visual observations obtained from the imaging results, as the higher SNR of synthetic PPT results measured on the shallower defects is indicating the reduced noise content that synthetic phasegrams presented after reconstructing the raw temperature data to synthetic and then applying PPT

technique to handle them. Contrary for the deeper defects (detected on lower frequencies), where the noise content is reduced, the SNR values of raw PPT and synthetic PPT are approximately the same.

The second SNR computation, as mentioned above investigated the impact of defect size on the produced contrast. Figure 5.14 represents the acquired SNR results as a function of the insertion lateral dimensions. As can be seen despite the fact that an enhanced defect visibility is produced from the post processing algorithms, no clear observations can be done regarding the influence of defect size on the visual outputs. This can be attributed to the combination of defect location and non uniform heat application. For instance regardless the depth, defects No 5 (15mm) and No 1 (3mm) were all accommodated at the edges of the panels. Contrary defects No 4 (10mm), No 3 (7mm) and No2 (5mm) were accommodated nearer to the respective centres receiving a greater amount of heat, which can be expounded as a better contrast. The only observation that can be done is that greater SNR values were acquired for all the inserts on the trapezoid sample, with respect to the respective contrasts produced on the other two samples.

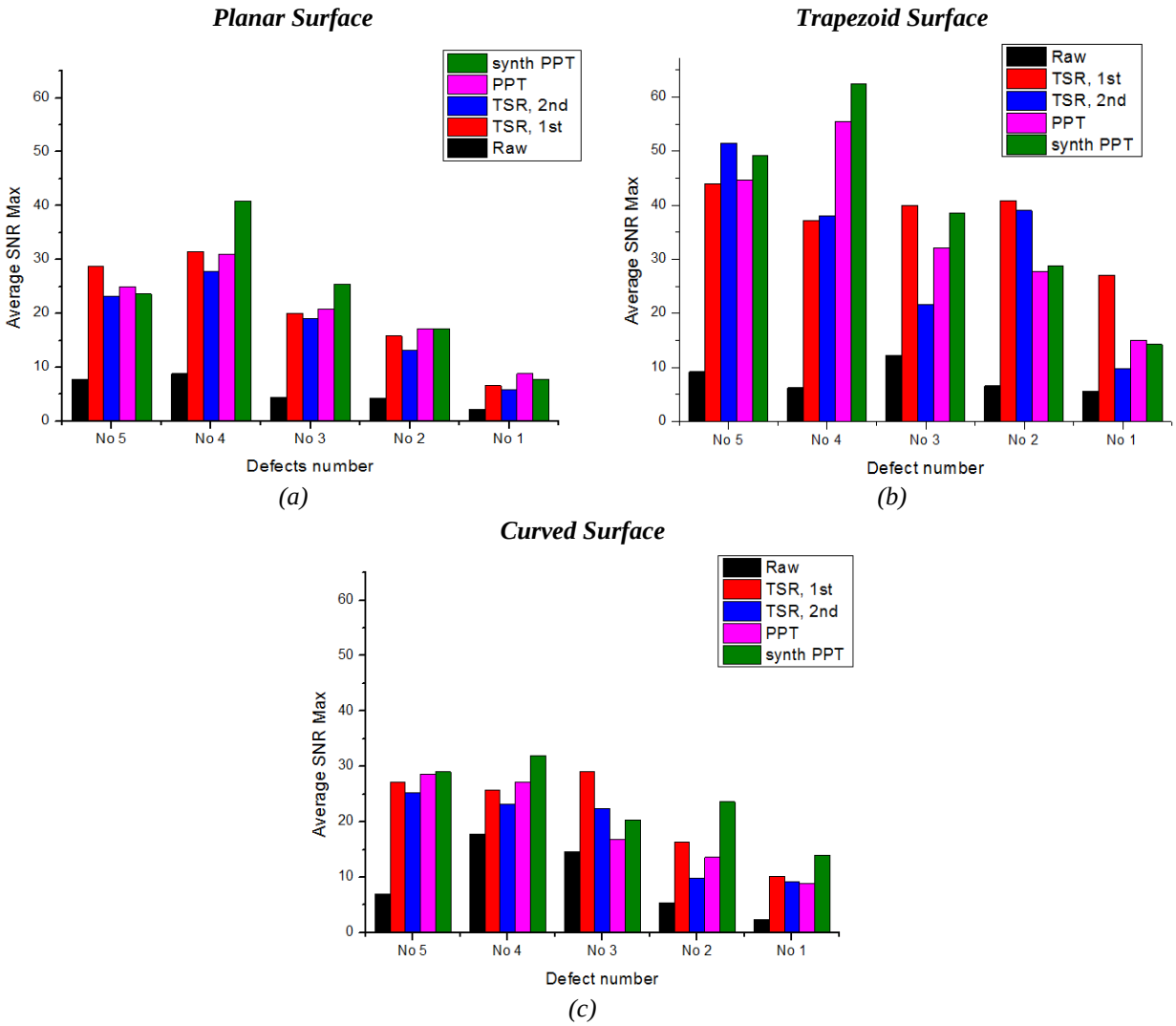

Fig. 5.14: *Comparative SNR results of the different processing methods as a function of defect size for (a) the planar, (b) the trapezoid and (c) the curved specimen respectively.*

5.5.6 Summary of qualitative results

The qualitative assessment of the three CFRP specimens based on visual observations and SNR calculations indicated that different signal processing techniques can provide an enhanced visibility for the internal inserts with respect to the information acquired when working with raw temperature data. More specifically, large and near the surface defects were easily detected from the raw thermal images, however the smaller and deeper ones required the application of advanced signal processing algorithms to produce the proper contrast enhancement, enabling their identification.

Table 5.2 summarises the detectability gradient produced in terms of detected to total insertions from the different unprocessed or post processed data elaborations. Here, it shall be mentioned that the results presented on this table are not taking into account if the produced contrast was weak or strong; the only fact considered was the identification of each internal insertion. The summary of the inspection results is indicating that the best visibility was observed on the trapezoid panel SP2, while the curved SP3 and planar SP1 are following. The fact that all the three samples had exactly the same defect characteristics and thermal properties is showing that the enhanced detectability rate (92%) on the trapezoid surface can be attributed to the more sufficient heat deposition procedure achieved in this inspection, which was further enhanced from the geometry of the respective panel. Additionally, similar results with a slightly reduced however detectability rate, were produced from the curved sample inspection (88%), while the less Teflon insertions were detected on the planar surface with a detection rate in the range of 80%. The above results were acquired due to the fact that the deepest and nearest to the edges defect series D and E, were more clearly visible on the complex geometry coupons contrary to the planar one. As stated above, this enhanced visibility regarding the aforesaid defect series can be attributed to the fact that the surface area above them is nearer to the stimulation source, producing an easier path for heat to be deposited on these areas. Thus apart from the heating process, the shape of the inspected surface is also having an impact on the retrieved qualitative information when these have to be manipulated from raw temperature data.

Table 5.2: *Summary of inspection results using different data processing techniques*

	Planar		***Trapezoid***		***Curved***	
Data Processing manipulation	***Number of insertions detected***	***Detection rate***	***Number of insertions detected***	***Detection rate***	***Number of insertions detected***	***Detection rate***
Raw temperature	20	***80%***	23	***92 %***	22	***88%***
1st time derivative	23	***92%***	25	***100%***	24	***94%***
2nd time derivative	23	***92%***	24	***94%***	24	***94%***
Raw PPT	24	***94%***	25	***100%***	24	***94%***
Synthetic PPT	24	***94%***	25	***100%***	24	***94%***
PCT	24	***94%***	25	***100%***	25	***100%***

However, the interesting point as regards the detectability produced on the planar surface is the fact that despite the relatively low detection rate that the raw thermal images provided, this condition was remarkably increased through the application of advanced signal processing, revealing the presence of defects which were undetected in the former analysis (raw thermograms). The aforesaid observation was also confirmed by the results acquired on the complex geometry panels, as enhanced defect detectability was produced in this case as well after the application of these image processing techniques. For instance, all the defects were detected on the trapezoid panel when data handled through TSR, PPT and PCT algorithms.

A comparison of the processing methods applied in this study, is indicating that PCT and PPT produced the best results regardless the shape of the specimen inspected. More specifically, in the former case all the defects could be indentified on the complex geometry samples and only one was undetected on the planar one, while in the latter case frequency domain analysis after the application of fast Fourier transform on either raw or synthetic temperature data was able to reveal all the defects as well on the trapezoid panel and all the defects except the smaller and deeper positioned E1 on the planar and curved samples respectively. Regarding the derivative analysis and the comparison of first time and second time derivate images similarly to the previous case, the interpretation of results in terms of cooling rate variations (1^{st} time derivative images) seems to produce a better visibility rate with respect to the correspondent one acquired from the 2^{nd} derivative images.

Additionally, a comparison of the best results derived from these processing techniques is illustrated in the plot of Figure 5.15. In particular, this plot represents the average SNR evaluation with respect to the depth of the internal insertions. Thus as can be seen, for the shallowest defects (located at the depth of 0.2 mm) TSR through its 1^{st} time derivative analysis and PPT over synthetic temperature data produced the highest signal-to-noise ratios, while 2^{nd} time derivative analysis and PPT over raw temperature data followed. However in deeper probing, these processing results tend to produce a similar result in terms of image quality and defect contrast, as at the respective depths of 0.6, 0.8 and 1 mm, all these processing methods provided approximately the same image quality.

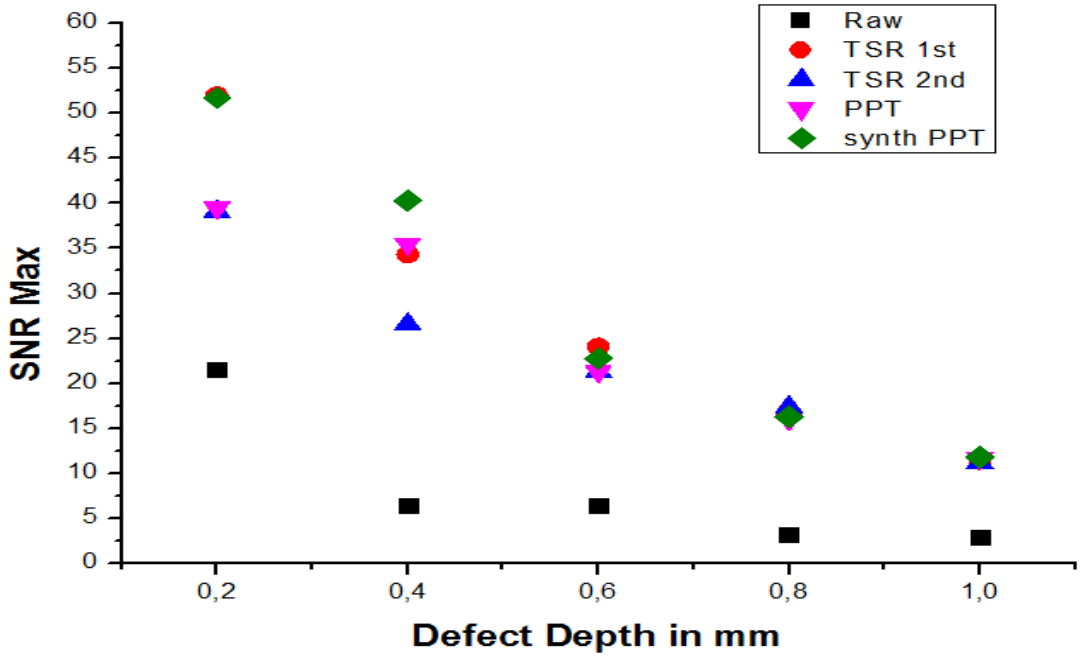

Fig. 5.15: *Plot of maximum SNR as a function of defect depth.*

5.6 Quantitative defect assessment- Depth estimation

As presented in detail in Chapter 4, the depth of a subsurface feature can be correlated with a characteristic point (i.e. time or frequency), enabling its determination. The most common in use depth estimation methods are requiring the selection of a sound and a defective region respectively, as the study of their intensity-contrast (i.e. temperature or phase) can provide information about the identification of the above mentioned characteristic point. However, the depth estimation accuracy is strongly related with the produced contrast evolution, which is further dependent from the selection of this point/area, acting as a reference.

The quantitative depth determination procedures applied in this study, evaluated the performance of two contrast-based methods, one in the time and one in the frequency domain respectively, and in particular through the study of the temperature-contrast slope temporal variations and the monitoring of the phase-contrast variations as a frequency function. The correlation expressions used in order to determine the depth *z* of the inserts were based on the determination of the thermal contrast peak slope time (time domain analysis) and the blind frequency (frequency domain analysis), using the formulas above:

$$z = \sqrt{\frac{\pi^2 \alpha t_{peak}}{3.64}} \qquad \text{and} \qquad z = C\sqrt{\frac{\alpha}{\pi f_b}} \qquad \text{(Eq. 5.2)}$$

where α is the thermal diffusivity of the CFRP specimen, t_{peak} is the peak slope time and f_b is the blind frequency respectively. As can be understood, when the thermal properties of the tested material are known, the determination of t_{peak} and f_b can be used for depth quantification purposes. Additionally, the correlation factor *C* used in this study (frequency domain analysis) had the typically adapted value

of 1.82 proposed from several research studies. In Table 5.3, the thermal properties of the composite specimens and the Teflon insertions are summarised as defined by the literature.

Table 5.3: *Thermal properties of CFRPs and Teflon insertions [29]*

Material	*Thermal Conductivity* ($Wm^{-1}K^{-1}$)	*Specific heat* ($Jkg^{-1}K^{-1}$)	*Density* (kgm^{-3})	*Thermal Effusivity* ($Ws^{1/2}\ m^{-2}K^{-1}$)	*Thermal diffusivity* ($x10^{-7} m^2\ s^{-1}$)	*Mismatch Factor Γ*
CFRP ⊥ ***fibres***	*0.8*	*1200*	*1600*	*1239*	*4.2*	*0.24*
Teflon	*0.25*	*1050*	*2170*	*755*	*1.1*	

As stated above, both methods require the selection of a sound area. However, an inappropriate sound area selection can be an important factor for error production when depth has to be estimated, and is the most crucial negative parameter which in combination with a non uniform stimulation process can provide large deviations from the actual depth in which the detected feature is located to. As a result, the main objective of this study was to evaluate the depth information accuracy produced from the aforementioned methods and to evaluate the influence of the sound area selection on the acquired quantitative results. Based on the qualitative assessment presented above, in order to eliminate the influence of uneven heating on temperature data elaboration, depth quantification in the time domain was performed selecting the sound area next to each defect, similarly to the procedure used for the SNR computations. However, as the application of PPT produced enhanced background uniformity, only an area from the background was selected for the calculations of the produced phase contrasts. Additionally, due to this enhanced background uniformity observed on the frequency domain analysis, this depth quantification method was performed and assessed, considering the field of view as the sound area.

5.6.1 Determination of thermal-contrast peak slope time

The qualitative assessment of the CFRP panels after the application of a pulse thermal energy, showed that a seeing-through condition on the three specimens can be achieved, revealing most of the internal simulated delaminations. The inserts detection phenomenon was produced due to the lower thermal conductivity that these features have with respect to the background. As a result, this variation in the thermal properties affected the penetration rate of the heat flux into the composite bulk and therefore the surface temperature distribution, resulting to the appearance of local "*hot spots*". The time points of these hot spots appearances were varied however according to the inserts' location (depth) and size. Thus when raw temperature data are handled, the depth at which these inserts are located to, can be determined by subtracting the cooling curve over a reference area from the cooling curve over the damaged one. The resulting temperature difference curve can produce the correlation of the detected feature's depth with two characteristic points, this of peak temperature difference and this of the peak slope of this difference, which are further associated with the correspondent times when these phenomena occur (peak difference time, peak slope time).

Before the actual depth information retrieval through the correlation of these specific time points with the depth of the Teflon squares, the temporal functions of the thermal contrast and of the slope of this contrast were studied, verifying that the selection of peak slope time for depth calculations is a more appropriate method, when working with raw temperature data. In the following subsections, the thermal response of all the detected defects on the trapezoid sample are presented in detail, while the respective behaviour of the planar SP1 and curved SP3 samples is presented through selective results. The thermal behaviour of specimen SP2 was selected to be presented in detail as most of the Teflon inserts were detectable in this case, from the acquired thermal images contrary to the detectability rate achieved on the two other panels.

5.6.1.1 Time domain analysis of SP2 specimen

The experimental results in terms of thermal contrast curves and of the correspondent slope curves as a function of time, obtained from the produced thermal effects on the trapezoid surface (SP2), are illustrated in Figures 5.16 to 5.20. More specifically, each figure indicates the thermal contrast evolutions and their respective contrast slope curves for all the detected defects in each individual series. In order to achieve a clearer representation and a higher resolution-clarity for these peaks determination, the time-dependent 1D contrast slope profiles were plotted only at the time region where the peaks occurred. Additionally, as the flash energy deposition was not uniform over the sample surface, the negative values of slopes measured at the very early time intervals were adjusted to zero, until the time point in which the slope of the thermal contrast was departing the zero value. In other words, the initial temperature rise at each defect was scaled to be the same as that of the respective reference area. The aforesaid thermal response representations provided the required information for quantitative analysis, determining the peak thermal contrast and the peak slope of this contrast along with the correspondent peak times.

As regards the shallowest defect series on the trapezoid sample (Figure 5.16), the time of peak thermal contrast occurrence was measured to be the same for all the detected defects, regardless the size of each square insertion. Usually, for features having larger lateral dimensions, it takes more time for the trapped heat above them to be diffused out through the sides of the "*trap*'', and this can be seen on the plot from the different time points in which each temperature difference curve is approaching zero. However the evolution of these temperature difference curves is indicating that when the defect depth is approaching zero, the peak thermal contrast time approaches zero as well (t=0.1019s) and thus the temporal characteristics of this phenomenon remain unaffected from the 3D conduction problem. Similar results were also produced by the study of the temporal function of the thermal contrast slopes, as these peaks occurred as well at exactly the same time for all the five insertions of series A. However, the peak slope appeared much earlier (t=0.02447 s) with respect to peak thermal contrast. On the other hand, the 3D heat conduction around the defects seems to affect the peak values of either the thermal contrast or of its slope. In particular, from the plots of Figure 5.16, it can be seen that larger inserts

generally presented higher peak contrast and peak contrast slope values with respect to these produced by smaller ones. For instance, the peak thermal contrast and peak contrast slope for defect A5 (15mm) were 2.25 and 52.95 respectively, while the correspondent values for defect A1 (3mm) were 0.63 and 8.19, indicating that as smaller is the dimension of the defect, the easier the heat diffusion can take place around this region, producing as well a reduced contrast. Nevertheless, some differentiations detected regarding this phenomenon (i.e. peak contrast values of defects A5 and A4) can be possibly attributed to the selection of different sound areas for each individual peak determination along with the non uniformity of heat deposition on the inspected surface.

Contrary to the results produced from the shallowest defects, as the depth of the Teflon insertions was increased, the consistency detected regarding the time points of the peak contrast appearance was altered. More specifically, by studying the produced thermal contrasts and their evolution to time for all the insertions to the depth of 0.4 mm (Figure 5.17a), it can be generally seen that the smaller defects produced an earlier time point of maximum thermal contrast appearance and vice versa. For instance, the temporal region where the peak thermal contrasts occurred for the five defects of this series was ranging from 0.3312s (for defect B1) to 0.4331 s (for defects B4 and B5), indicating that smaller lateral sizes produced an easier path for heat to be laterally diffused and consequently a reduced contrast on an earlier time interval. Thus, the above results verify that the peak contrast time is appropriate for relative comparisons but not reliable for quantitative information retrieval on deeper probing, as the 3D conduction effect has an impact on the acquired information. Some deviations from the above general observation were although detected in this case (i.e. time points of defect B3 and defect B4), which can be also a result of the procedure used to produce these temperature difference functions (selection of sound area). On the other hand, the study of contrast slope evolution to time (Figure 5.17b), revealed that the characteristic time points of this peak occurrence remained more constant and less affected from the negative effects of lateral heat conduction around the Teflon squares. For instance, the time range when the peak slopes occurred, was between 0.2547 s and 0.3057 s and even though the peak slope times did not have exactly the same value, the shorter time range (approximately the half) observed in this case, is indicating the reliability of this quantity for depth prediction, despite the selection of different sound areas for these respective measurements. However, similarly to the temperature difference evolution study, the 3D conduction is strongly influencing only the peak slope values, but this parameter is not of prime interest when the objective is the quantitative depth analysis.

The thermal behaviour assessment regarding the detected defects on series C, D and E provided similar results, as Figures 5.18, 5.19 and 5.20 indicate. As can be seen from the respective plots, the observations discussed above were further confirmed from the study of the thermal profiles acquired for the deeper inserts. In particular, as deeper was the probing, a high divergence on the characteristic peak contrast time range was observed for defects of the same depth but with different lateral dimensions. For instance while Series A defects had the same peak contrast time, Series B and C defects produced a peak time range of approximately 0.1 s, and Series D and E produced a temporal range of

approximately 0.37 s and 0.15 s respectively. Contrary, these time differences were remarkably reduced by studying the correspondent contrast slope variations. For instance, series C defects produced a peak slope time range from 0.40s to 0.48 s, while the ranges for series D and E defects were between 0.66 s to 0.76 s and from 0.91s to 0.99 s respectively. Additionally, comparing the plots retrieved from each individual series investigation, it can be seen that the high noise levels produced as increasing the depth, did not have an impact to the determination of the two characteristic time points. Nevertheless, for the deeper defects no clear observations can be done regarding the correlation of square size and the 3D conduction phenomenon around it. As can be seen from the raw thermal images presented above, a reduced contrast was produced mainly for the defects on series D and E, indicating that the thermal wave did not penetrate efficiently enough to these locations and a weak thermal effect was produced from these defects. As a result, the reduced amount of heat reached these areas, was not able to produce sufficient lateral heat diffusion around these defects. The above observation was mainly detected on defect series D and E, as for instance the smaller detected defects D3 and E2 had a longer peak contrast time with respect to the larger defects D5 and E5.

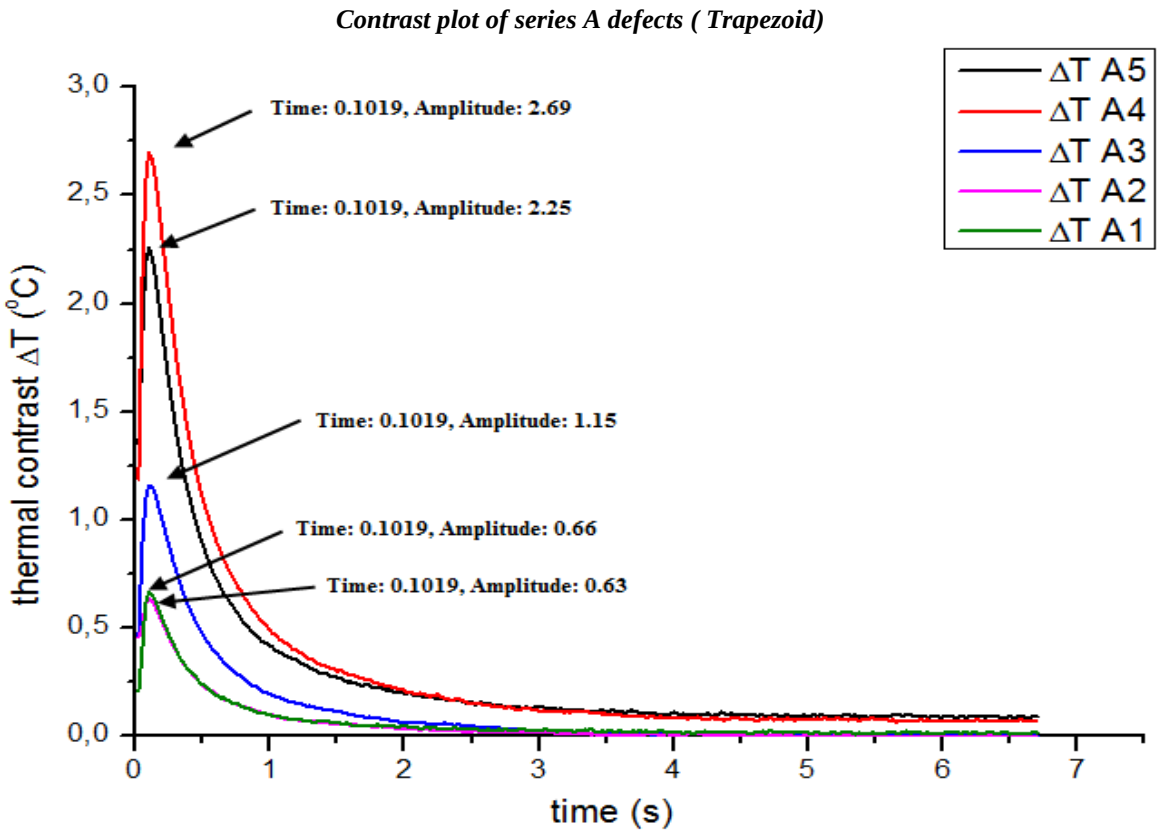

(a)

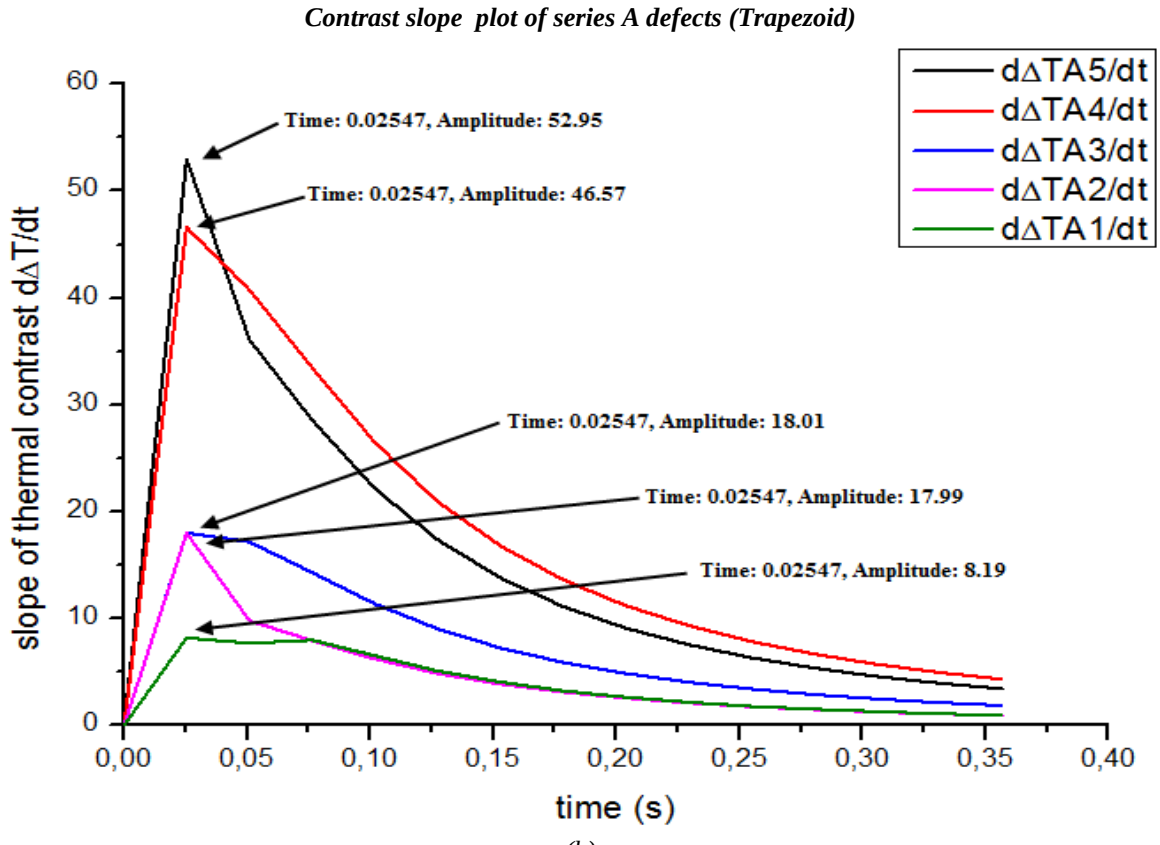

(b)

***Fig. 5.16**: Temporal evolution of (a) the thermal contrast curves and (b) the correspondent slope of thermal contrasts for the detected insertions on the trapezoid surface located to the depth of 0.2 mm (Series A).*

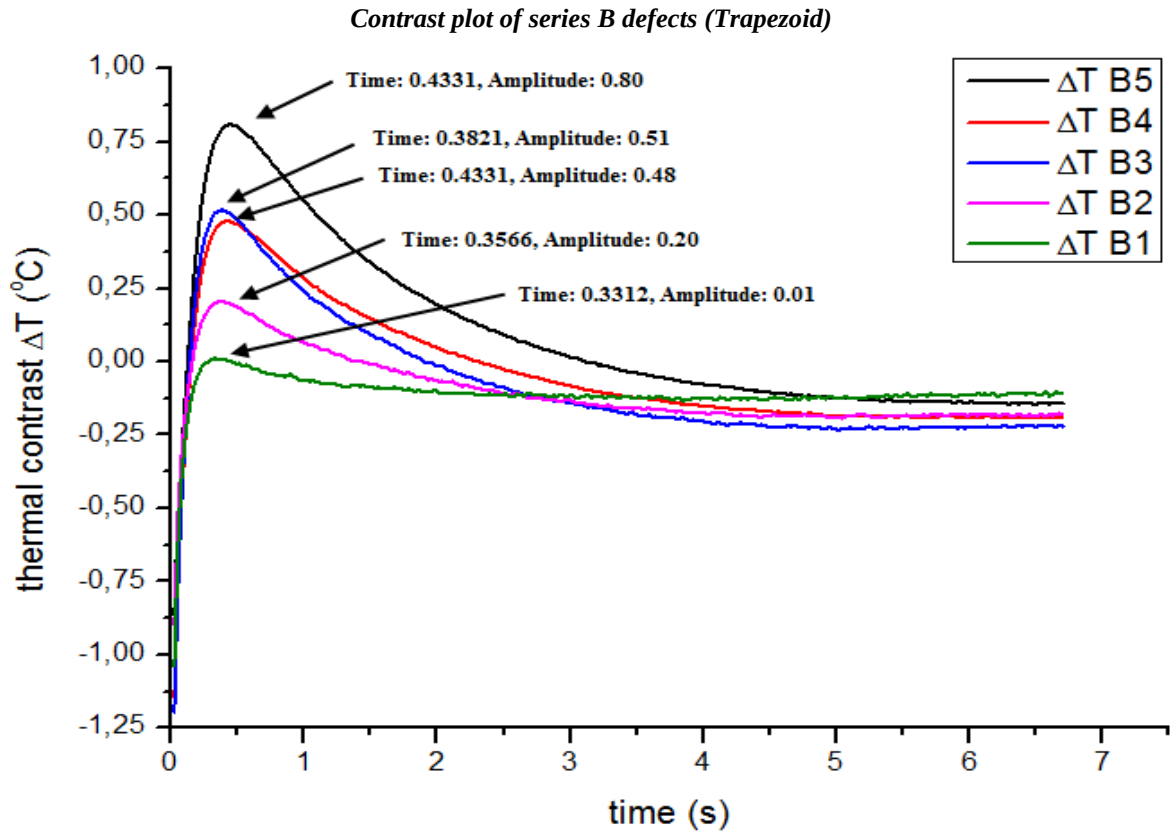

(a)

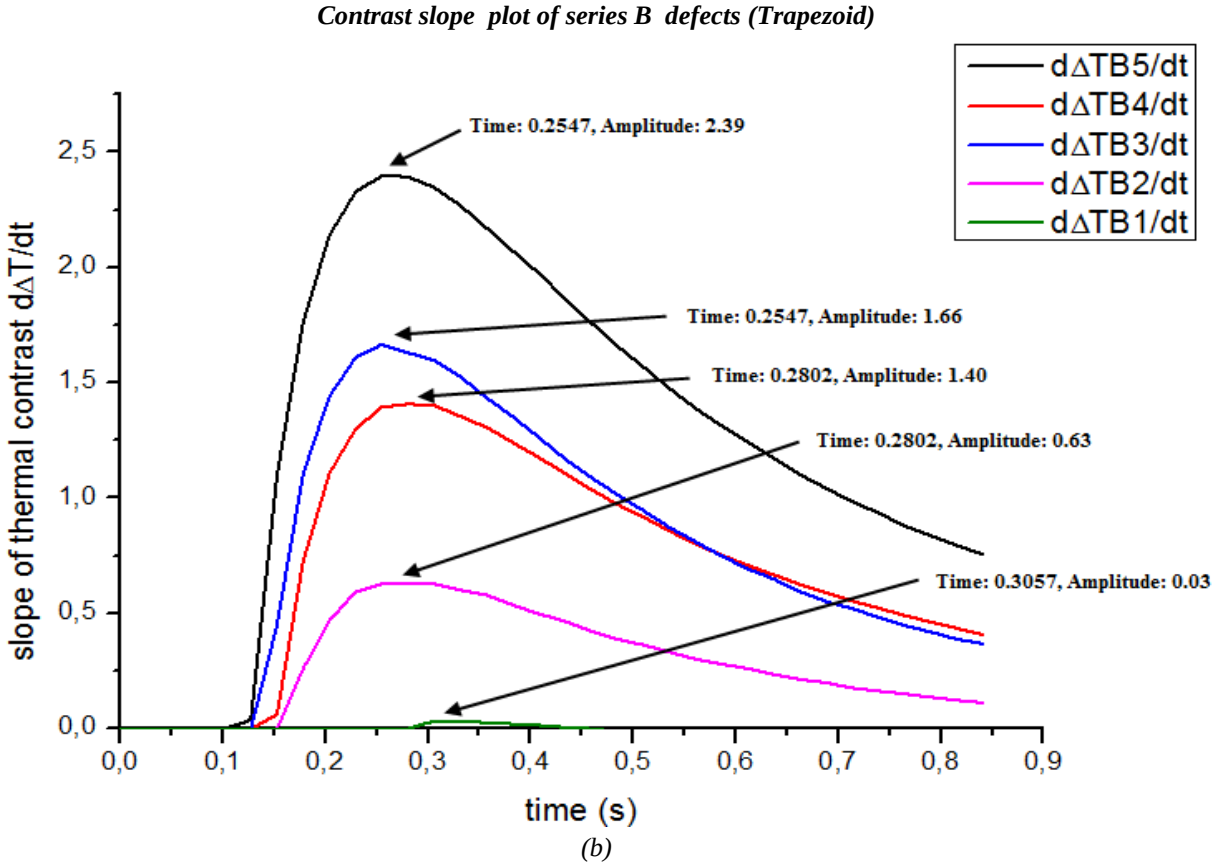

(b)

***Fig. 5.17**: Temporal evolution of (a) the thermal contrast curves and (b) the correspondent slope of thermal contrasts for the detected insertions on the trapezoid surface located to the depth of 0.4 mm (Series B).*

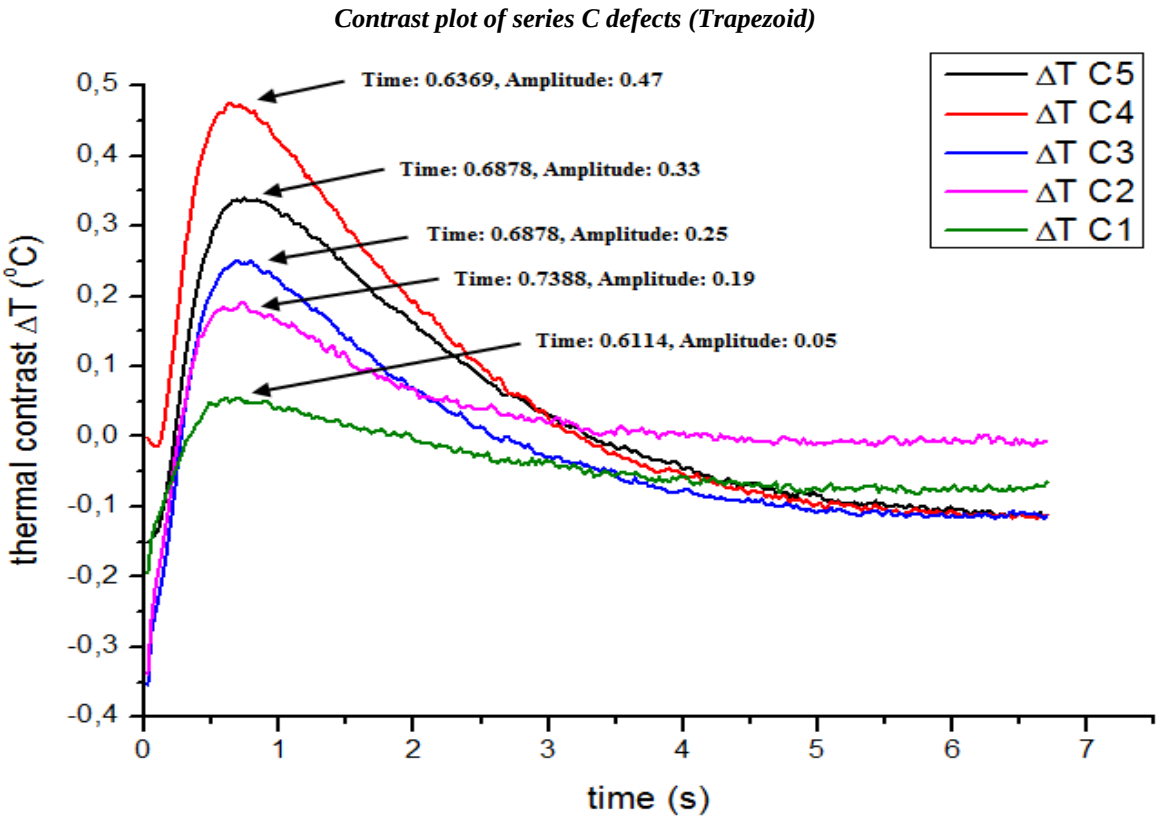

(a)

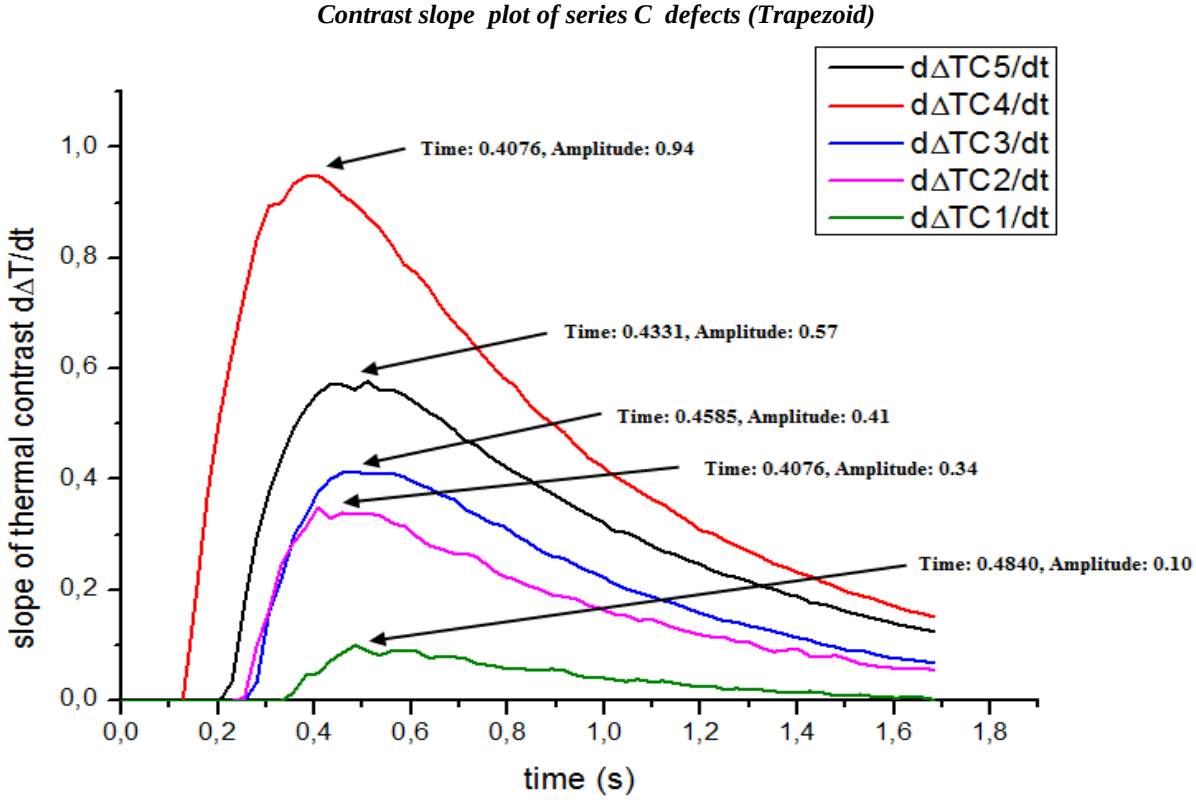

(b)

***Fig. 5.18**: Temporal evolution of (a) the thermal contrast curves and (b) the correspondent slope of thermal contrasts for the detected insertions on the trapezoid surface located to the depth of 0.6 mm (Series C).*

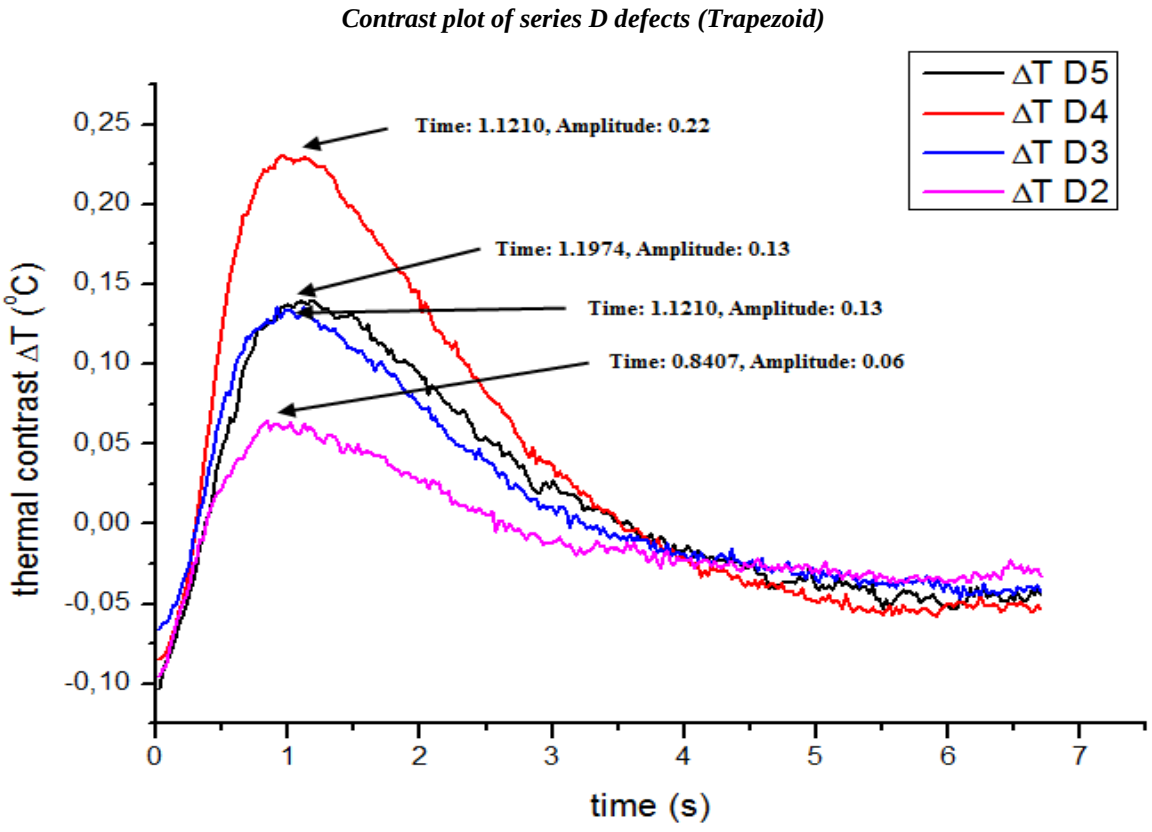

(a)

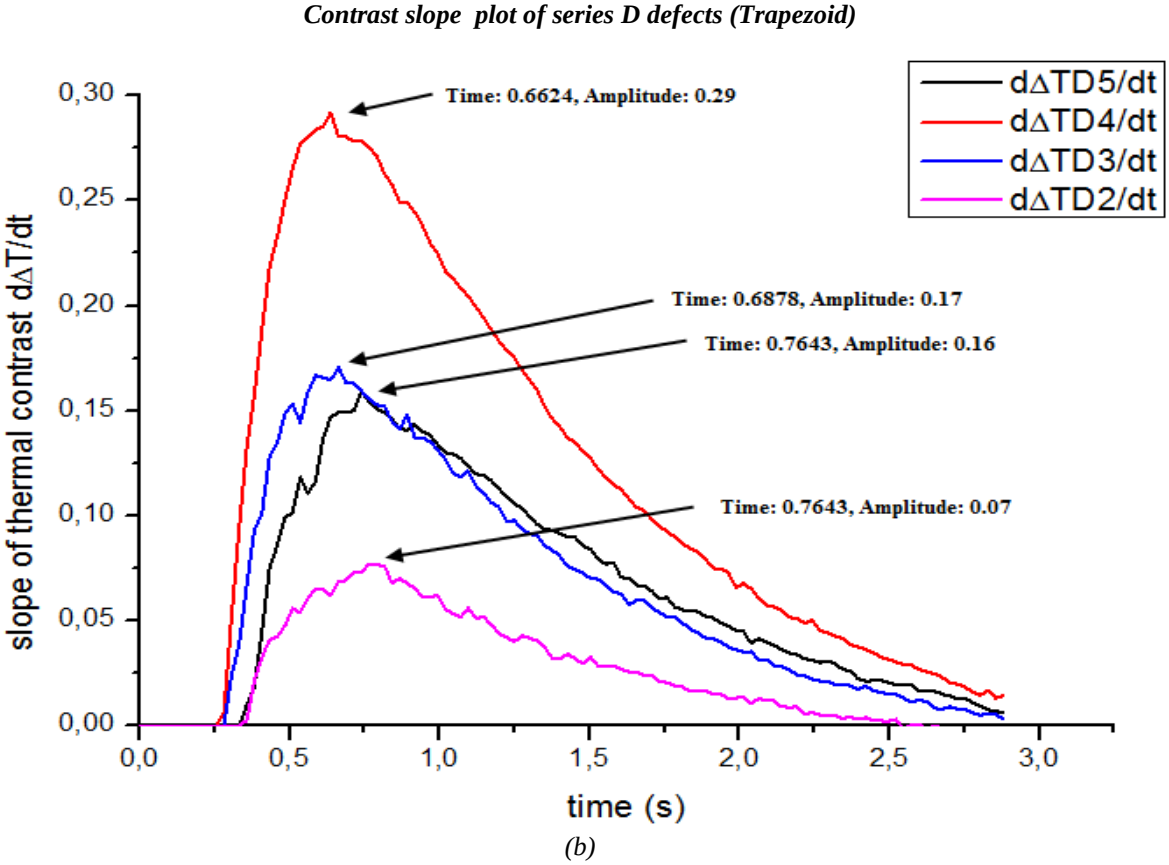

(b)

***Fig. 5.19**: Temporal evolution of (a) the thermal contrast curves and (b) the correspondent slope of thermal contrasts for the detected insertions on the trapezoid surface located to the depth of 0.8 mm (Series D).*

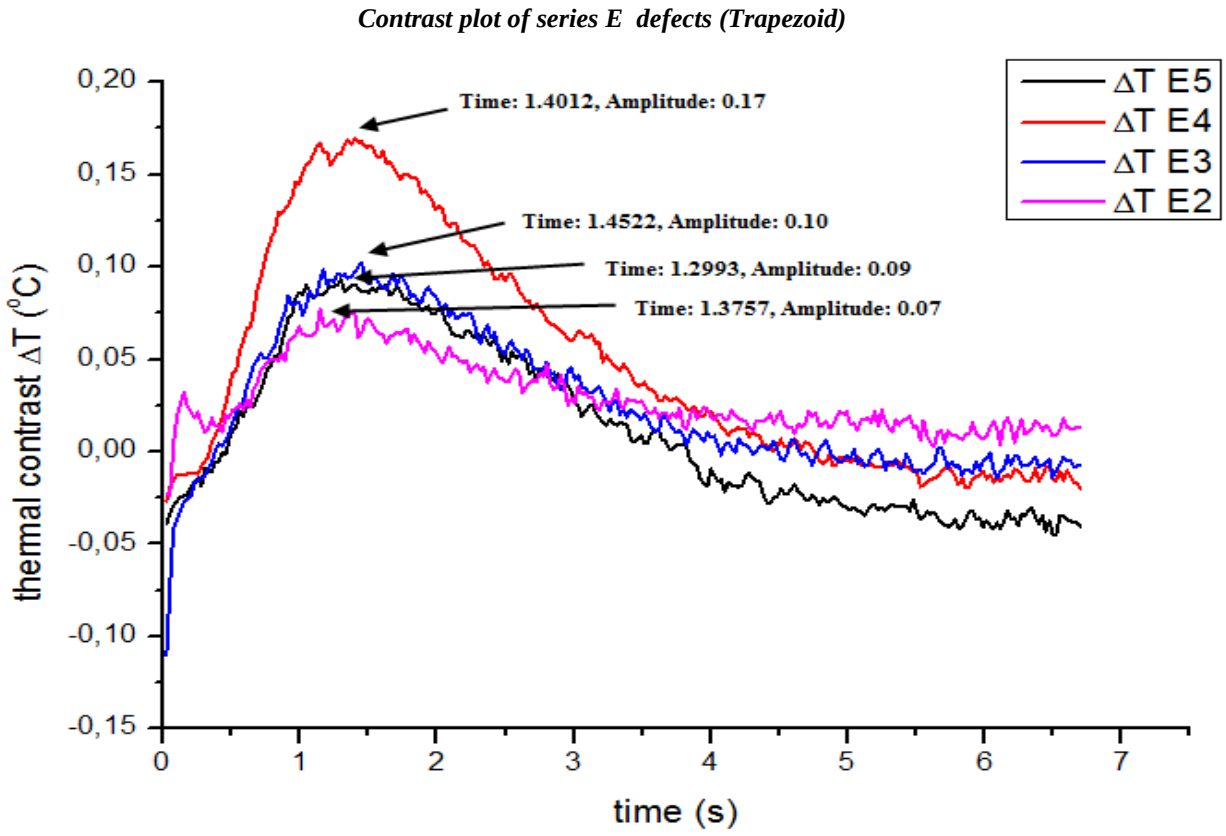

(a)

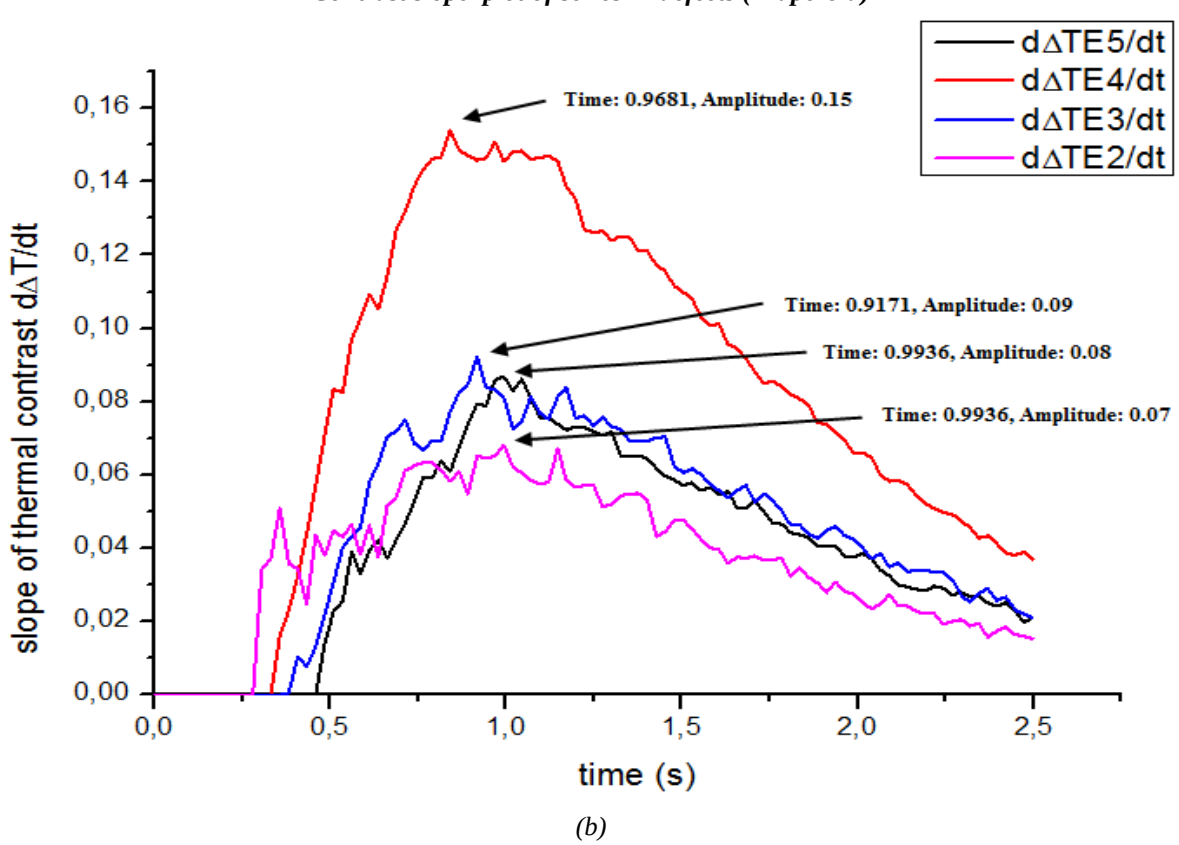

(b)

***Fig. 5.20**: Temporal evolution of (a) the thermal contrast curves and (b) the correspondent slope of thermal contrasts for the detected insertions on the trapezoid surface located to the depth of 1 mm (Series E).*

5.6.1.2 Time domain analysis of SP1 and SP3 specimens

The above presented results regarding the analysis of the thermal contrast and thermal contrast slope evolution curves were further confirmed by measuring the produced temperature differences for all the detected defects on the planar SP1 and curved SP3 samples, respectively. In Figures 5.21 to Figure 5.24, the temporal functions of the temperature contrasts and of their slope are presented for the defects of series A and C.

Generally the consistency observed through the study of the shallowest defects of the trapezoid sample, was further confirmed from the results obtained both from the planar and the curved specimen inspections. In particular, the peak thermal contrast time for all the defects on these two panels was 0.12 s, very close to the value measured in the former inspection (0.10 s); the only differentiation observed was concerning defect A3 on the planar panel, which had a peak contrast time value of 0.15 s. On the other hand, the correspondent peak slope times were measured to be 0.025 s (regardless the insert size) on the planar sample and 0.050 s on the curved one. In other words, considering that the truncated time interval Δt used in this study was 0.025 s, the peak slope time for the series A defects (regardless the specimen shape) was found to be unaffected from the sample geometry, as this temporal characteristic was measured on the lower time interval for the planar and trapezoid samples and on the second lower time interval for the curved SP3.

The above described stable condition was differentiated as well by increasing the inspection depth, similarly to the trapezoid sample investigation. In particular, even that the peak contrast times presented in some instances great divergences between them for inserts placed to the same depth, the measured peak contrast slope times produced a more enhanced consistency. For instance, defect C4 on the trapezoid sample presented a peak contrast at approximately 0.63 s, contrary the respective values measured for the same defect on the planar and curved samples, which were 0.84 s and 0.74 s respectively. However the respective peak slope times for the same defect had the values of approximately 0.41s, 0.53s and 0.48s respectively, confirming as well that this temporal characteristic is a more reliable quantity for depth estimations and peak slope time is less influenced from the geometry of the inspected surface. Nevertheless, as the three samples were measured under the same experimental conditions and had the same defect characteristics and thermal properties, the differentiations observed either slight or great on the acquired results of the peak contrast and peak slope values or the correspondent times of these occurrences can be attributed to the shapes of the panels. As stated above, these deviations were mainly detected on the peak thermal contrast intensities and times, while a more detailed study is revealing that the above variation had a low to negligible impact on the determination of the respective peak slope times, which are presented in the tables of the next subsection.

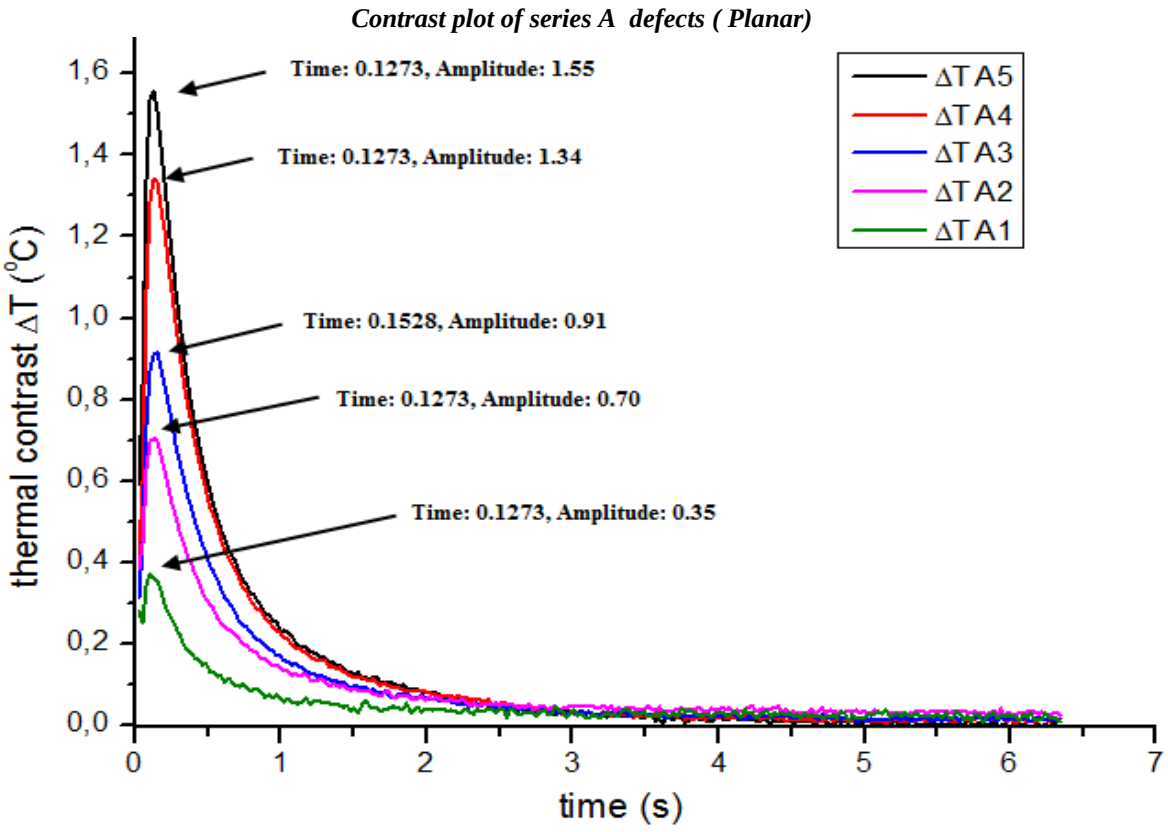

(a)

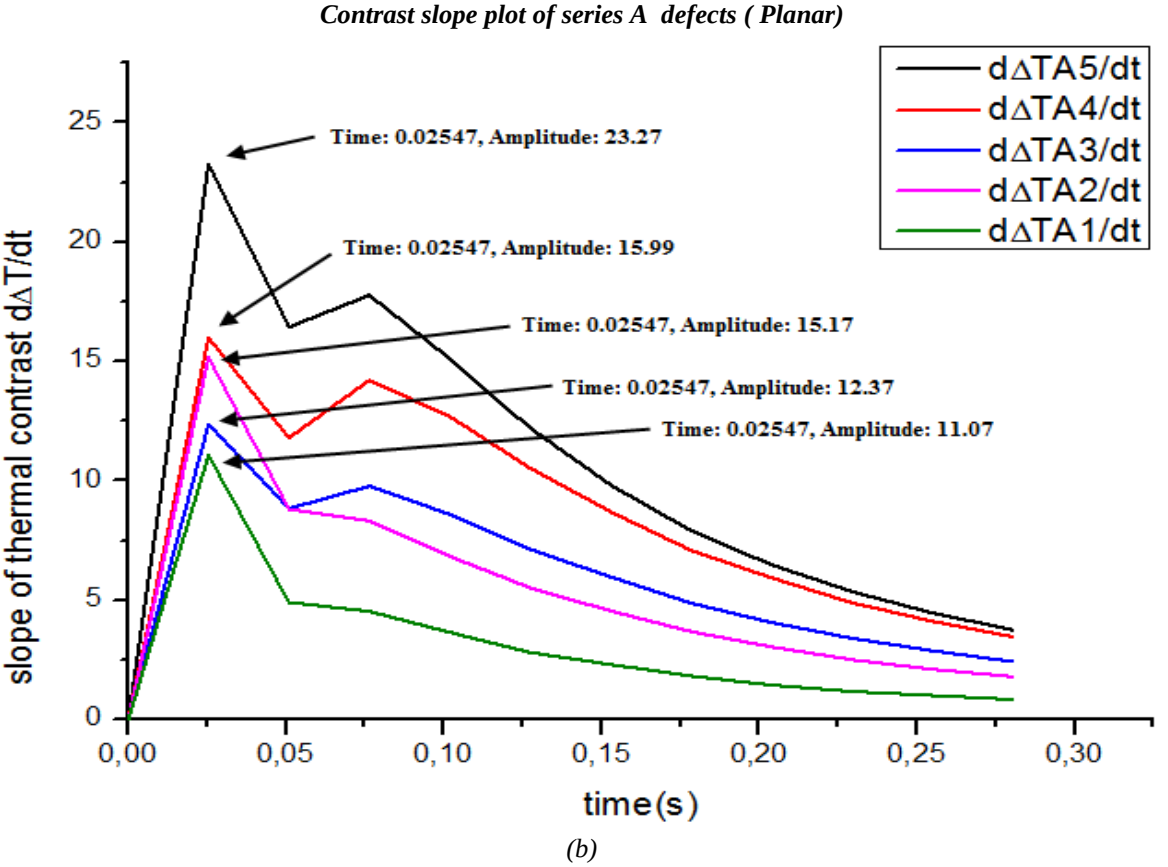

(b)

Fig. 5.21*: Temporal evolution of (a) the thermal contrast curves and (b) the correspondent slope of thermal contrasts for the detected insertions on the planar surface located to the depth of 0.2 mm (Series A).*

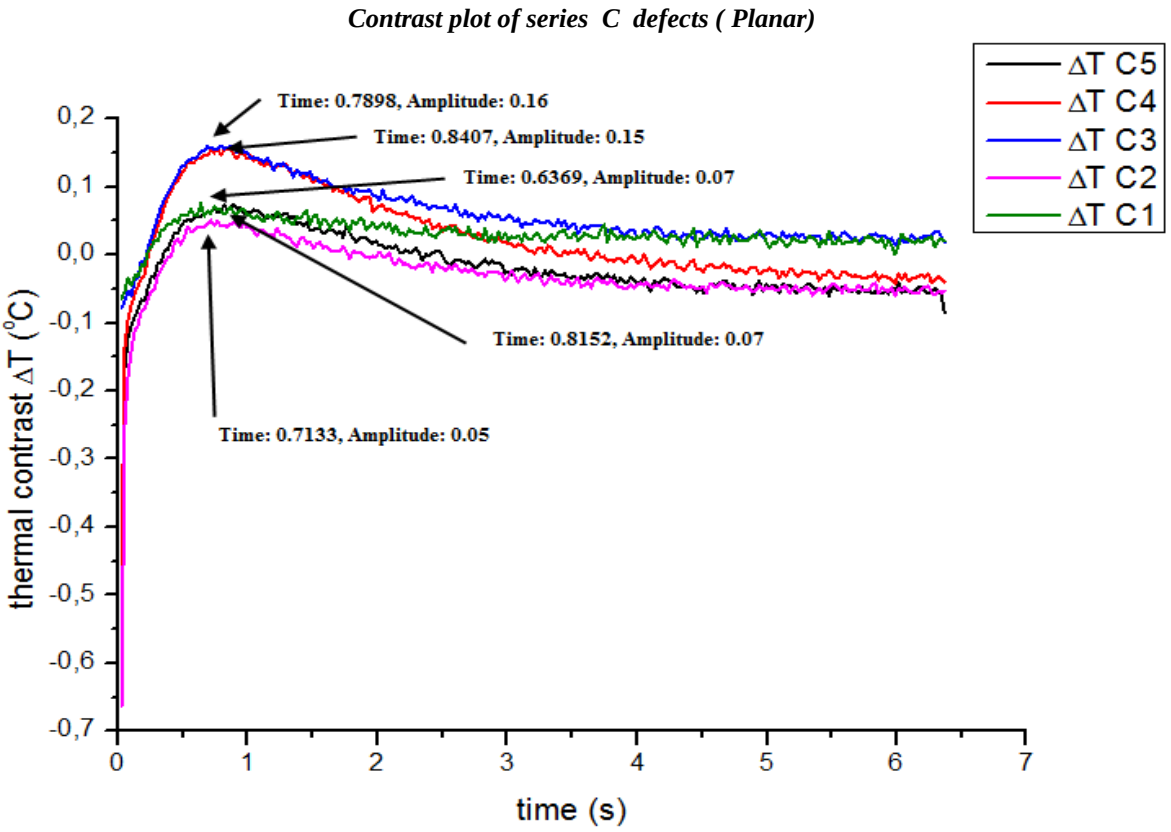

(a)

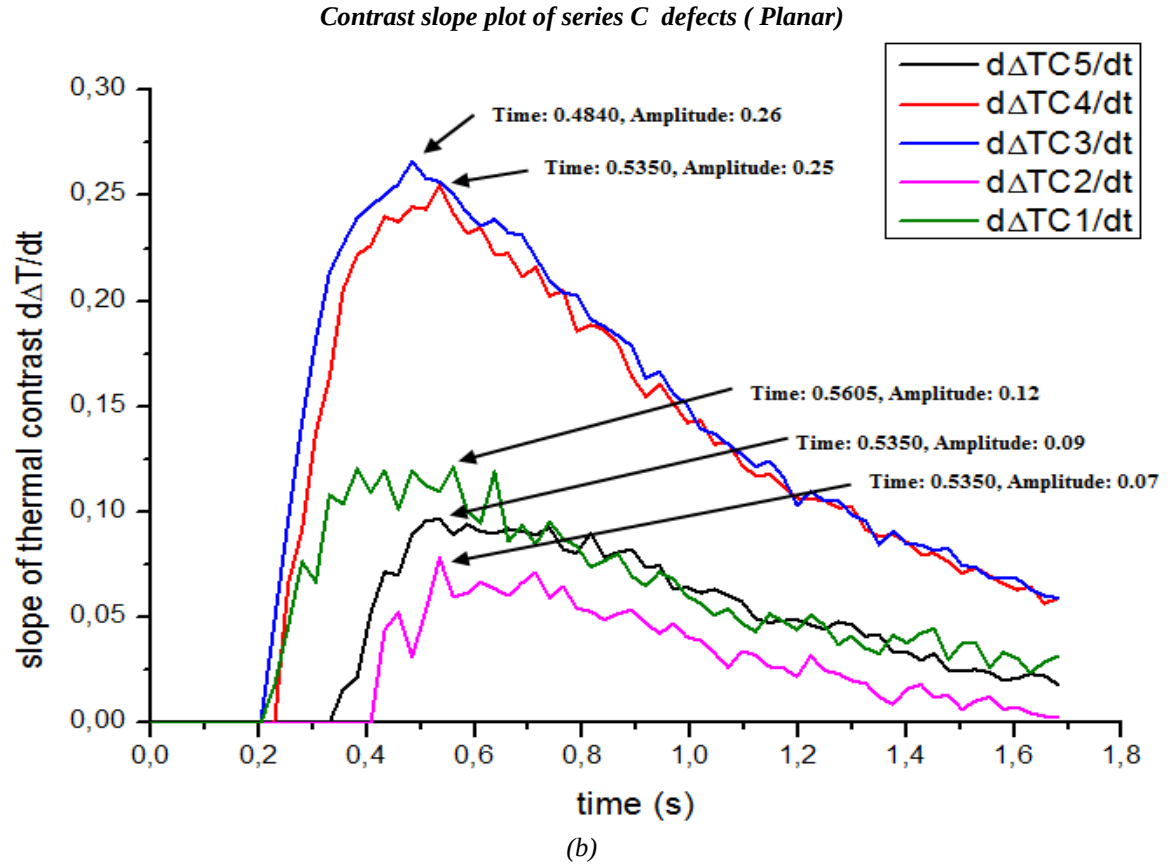

(b)

***Fig. 5.22**: Temporal evolution of (a) the thermal contrast curves and (b) the correspondent slope of thermal contrasts for the detected insertions on the planar surface, located to the depth of 0.6 mm (Series C).*

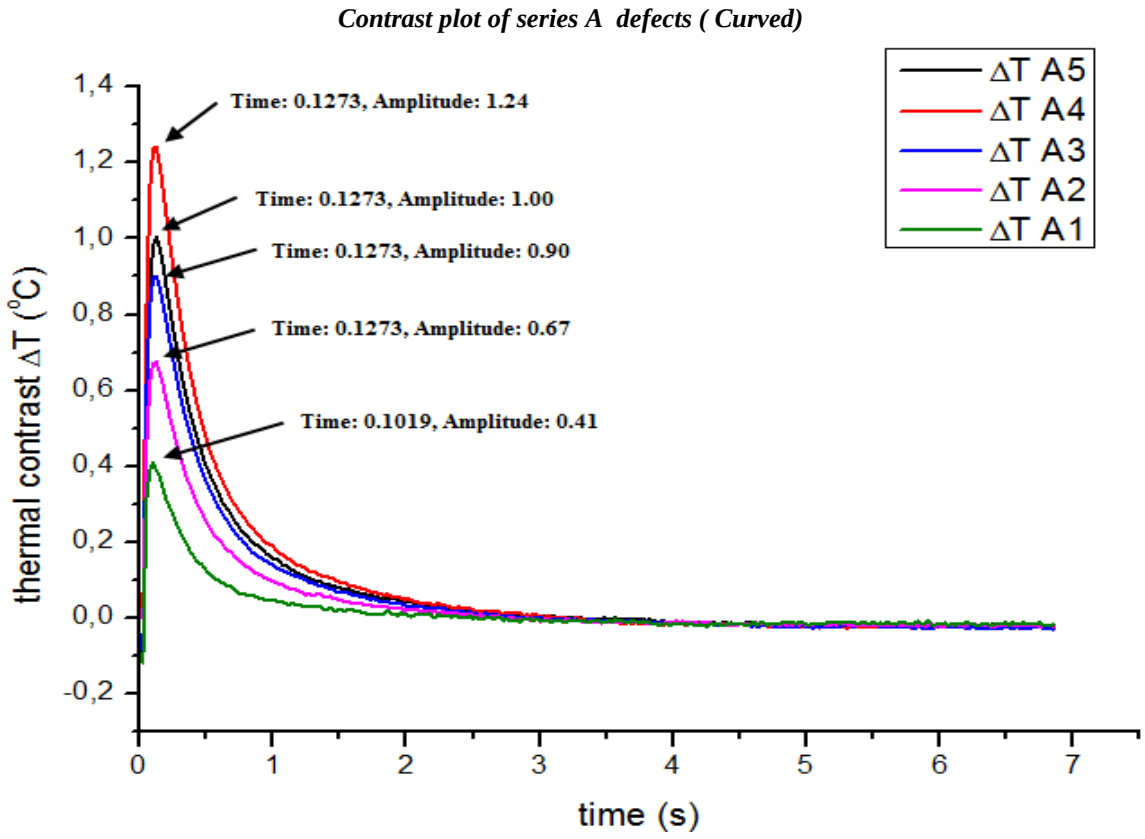

(a)

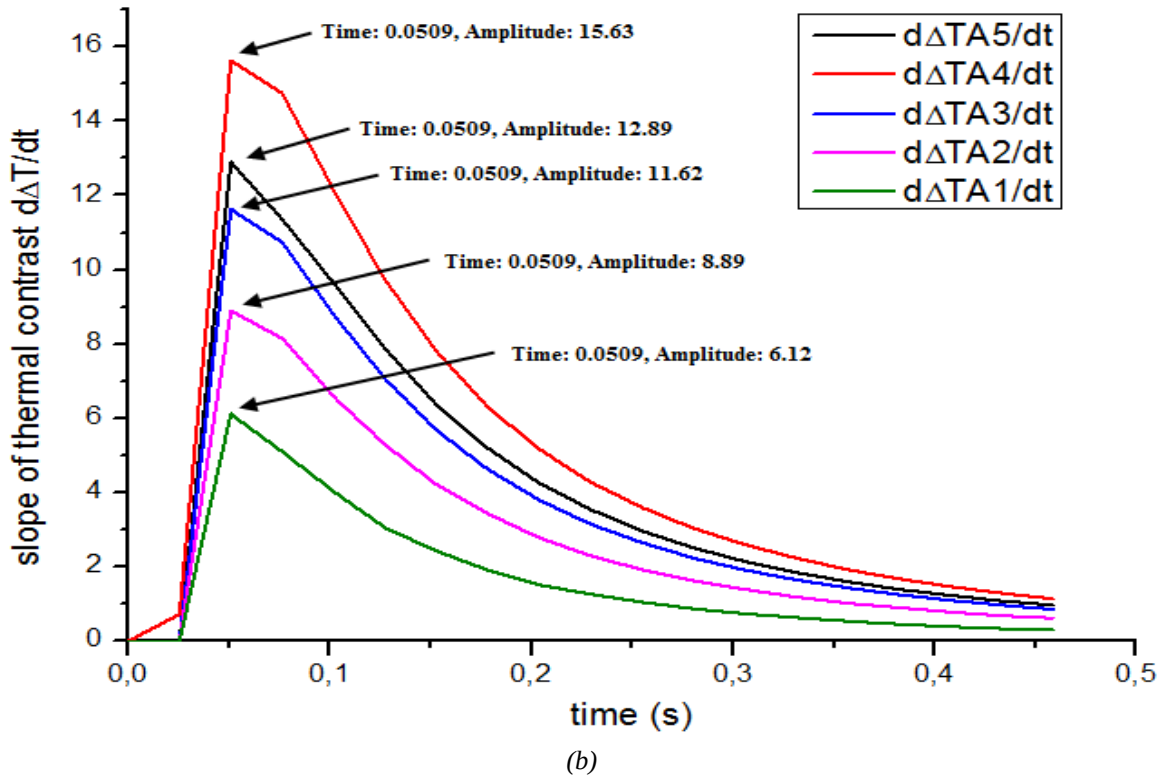

(b)

***Fig. 5.23**: Temporal evolution of (a) the thermal contrast curves and (b) the correspondent slope of thermal contrasts for the detected insertions on the curved surface located to the depth of 0.2 mm (Series A).*

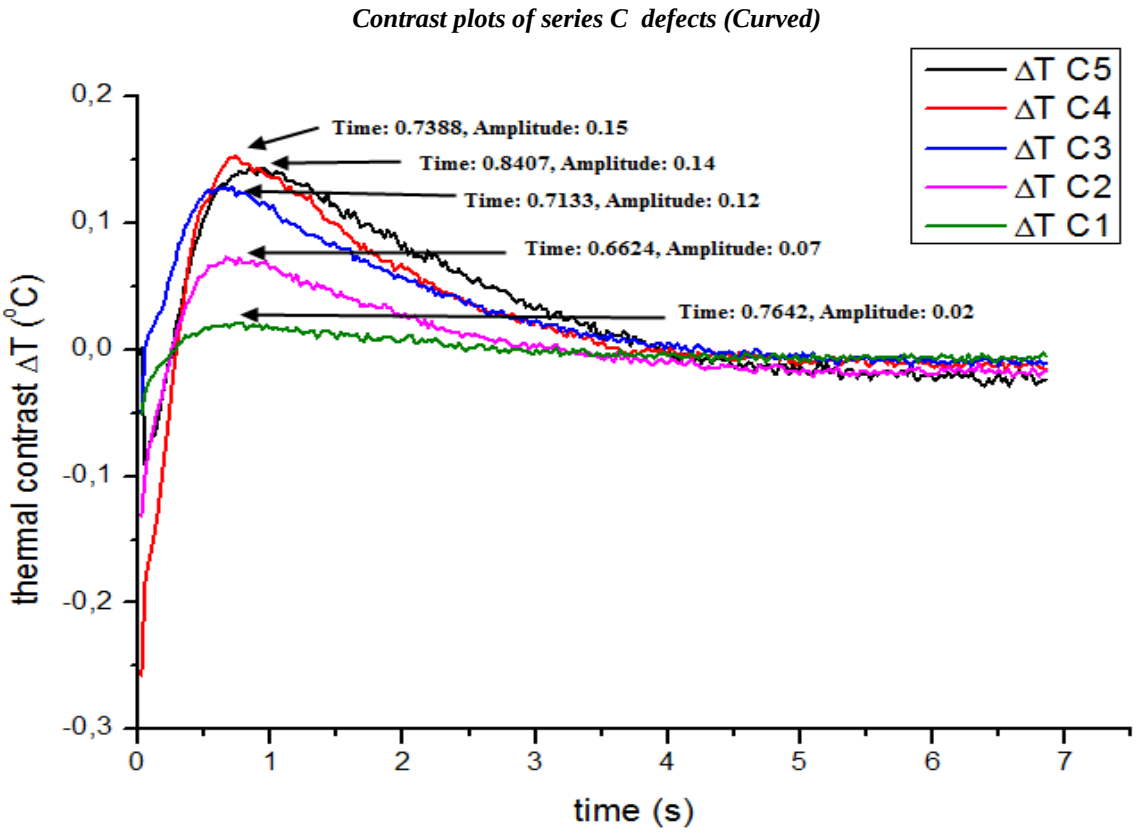

(a)

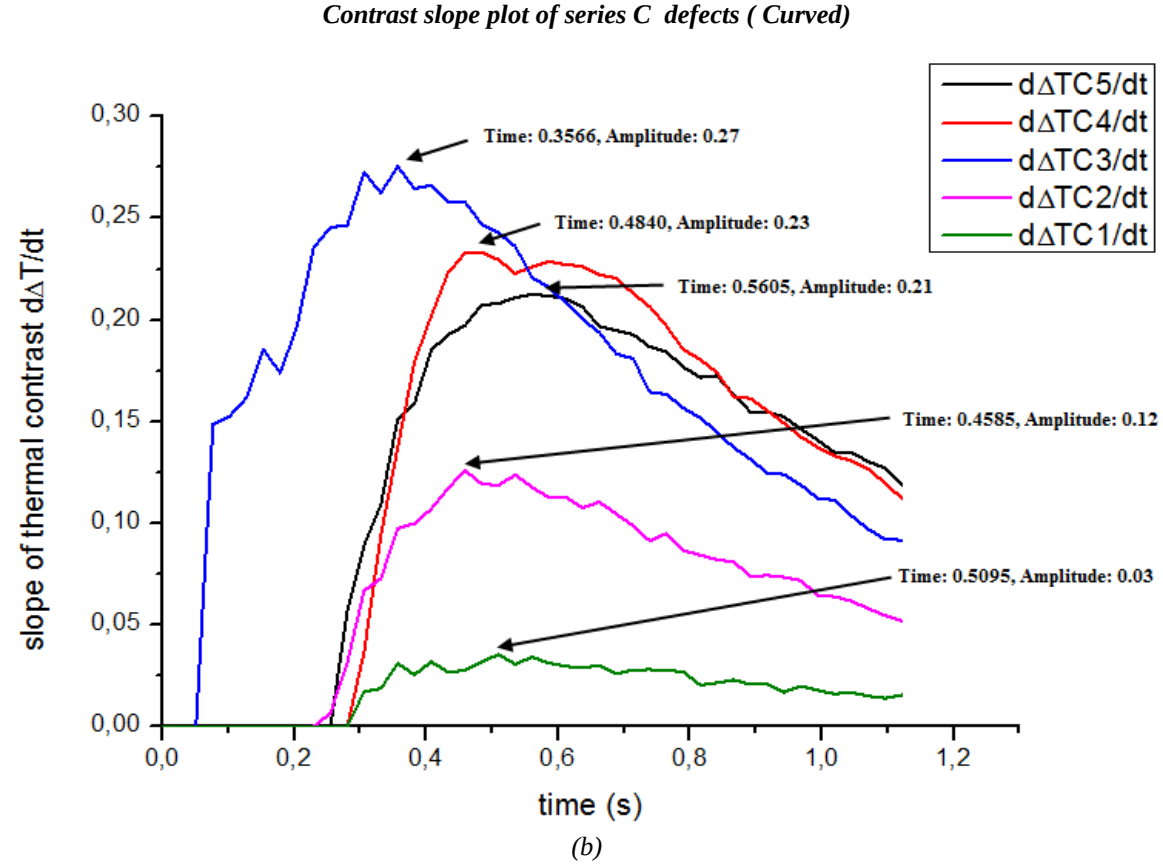

(b)

***Fig. 5.24**: Temporal evolution of (a) the thermal contrast curves and (b) the correspondent slope of thermal contrasts for the detected insertions on the curved surface located to the depth of 0.6 mm (Series C).*

5.6.1.3 Depth estimation through peak slope time

Through the above presented procedure, the depths of all the detected Teflon inserts into the three CFRP specimens were quantitatively estimated, correlating the measured peak slope time with the depth. This method for depth calculations was selected, as the peak contrast time was proven to be seriously affected by the lateral dimensions of the detected features, whereas peak slope time appeared to remain more constant regardless these size variations. Table 5.4 and Table 5.5 summarise the experimental values of peak slopes and peak slope times along with the produced depth results for all the detected defects in the three samples.

In general, peak slope time provided an efficient estimation of the Teflon depths; however in some instances increased errors were produced. From the summary of the depth results, it can be seen that regardless the shape of the specimen, the more accurate results were produced for the deeper insertions (despite the noise exhibited in this case) and the larger errors were observed on the defects series B and C. A possible explanation about these large deviations from the actual depth on series B and C defects, can be attributed to the fact that these inserts were more strongly affected from the 3D heat conduction, contrary to the shallowest and deepest insertions which seem to be unaffected from the above phenomenon for different reasons as discussed above. As regards the depth results produced individually from the inspection of each sample, these can be related to the qualitative accuracy produced from the images elaboration. In particular, the more sufficient seeing-through condition produced on the trapezoid sample (both through raw temperature data and advanced image processing interpretation) was also verified from the more accurate results (in terms of error production) acquired in this case. However these error deviations among the different inspections were relatively low, indicating that in depth quantifications through peak slope time, the shape of the inspected sample has a low impact on the acquired results.

On the other hand, a factor that can produce deviations between the measured and actual depth could be the anisotropy of these materials and the uncertainty on the thermal properties which might contribute to error as well. In particular, the actual value of the thermal diffusivity might differ greatly in anisotropic materials from that presented Table 5.3. Besides the uncertainty related with the thermal properties, the selection of the truncation parameters in order to overcome the processing limitations could be a factor of extra error. For instance, the peak slope time of the defects in series A (0.2 mm) was determined in the lower time interval of the truncated sequence producing an error of 15% for SP1 and SP2 and 20% for SP3 respectively (peak slope time in SP3 was determined at the second lower time interval). The appearance of the peak slope time in these very early time points and the correspondent error produced may be further reduced if new truncated parameters are defined, increasing the temporal resolution of the cooling down process study. Finally, the slight variability of peak slope times detected for defects located to the same depth (except the shallowest ones) can be attributed the variability of the sound area selection in each particular defect depth measurement which can be as well an extra error production factor.

Table 5.4: *Depth estimation using peak slope time for samples SP1 and SP2*

		Planar SP1				***Trapezoid SP2***			
Def. No	***Nominal depth in x 10^{-1}mm***	***Measured Peak slope***	***Measured peak slope time in s***	***Measured depth in x 10^{-1}mm***	***Error (%)***	***Measured Peak slope***	***Measured peak slope time in s***	***Calculated depth in x 10^{-1}mm***	***Error (%)***
A5	2	23.27	*0.0254*	**1.70**	***-15***	52.95	*0.0254*	**1.70**	***-15***
A4	2	15.99	*0.0254*	**1.70**	***-15***	46.57	*0.0254*	**1.70**	***-15***
A3	2	12.37	*0.0254*	**1.70**	***-15***	18.01	*0.0254*	**1.70**	***-15***
A2	2	15.17	*0.0254*	**1.70**	***-15***	17.99	*0.0254*	**1.70**	***-15***
A1	2	11.07	*0.0254*	**1.70**	***-15***	8.19	*0.0254*	**1.70**	***-15***
B5	4	0.56	*0.2802*	**5.65**	***41.25***	2.39	*0.2547*	**5.38**	***34.5***
B4	4	0.79	*0.2547*	**5.38**	***34.5***	1.40	*0.2802*	**5.65**	***41.25***
B3	4	0.67	*0.3057*	**5.89**	***47.4***	1.66	*0.2547*	**5.38**	***34.5***
B2	4	0.69	*0.3057*	**5.89**	***47.4***	0.63	*0.2802*	**5.65**	***41.25***
B1	4	0.30	*0.2802*	**5.65**	***41.25***	0.03	*0.3057*	**5.89**	***47.4***
C5	6	0.09	*0.5350*	**7.80**	***30***	0.57	*0.4331*	**7.01**	***16.8***
C4	6	0.25	*0.5350*	**7.80**	***30***	0.94	*0.4076*	**6.8**	***13.3***
C3	6	0.26	*0.4844*	**7.42**	***23.6***	0.41	*0.4588*	**7.22**	***20.4***
C2	6	0.07	*0.5350*	**7.80**	***30***	0.34	*0.4076*	**6.8**	***13.3***
C1	6	0.12	*0.5605*	**7.98**	***33.1***	0.10	*0.4840*	**7.42**	***23.6***
D5	8	0.12	*0.7388*	**9.16**	***14.5***	0.15	*0.7643*	**9.32**	***16.5***
D4	8	0.14	*0.7133*	**9.00**	***12.6***	0.29	*0.6624*	**8.68**	***8.51***
D3	8	0.08	*0.7898*	**9.47**	***18.4***	0.17	*0.6879*	**8.84**	***10.6***
D2	8	*N/D*	*N/D*	**N/D**	***N/D***	0.07	*0.7643*	**9.32**	***16.5***
D1	8	*N/D*	*N/D*	**N/D**	***N/D***	*N/D*	*N/D*	***N/D***	***N/D***
E5	10	0.02	*1.1210*	**11.29**	***12.9***	0.08	*0.9936*	**10.63**	***6.3***
E4	10	0.05	*0.9936*	**10.63**	***6.3***	0.15	*0.9681*	**10.49**	***4.9***
E3	10	*N/D*	*N/D*	**N/D**	***N/D***	0.09	*0.9171*	**10.21**	***2.1***
E2	10	*N/D*	*N/D*	**N/D**	***N/D***	0.06	*0.9936*	**10.63**	***6.3***
E1	10	*N/D*	*N/D*	**N/D**	***N/D***	*N/D*	*N/D*	***N/D***	***N/D***

**N/D: Not Detected*

Table 5.5: *Depth estimation using peak slope time for sample SP3*

		Curved SP3			
Def. No	***Nominal depth in x10^{-1}mm***	***Calculated Peak slope***	***Calculated peak slope time in s***	***Calculated depth in x10^{-1}mm***	***Error (%)***
A1	2	12.895	*0.0509*	**2.40**	***20***
A2	2	15.63	*0.0509*	**2.40**	***20***
A3	2	11.62	*0.0509*	**2.40**	***20***
A4	2	8.90	*0.0509*	**2.40**	***20***
A5	2	6.12	*0.0509*	**2.40**	***20***
B5	4	0.98	*0.2547*	**5.38**	***34.5***
B4	4	1.35	*0.2292*	**5.10**	***27.6***
B3	4	0.98	*0.2292*	**5.10**	***27.6***
B2	4	0.83	*0.2292*	**5.10**	***27.6***
B1	4	0.38	*0.2038*	**4.81**	***20.2***
C5	6	0.21	*0.5605*	**7.98**	***33.1***
C4	6	0.23	*0.5095*	**7.61**	***26.8***
C3	6	0.27	*0.3566*	**6.36**	***6***
C2	6	0.12	*0.4585*	**7.22**	***20.4***
C1	6	0.03	*0.5095*	**7.61**	***26.8***
D5	8	0.08	*0.9426*	**10.35**	***29.4***
D4	8	0.06	*0.8917*	**10.07**	***25.8***
D3	8	0.03	*0.9681*	**10.49**	***31.1***
D2	8	0.05	*0.9171*	**10.21**	***27.6***
D1	8	*N/D*	*N/D*	***N/D***	***N/D***
E5	10	0.06	*0.9936*	**10.63**	***6.3***
E4	10	0.03	*1.0445*	**10.90**	***9***
E3	10	0.03	*0.9936*	**10.63**	***6.3***
E2	10	*N/D*	*N/D*	***N/D***	***N/D***
E1	10	*N/D*	*N/D*	***N/D***	***N/D***

**N/D: Not Detected*

5.6.2 Determination of the blind frequency

The second depth estimation procedure was performed by means of quantitative pulsed phase thermography, investigating the accuracy produced on depth information retrieval from the analysis of the phase data, the phase contrast calculations and the determination of the blind frequency f_b. The blind frequency is the frequency at which the phase contrast function crosses the x-axis from negative to positive values (or a threshold level), for the first time with reducing frequency and continues having an increasing slope. As presented above, when working with temperature data, the selection of the sound area can have an impact on the thermal contrast calculations and this impact can be additionally enhanced in the case of uneven heating. However, from the qualitative interpretation of phase images, it was observed that the frequency domain analysis greatly increased the visual appearance of these results (enhanced uniformity of the background variations), since phase delay variations are less affected by the above problem. Based on the aforesaid, the first depth estimation method in the frequency domain was performed by measuring the correspondent phase contrasts between the defective areas and a region acting as the sound area selected randomly from the background (top left corner of the CFRP surface). Additionally, this procedure was repeated by calculating the average phase intensity from all the pixels on the surface (as the overall surface occupied by the defects was much smaller than the field of view).

For the purposes of this study, similarly to the temporal analysis, the phase contrasts profiles were plotted as a function of frequency for all the detected inserts in each panel, aiming to define the characteristic frequency point when the phase contrast diverged zero. Additionally, a comparison of sound area selection impact is performed through the two different procedures used and described above. Nevertheless before continue with the actual depth characterisation procedure, the phase contrast profiles obtained from the study of the three CFRPs are discussed, investigating the influence of depth and size on the produced contrast and the blind frequency determination. As in the case of the thermal data, initially the phase contrasts measured on the trapezoid sample SP2 are discussed in detail and some indicative results are presented from the planar and curved samples analyses.

5.6.2.1 Frequency domain analysis of SP2 specimen

In the following plots, the phase contrast profiles as a function of the modulation frequency are presented for all the detected internal inserts on the trapezoid sample. Figure 5.25 illustrates the phase contrasts produced by the shallowest insertions series (series A), either selecting a random sound area from the background (left column plots) or by using the entire surface as a sound area (right column plots). Similarly to the thermal contrast slope function, phase contrasts were plotted only at the region of interest (frequency region where the defect was visible), expunging the frequency spectrum in which only noise variations were appeared. As can be seen from the 1D phase contrast profiles similarly to the thermal data, in general larger defects produced a greater phase contrast. However, a deviation can be seen between the phase contrast intensities measured for defects No.3 and No. 4 (located at the

centre of the panel) and that of defect No.5 (located at the lower edge of the panel). Given that the information acquired from PPT by its frequency components are deriving from the temporal variations of the surface temperature, a change in the time domain will produce an effect on the frequency spectrum. Thus, the phase results produced for series A defects can be related to the variations detected on the correspondent temporal counterparts, which were further influenced from the greater amount of heat deposited on the centre of the panel. Nevertheless, for depth calculations the parameter of prime interest is the blind frequency, which as can be seen from the correspondent plots, it is approximately the same regardless the size of the insertion inspected. The comparison of the two procedures used for the determination of the blind frequency, is revealing that an enhanced similarity was produced regarding the phase contrast evolutions either working with the random sound area or the overall surface, thus its selection has a low impact on the determination of the blind frequency on Series A defects. However, the interesting point observed by this comparison is the fact that less noise content can be observed in the latter case, which is important when the depth of a shallow defect has to be estimated.

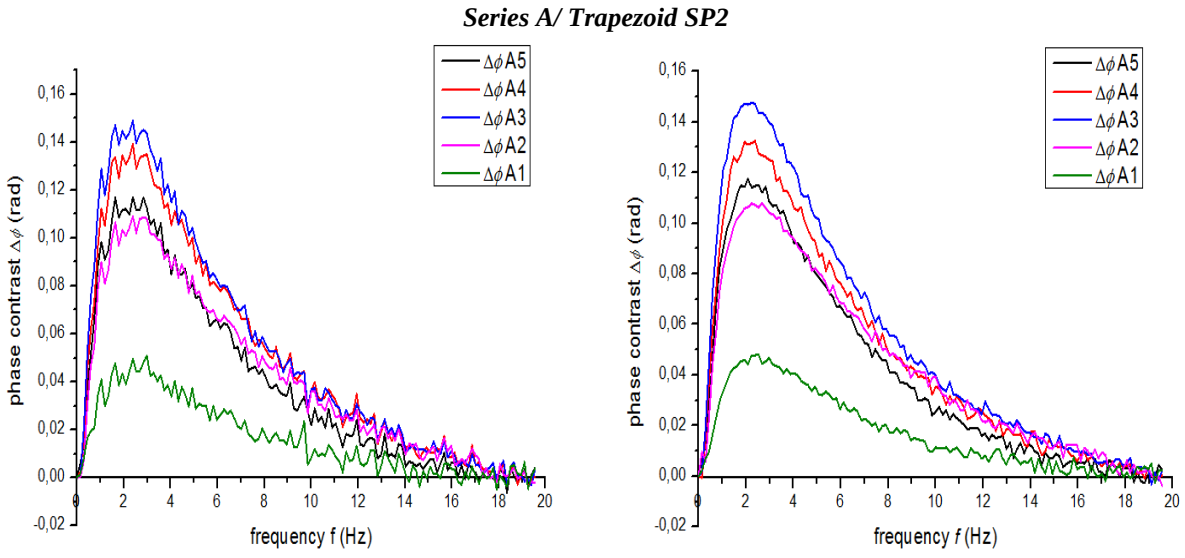

Fig. 5.25: *Phase contrast profiles of the series A insertions (0.2 mm) on specimen SP2 after (a) selecting the left top corner and (b) the whole surface as a sound area.*

However, as the depth of the detected features was increased, the phase contrast was affected by the detected feature's size, while the heating process had a negligible impact on the acquired results. More specifically, as can be seen from Figure 5.26, as larger was the size of the detected insertion on series B, the greater was the phase contrast produced regardless the selection of the sound area. However, the size of the insertions had an impact only to the produced contrast as all defects at this depth are visible in approximately the same frequency range (from the minimum available frequency to the blind frequency). A comparison with the results acquired in the previous case, is indicating that for deeper insertions a smaller frequency range is useful in order to acquire the information needed, but despite the shorter frequency range data in this case is more disperse, and this dispersion is enabling a more

accurate blind frequency determination. On the other hand, shallow defects (i.e. series A defects) form a compact phase contrast curve, and a wider frequency range of visibility but this is accompanied with increased noise content. The noise reduction observed in the previous inspection through the selection of the whole surface as a sound area can be also seen in the respective plots of series B defects inspection, as the right side plot of Figure 5.26 is much more free of noise with respect to left side plot.

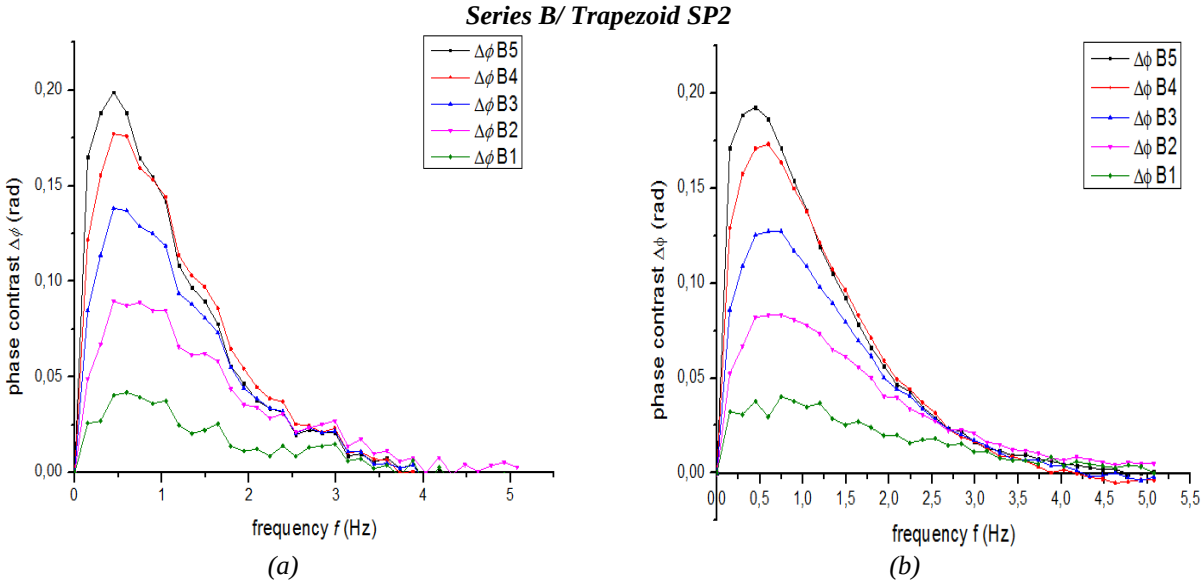

Fig. 5.26: *Phase contrast profiles of the series B insertions (0.4 mm) for specimen SP2 after (a) selecting the left top area and (b) the whole surface as a sound area.*

The above presented results for series B insertions were further confirmed from the plot results of the deeper defects of this panel, illustrated in Figure 5.27. As can be seen from the correspondent plots as greater is the defect depth as shorter is the frequency range in which the defects are obvious. For instance, Teflon insertions of series C have a frequency range of visibility from the minimum available frequency (0.149Hz) to approximately 1 Hz, while for the deeper defects (series E) the corresponding frequency range is between 0.149Hz to approximately 0.5 Hz. However, as shorter is the detection frequency range a clearer determination of the blind frequency can be done and less noise contents are presented in these cases. The plot results presented in Figure 5.27 are further indicating the impact of feature's lateral dimensions on the produced contrast, as smaller inserts regardless their location produced a weaker phase contrast with respect to the larger ones.

The reasons for this behaviour can be devised by considering the frequency spectrum of both the heat pulse excitation and the thermal response at the surface. A heat pulse of short duration generates periodic thermal waves at different frequencies. Each one of these thermal waves arrives to the specimen surface, travel through the material and is reflected back to the surface when a defect is presented. High frequency waves are able to travel fast but they are strongly damped, subsequently they can only reach shallow defects, while waves at low frequencies are slower but are able to reach deeper features. On the other hand, through the Fourier transform, the thermal response of the surface can be decomposed as well into a set of sinusoidal waves at different frequencies. These waves possess a

unique property named sinusoidal fidelity, which means that the magnitude of the thermal input will affect the phase of the response, but not its shape and frequency. As a result, defects at the same depth but different sizes will all be reached by thermal waves at specific frequencies, and even though larger defects will show greater phase contrast than smaller defects, these differences will be reflected only in the phase of the response.

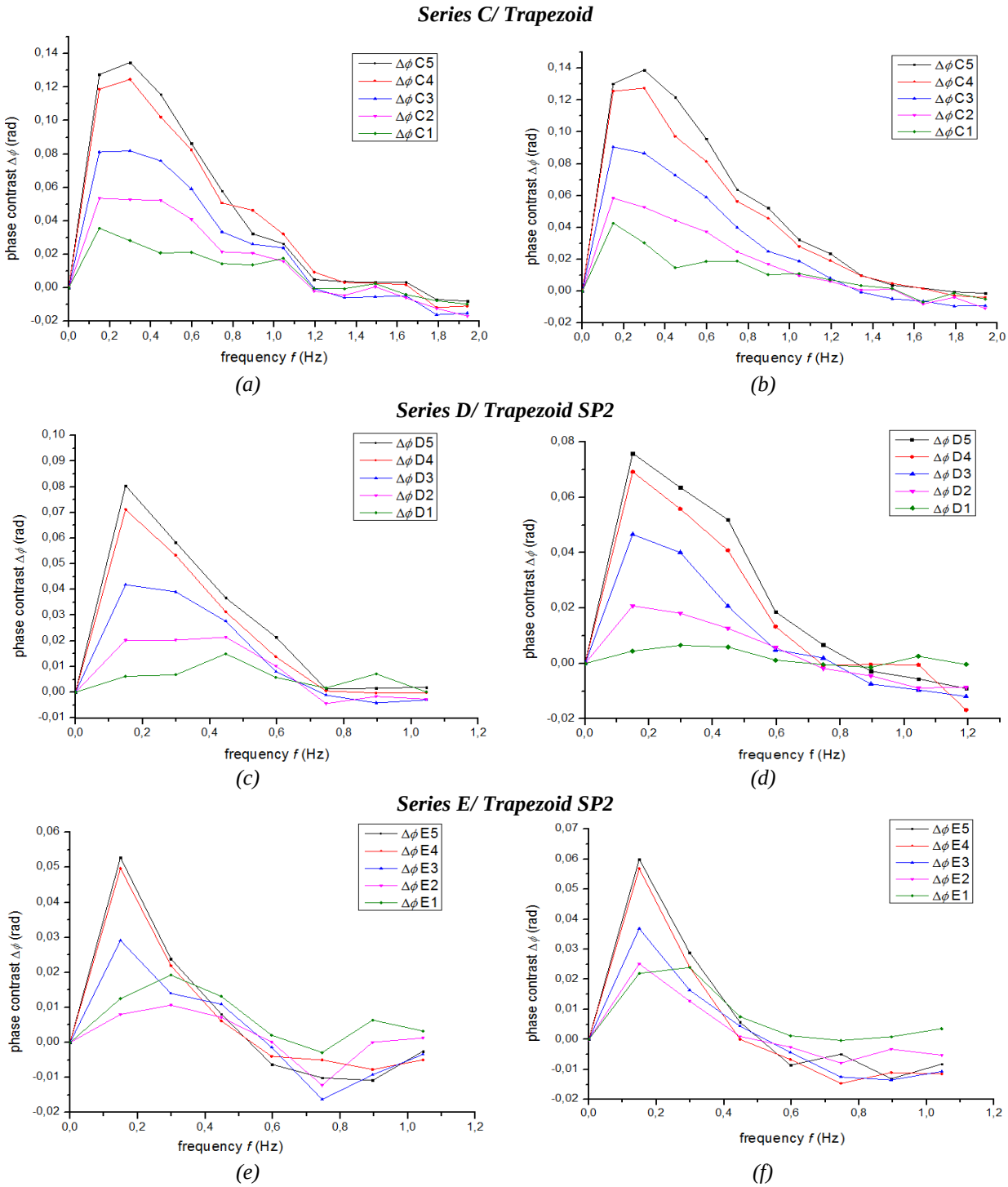

Fig. 5.27: *Phase contrast profiles of specimen SP2 for (a), (b) the defects of series C (0.6mm), (c), (d) the defects of series D (0.8mm) and (e), (f) the defects of series E (1 mm). The left side plots correspond to the phase contrasts from the top left sound area and the right plots correspond to the phase contrasts selecting the average phase intensity.*

5.6.2.2 Frequency domain analysis of SP1 and SP3 specimens

The phase data derived from the frequency domain analysis of the planar SP1 and curved SP3 inspections provided similar results as in the case of the trapezoid sample. Figures 5.28 and 5.29 are illustrating the respective phase contrast profiles as a frequency function acquired from the phase effects of the detected series A and C features. As can be seen from the correspondent plots, the phase contrast profiles for series A defects did not provide results regarding the impact of defect size on the phase, as insertions located to the centre of the panels produced a stronger phase contrast with respect to these located at the edges, indicating as well the above discussed effect of heat deposition on the surface. Contrary this condition was changed for the deeper probing, as series C plots present.

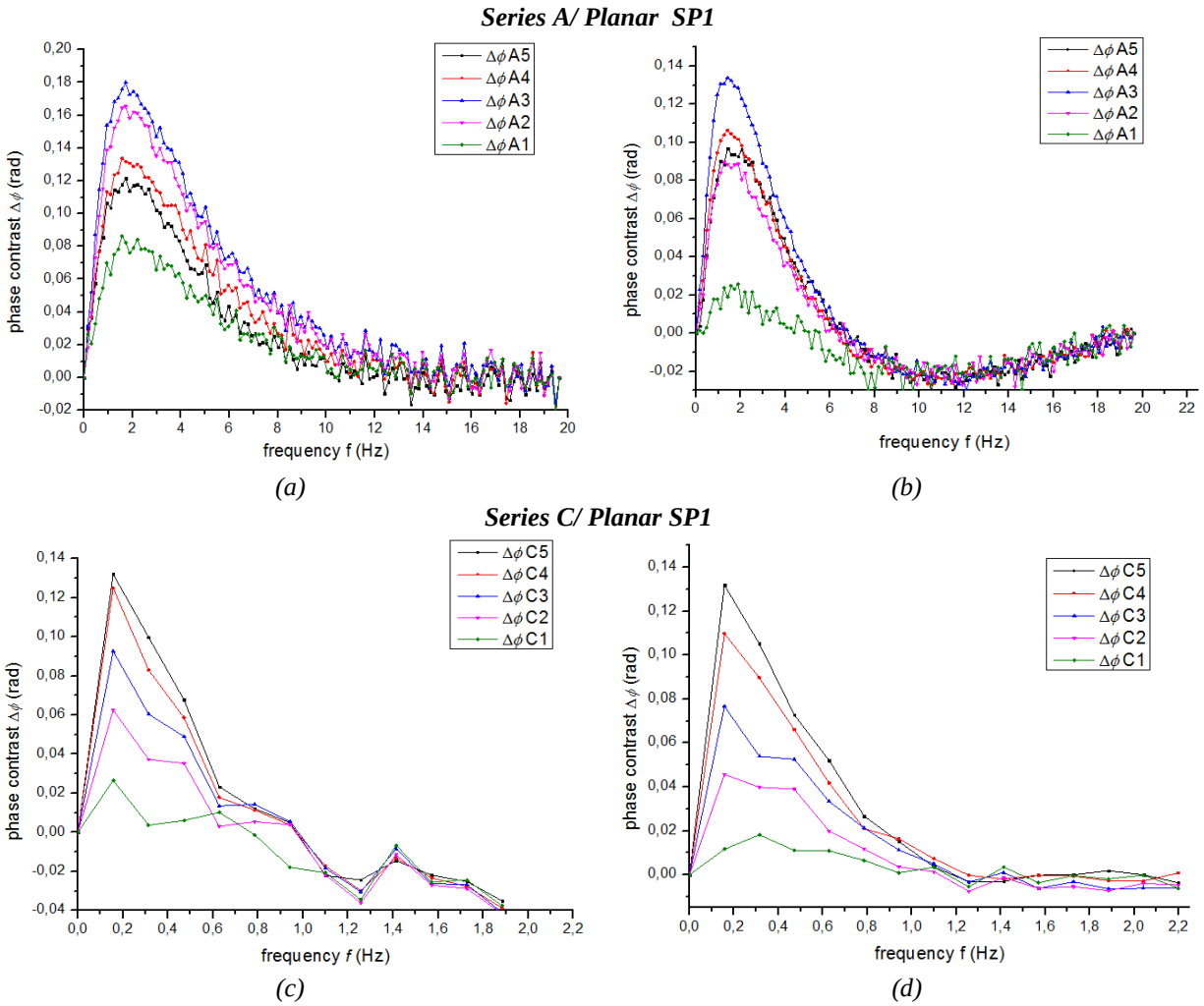

Fig. 5.27: *Phase contrast profiles of specimen SP1 for (a), (b) the defects of series A (0.2mm), (c), (d) the defects of series C (0.6mm). The left side plots correspond to the phase contrasts from the top left sound area and the right side plots correspond to the phase contrasts selecting the entire surface as a sound area.*

Additionally, some observations were also retrieved regarding the detection of the blind frequency. More specifically, while the trapezoid inspection provided a similarity on the acquired results, this was not observed on the planar sample. The two plots acquired from the planar specimen inspection showed that divergences were produced regarding the determination of the blind frequency from the two different analysis procedures. In particular, when using a random sound area, the phase contrast

deviation from zero is determined at approximately a frequency value of 15 Hz, while the respective value when using the entire surface as a sound area was measured to be at approximately 7 Hz.

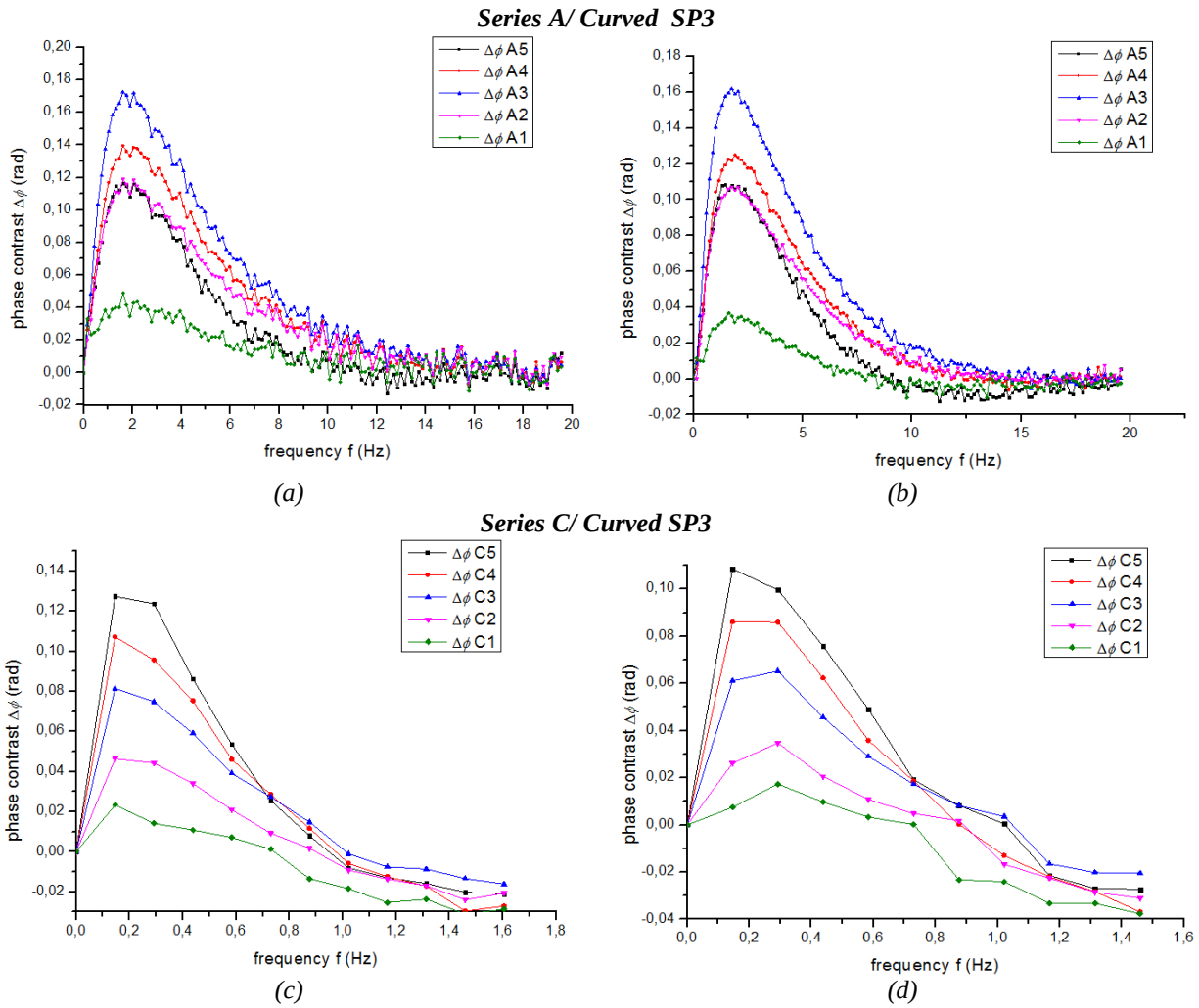

Fig. 5.28: *Phase contrast profiles of specimen SP3 for (a), (b) the defects of series A (0.2mm) and (c), (d) the defects of series C (0.6mm). The left side plots correspond to the phase contrasts from the right lower area sound area and the right plots correspond to the phase contrasts selecting the average phase intensity as a sound area.*

5.6.2.3 Depth estimation through the blind frequency

From the phase contrast measurements and the determination of the blind frequency, the depths of all the detected Teflon insertions into the three CFRP panels were quantitatively estimated. Tables 5.6 to 5.8 summarise the experimental values of the blind frequencies, the measured diffusion lengths and the calculated depths as the product of the diffusion length and the correlation factor C=1.82. In general, frequency domain analysis and phase data manipulation provided an efficient estimation of the inserts depth, regardless their location and size. Additionally, the similarity of results in terms of error production for inserts having the same depth, are indicating that the shape of the inspected surface and the potential non uniform heat deposition on the inspected surface have a negligible impact on the quantitative information retrieval. Based on the aforesaid, no obvious correlation can be done between the defect size and the estimated depth, despite the fact that in some instances the smaller defects produced the larger error with respect to the rest defects on the same series (i.e. defects C1 and E2 on

the planar sample and defect C1 on the curved sample). Contrary, as regards the quantitative information retrieval and their correlation with the investigated depth, it can be seen that generally defects nearer to the surface produced a larger divergence from the actual depth contrary to the deeper ones where the error production was lower. This can be attributed to the increase noise levels produced as higher was the frequency range of detection, obstructing the accurate detection of the blind frequency.

The comparison of the two different procedures used for the depth measurements with the phase, referring to the two different sound areas selection, indicates that the selection of the entire surface as a sound area either provided similar results with these produced from the random area selection or it was reducing the error production as in the cases of the series C defects on the planar sample and series B defects on the curved one. Thus the use of the overall surface as a sound area primary eliminates the need for a sound area/point selection and secondly may reduced the potential uncertainty produced of a random selection from the background. The only deviation from the above observation was presented on the depth determination of the shallowest defect series on the planar sample, where while relatively accurate results were produced in the former case, the selection of the entire surface as a reference introduced increased errors on the acquired results (this was also observed from the plots as different blind frequencies detected in each case). The above observation can be attributed to the non uniform heating impact, influencing as well the phase contrast evolution when selecting the average surface phase for the respective calculations.

Some deviations were further detected on depth determinations for defects of the same depth. For instance, by calculating the series E defects depth, by setting the whole surface as a reference, this was measured to be 0.10006 mm for E1, E2, E4 and E5 defects and 0.871 mm for defect E3. A more careful study of the measured blind frequencies is indicating that the phase contrast deviation from zero was detected very nearly for all the defects. In particular, it was detected at 0.437 Hz in the former case and at 0.583 Hz in the latter case. Taking into consideration that the truncated frequency interval Δf is 0.146 Hz, this means that the error produced in the second case 12.9% (0.6% in the first case) can be possibly attributed as well to the truncated parameters selected to process the acquired sequences, as the frequency is inversely related to the time interval. However, in frequency domain analysis, deeper probing estimations seem to be more affected by the truncated parameters due to the lower frequency range in which the defects are visible. Finally, as in the case of temporal analysis, source of extra error could be the deviation from the actual thermal properties of the inspected panels.

Table 5.6: *Depth estimation using the blind frequency for sample SP1*

Planar SP1									
		Sound Area top left corner				***Sound Area overall surface***			
Def. No	***Nominal depth in x 10^{-1}mm***	***Blind frequency f_b [Hz]***	***Measured diffusion length μ in x 10^{-1}mm***	***Measured depth z in x 10^{-1}mm***	***Error (%)***	***Blind frequency f_b [Hz]***	***Measured diffusion length μ in x 10^{-1}mm***	***Measured depth z in x 10^{-1}mm***	***Error (%)***
A5	2	10.048	*1.15*	**2.09**	***4.5***	6.594	*1.42*	**2.59**	***29.5***
A4	2	12.246	*1.04*	**1.90**	***-5***	6.280	*1.45*	**2.65**	***32.5***
A3	2	13.188	*1.005*	**1.83**	***-8.5***	6.751	*1.40*	**2.56**	***28***
A2	2	13.188	*1.005*	**1.83**	***-8.5***	6.280	*1.45*	**2.65**	***32.5***
A1	2	13.345	*1.00*	**1.82**	***-9***	5.024	*1.62*	**2.96**	***48***
B5	4	3.297	*2.01*	**3.66**	***-8.5***	2.198	*2.46*	**4.48**	***12***
B4	4	3.297	*2.01*	**3.66**	***-8.5***	2.198	*2.46*	**4.48**	***12***
B3	4	2.983	*2.11*	**3.85**	***-3.75***	2.041	*2.56*	**4.66**	***16.5***
B2	4	3.297	*2.01*	**3.66**	***-8.5***	2.041	*2.56*	**4.66**	***16.5***
B1	4	3.454	*1.98*	**3.58**	***-10.5***	1.727	*3.07*	**5.06**	***26.5***
C5	6	0.942	*3.76*	**6.85**	***14.2***	1.099	*3.48*	**6.34**	***5.7***
C4	6	0.942	*3.76*	**6.85**	***14.2***	1.099	*3.48*	**6.34**	***5.7***
C3	6	0.942	*3.76*	**6.85**	***14.2***	1.099	*3.48*	**6.34**	***5.7***
C2	6	0.942	*3.76*	**6.85**	***14.2***	1.099	*3.48*	**6.34**	***5.7***
C1	6	0.785	*4.13*	**7.51**	***25.1***	1.099	*3.48*	**6.34**	***5.7***
D5	8	0.628	*4.61*	**8.39**	***4.9***	0.785	*4.13*	**7.51**	***-6.1***
D4	8	0.628	*4.61*	**8.39**	***4.9***	0.785	*4.13*	**7.51**	***-6.1***
D3	8	0.628	*4.61*	**8.39**	***4.9***	0.785	*4.13*	**7.51**	***-6.1***
D2	8	0.471	*5.32*	**9.69**	***21.1***	0.785	*4.13*	**7.51**	***-6.1***
D1	8	0.471	*5.32*	**9.69**	***21.1***	0.785	*4.13*	**7.51**	***-6.1***
E5	10	0.628	*4.61*	**8.39**	***-16.1***	0.471	*5.32*	**9.69**	***-3.1***
E4	10	0.471	*5.32*	**9.69**	***-3.1***	0.471	*5.32*	**9.69**	***-3.1***
E3	10	0.471	*5.32*	**9.69**	***-3.1***	0.471	*5.32*	**9.69**	***-3.1***
E2	10	0.628	*4.61*	**8.39**	***-16.1***	0.628	*4.61*	**8.39**	***-16.1***
E1	10	N/D	*N/D*	**N/D**	***N/D***	N/D	*N/D*	**N/D**	***N/D***

Table 5.7: *Depth estimation using the blind frequency for sample SP2*

Trapezoid SP2									
		Sound Area top left corner				***Sound Area all pixels***			
Def. No	***Nominal depth in x 10^{-1} mm***	***Blind frequency f_b [Hz]***	***Measured diffusion length μ in x 10^{-1}mm***	***Measured depth z in x 10^{-1}mm***	***Error (%)***	***Blind frequency f_b [Hz]***	***Measured diffusion length μ in x 10^{-1}mm***	***Measured depth z in x 10^{-1}mm***	***Error (%)***
A5	2	14.476	*0.96*	**1.74**	***-13***	15.222	*0.93*	**1.70**	***-15***
A4	2	15.371	*0.93*	**1.69**	***-15.5***	15.222	*0.93*	**1.70**	***-15***
A3	2	16.267	*0.91*	**1.65**	***-17.5***	15.222	*0.93*	**1.70**	***-15***
A2	2	15.222	*0.93*	**1.70**	***-15***	15.222	*0.93*	**1.70**	***-15***
A1	2	15.073	*0.94*	**1.71**	***-14.5***	14.028	*0.97*	**1.77**	***-11.5***
B5	4	3.730	*1.89*	**3.44**	***-14***	4.029	*1.82*	**3.31**	***-17.2***
B4	4	3.880	*1.85*	**3.37**	***-15.7***	4.029	*1.82*	**3.31**	***-17.2***
B3	4	3.880	*1.85*	**3.37**	***-15.7***	4.178	*1.78*	**3.25**	***-18.7***
B2	4	3.581	*1.93*	**3.51**	***-12.2***	3.581	*1.93*	**3.51**	***-12.2***
B1	4	3.880	*1.85*	**3.37**	***-12.2***	3.581	*1.93*	**3.51**	***-12.2***
C5	6	1.492	*2.99*	**5.44**	***-7.3***	1.492	*2.99*	**5.44**	***-7.3***
C4	6	1.641	*2.85*	**5.19**	***-13.5***	1.492	*2.99*	**5.44**	***-7.3***
C3	6	1.044	*3.57*	**6.51**	***8.5***	1.193	*3.35*	**6.09**	***1.5***
C2	6	1.193	*3.35*	**6.09**	***1.5***	1.492	*2.99*	**5.44**	***-7.3***
C1	6	1.044	*3.57*	**6.51**	***8.5***	1.492	*2.99*	**5.44**	***-7.3***
D5	8	0.746	*4.23*	**7.70**	***-3.7***	0.746	*4.23*	**7.70**	***-3.7***
D4	8	0.596	*4.73*	**8.61**	***7.6***	0.596	*4.73*	**8.61**	***7.6***
D3	8	0.596	*4.73*	**8.61**	***7.6***	0.746	*4.23*	**7.70**	***-3.7***
D2	8	0.596	*4.73*	**8.61**	***7.6***	0.596	*4.73*	**8.61**	***7.6***
D1	8	0.596	*4.73*	**8.61**	***7.6***	0.596	*4.73*	**8.61**	***7.6***
E5	10	0.447	*5.46*	**9.94**	***-0.6***	0.447	*5.46*	**9.94**	***-0.6***
E4	10	0.447	*5.46*	**9.94**	***-0.6***	0.447	*5.46*	**9.94**	***-0.6***
E3	10	0.447	*5.46*	**9.94**	***-0.6***	0.447	*5.46*	**9.94**	***-0.6***
E2	10	0.447	*5.46*	**9.94**	***-0.6***	0.447	*5.46*	**9.94**	***-0.6***
E1	10	0.596	*4.73*	**8.61**	***16.1***	0.596	*4.73*	**8.61**	***16.1***

Table 5.8: *Depth estimation using the blind frequency for sample SP3*

Curved SP3									
		Sound Area top left corner				***Sound Area all pixels***			
Def. No	***Nominal depth in x 10^{-1}mm***	***Blind frequency f_b [Hz]***	***Measured diffusion length μ in x 10^{-1}mm***	***Measured depth z in x 10^{-1}mm***	***Error (%)***	***Blind frequency f_b [Hz]***	***Measured diffusion length μ in x 10^{-1}mm***	***Measured depth z in x 10^{-1}mm***	***Error (%)***
A5	2	9.192	*1.20*	**2.19**	***9.5***	8.754	*1.23*	**2.24**	***12***
A4	2	9.338	*1.19*	**2.17**	***8.5***	11.089	*1.09*	**1.99**	***-0.5***
A3	2	9.192	*1.20*	**2.19**	***9.5***	12.986	*1.01*	**1.84**	***-8***
A2	2	8.316	*1.26*	**2.30**	***15***	10.797	*1.10*	**2.02**	***1***
A1	2	8.462	*1.25*	**2.28**	***14***	8.025	*1.28*	**2.34**	***17***
B5	4	2.042	*2.55*	**4.65**	***16.25***	2.626	*2.25*	**4.10**	***2.5***
B4	4	2.334	*2.39*	**4.35**	***8.75***	2.772	*2.19*	**3.99**	***-0.25***
B3	4	2.480	*2.32*	**4.22**	***5.5***	2.918	*2.14*	**3.89**	***-2.7***
B2	4	2.188	*2.47*	**4.49**	***12.25***	2.772	*2.19*	**3.99**	***-0.25***
B1	4	2.042	*2.55*	**4.65**	***16.25***	2.772	*2.19*	**3.99**	***-0.25***
C5	6	0.875	*3.91*	**7.11**	***18.5***	1.021	*3.61*	**6.58**	***9.66***
C4	6	0.875	*3.91*	**7.11**	***18.5***	0.875	*3.91*	**7.11**	***18.5***
C3	6	1.021	*3.61*	**6.58**	***-7***	1.021	*3.61*	**6.58**	***9.66***
C2	6	0.875	*3.91*	**7.11**	***18.5***	0.875	3.91	**7.11**	***18.5***
C1	6	0.729	*4.28*	**7.79**	***29.8***	0.729	*4.28*	**7.79**	***29.8***
D5	8	0.583	*4.78*	**8.71**	***8.8***	0.583	*4.78*	**8.71**	***8.8***
D4	8	0.729	*4.28*	**7.79**	***-2.6***	0.729	*4.28*	**7.79**	***-2.6***
D3	8	0.729	*4.28*	**7.79**	***-2.6***	0.583	*4.78*	**8.71**	***8.8***
D2	8	0.583	*4.78*	**8.71**	***8.8***	0.583	*4.78*	**8.71**	***8.8***
D1	8	0.583	*4.78*	**8.71**	***8.8***	0.583	*4.78*	**8.71**	***8.8***
E5	10	0.437	*5.53*	**10.06**	***0.6***	0.437	*5.53*	**10.06**	***0.6***
E4	10	0.583	*4.78*	**8.71**	***-12.9***	0.437	*5.53*	**10.06**	***0.6***
E3	10	0.583	*4.78*	**8.71**	***-12.9***	0.583	*4.78*	**8.71**	***-12.9***
E2	10	0.437	*5.53*	**10.06**	***0.6***	0.437	*5.53*	**10.06**	***0.6***
E1	10	N/D	*N/D*	**N/D**	***N/D***	*N/D*	*N/D*	***N/D***	***N/D***

Beside the above discussed circumstances that may introduce error on the acquired results, another parameter that may affect the depth quantification could be the correlation factor *C*. As presented in Chapter 4, when working the with phase depth quantifications require the determination of the correlation factor C which is ranging from 1.5 to 2, with the value of 1.82 to be typically adapted. However, when investigating anisotropic materials such as the panels used in this study, the above value may be different, creating uncertainties on the acquired depth results.

Thus, the selection of the correlation factor was assessed in a graphical manner, plotting the nominal depth *z* of the insertions as a function of the measured diffusion length μ and retrieving the slope of the produced linear function after linearly fitting these experimental data. Figure 5.28 presents the correlation results acquired from both the three samples either selecting a random sound area from the background (left column plots) or selecting the entire surface as a sound area (right column plots). As stated above, the experimental data was fitted by a least square linear fitting function resulting to high correlation coefficients (from 0.95 to 0.98). Regardless the procedure used to estimate the depth, the constant *C* was estimated to be from 1.67 to 1.85 (between the range discussed above and very close to the value used in this study), while the only divergence observed was in the case of the planar inspection when working with the entire surface as a reference, as the slope of 2.19 was acquired in this case. A more detailed study of the depth results produced from the respective inspection is indicating that large errors were also produced from this quantitative analysis mainly for the two shallower defect series A and B. Contrary the respective results on these series, using the random sound area, provided measured depths with reduced errors.

In general, from the graphical assessment of the correlation factor, it can be seen that the value used in this study had a low impact on the acquired results and seems to be unaffected from the sample shape as in general slight differences on the slope and the offset were measured from the different inspections and analyses. However if these graphically retrieved slopes were used for depth quantifications, the results presented on the tables above would provide a greater accuracy than these derived using the value of 1.82.

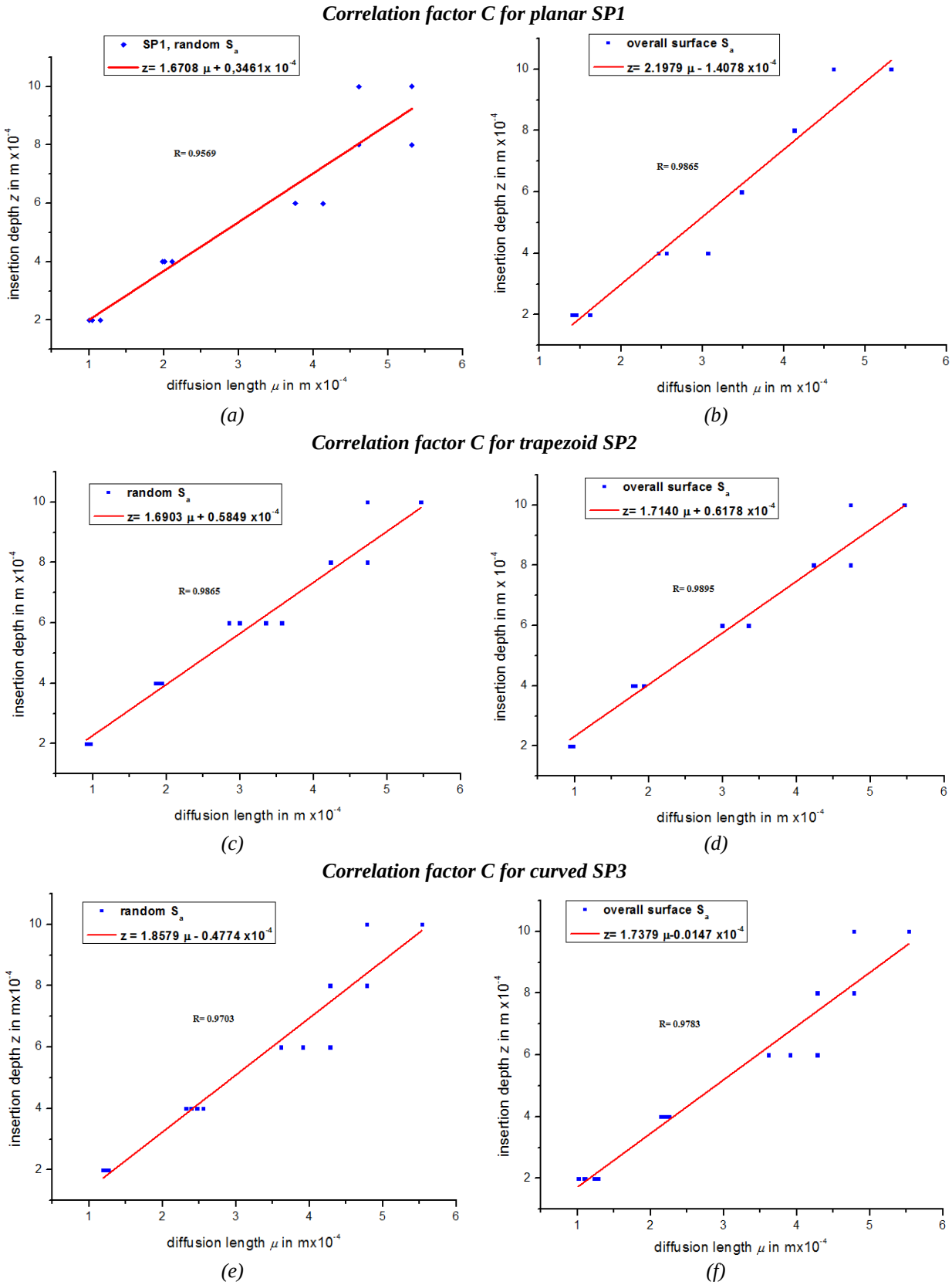

Fig. 5.28: *Correlation results for all three specimens. The left column plots correspond to the procedure used selecting a random sound area from the background and the right column plots correspond to the procedure used selecting the entire surface as a sound area.*

5.6.3 Comparison of temporal and frequency domain analyses for depth information retrieval

In the previous subsections, a quantitative analysis of CFRP composites was presented, based on two representative depth prediction methods. More specifically, depth estimation procedures were based on the determination of thermal contrast peak slope time t_{peak} and on the determination of the blind frequency f_b, while the second procedure was performed by considering two different sound areas for its identification. In Figures 5.29 to 5.31 show a comparison of the measured depths from each individual method in terms of prediction errors. These 3D representation plots include all the detected defects and the location of each error bar corresponds to the location of a specific insertion with respect to the defect description figure included on the top right side of each figure. Additionally the scale of the error axis was fixed to be the same in all the plots regardless the depth estimation procedure used or the investigated sample, for relative comparisons.

As can be seen from the aforesaid figures, generally temporal analysis for depth determination produced larger prediction errors with respect to the correspondent method on the frequency domain. This can be observed in all the results regardless the sample inspected. For instance, while peak slope time method provided large divergences on depth prediction of series B and C defects; this was importantly reduced on the results acquired from the two respective procedures on the frequency domain. Contrary, for some defects mainly in the deeper series where relatively large errors were produced from the phase results, these were not able to be detected and quantified in the temporal domain. Additionally as stated above, the comparison of quantification results using phase data showed that the selection of the entire surface as sound area either produced similar results with those provided from the random sound area, while in some instances this method produced results closer to the actual depth. The only deviation observed from the above described behaviour was in the case of Series A defects on the planar inspection.

As regards, the error production and its correlation with the depth, it can be seen that the larger errors were produced mainly on series B and C when working with temperature data, while in phase data manipulation a considerable error was produced for defects located to the depth of 0.2 mm, then it was reduced (0.4 mm) and increased again for series C (0.6 mm). Contrary, very accurate results were produced for the deeper series D and E inspections. As stated above, the increased errors produced for series B and C on the temporal analysis can be attributed to the 3D conduction problem, which is not presented on the shallower defects series due to the early time detection on the shallowest series and its weak impact on the deeper series. Similarly deviations from the actual depth on frequency analysis can be attributed to the increased noise levels on the phase contrast plots when the defect is visible in a large frequency range. Additionally, the error incensement produced for series C defects can be attributed to the reduction of the frequency resolution by the truncation procedure used to analyse the data. Finally, a comparison of the produced results in terms of sample geometry impact is indicating that this has a little to negligible impact on depth estimations acquired both from the frequency and the time domain analyses, as similar results either good or bad were produced regardless the shape.

3D representations of produced error in planar surface inspection (SP1)

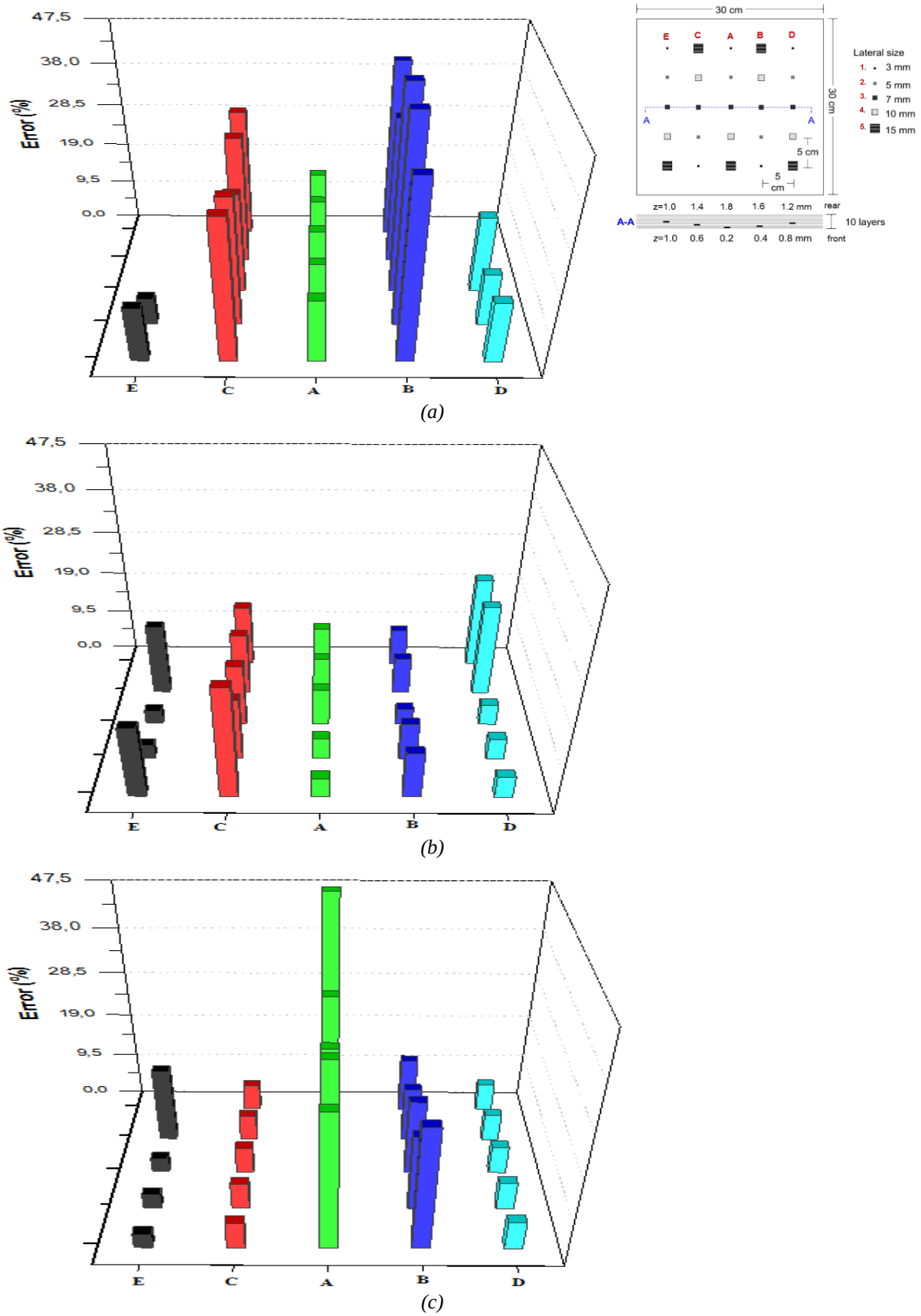

Fig. 5.29: *3D representation of insertions estimated depth in terms of error production for specimen SP1 through (a) peak slope time (b) blind frequency (random sound area) and (c) blind frequency (overall surface).*

3D representations of produced errors in trapezoid surface inspection (SP2)

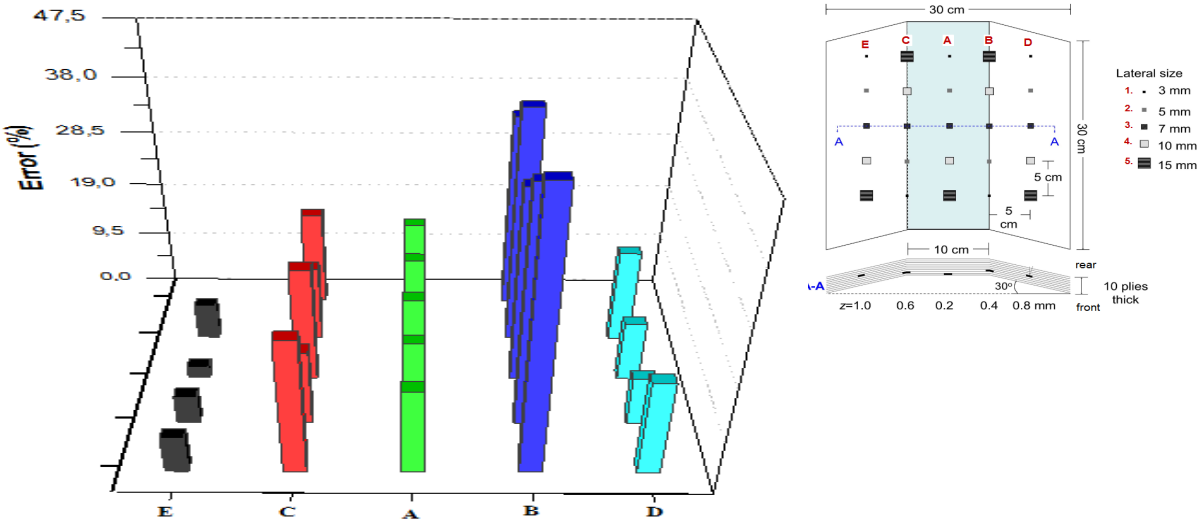

(a)

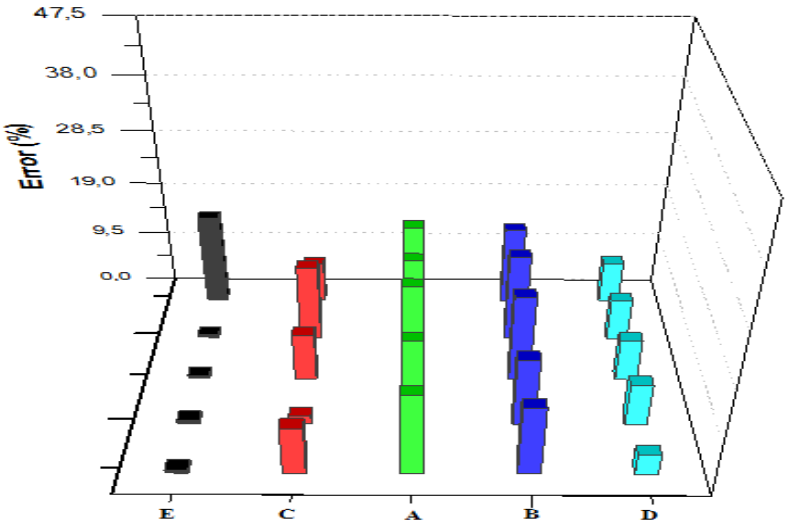

(b)

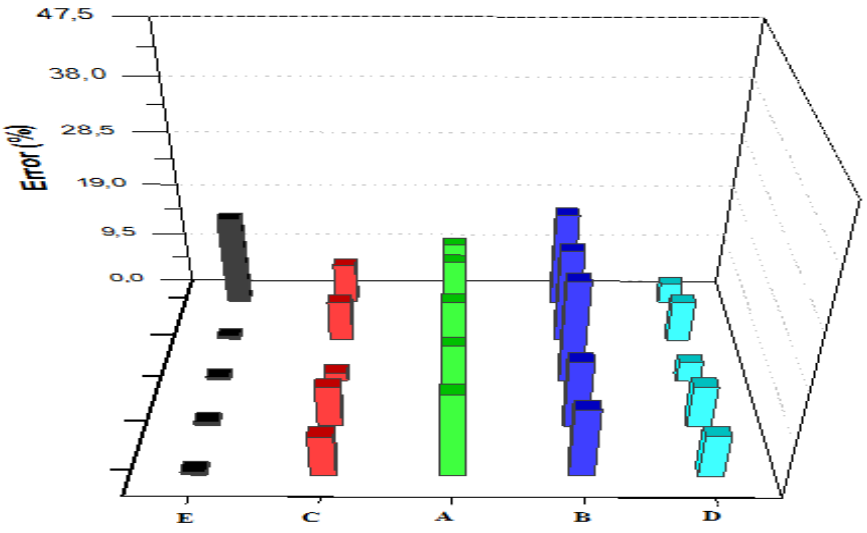

(c)

Fig. 5.30: *3D representation of insertions estimated depth in terms of error production for specimen SP2 through (a) peak slope time (b) blind frequency (random sound area) and (c) blind frequency (overall surface).*

3D representations of produced errors of curved surface inspection (SP3)

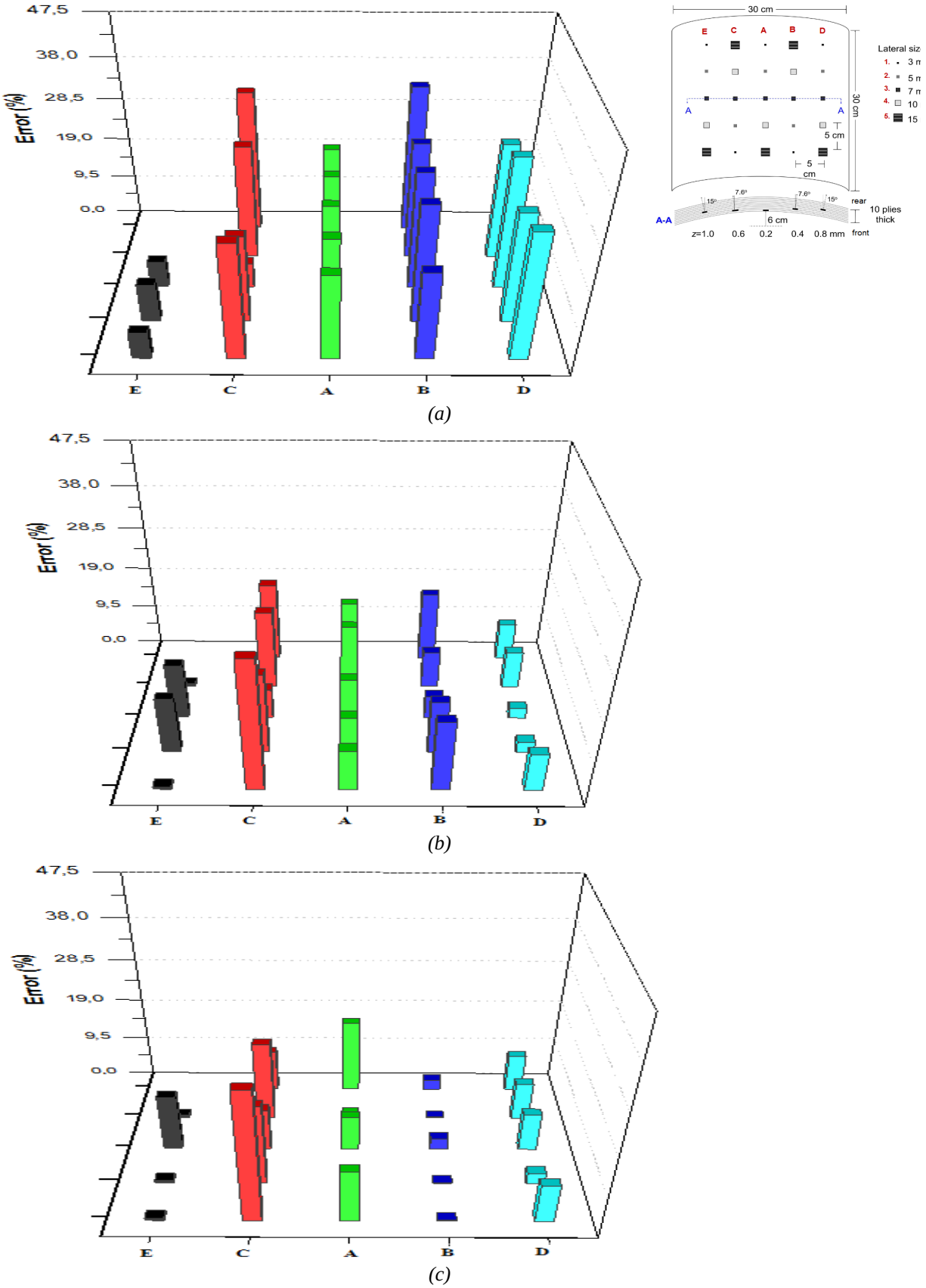

Fig. 5.31: *3D representation of insertions estimated depth in terms of error production for specimen SP3 through (a) peak slope time (b) blind frequency (random sound area) and (c) blind frequency (overall surface).*

5.7 Conclusions

In this study three different CFRP specimens with internal stimulated delaminations of various sizes and located to different depths were investigated by means of PT under laboratory conditions. From the acquired results, it can be concluded that the implementation of PT along with data manipulation through advanced signal processing algorithms can be a useful technique for NDT assessment, providing either enhanced qualitative information or quantitative estimations regarding the depth in which the feature of interest is detected [30,31].

Despite the fact that PT is a fast and easy to deploy technique, unprocessed results can be easily affected by a series of different problems. Furthermore, although the raw thermal images can contain the complete information of the test material and can be used to detect delaminations, the thermal effects of deeper features can be extremely small or undistinguishable, especially when anisotropic materials have to be studied. The qualitative assessment of the three CFRP panels showed that techniques such as TSR, PPT and PCT, can improve the visibility of the recorded pulsed thermographic signal and further enhance the thermal *"footprints"* mainly of deep and/or small defects. Additionally, by countering the problems affecting the raw temperature data, a greater amount of information can be retrieved with enhanced visual appearance and reliable quality. In other words, the algorithms used in this study were able to reduce the effects of uneven heating, which significantly increases the defect contrast and geometry representation providing as well de-noised data (i.e. planar specimen analysis). Nevertheless, SNR analysis showed that despite the enhanced visibility that these algorithms produced, they can be further applied properly in order to gain the best possible information retrieval according to the user's demands. More specifically, the 1st time derivative analysis and the PPT treatment of synthetic temperature data can provide better imaging results for shallow defects with respect to the other processing routines used in this study. Additionally, PCT analysis produced also promising results as from the respective EOF images it was possible to acquire the best possible information. However, despite the enhancement that these processing techniques can provide, their operation is based on a pixel-wise transformation and as can be understood the processed result is related to the initial thermal effects mapped on the thermal data. This can be seen from the enhanced defect detectability produced on the trapezoid sample, which also provide the best visibility from the raw thermographic images. Thus, the qualitative information retrieval can be affected from the heating process and the shape of the inspected surface, despite the fact that advanced signal processing techniques are remarkably reducing this impact.

Contrary, the quantitative assessment either working with the temperature or the phase showed that the shape of the inspected surface has a low to negligible impact on the acquired depth information. The low impact of specimen geometry is of great importance when non planar surfaces such as wings, fuselage and other aerospace components have to be quantitatively characterised. More specifically, despite the large errors produced from the correlation of peak slope time with the depth, a similar

behaviour was observed in all the three samples regardless their surface geometry. Additionally, the enhanced accuracy produced from the blind frequency was also similarly observed on the three surfaces. The comparison of the two quantification methods showed that frequency domain analysis provided measured depth closer to their nominal value with respect to the these acquired, manipulating raw temperature data. In other words, phase is more likely to respond to differences related to the materials thermal properties, while thermal effects on thermal data may be affected from other factors as well. Additionally, the quantification in the frequency domain can be further improved considering the entire surface of the panel as the sound area when the defective zones occupy a small region with respect to the entire surface. Contrary, when working with peak slope time and especially when an uneven heating application is performed, quantification shall be performed selecting different sound areas for depths determinations which can be a time consumable procedure.

However, one of the main factors that shall be considered and is of prime importance when quantitative assessment has to be implemented is the selection of the experimental and truncated parameters used for the acquisition and analysis. In particular, time resolution has a great impact on the determination of the characteristic times used for depth estimations and this parameter can produce great errors when defects near the surface has to be quantitatively determined. Similarly, as frequency is inversely proportional to time, the temporal resolution has an impact on the frequency resolution as well. Contrary to temporal data analysis, a low frequency resolution can have an impact on the deeper defects as the frequency visibility range is lower for these features. The above described parameters either sampling or truncated resolution should be defined according to the inspected depth and the inspected material thermal properties. Fast phenomena require a high temporal resolution and a high sampling frequency and vice versa.

The above study of CFRP specimens showed that when implementing PT as an inspection technique, there is no analysis method of perfectly solving all situations, and thus an effort was made to expose the positive and negative points from the application of some advanced signal processing algorithms and quantitative data analysis methods. According to the user's demands, these signal processing algorithms can be properly applied, aiming to the best possible result. For instance, PPT allows quantitatively retrieve depth information from the inspected sample, but the processed data generally contains considerable amounts of noise especially for shallower probing (high frequencies). On the other hand, although no quantitative approach is available for PCT analysis, or quantitative analysis through TSR may produce large errors (as special care is required to ensure that the polynomial function actually fits the exact peak position of the second derivative peak), these two approaches provided enhanced visibility and detection.

5.8 References

[1] E.A. Birt (2000). *The applicability of X-radiography to the inspection of composites.* In Insight Journal, Vol. 42(3), pp. 335-339.

[2] M.Y.Y. Hung, Y.S. Chen, S. Pang, S.M. Shepard, Y. Hou, J.R. Lhota (2007). *Review and comparison of shearography and pulsed thermography for adhesive bond evaluation*. Journal of Optical Engineering, SPIE Publishing, Vol. 46(5), pp. 051007.1-16.

[3] N.P. Avdelidis, D.P. Almond, A. Dobbinson, B.C. Hawtin (2006). *Pulsed thermography: philosophy, qualitative and quantitative analysis on certain aircraft applications*. Journal of Insight, Vol. 48, pp. 286-289.

[4] D.K. Shu (2006). *Nondestructive testing using air-borne ultrasound.* In Ultrasonics, Vol. 44(1), pp. 1019-1024.

[5] A. Dobbinson, N.P. Avdelidis, D.P. Almond, B. Drinkwater (2003). *A comparison of acoustography, thermography and the ultrasonic wheel array for imaging impact damage in aerospace composites*. in Proc. of 42nd Conference of the British Institute of NDT, BINDT 2003, Bransford – United Kingdom, pp. 29-34.

[6] C. Souits (2005). *Fibre reinforced composites in aircraft construction.* Progress in Aerospace Science, Vol. 41, pp. 143-151.

[7] B. Harrys (1999). *Engineering composite materials.* Institute of Materials, London, UK.

[8] T. Richardson (1987). *Composites: A design Guide.* Industrial Press Inc, New York, USA.

[9] F.C. Campbell (2010). *Structural Composite materials.* ASM International, Ohio, USA.

[10] K.L. Reinfsnider (1990). *Damage and Damage Mechanics.* Elsevier Science Publishing, New York, USA.

[11] D. Hull, T.W. Clyne (1996). *An introduction to composite materials.* Cambridge University Press.

[12] A.T. Nettles (1994). *Basic Mechanics of laminated composites.* National Aeronautics and Space Administration, Marshall Space Flight Center, Alabama, USA.

[13] B.T. Astrom (1997). Manufacturing of polymer composites. 1st Edition, B.T. Astrom (Ed.), Chapman & Hall, London, UK.

[14] T.G. Gutowski (1997). *A brief introduction to composite materials and manufacturing techniques.* In T.G. Gutowski (Ed.): Advanced composites manufacturing. Wiley &Sons, New York, USA, pp. 5-41.

[15] B. Hawtin (2003). *Defect criticality in carbon fibre composites*. PhD Thesis, University of Bath, U.K.

[16] P. Cawley, R.D. Adams (1989). *Defect types and non-destructive testing techniques for composites and bonded joints.* Construction and Building Materials, Vol. 3(4), pp. 170-183.

[17] R. Ruzek, R. Lohonka, J. Jironc (2006). *Ultrasonic C-scan and shearography NDI techniques*

evaluation of impact defects identification. NDT&E International, Vol. 39(2), pp.132-142.

[18] M.J. Pavier, M.P. Clarke (1995). *Experimental techniques for the investigation of effects of impact damage in carbon- fibre composites.* Composites Science and Technology, Vol. 55(2), pp. 1237-1242.

[19] M.V. Hosur, C.L.R. Murrhy, T.S. Ramamurthy, A. Shet (1998). *Estimation of impact-induced damage in CFRP laminates through ultrasonic testing.* NDT&E International, Vol. 31(5), pp. 359-374.

[20] C. Meloa, C. Toscano (2012). *Nondestructive evaluation of carbon fibre reinforced polymers with ultrasonics and infrared thermography: An overview of historical steps and patents.* Recent Patents on Materials Science, Vol. 5(1), pp. 48-67.

[21] Y. Duan, P. Servais, M. Genest,C. Ibarra-Castanedo, X.P.V. Maldague (2012). *ThermoPoD: A releiabilty study on active infrared thermography for the inspection of composite materials.* J. of Mechanical Science and Technology, Vol. 26(7), pp. 1985-1991.

[22] C.Zoecke, A. Langmeier, W. Arnold (2010). *Size retrieval of defects in composite materials with lockin thermography.* Journal of Physics: Conference Series, IOP Publishing, Vol. 214, art. no. 012093.

[23] G. Riegert, A. Gleiter, H. Gerhand, G. Busse (2007). *Active thermography for defect detection in carbon fibre reinforced materials.* In D.O. Thomphon, D.E. Chimenti (eds.): Review of Progress in Quantitative Nondestructive Evaluation, AIP Conference Proceedings, Plenus Press, New York, Vol. 894, pp. 1044-1051

[24] S.R. Baughman (1998). *Applications of thermal NDT on advanced composite in aerospace structures.* In J.R. Snell, R.N. Wurzbach (Eds.): Proc. SPIE- The International Society for Optical Engineering, Thermosense XX, Orlando, Florida, Vol. 3361, pp. 311-319.

[25] R.J. Ducar (1999). *Pulsed thermographic inspection and application in Commercial aircraft repair.* In D.H. LeMieux, J.R. Snell (Eds.): Proc. SPIE- The International Society for Optical Engineering, Thermosense XX, Orlando, Florida, Vol. 3700, pp. 77-83.

[26] M. T. Klein, C. Ibarra-Castanedo, X. P. Maldague, A. Bendada(2008). *A straightforward graphical user interface for basic and advanced signal processing of thermographic infrared sequences.* In V.P. Vavilov, D.D. Burleigh (eds.): Proc. SPIE- The International Society for Optical Engineering, Thermosense XXX, Orlando, Florida, Vol. 6939, pp. 693914.1-9.

[27] P. Albendea, F. J. Madruga, A. Cobo and J. M. López-Higueral (2010). *Signal to noise ratio (SNR) comparison for pulsed thermographic data processing methods applied to welding defect detection.* In X.P.V. Maldague (ed.): Proc. the 10th Quantitative Infrared Thermography Conference (QIRT10), Quebec, Canada, pp.375-382.

[28] C. Maierhofer, M. Rollig a, H. Steinfurth, M, Ziegler, M. Kreutzbruck, C. Scheuerlein, S. Heck (2012). *Non-destructive testing of Cu solder connections using active thermography.* In J.

NDT&E International, Vol. 52, pp.103-111.

[29] X. Maldague (2001). *Theory and Practice of Infrared Technology for Non Destructive Testing.* John-Wiley & Sons, New York, USA.

[30] P. Theodorakeas, N.P. Avdelidis, K. Hrissagis, C. Ibarra-Castanedo, M. Koui, X. Maldague (2011). *Automated transient thermography for the inspection of CFRP structures: experimental results and developed procedures.* In Proc. of SPIE- The International Society for Optical Engineering, Thermosense XXXIII, Orlando, Florida, Vol. 8013, pp. 8013W1-11.

[31] N.P. Avdelidis, C. Ibarra-Castanedo, P. Theodorakeas, A. Bendada, E. Saarimaki, T. Kauppinen, M. Koui, X.P.V. Maldague (2010). *NDT characterisation of carbon-fibre and glass-fibre composites using non-invasive imaging techniques.* In X.P.V. Maldague (ed.): Proc. the 10th Quantitative Infrared Thermography Conference (QIRT10), Quebec, Canada, pp. 703-710.

Chapter 6

Quantitative Analysis of Multilayered Structures: Comparison of numerical and experimental results

6.1 Introduction

During their lifetime, the different historic structural complexes have been subjected to various conservation and restoration interventions. In a large number of cases, such interventions have led to the covering of materials of great historical value and significance, as in the case of wall mosaic surfaces and fresco paintings. Based on historical evidence, these interventions were usually performed, aiming to hide the existing artwork and change the general use of the complex structure (e.g. Hagia Sophia monument). In several instances however, such interventions were carried out by conservators in order to enhance the structural integrity of the complex. The aesthetic artifact was usually covered with a limewater coating; but in some instances the application of thicker covering mortar layers has also been reported. Thus according to the application and the intervention purposes, the thickness of the coated surface could vary from some millimeters to a few centimeters. As a result, the use of non destructive testing and evaluation (NDT&E) techniques is considered to be essential in such applications, both due to the strict conservation regulations regarding the cultural heritage structures and historical sites in general (sampling for destructive testing and investigation is prohibited) as well as to acquire valuable information about internal features beneath the plastered surfaces.

Among the different NDT&E techniques, non destructive thermal imaging engenders with the responsibility to accurately obtain subsurface features information without compromising structural integrity and has been widely used in the cultural heritage conservation field [1,2]. For many years, passive thermography was applied as a standard quality control technique of historic structures [3], however the thermographic investigation during and after a heating process, has been proven to present much more potentiality than the conventional passive approach [4]. In cases of structural multilayered constructions where an inhomogeneous regime is presented, active thermography is very well suited to investigate quality problems due to the fact that possible variations of the thermal properties of each layer are producing thermal effects which are easy to be observed after the application of a heat flow into the material bulk. Furthermore, recent advances in signal processing, combined with the development of efficient numerical algorithms, have made it practical to implement active thermal imaging for quantitative purposes as well [5-7]. For instance, the difference between temperature distribution and its change as a function of time above non-defective regions and above inhomogeneities can provide information about internal features parameters such as depth and lateral size of the defect [8]. As a result, the sophisticated analysis of thermographic data permits the detection of multilayered structures with high reliability, while modelling thermal phenomena, occurring during and after the thermal excitation, is helpful to fully understand all the aspects of their thermal behaviour and enhance IRT effectiveness and visibility. This progress in active IR thermographic testing posses several advantages for the non- invasive evaluation of materials and can contribute to the cultural heritage conservation field, as the value of such structures is very high, requiring an observation technique that is safe, highly efficient, and sensitive enough to detect internal features and/or defects.

Aside from these requirements, active thermal imaging produces the possibility to see under the investigated surface without harmful effects on the artefact and with the proper data analysis, an increased probability of detection (*PoD*) is produced reducing the chance of a false detection.

The main objective of this study was to investigate and assess the reliability and suitability of active thermography based on long pulsed excitation heating in order to test multilayered structures and identify hidden mosaic artefacts beneath layers of plaster. Moreover, the combination and comparison of results from experimental testing and numerical simulations was investigated, with the goal to quantitatively characterise the subsurface features of interest. For this reason, fabricated plastered panels consisted of different tesserae materials and simulating different wall mosaics covering procedures, were investigated under laboratory conditions aiming to identify their subsurfaces –reveal of mosaics-, and retrieve quantitative information about the covering layer and the mosaic layer thicknesses as well as to characterise the hidden mosaic surfaces by means of their thermophysical properties determination.

Initially in order to acquire information about the effect of specific parameters variations on informative characteristics such as temperature decay and thermal contrast evolution curve, a numerical simulation software was involved modelling transient thermographic problems on the predefined samples (models). Through numerical simulations, the temporal changes of the surface temperature distribution over a reference (just plaster) and over an area of interest (covered mosaic) were calculated after varying geometrical parameters (i.e. thickness of covering layer, thickness of mosaic layer) and after varying the thermophysical properties (i.e. thermal conductivity, density, and specific heat) of the hidden mosaic artefact. Along with the numerical simulations, experimental measurements were performed by externally heating the specimens' surface. After the application of a long excitation pulse and as the samples were cooling down, the temporal changes of the surface temperature above a covered mosaic and a mosaic-free region were monitored aiming to identify temperature differences, related with the presence of a different material beneath the plaster. Once the hidden mosaic layer was qualitatively detected by cooling down thermographic testing, quantitative information in terms of mosaic parameters (e.g. location, thickness, nature) were acquired through the correlation of numerical and experimental results and by solving the inverse problem (parameter estimation). The above procedure was able to interpret the measured physical quantities of maximum thermal contrast and of the relative time of this maximum occurrence as a function of the investigated parameters.

The thermal excitation applied for the purposes of this study, as stated above was of long pulsed nature. This way of heating was selected with respect to the testing problem and the materials thermal properties (relative low thermal conductivities). More specifically, the application of a large amount of heat in such type of constructions (i.e. building materials) preserves the non destructive character of the testing procedure as no harmful effects can be produced and simultaneously a signal-to-noise ratio improvement can be achieved.

6.2 Practical considerations in cooling-down thermographic testing

Cooling-down thermography is a relatively well established method for the non destructive testing of materials like metals, ceramics and plastics [9]. To get information about the structure under test, the surface of the specimen is heated up with a heating unit and depending on the application, the heating duration can vary between seconds and several minutes. After the end of the heating up procedure, the cooling down phase is monitored by capturing thermal images in predefined time intervals. Some of the applications of cooling down thermography include the characterisation and inspection of building materials - historic buildings [10], moisture monitoring and assessment in ancient buildings [11], the diagnosis of surface and near-surface defects [12], and the identification of subsurface layers [13,14].

The monitoring of the cooling down behaviour at different surface positions can reveal near- surface internal features if they present different thermal conductivity, specific heat or density with respect to the material bulk. As can be understood, in all active thermographic scenarios and especially in cooling down thermography, the above parameters are of significant importance in order to understand the outcome of a thermographic survey and to evaluate the detected thermal effects during the thermographic examination.

At transient thermal regimes, thermal conductivity k, density ρ and specific heat c_p can be combined in two different terms; this of thermal inertia *e* (effusivity) and this of thermal diffusivity α. Thermal inertia is property that measures the reaction of the material to the delivery of a certain amount of energy with a temperature variation. As greater is the thermal inertia, the lower the temperature variation in a medium. By definition thermal inertia is expressed as:

$$e = \sqrt{k\rho c_p} \qquad [Ws^{1/2}\, m^{-2}K^{-1}] \qquad \text{(Eq. 6.1)}$$

In multilayered structures, for the one dimensional case, the reflection coefficient *R* of a plane thermal wave for transmission from medium 1 to medium 2 is equal to:

$$R_{12} = \frac{e_1 - e_2}{e_1 + e_2} \qquad \text{(Eq. 6.2)}$$

Thus for a successful detection of inhomogeneities, there must be a sufficient difference between the thermal properties of media 1 and 2. As larger the effusivities difference between two media, the higher the detectability of the inhomogeneities.

On the other hand thermal diffusivity describes how fast temperature differences are compensated in a material and can be expressed as:

$$\alpha = \frac{k}{\rho c_p} \qquad [m^2 s^{-1}] \qquad \text{(Eq. 6.2)}$$

All of the above mentioned features are strongly related with the thermal response of a structure detected through cooling –down thermographic inspections and should be taken under consideration for the proper explanation of the final output. For instance, a material with voids or pores decreases its thermal conductivity and density resulting to thermal diffusivity alteration and so the conduction of heat

within the material is affected. Another example is when the investigated material presents moisture. In such case, the thermophysical properties are affected and so any temperature change during the cooling down phase is much slower than an area that is unaffected by water indicating localized alterations of thermal effusivity [15].

6.3 Description of specimens

For the purposes of this study, six (6) assorted panels, four (4) mosaic samples consisted of either marble or glass with sheet of gold tesserae covered with different plasters and two (2) blank samples with just plaster and no tiles underneath them, were prepared under laboratory conditions, simulating different cases of covering interventions. The fabrication of the aforementioned test mosaic-consisted panels was carried out using the indirect method for applying tesserae. More specifically, the tiles were applied face-down to a backing paper using as adhesive water-soluble glue and later transferred onto fresh mortar. After the set of the subsurface plaster layer (tesserae accommodation layer), the paper was removed with the aid of water and at the end of this process the mosaic was covered with plaster of certain proportion and thickness. For the covering purposes, two different kinds of mortar were used. Particularly, one mosaic panel consisted of glass tesserae with sheets of gold (**M1**) was covered with 1 cm thickness of lime mortar (50% w/w fine aggregative sand and 50% w/w lime) and 1cm thickness of cement mortar (30% w/w sand and 70% w/w cement), with the cement layer applied straight upon the mosaic surface, while in the second one (**M3**) a 2 cm thickness of hydraulic lime mortar (35% w/w marble powder and 65% w/w hydraulic lime) was applied above the glass tiles. In addition, two mosaic surfaces consisted of marble tesserae were prepared **(M2, M4**) and covered in a similar way as in the case of samples M1and M3 respectively. The aggregative size distribution of the three mortars was in the range of 0-1 mm. As regards the material used for the preparation of the tesserae accommodation layer (mosaic subsurface), this was of hydraulic lime for samples M3 and M4 with 2 cm thickness, while for samples M1 and M2 it was composed based on lime with the same thickness as in the case of the previous panels. A cross-section schematic of the covered mosaics is illustrated in Figure 6.1b.

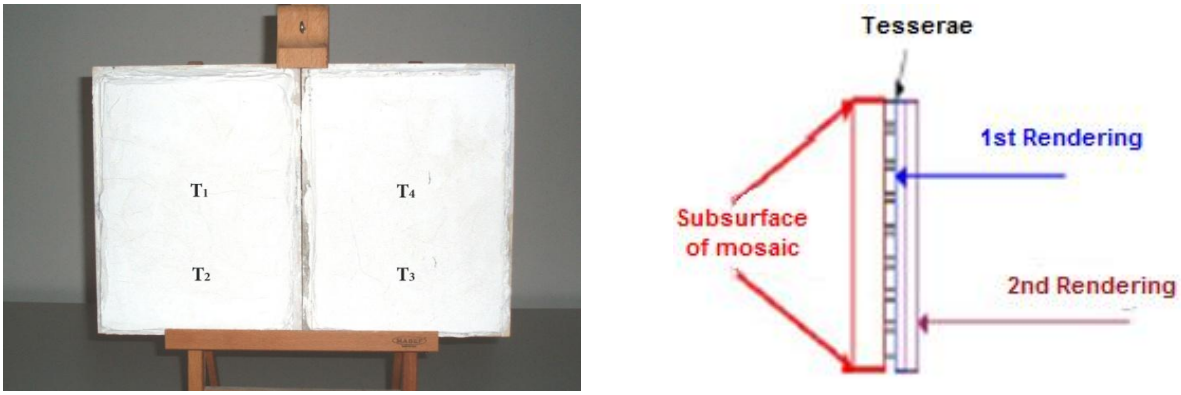

(a) *(b)*

Fig. 6.1: *a) Real image of the investigated surfaces. The panel on the left side is the reference sample and the panel on the right side of the figure is the plastered mosaic. b) Cross-section schematic of the plastered mosaic panels.*

As mentioned above, two samples were further fabricated with no tesserae pieces, which were acting as reference samples. In particular, starting from the top surface layer, one blank sample (**M5**) was consisted from 1cm of lime and 1 cm of cement mortars respectively and the second one (**M6**) was consisted from a 2 cm thickness of the hydraulic lime mortar. In both blank samples a subsurface layer of 2 cm thickness of either lime mortar **(M5)** or hydraulic lime mortar (**M6**) was initially prepared. From the set of the totally six samples, in each individual thermographic inspection the covered mosaic was tested with respect to the correspondent in terms of covering layer reference sample, simulating a wall surface with a hidden tesserae layer in a portion of it. The dimensions of each panel were 20cm (L) x 33cm (W) x 4 cm (H) and the detailed description of the materials used along with the samples' lay-up are presented in Table 6.1.

Table 6.1: *Test samples description*

Sample No.	***Tesserae Material***	***Lay-up Description (starting from the top surface layer)***	***Lateral dimensions (L x W)***
M1	*Glass*	*1cm lime mortar* *+ 1 cm of cement mortar* *+ 0.5 cm tesserae layer* *+2cm lime mortar*	*20 cm x 33cm*
M2	*Marble*	*1cm lime mortar* *+ 1 cm of cement mortar* *+ 0.5 cm tesserae layer* *+2cm lime mortar*	*20 cm x 33cm*
M3	*Glass*	*2cm hydraulic mortar* *+ 0.5 cm tesserae layer* *+2cm hydraulic mortar*	*20 cm x 32cm*
M4	*Marble*	*2cm hydraulic mortar* *+ 0.5 cm tesserae layer* *+2cm hydraulic mortar*	*20 cm x 33cm*
M5	*No tesserae*	*1cm lime mortar* *+ 1 cm of cement mortar* *+ 2cm lime mortar*	*20 cm x 33cm*
M6	*No tesserae*	*4cm hydraulic lime mortar*	*20 cm x 33cm*

6.4 Testing procedures of plastered mosaics

6.4.1 Experimental testing and analysis

The experimental setup for the performance of cooling –down thermographic investigations is illustrated in Figure 6.2. It consists of a thermal heating unit, an infrared camera and a computer system which enables digital data recording in real time. In particular, for the CDT approach the inspected specimens were heated uniformly with the use of an external 1500 W heat source (infrared lamp of INFRATECH type), that was placed at the distance of 40 cm from the inspected surfaces. The thermal excitation process was performed for 90 min, whilst the recording of the transient cooling phase was performed for 60 min. A transient heat flow inside the test specimen was produced, the penetration rate

of which was depended on the physical and thermal properties of the material (thermal conductivity *k*, specific heat capacity c_p and density ρ). As a result, only for a homogeneous material the heat propagation is uniform. In any other case, the presence of inhomogeneities inside the material with different thermal properties from the surrounding, results to an accelerated or slowed down heat loss process in this local area, producing a measurable difference of the surface temperature distribution, which can be detected during the thermographic monitoring.

The recording of cooling down procedure was performed with the aid of an infrared camera placed always vertical to the surface of the panels at the distance of 60 cm. The thermographic system used for this study (ThermaCAM SC640) was detecting the emitted radiation from the surface of the specimen in the wavelength region from 7.5 to 13.5 μm and it was a focal plane array having 640 x 480 detectors of uncooled microbolometer technology. For the monitoring of the cooling down process, thermal images were recorded sequentially with a time step of 30 *s* and transferred to the computer which was used to analyze the thermal data and convert them to temperature data with the aid of ThermaCAM Researcher Pro 2.8 analysis software.

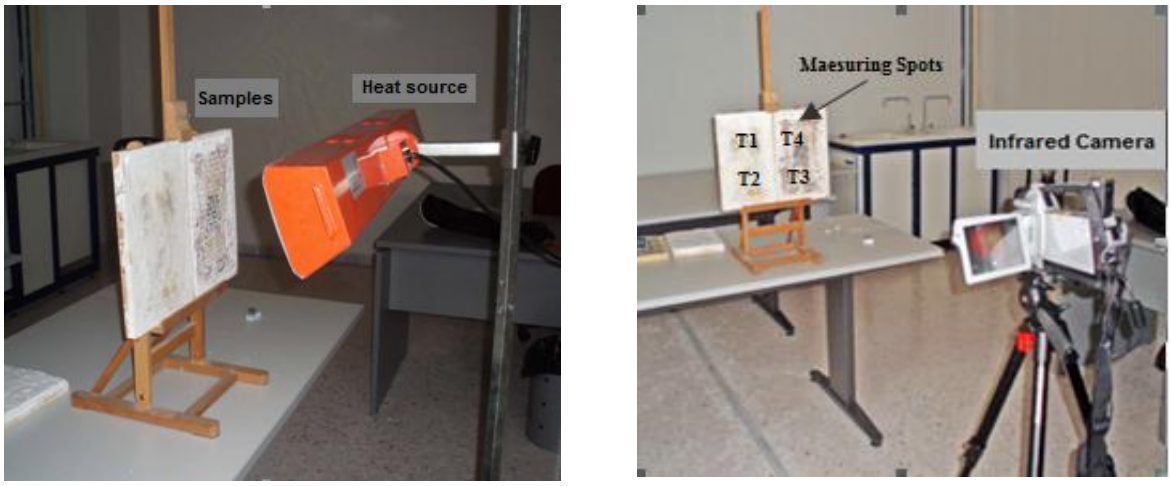

(a) *(b)*

Fig. 6.2: *Test arrangement for the cooling down thermographic measurements. a) The covered mosaic and the corresponding reference sample were heated for 90 min. b) Thermal images were recorded during the cooling down process for 60 min. For clarity an uncovered mosaic is presented instead of the covered one.*

The concept of the measurements performed in the present case study, was based on the assumption that infrared thermography will be able to detect the subsurfaces of the plastered panels, presented with temperature variations on the surface, due to the dissimilar thermal diffusion that each layer renders. Thus each individual measurement was performed by comparing the thermal behaviour of a covered mosaic with respect to the behaviour of the corresponding in terms of plastering reference sample. As a result, the sets of samples studied had as follow: M1-M5, M2-M5, M3-M6 and M4-M6. The description of the above panels has already been presented in Table 6.1.

For quantitative analysis, transient curves (surface temperature as a function of time) from areas above the plastered mosaic and above the blank sample were compared and the produced temperature differences were further plotted as a function of time. The purpose of ΔT vs. time plotting was to

monitor how this quantity changes as a function of time and to identify the maximum ΔT_{max} and the distinct time of occurrence t_{max}. In order to compute the above quantity two different options were investigated in the sequential analysis of the cooling down process:

- Select a single pixel above the plastered mosaic and a single pixel above the mosaic-free surface.
- Identify and average the temperature values in the area of the covered mosaic and in the area of the reference sample.

As the first option raises the important issue of how the points should be selected (the feature of interest occupies a large volume of pixels in the thermal image), four different control points were selected –two on each sample surface- accommodated in diametrically opposed positions between them. Thus as can be seen from Figure 6.3a, pixels T1 and T4 were selected at the center of each panel, whilst pixels T2 and T3 were selected near the bottom edges of each panel respectively (spots T1 and T2 correspond each time to the reference sample). By selecting two different control spot analysis procedures, the aim was to evaluate the influence of the heating process on quantitative information retrieval and to assess the degree of uniformity in thermal excitation. A summary of the inspection and analysis procedures is illustrated in Figure 6.3.

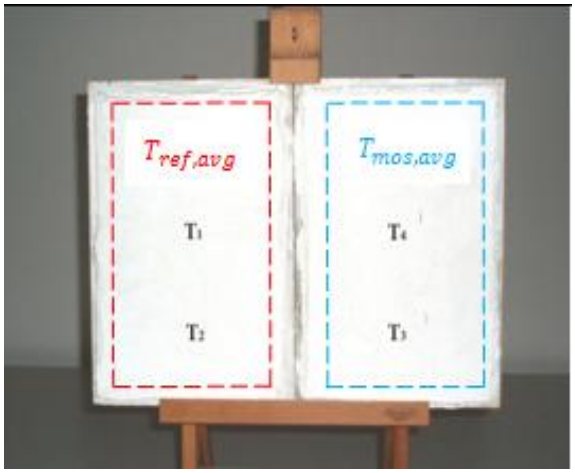

(a)

Thermal contrast definition according to the selected pixels-areas	
Centre of the panel	$T_4 - T_1$
Down edge of the panel	$T_3 - T_2$
Average areas	$T_{mos,avg} - T_{ref,avg}$

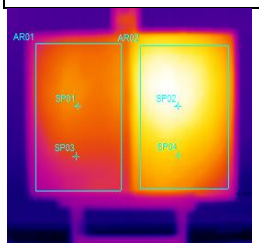

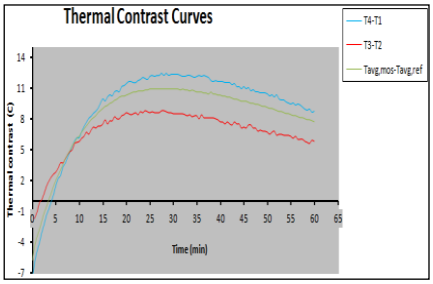

(b)

Fig. 6.3: *Schematic illustration of measurements and analysis. a) Measuring spots and areas of the temperature distribution on the tested surfaces. b) Thermal contrasts definition with respect to the selected spots and areas on the surfaces of the panels. Data can be interpreted in terms of digital thermal images and plot curves.*

6.4.2 Numerical modelling of cooling down testing

As discussed above, the goal of this methodology was to quantitatively characterise the above multilayered mosaic panels. Before the implementation of experimental testing, parametric studies were

conducted through numerical simulations investigating the mosaic detectability by altering the covering intervention thickness, the mosaic layer thickness and the thermophysical properties of the hidden mosaic. As a result, a thermal heat pulse was simulated which was hitting the surface of the panel and the transient thermal behaviour of the specimen was calculated. The results from the calculations gave a matrix containing the temperature distribution for each surface element at predefined time steps during heating and cooling and the matrix was analysed in terms time-history temperature plots above the plastered mosaic area and the correspondent reference area.

For implementing numerical simulations, the ThermoCalc-3D^{TM} heat transfer model was used, developed by Tomsk Polytechnic University [16]. This software was developed based on solving heat conduction problems by means of an implicit finite element numerical scheme and simulates thermal nondestructive testing scenarios where transient temperature signals over subsurface features are of prime interest. It is intended for calculating three-dimensional (3D) temperature distributions in thermally isotropic and/or anisotropic solids of various layers that may contain subsurface features. An advantage of the aforementioned modelling software package is its ability to model very thin subsurface features in rather thick materials without losing computation accuracy (the thin sheets of gold on glass tiles were included into the model). Along with the main heating or cooling stimulation, both front and rear surfaces are cooled down according to Newton's law (within such approach, both convection and radiant heat exchange mechanisms are combined and described with a particular value of a heat exchange coefficient *h*). In addition, as it will be presented below, thermal properties of the specimen and defects can be specified separately in all three spatial directions thus modelling a fully anisotropic specimen, while on the boundaries between the specimen layers and between the host material, the temperature and heat flux continuity conditions are taking place. Finally, by implementing simulations through this heat transfer model, losses due to radiation and convention are only considered at the surface of the panel as its other sides are supposed to be thermally insulated.

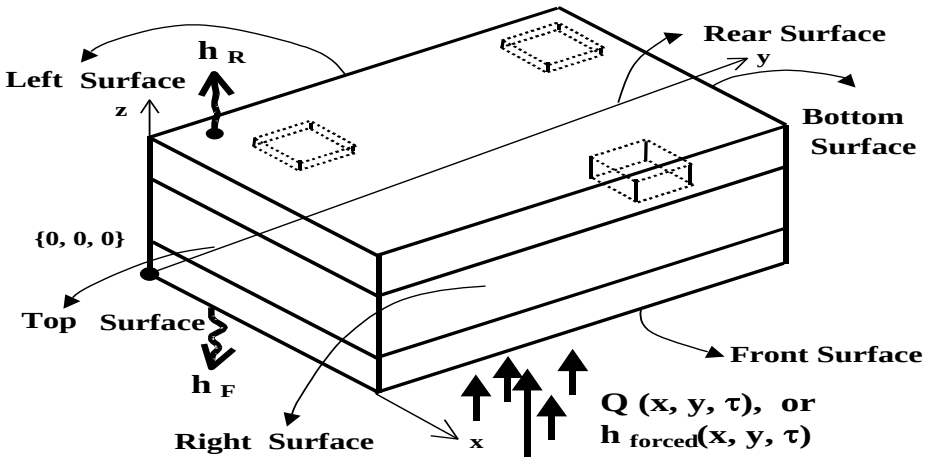

Fig. 6.4: *3D model description of a three-layer specimen with subsurface defects [16].*

The above described thermal modelling environment was used in order to calculate the thermal response of the covered mosaics after the application of a heat flux. The dimensions of the models were

40cm x 33cm x 4 cm with the half area referring to the blank panel (20cm x 33cm), whilst the other half was designed consisting a simulated subsurface mosaic area (20cm x 33 cm). For the development of the simulation regime, the following parameters were initially predefined:

- sample geometry and lay-up specification
- layers geometry and their thermophysical properties specification
- definition of temporal testing characteristics
- heat flux and heating procedure characteristics

In particular, as stated above in order to create the physical model of the simulated testing scenario, its geometrical characteristics (length and width) were assigned with respect the real panels' specifications along with the layers/defects number composing the model. As ThermoCalc software has the limitation to model structures consisted of three layers maximum, for the purpose of the present numerical study, the mosaic area in each individual test was simulated as a defect area into the material bulk. In addition, the unknown parameter of convective heat transfer exchange coefficient of the panel surface was defined after inputting different values of heat exchange coefficients and performing numerical simulations. From the different parametric studies, the value of 10 W/m^2K was selected. This value was chosen as the temperature increase observed on numerical simulations was fitting better with the temperature increase on the surface of the panels, observed during experimental testing. After the general determination of the physical model each of its predefined layers and defects (defect always refers to the mosaic area as stated above) had to be characterized in terms of geometrical dimensions (length, width and thickness), spatial location and thermophysical properties. The materials properties used in this study were obtained by the literature [15-17] and a complete description of the layers specifications is presented in Table 6.2, while a schematic illustration of the physical model in the simulation environment is presented in Figure 6.5.

Last to fully describe the cooling down simulation, input parameters such as heat stimulation and data recording duration were described along with the interval time step for the computations. In addition, the density of the heat flux deposited on the samples' surface as well as the position of the energy source with respect to the panel's geometrical dimensions, were also inputted into the test model. The above parameters were set in accordance to the experimental procedure and are summarized as well in Table 6.2.

In this point, it should be mentioned that the development of the simulated thermographic procedure was created taking into account some simplifications. Particularly, the heating process in numerical testing was performed in a uniform manner (something that cannot be achieved in real testing conditions) and the specimen lateral sides were acting as adiabatic surfaces. As a result losses due to radiation and convection were only considered at the surface. Furthermore, the initial sample and ambient temperatures were set to zero in order to all the calculated results be related to excess specimen temperatures. A non-zero ambient temperature would mean the additional heating with both the heat pulse and the ambient and a non-zero initial temperature would only shift results by the corresponding

initial temperature value. In practice, these simplifications allowed the comparative study of numerical and experimental results as the thermal response of the structures was evaluated in terms of thermal contrast evolution to time rather than temperature decay to time. In other words, the informative characteristic used for the mosaic detectability evaluation was the temperature difference produced among the respective mosaic consisted and mosaic-free surfaces and not their temperature shifts.

Table 6.2: *Input parameters for the description of the simulated samples' layers and testing procedure*

	Thermal Conductivity ***($Wm^{-1}K^{-1}$)***	***Specific heat*** ***($Jkg^{-1}K^{-1}$)***	***Density*** ***(kgm^{-3})***	***Thermal Effusivity*** ***($Ws^{1/2}\ m^{-2}K^{-1}$)***	***Thermal diffusivity*** ***($x10^{-7}m^2\ s^{-1}$)***
Lime Plaster	0.87	800	1440	1001	7.55
Geometrical sizes of plaster layer in **cm**	length = 40	width = 33	height*= 1 height** = 2		
Concrete Plaster	1.4	1100	2000	1755	6.36
Geometrical sizes of concrete layer in **cm**	length = 40	width = 33	height*= 1		
Hydraulic Lime Plaster	0.5	900	1100	703	5
Geometrical sizes of hydraulic layer in **cm**	length = 40	width = 33	height*= 1 height** = 2		
Marble tesserae layer	3.14	870	2700	2715	13.4
Geometrical sizes of marble layer in **cm**	length = 20	width = 33	thickness= 0.5		
Glass tesserae Layer	1.4	750	2500	1620	7.46
Geometrical sizes of glass layer in **cm**	length = 20	width = 33	thickness= 0.4		
Gold tesserae Layer	317	129	19300	28092	1273
Geometrical sizes of gold layer in **cm**	length = 20	width = 33	thickness= 0.1		
Power input in **W/m^2**	1500				
Duration of energy input in **min**	90				
Duration of observation in **min** (including heating)	150				
Time interval in **s**	30				

** corresponds to the covering layer thickness*
***corresponds to the subsurface layer thickness*

For numerical analysis and data interpretation, transient curves were calculated in a similar manner as in the case of experimental measurements. Nevertheless, in order to plot the temperature decay and the thermal contrast evolution curves above the mosaic-free and covered mosaic regions, only two points

accommodated in diametrically opposed positions and placed at the centers of each respective area, were selected due to the thermal stimulation uniformity that the modelling test provided. A summary of the numerical testing procedure, presenting the creation of the physical model and the interpretation of the numerical results, is illustrated in Figure 6.5.

Thermal contrast definition according to the selected model's elements	
Center of the panels	$T_{mos} - T_{ref}$

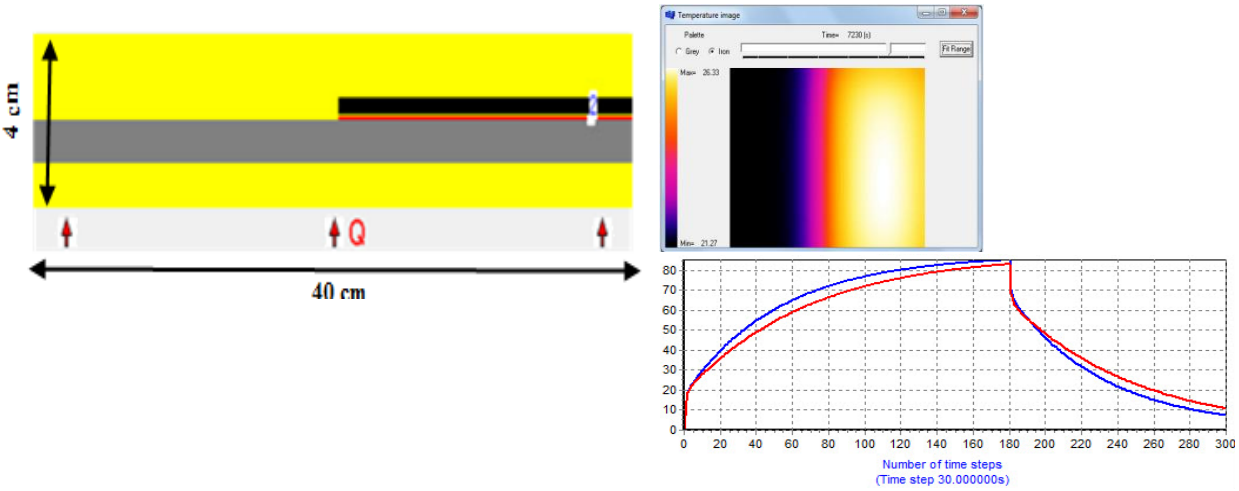

(a) *(b)*

Fig. 6.5: *Schematic illustration of simulations and analysis. (a) Physical model of the inspected covered mosaic containing two layers of covering (yellow, grey layers) and glass tesserae (black layer) with sheets of gold (red layer). b) Thermal contrasts definition with respect to the selected spots and data interpretation in terms of calculated thermal images and transient temperature curves.*

6.4.3 Parameters studied by numerical simulation

The materials parameters (thermophysical properties and dimensions) presented on Table 6.2 are referring to the physical model description of the fabricated plastered mosaics. Similarly, the testing parameters correspond to the predefined experimental procedure. However, in order to conduct the parametric studies discussed above and to extract results as regards the influence of specific variations to the identification of mosaics, a series of simulations was carried out with some differentiations.

Particularly, in order to study the influence of covering layer thickness on hidden mosaic detectability, simulations were performed for a mosaic layer of stable thickness (5mm) covered with plaster varying from 0.5 to 3.5 cm. The thickness step increase was of 0.5 cm and in the case of cement/lime covering models each layer was increased equally from 0.25 to 1.75 cm in order to achieve the aforementioned range. The numerical investigation was fitted to simulate the experimental testing conditions, as calculations were performed for 60 min in the transient cooling phase after heating up the surface for 90 min. In the same way, the influence of mosaic layer thickness on the thermal response of the structure was studied in a 2cm covering model with tiles thickness varying from 2 to 14mm. The mosaic thickness was increased by a 2mm step each time and as regards the glass tesserae constructed panels,

the sheets of gold were considered into the model having a stable thickness of 1mm. As a result, parametric studies were performed by increasing only the glass tiles thickness from 1 to 13 mm.

Finally, the thermal response of the covered mosaic was evaluated in terms of their thermophysical properties taking into consideration the material properties of thermal effusivity and thermal diffusivity respectively. In a model having the physical dimensions of the real samples, the influence of the mosaic thermophysical characteristics was investigated by varying simultaneously the thermal conductivity of the mosaic surface from 1 to 4.5 W/(mK), the density from 1500 to 3000 kg/m^3 and the specific heat from 700 to 1300 Jkg^{-1}K^{-1}. The above variations produced 7 models, where the thermal effusivity of the investigated feature was varied from 1024 to 4189 Ws$^{1/2}$m^{-2}K^{-1} and its respective thermal diffusivity from 9.5 to 11.5 x10^{-7} m^2 s^{-1}. A more detailed description of the values set used for this parametric study are presented in the correspondent subsection (6.5.3) in which the obtained results for altering the thermophysical properties of the hidden mosaic layer are also presented.

6.5 Results of numerical simulations

The finite difference simulations were carried out for all the sets of covered panels examining the thermal behaviour of the plastered mosaic region in comparison with the thermal behaviour of the respective mosaic-free area. In the following subsections, the results from the numerical simulations are presented.

6.5.1 Effect of covering layer thickness in plastered mosaics detection

A series of models were created with different covering heights (from 0.5 to 3.5cm) both for the glass and the marble tesserae constructed samples. The geometrical characteristics in terms of lateral dimensions, the thermophysical properties and the testing parameters used in order to model the transient thermographic tests, are these presented in Table 6.2. The only parameter varied in this study, was the depth at which the mosaic surface was located to by changing the height of the corresponding covering layer(s).

6.5.1.1 Models of M1-M5 test

The first numerical simulation was performed for the set of M1-M5 samples with the glass mosaic layer located to a depth of 0.5 cm (covered by 0.25 cm cement and 0.25 cm lime mortars respectively). For numerical analysis and data interpretation, thermal images were obtained and transient temperature decay curves, indicating the cooling behaviour of the reference and of the plastered mosaic areas, along with their corresponding temperature difference evolution vs. cooling time were calculated.

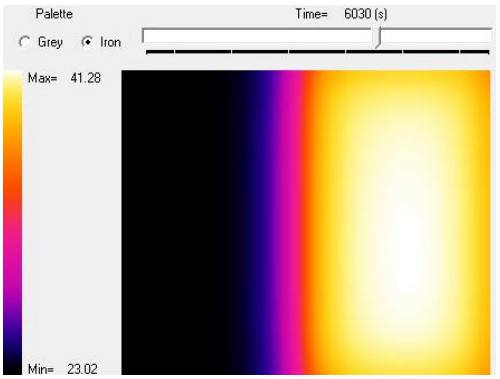

Fig. 6.6: *Surface temperature gradient at the time of maximum thermal contrast occurrence of M1-M5 simulation for the 0.5 cm covering simulation.*

Figure 6.6 illustrates a selected surface temperature gradient from the calculations of the 0.5cm covering model. The thermal image has been calculated at t= 10.5 min after the beginning of the cooling down process (corresponds to 6030 s in the representative figure as the heating up temporal duration is also included), which was the time of the maximum thermal contrast occurrence (17.95 ^{0}C). As can be seen, the simulated area with the mosaic surface beneath it (refers to the right side of the figure) has a slower heat loss rate with respect to the adjacent blank area (left side of the figure), presented with an increased surface temperature distribution over this region. Similar results were extracted from the calculations of the rest models, as increasing the covering layer with a 0.5 cm step. Indicative calculated thermal images are presented in Figure 6.7, where as it was expected the temperature difference over the two areas decreases rapidly for rising the covering thickness along with a longer time of this maximum thermal contrast appearance. For instance, the time of peak thermal contrast for the 2 cm model was calculated at 30 min after the beginning of the cooling down, with a temperature difference of 4.91 ^{0}C, whilst the respective time on the 3.5 cm covering model was calculated at 60 min with a temperature difference value in the range of 1.76 ^{0}C. However from the results obtained through the above numerical simulations, it was observed that the glass mosaic surface can still be identified beneath the covering layer of 3.5 cm thickness, as a temperature difference on the simulated surface was produced.

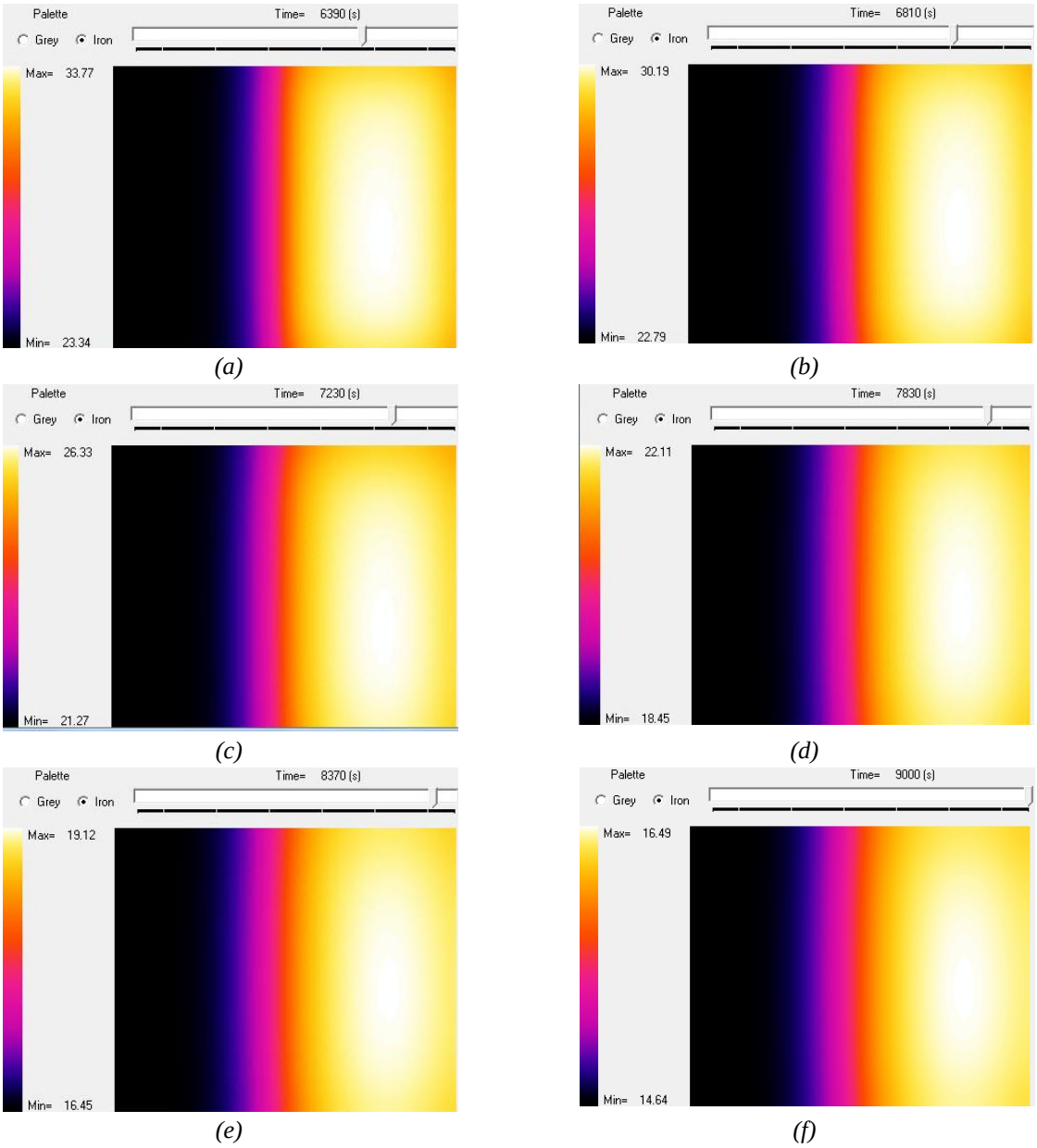

Fig. 6.7: *Surface temperature gradients of M1-M5 simulation at the time of maximum thermal contrast occurrence for the (a) 1 cm, (b) 1.5cm, (c) 2cm, (d) 2.5cm, (e) 3cm and (f) 3.5 cm covering models.*

The next step in numerical analysis was the calculation of the temperature decay vs. cooling time on the centre of the blank area and on the centre of the plastered mosaic area respectively. Figure 6.8 presents the thermal behaviour of the aforementioned areas on two simulated interventions having 0.5 cm and 2 cm covering thicknesses respectively. At the same graph, the correspondent thermal contrast evolution curve has also been plotted for clarity. The graphical representations of transient temperature decay and thermal contrast evolution vs. cooling time confirmed the results observed from the calculated thermal images, as the plastered mosaic (red dotted line) cools down with a slower rate in relation with the reference blank area (black dotted line). Moreover, the representative contrast curves even that they present some differentiations (as regards the ΔT_{max} *and* t_{max} values), in general they follow a similar trend. Initially an upward trend is observed for both curves until reaching a maximum

ΔT value and as the cooling down procedure progresses, the signal decays with a slower rate for the thicker covering model.

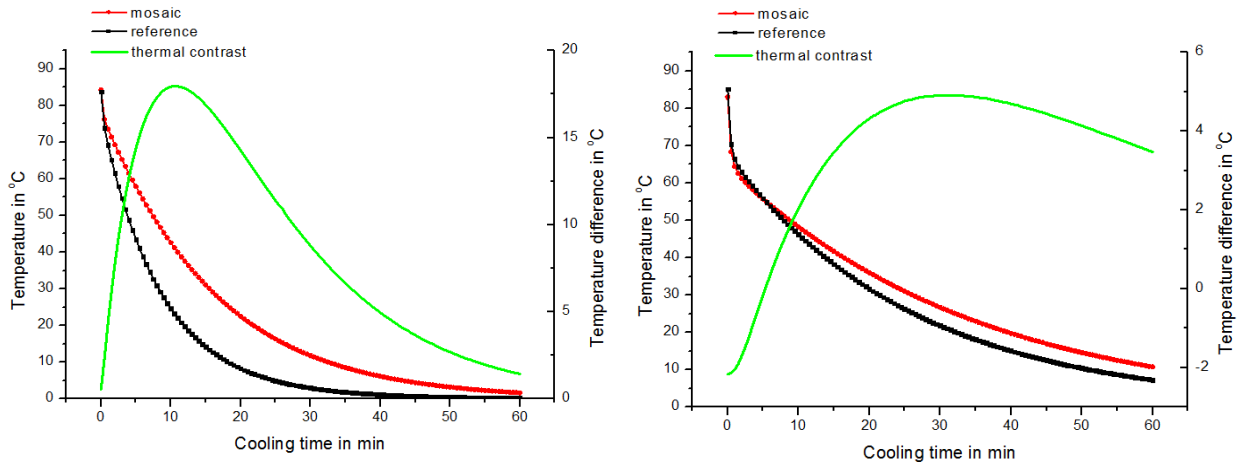

Fig. 6.8: *Calculated transient temperature curves for M1-M5 simulated set, above the refernce centre and above mosaic centre along with the respective temperature difference curve for (a) the 0.5cm and (b) the 2 cm covering models.*

In order to describe the effect of the covering intervention thickness and study the capabilities of cooling down thermography as a means of investigating multilayered structures, totally 7 different models were created. The calculated temperature difference curves above the area of interest (mosaic) and the reference area are presented in Figure 6.9. As can be seen from the plot, all curves have a distinct point of maximum temperature contrast, however as thicker is the covering as reduced is the thermal contrast between the reference and the mosaic covered regions and as longer is the time point of this peak *ΔT* appearance. Furthermore, a negative thermal contrast was initially calculated above the two modeled surfaces, which had lower value and a longer time of occurrence for thicker coverings. In addition, as mentioned above, as thinner is the covering layer the sharper is the slope of the corresponding curve, indicating that the temperature difference variations in time are taking place in a more rapid manner due to the higher heat loss rate from the surface.

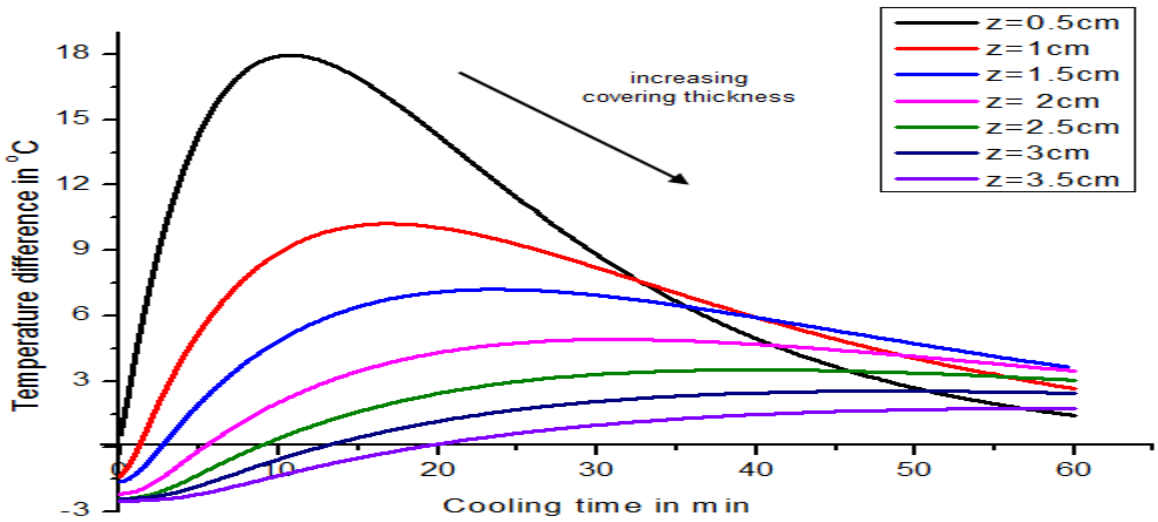

Fig. 6.9: *Temperature difference curves as a function of cooling time for the M1-M5 simulations, calculated for coverings from 0.5 to 3.5 cm.*

6.5.1.2 Models of M2-M5 test

The second series of numerical modelling was differing from the above presented simulation in terms of tesserae material. In particular, the glass mosaic structure was remodeled by replacing the glass/gold subsurface with a layer of marble tiles. After the creation of the physical model, the same numerical testing procedures were conducted by increasing the cement/lime covering thickness. In general as in the case of M1-M5 set, similar results were observed for the simulated M2-M5 models. However, the short deviations regarding the thermal behaviour of this structure, presented with differences of the ΔT values with respect to corresponding ones of M1-M5 set, verified the presence of marble instead of glass/gold tiles beneath the layers of plaster.

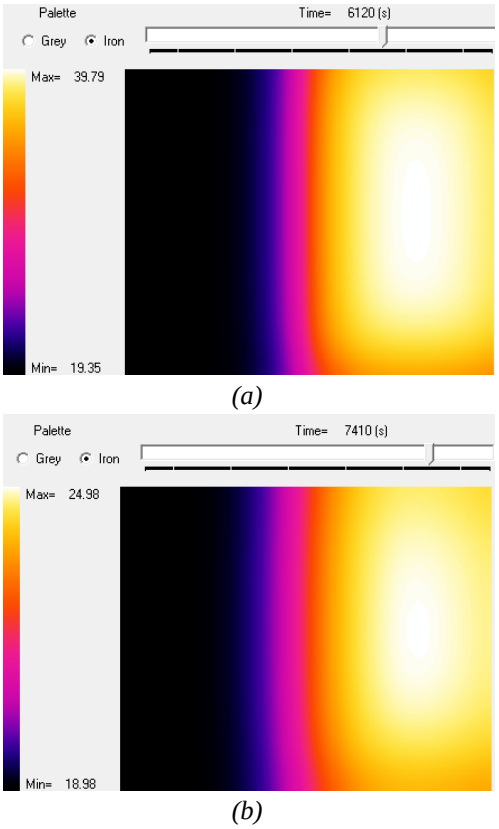

Fig. 6.10: *Surface temperature gradients of M2-M5 simulations for (a) 0.5 cm and (b) 2cm coverings.*

Figure 6.10 shows the calculated temperature gradient images acquired from the 0.5 cm and the 2 cm physical models, at the time when the maximum thermal contrast occurs. Similarly to the previous case, the simulated area above the mosaic subsurface presented a higher temperature compared to that calculated on the blank surface, revealing that the detection of the marble tesserae layer is also possible. More specifically, the marble tesserae structure in the first case presented a peak temperature difference of 19.98 ^{0}C at t=12 min as the sample was cooling down, while the latter model calculations produced a thermal contrast peak of 5.75 ^{0}C, 33.5 min after the beginning of the cooling down process. The representative results of the calculated thermal images, are summarised in the plots of Figure 6.11, confirming as well that the mosaic area cools down with a slower rate compared with the reference area (Figure 611.a and 6.11.b). Furthermore, the results produced from this set of simulations also verified the faster seeing through condition achieved for thinner coverings, as the reduced plaster layer allows thermal waves to reach the inner subsurface faster and reflected back to the surface earlier than the thermal waves under a thicker covering (Figure 6.11 c).

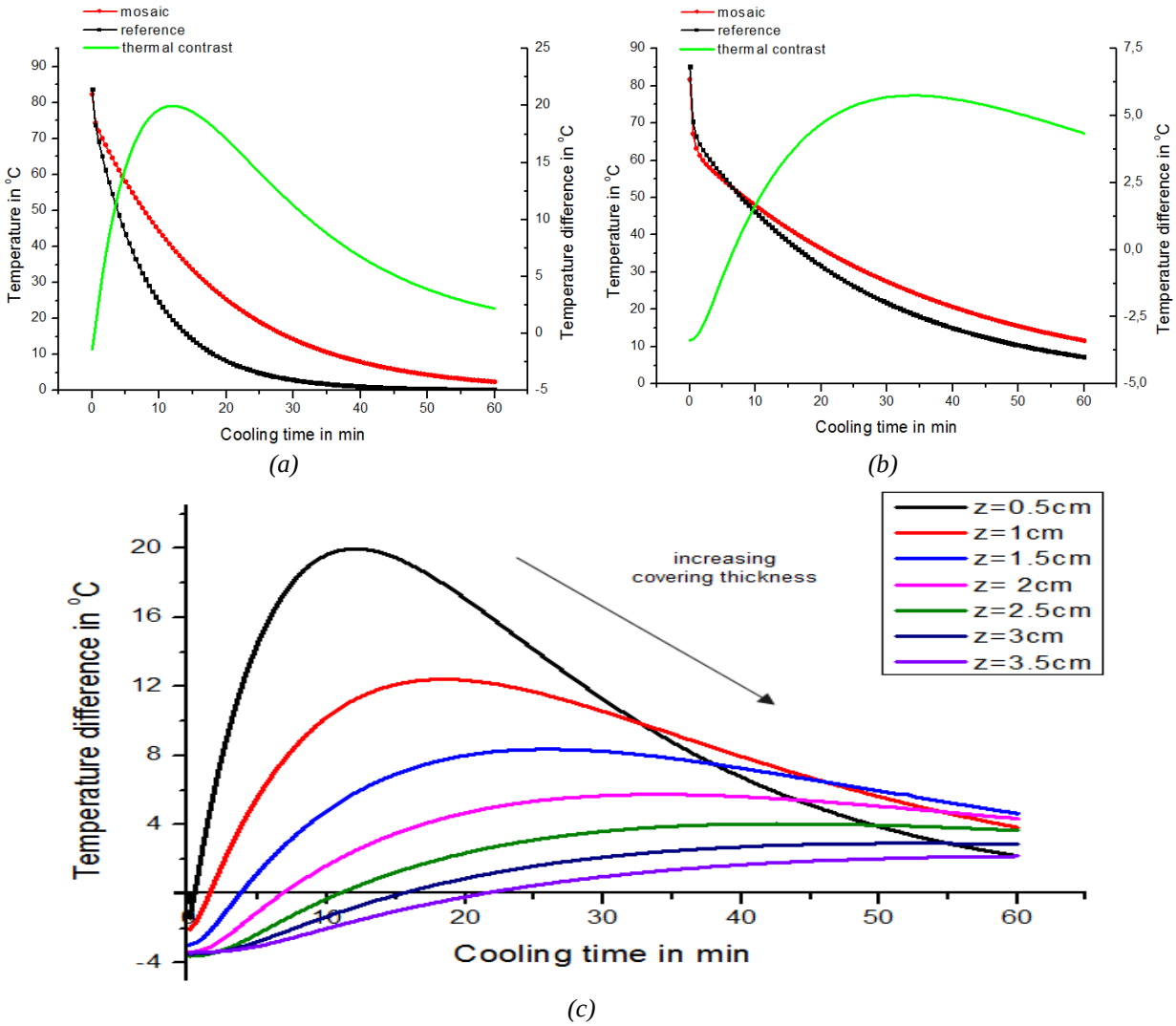

Fig. 6.11: *Calculated surface temperature decay plots above reference and covered mosaic points and the respective temperature difference curves for (a) the 0.5cm and (b) the 2 cm covering models. (c)Temperature difference curves as a function of cooling time for the M2-M5 simulations, calculated for covering from 0.5 to 3.5 cm.*

6.5.1.3 Models of M3-M6 test

From the numerical modelling of M3-M6 set, contrary to the previous simulations, the seeing through potential of thermal imaging was investigated, studying a different covering intervention. In particular, M3-M6 set was modeled taking into account the thermophysical properties of hydraulic mortar as a cover layer instead of the cement/lime covering, studied in the previous simulations. From the acquired results, it was observed that the identification of the hidden glass mosaic layer was possible as a thermal contrast was also produced on the plastered surface but the thermal response of this structure was completely different in terms of cooling down behaviour with respect to the thermal responses observed above. This can be seen from the results presented in Figure 6.12, where the calculated thermal images for the 2cm model at the time point of the maximum thermal contrast occurrence and at a time point near the end of the cooling down phase are illustrated. In particular, the time of maximum thermal contrast occurrence is relatively short (2.5 min after the beginning of the cooling down process),

compared with the respective times calculated in the previous models (Figure 6.12a), and in this specific time point the blank surface presents a higher temperature with respect to the surface temperature distribution calculated over the covered mosaic, indicating that more heat is accumulated on the reference area rather than the covered mosaic region. However, as the cooling down process was evolving, the two simulated areas tend to have the same temperature, with this of the plastered mosaic being slightly greater, something that can be confirmed from Figure 6.12b.

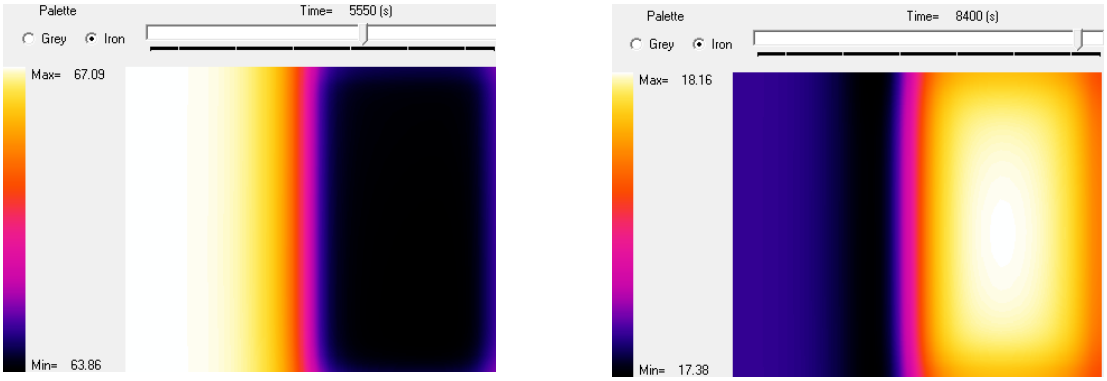

(a) *(b)*

Fig. 6.12: *Calculated thermal images from the 2cm model at (a) t= 2.5 min and t=50 min after the beginning of the cooling down procedure.*

The differentiation in the thermal response of this simulated structure in comparison with the previous tested models derives from the fact that the mosaic area appears to cool down more rapidly and for a longer time, approximately for the first 30 min of calculations. Moreover, as the cooling down procedure continues, this condition does not change significantly as the heat loss from the two surfaces is approximately the same. The reduced values of the calculated thermal contrast during the whole cooling down process as Figure 6.13 presents, are further indicating the reduced mosaic detectability condition produced in this case. For clarity, the thermal contrast curve in the above figure has been plotted by subtracting the temperature of the mosaic surface from that of the reference area (the opposite procedure was followed in all experimental and modelling analyses as mentioned in the numerical modelling and experimental measurements description). Despite the differentiations observed regarding the thermal behaviour on this model, in terms of covering thickness influence on the detection of the hidden mosaic it was observed that temperature differences above the reference and

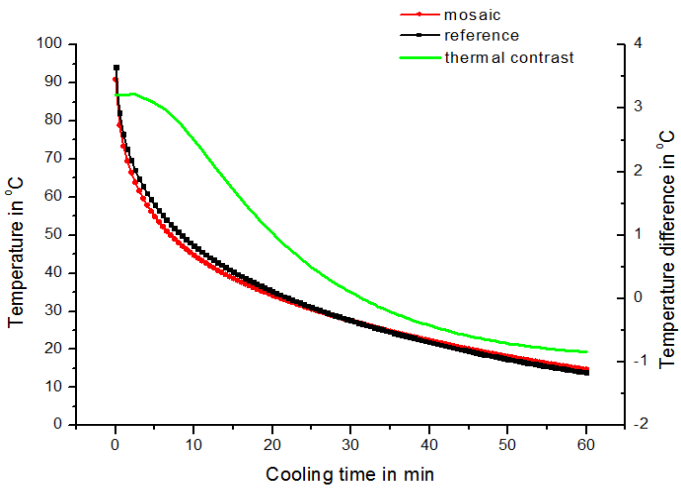

Fig. 6.13: *Calculated surface temperature decay plots over the reference and covered mosaic points and the respective temperature difference (Tref – Tmos) curve for the 2 cm covering model.*

above the mosaic area were detected as well in all the models and this contrasts were reduced as increasing the covering thickness.

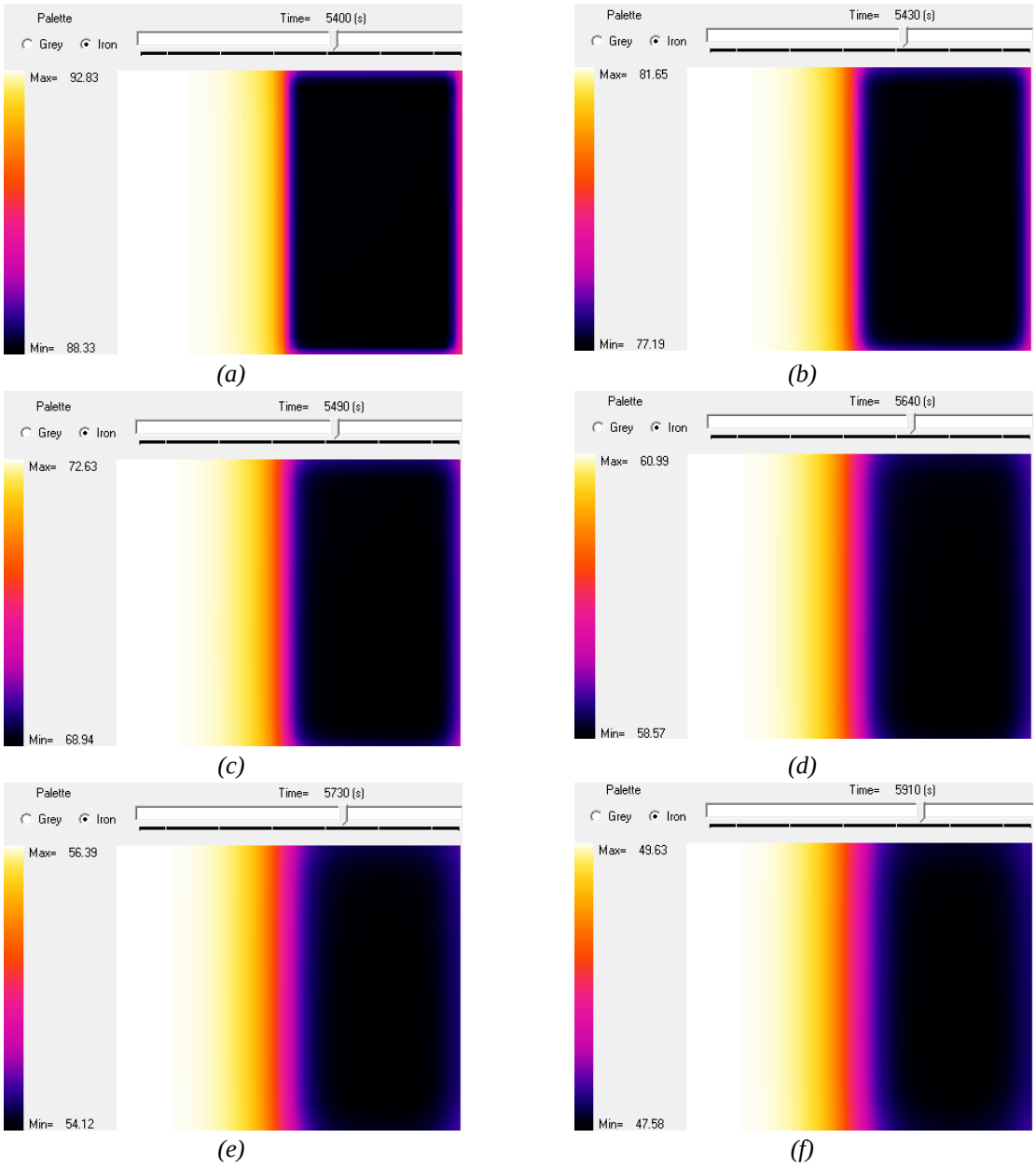

Fig. 6.14: *Surface temperature gradients of M3-M6 simulation for (a) 0.5 cm, (b) 1cm, (c) 1.5cm, (d) 2.5cm, (e) 3cm and (f) 3.5 cm covering thicknesses.*

The calculated cooling responses of all M3-M6 models after the application of the same heat flux are summarised in Figure 6.15. The detected higher heat loss rate from the mosaic covered surface is indicating that the glass mosaic layer in this structure acts as a "*heat resistance*" reflecting the thermal waves back to the surface faster than the reference blank region. The above condition verified that each structure responds differently to heat application according to the thermophysical properties of both the feature of interest and the background. More specifically, assuming that the selected heating up procedure created an efficient penetration of heat flow into the structure, the heat accumulation observed on the blank region can be deduced to the decelerated conductive heat transfer back to the

surface, due to the low conductivity that this type of mortar has. However, in the heat flow "*resistive*" region (mosaic consisted subsurface), thermal waves penetrated in a lower depth, while the presence of gold sheets may facilitated the conductive heat transfer back to the surface due to the high thermal diffusivity and conductivity that these features present.

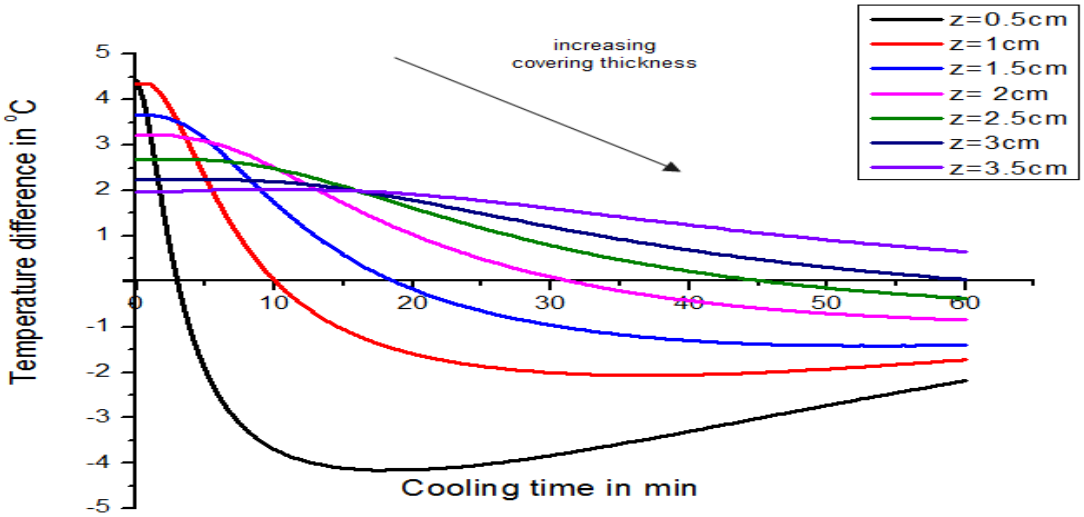

Fig. 6.15: *Temperature difference curves as a function of cooling time for the M3-M6 simulations, calculated for coverings from 0.5 to 3.5 cm.The temperature difference in y-axis corresponds to (Tref – Tmos) values.*

6.5.1.4 Models of M4-M6 test

The last series of simulations was created in order to evaluate the thermal behaviour of the structure, replacing the glass tiles with marble tiles under the hydraulic plaster. In general, as in the case of the previous numerical test, the detection of the marble tesserae layer was possible from the simulated transient thermographic testing. From the calculated images of the 1cm and 2cm models, presented in Figure 6.16, it can be observed that the simulated mosaic- consisted area presented a higher surface temperature compared with this of the reference area, indicating the presence of a material with different thermophysical properties beneath the half portion of the plastered surface. In particular, the simulated marble tesserae structure covered with 1 cm of hydraulic mortar presented a peak temperature difference of 8.02 ^{0}C at t=8.5min, while the 2cm model had a similar peak of 6.04^{0}C at t= 11.5 min after the beginning of the cooling down process. Along with the increased heat accumulation detected on the mosaic region, longer times of maximum thermal contrast appearance were calculated with respect to the previous numerical model. Since these two models were created taking into consideration that the covering material had the same thermophysical properties, these deviations on the surface temperature distribution verified the presence of a different subsurface materials under the hydraulic plaster.

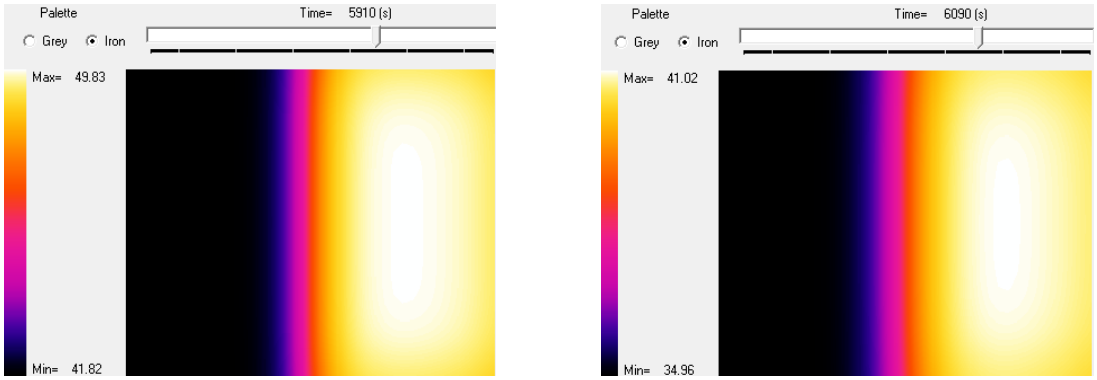

(a) *(b)*

Fig. 6.16: *Surface temperature gradients of M4-M6 simulation for (a) 1cm and (e) 2cm covering thicknesses.*

As regards the effect of covering thickness on the detectability of the hidden mosaic layer, similar results were observed revealing that a thicker covering produces reduced thermal contrast, as illustrated in Figure 6.17. The variations of the acquired results with respect to the results obtained in M3-M6 model, reveal that the marble tiles act as a "*heat tank*" rather than a "*heat resistance*" beneath the hydraulic covering. However, even if the mosaic area cools down with a slower rate in relation to the blank area, the time points of maximum thermal contrasts are relatively short, which could be a characteristic of the thermal properties of the covering material, as similar results for the peak time were produced on the previous model as well.

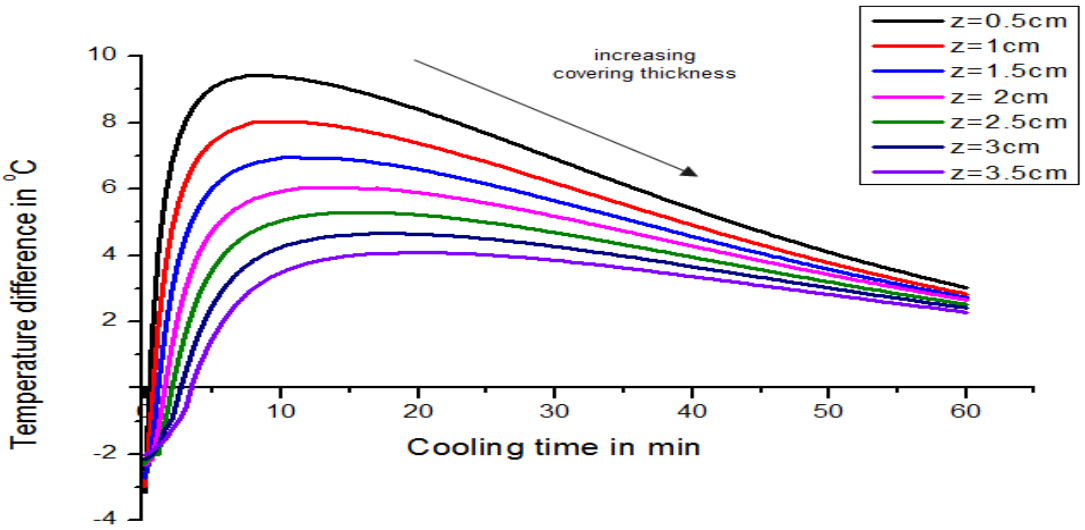

Fig. 6.17: *Temperature difference curves as a function of cooling time for the M4-M6 simulations, calculated for covering width from 0.5 to 3.5 cm.*

6.5.2 Effect of tesserae thickness in plastered mosaics detection

Beside the cover thickness influence on the detectability of the hidden mosaic features, another parameter evaluated in this study was the variation of mosaic layer thickness and its effects to the thermal behaviour of the plastered panels. As it will be presented below, a series of models was created with different tesserae thicknesses ranging from 2 to 14 mm, for both the glass and the marble constructed panels. The mosaics consisted of glass tiles were increased in a thickness range from 1 to 13 mm, as the sheets of gold were included into the physical model having a stable thickness of 1mm.

The influence of tiles thickness on the detection of the hidden tesserae layer was numerically tested on coating simulations with a 2 cm thickness cover for both the hydraulic and the cement/lime covering interventions.

6.5.2.1 Modelling of the two layers covering intervention

The first numerical test was performed for the set of M1-M5 samples with the glass mosaic layer having a thickness of 1mm (the total thickness of the tesserae layer was 2 mm including the 1mm thickness of the gold sheets). As in the case of the covering increase investigation, thermal images were acquired and transient temperature curves were calculated above the reference and above the plastered mosaic regions. Figure 6.18 illustrates the surface temperature gradient derived from the calculations of the 2mm thickness model along with the corresponding temperatures and thermal contrast curves. The thermal image has been calculated at t= 28 min after the beginning of the cooling down process, which was the time of the maximum thermal contrast occurrence (2.65 ^{0}C). As can be seen, the simulated area with the mosaic surface beneath it (right side of the figure) has a slower heat loss rate with respect to the adjacent blank area (left side of the figure), indicating that the thin tesserae layer can be detected. In general, the numerical calculations of the M1-M5 model revealed that the thicker mosaic layers are producing increased thermal contrasts. The fact that the thermal resistance of a feature is proportional to its thickness and inversely proportional to its thermal conductivity, in combination with the efficient long thermal excitation time, are producing an enhanced detectability of the hidden feature if rising its thickness, as more heat is deposited on the mosaic layer. The thermal behaviours overview of the simulated models M1-M5 for different tesserae thicknesses is illustrated in Figure 6.19.

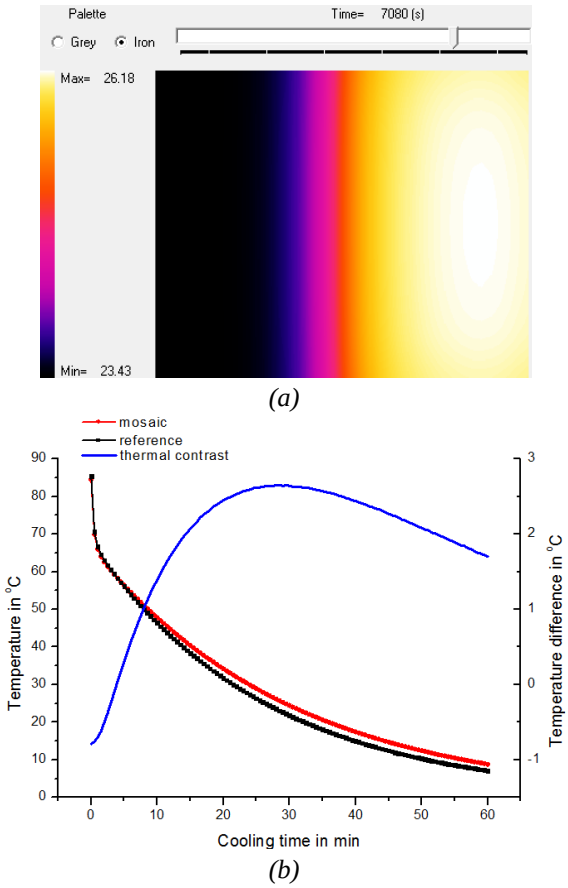

Fig. 6.18: *(a) Surface temperature gradient at the time of maximum thermal contrast occurrence and (b) Calculated surface temperature decay plots above reference and covered mosaic points and the respective temperature difference curve. for the 2mm M1-M5 model.*

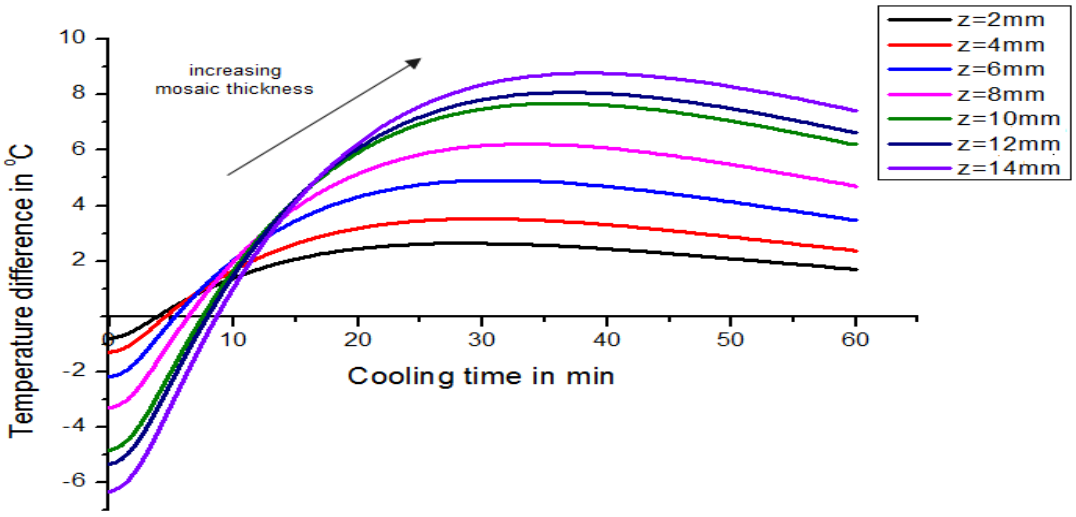

Fig.6.19: *Temperature difference curves as a function of cooling time, calculated for mosaic thicknesses from 2mm to 14 mm for the M1-M5 simulations.*

In the second series of simulations (M2-M5), similar results were acquired with short deviations due to the fact that the glass tiles were replaced by the marble mosaic layer, thus the thermal resistance of the subsurface feature was changed. The calculated thermal image acquired at the time point of maximum thermal contrast occurrence and the corresponding temperatures and thermal contrast curves vs. cooling time for the 2mm model are presented in Figure 6.20, where a peak thermal contrast of 2.68 ^{0}C was calculated at the time of 31.5min after the beginning of the cooling down process. As in the case of the glass tiles structure, the thinner marble layer can be still detected by producing a measurable temperature difference on the surface of the panel, while as the tesserae thickness was increased stronger thermal effects were produced, as illustrated in Figure 6.21.

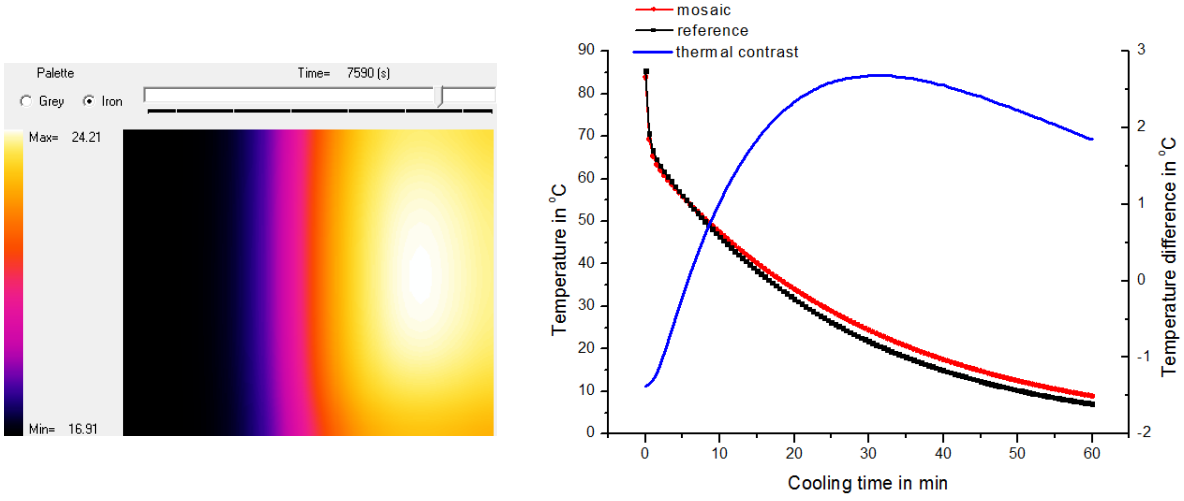

(a) *(b)*

Fig. 6.20: *(a) Surface temperature gradient at the time of maximum thermal contrast occurrence and (b) Calculated surface temperature decay plots above reference and covered mosaic points and the respective temperature difference curve for the 2mm M2-M5 simulation model.*

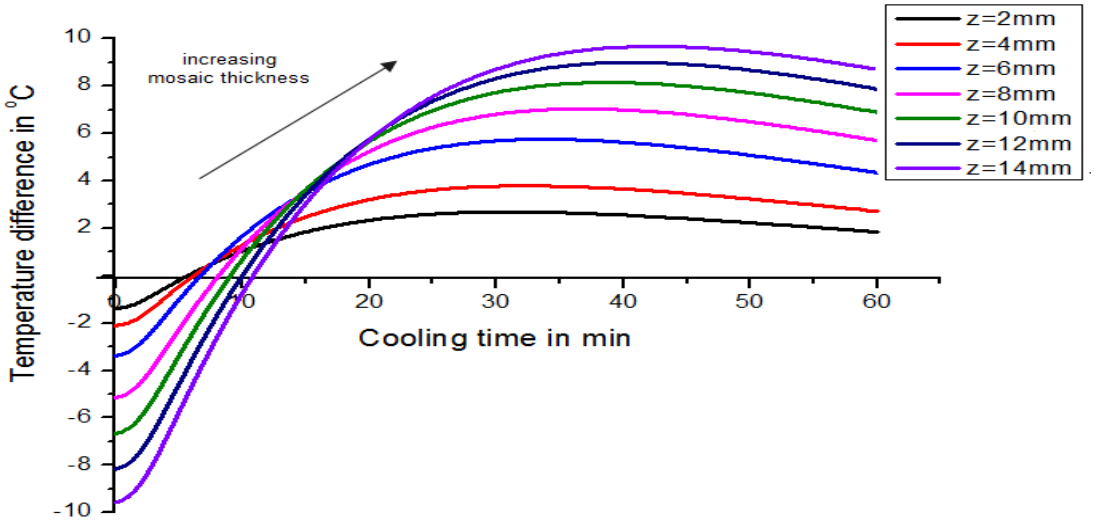

Fig.6.21: *Temperature difference curves as a function of cooling time, calculated for mosaic thicknesses from 2mm to 14 mm for the M2-M5 simulations*

6.5.2.2 Modelling of the hydraulic covering intervention

Similar procedure was followed in order to investigate the effect of tiles thickness increase for the glass (M3) and the marble tesserae (M4) mosaics respectively, under the covering intervention with hydraulic mortar (M6). As regards the first set of modelling (M3-M6), the calculated results revealed that the reference area presented in all simulations a slower heat loss rate with respect to the corresponding heat loss rate of the covered mosaic area, regardless the thickness of the tiles. However, as greater was the mosaic thickness the greater was the temperature difference calculated above the two areas, demonstrating that the heat loss rate from the mosaic surface was increased in analogy with its tiles thickness increase. The reverse thermal behaviour (impedance of heat deposition on the mosaic subsurface) that this simulated structure presented, indicates as well that the thermal response of the investigated structure is strictly related to its lay up and the thermal properties of each layer have a significant role to the thermal characterisation and response of the structure. This can be more clearly observed from Figure 6.22a where the thermal response of M3-M6 model for different glass mosaic thicknesses is presented. As in the case of cover influence, in terms of simplicity and clarity the thermal contrast curves plotted on the respective graph are presenting the reversed thermal behaviour than that observed during the numerical testing, as the ΔT to time curves have been obtained by subtracting the temperature of the mosaic surface from that of the reference panel.

Contrary, the influence of tiles thickness in the series of M4-M6 simulations followed the thermal behaviour observed in the two layers cover models with the differentiations observed as regards the maximum thermal contrast and the correspondent maximum time point, being attributed to the different material of the covering layer. However, as can be confirmed from the thermal contrast curves vs. cooling time in Figure 6.22b by increasing the marble tesserae thickness, the increased heat accumulated on the mosaic layer is enhancing its detectability.

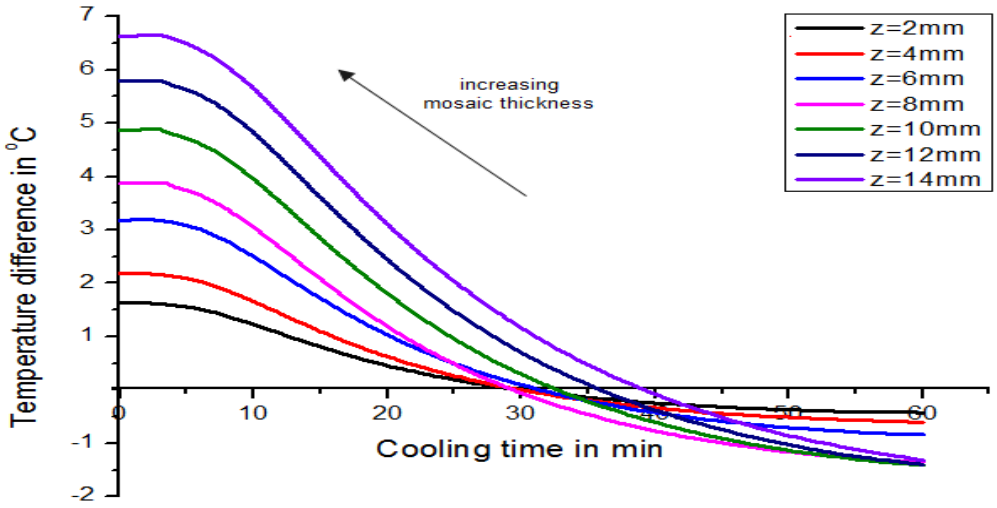

(a)

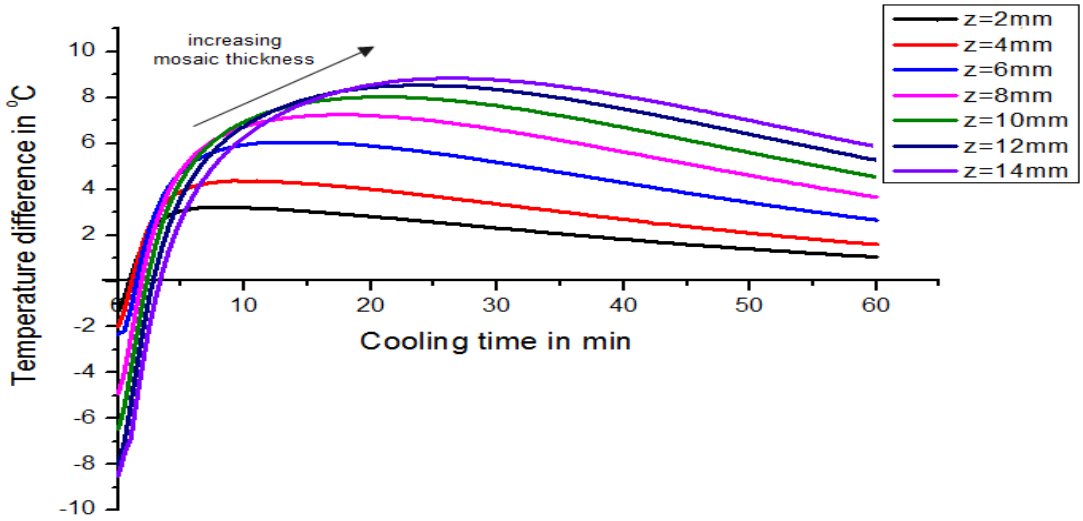

(b)

Fig.6.22: *Temperature difference curves as a function of cooling time, calculated for mosaic thicknesses from 2mm to 14 mm for (a) the M3-M6 simulations and (b) the M4-M6 simulations.*

6.5.3 Effect of mosaic thermophysical properties in plastered mosaics detection

The last series of numerical simulations investigated the influence of the mosaic thermophysical properties on the detection of the hidden layer. Considering as unknown parameter the nature of the mosaic material beneath the plaster, simulations were performed on the 2 cm covering models by changing the properties of the hidden material in each individual simulation. The influence of mosaic thermophysical properties on its detectability was investigated for both the cement/lime and hydraulic coverings respectively. In each particular model, the thermal conductivity, specific heat and mass density were altered, affecting the thermal effusivity and diffusivity of the hidden feature and thus the produced thermal contrast between the reference and covered mosaic areas. The properties inputted in this series of models are presented in Table 6.3. Essentially, the thermal behaviour (produced thermal contrast) is related, as presented above, to the effusivity difference between the plaster and the mosaic. As a result, this material property can indicate the rate at which the mosaic can be identified beneath the

plaster. On the other hand, in order to evaluate the produced visibility in terms of mosaic thermal diffusivity, this was performed considering the assumption that during the cooling down process, after bringing the sample to a moderate uniform temperature, it starts loosing heat from its surface, while inside the sample the temperature gradient between the surface and the deeper layers is producing a conductive heat flow. This phenomenon is taking place in each individual internal layer (i.e. conductive heat flow is also presented on the mosaic layer). As a result, the amount of heat reaching the surface during cooling down is related to the diffusivity that each of its internal layers renders. In this subsection the thermal response of the modeled covered mosaics was evaluated with respect to the parameter of thermal effusivity. However, as it will be presented below, the examination of the thermal response of the structure with respect to the mosaic thermal diffusivity is also important in order to quantitative estimate the thermophysical properties of the hidden structure.

Table 6.3: *Mosaic thermophysical properties for the creation of the models*

Thermal Conductivity ***($Wm^{-1}K^{-1}$)***	***Specific heat*** ***($Jkg^{-1}K^{-1}$)***	***Density*** ***(kgm^{-3})***	***Thermal Effusivity*** ***($Ws^{1/2}\ m^{-2}K^{-1}$)***	***Thermal Diffusivity*** ***($x10^{-7}m^2\ s^{-1}$)***
1	*700*	*1500*	***1024***	***9.5***
1.5	*800*	*1800*	***1469***	***10.4***
2	*900*	*2100*	***1944***	***10.6***
2.5	*1000*	*2300*	***2398***	***10.9***
3.3	*1100*	*2700*	***3130***	***11.1***
4.1	*1200*	*3000*	***3841***	***11.4***
4.5	*1300*	*3000*	***4189***	***11.5***

As a result seven different models were created, investigating the visibility of the covered mosaic for materials having different thermophysical properties. Figure 6.23 shows the calculated temperature gradient images from the two layers simulation model, for mosaics with thermal effusivity values of 1024 $Ws^{1/2}\ m^{-2}K^{-1}$ and 3130 $Ws^{1/2}\ m^{-2}K^{-1}$ respectively. As can be seen, the greater the value of the hidden mosaic thermal effusivity, the greater the difference of surface temperatures above the mosaic and the mosaic- free areas, indicating the increased contrast produced between the two areas. More specifically, for a hidden material having thermal effusivity of 1024 $Ws^{1/2}\ m^{-2}K^{-1}$, the peak thermal contrast was calculated at t=29 min and with a temperature difference value of 2.73^0C, while for the hidden material having thermal effusivity of 3130 $Ws^{1/2}\ m^{-2}K^{-1}$ an enhanced detectability was observed as a maximum thermal contrast of 6.83 ^{0}C at t= 32.5 min was calculated. Similar results were obtained as well for the hydraulic mortar covering intervention as can be seen from Figure 6.24. As higher was the thermal effusivity of the covered material the greater was its detectability related with temperature differences observed on the simulated surfaces. For instance, the 1469 effusivity model presented a peak thermal contrast of 3.29 ^{0}C at t= 8.5 min and the 2398 effusivity model had the same peak at t=13.5 min in the range of 6.26 ^{0}C.

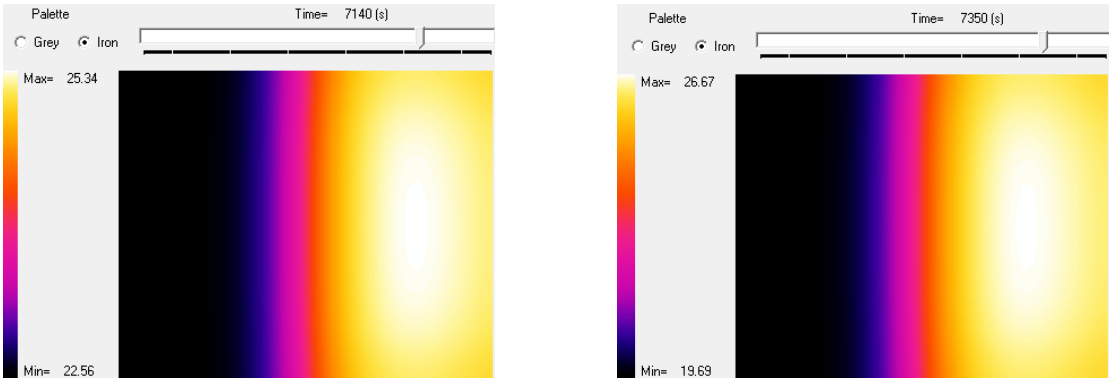

(a) *(b)*

Fig 6.23: *Surface temperature gradients of the two layers covering intervention models for hidden mosaic layers having thermal effusivities of (a) 1024 $Ws^{1/2}$ $m^{-2}K^{-1}$and (b) 3130 $Ws^{1/2}$ $m^{-2}K^{-1}$.*

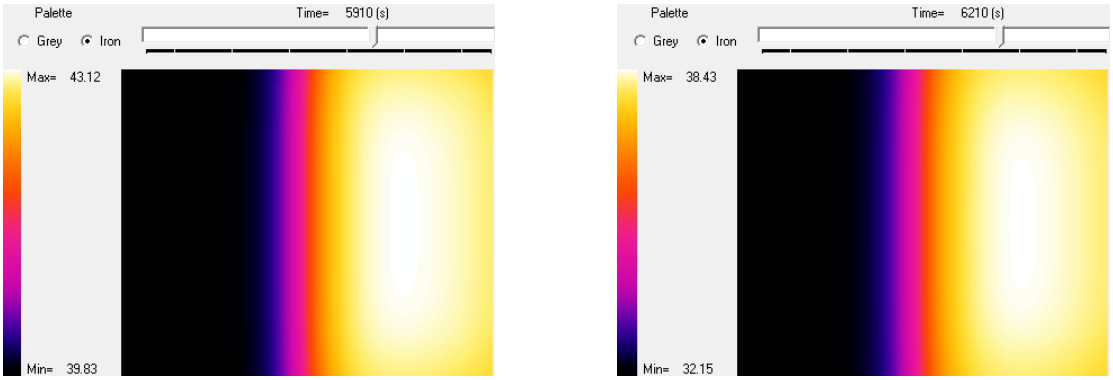

(a) *(b)*

Fig 6.24: *Surface temperature gradients of the hydraulic covering intervention models for hidden mosaic layers having thermal effusivities of (a) 1469 $Ws^{1/2}$ $m^{-2}K^{-1}$and (b) 2398 $Ws^{1/2}$ $m^{-2}K^{-1}$.*

The above observations are summarized in Figure 6.25, where the thermal responses of the structures are presented in terms of thermal contrast curves vs. cooling time. As can be seen, increasing the thermophysical properties of the hidden material, an enhanced seeing-through condition is observed. Slight differences as regards the thermal contrast values were observed in the two models which are deduced to the thermal properties of the covering layers and thus to the differences of the reflection coefficient of the two media.

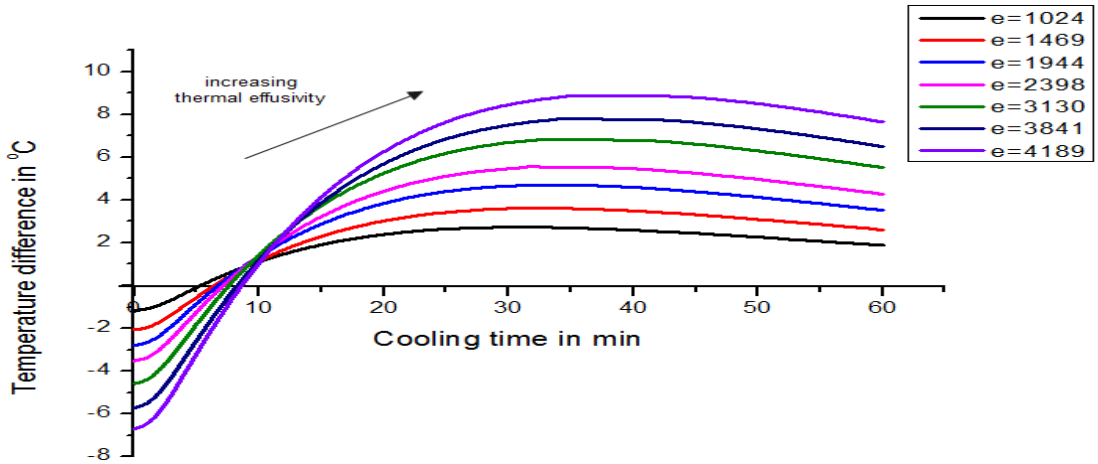

Fig.6.25a: *Temperature difference curves as a function of cooling time, calculated for the two layers covering intervention.*

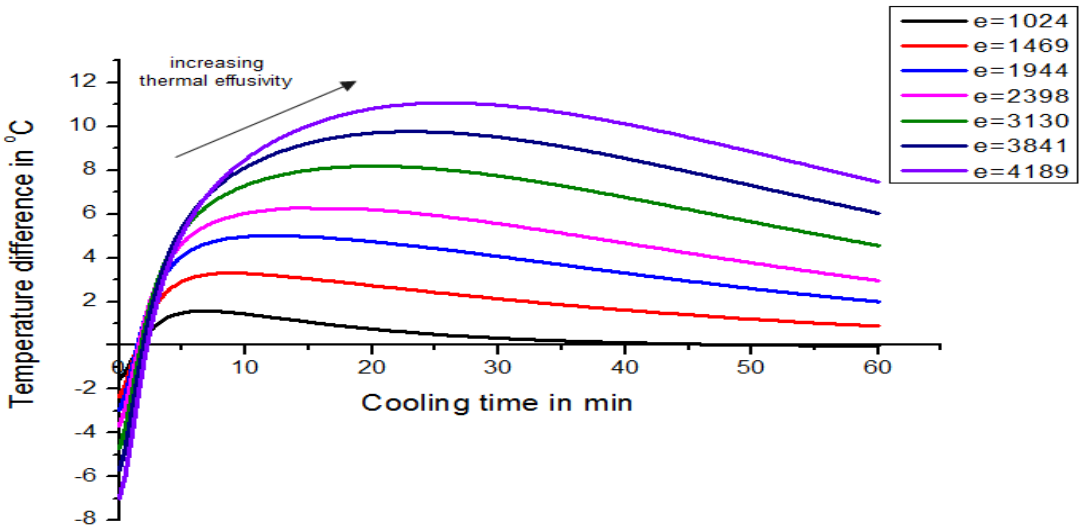

Fig.6.25b: *Temperature difference curves as a function of cooling time, calculated for the hydraulic mortar covering intervention.*

6.5.4 Summary of numerical simulation results

As presented above the potential of cooling down thermal NDT for the detection of hidden mosaics beneath plaster was numerically evaluated by varying important parameters that affect the feature of interest identification. In each individual analysis, the characteristic maximum of temperature difference above the reference and above the mosaic areas as well as the respective distinct times of this maximum occurrence were calculated, aiming to correlate the variation of these physical quantities with respect to the parameter investigated in each set of numerical simulations (covering thickness, mosaic thickness and mosaic thermophysical properties).

The variation of the peak thermal contrast and peak time values with respect to covering thickness increase, are illustrated in Figure 6.26. The graphs give an idea of the capabilities of using cooling down thermography as a method for identifying hidden mosaic artefacts beneath different covering interventions. Obviously as can be seen from these plots, for thicker covering interventions the hidden mosaic layer can be identified as well, despite the reduced ΔT produced. Contrary, the simulated thermographic monitoring of thinner interventions can produce a faster seeing-though condition of the covered feature. As a result in terms of mosaic detectability, the depth at which the mosaic is located to plays a significant role to its identification. However, numerical simulations revealed that the contrast produced is also related to both mosaic's and plaster's thermophysical properties, as differentiations were observed from the comparative study of the results acquired. In particular the simulated models with the marble tesserae, produced a more enhanced visibility of the hidden mosaic with respect to the models simulating the glass consisted structures, as an increased ΔT was calculated in the former covering simulations regardless the covering material used. The visibility produced from the above presented numerical results can be attributed to the thermal conductivity differences, that each material used for the manufacturing of the panels, possesses. In particular marble has the higher value with respect to that of the glass and plastering materials, enabling this subsurface layer to be more clearly

detectable (enhanced temperature difference), as more heat can be accumulated on this internal layer. As regards the comparison of the two covering procedures, a more enhanced detectability was produced on the cement/lime intervention which could be a characteristic of the different heat transfer rates that these covering regimes present. In other words, both lime and hydraulic mortars present similar thermophysical properties indicating that the presence of cement in the two layers covering permits the efficient heat flow into the tesserae structure, contrary to the low conductivity regime presented in the hydraulic covering structures.

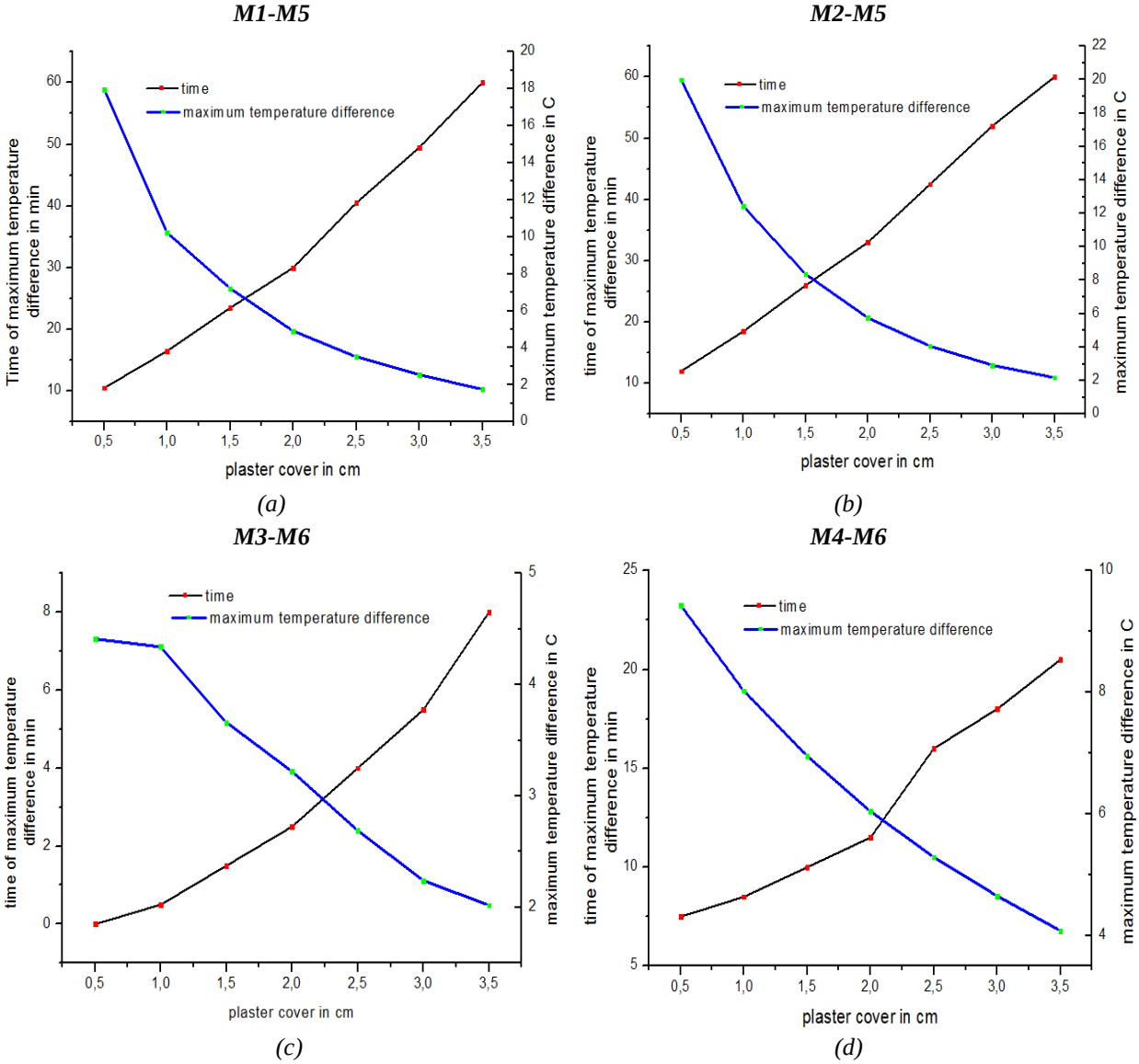

Fig.6.26: *Variation of maximum temperature differences and of the correspondent maximum times with respect to the plaster cover thickness for (a) M1-M5, (b) M2-M5, (c) M3-M6 and (d) M4-M6 numerical simulations.*

Along with the covering influence, the thickness of the tesserae layer is another parameter affecting the identification of the covered features. In Figure 6.27 the peak thermal contrast values and the correspondent time points associated with the mosaic thickness variation are presented, indicating that an enhanced visibility can be achieved for more resistive subsurface features. Furthermore, the results acquired from the numerical calculations showed that the hidden mosaic layers react better in heat

accumulation for rising their thickness in the two layers covering regime, as the plots in Figures 6.27a and 6.27b indicate. Contrary, an interesting observation was acquired as regards the influence of mosaic thickness to the thermal behaviour of M3-M6 set. As can be seen from the representative plot (Figure 6.27c), the time of the maximum thermal contrast was calculated to be the same for tiles thickness from 8 to 14mm. Additionally, the corresponding maximum times in this simulation have a relatively short range from 1 to 3 min. This different temporal condition is verifying as well, the observation detected on the covering influence investigation, that the glass tiles in this structure are acting as a heat resistance rather than a heat tank, as the increase of thickness is not importantly influence the heat accumulation in this structure and thus its thermal response in terms of peak contrast and peak time.

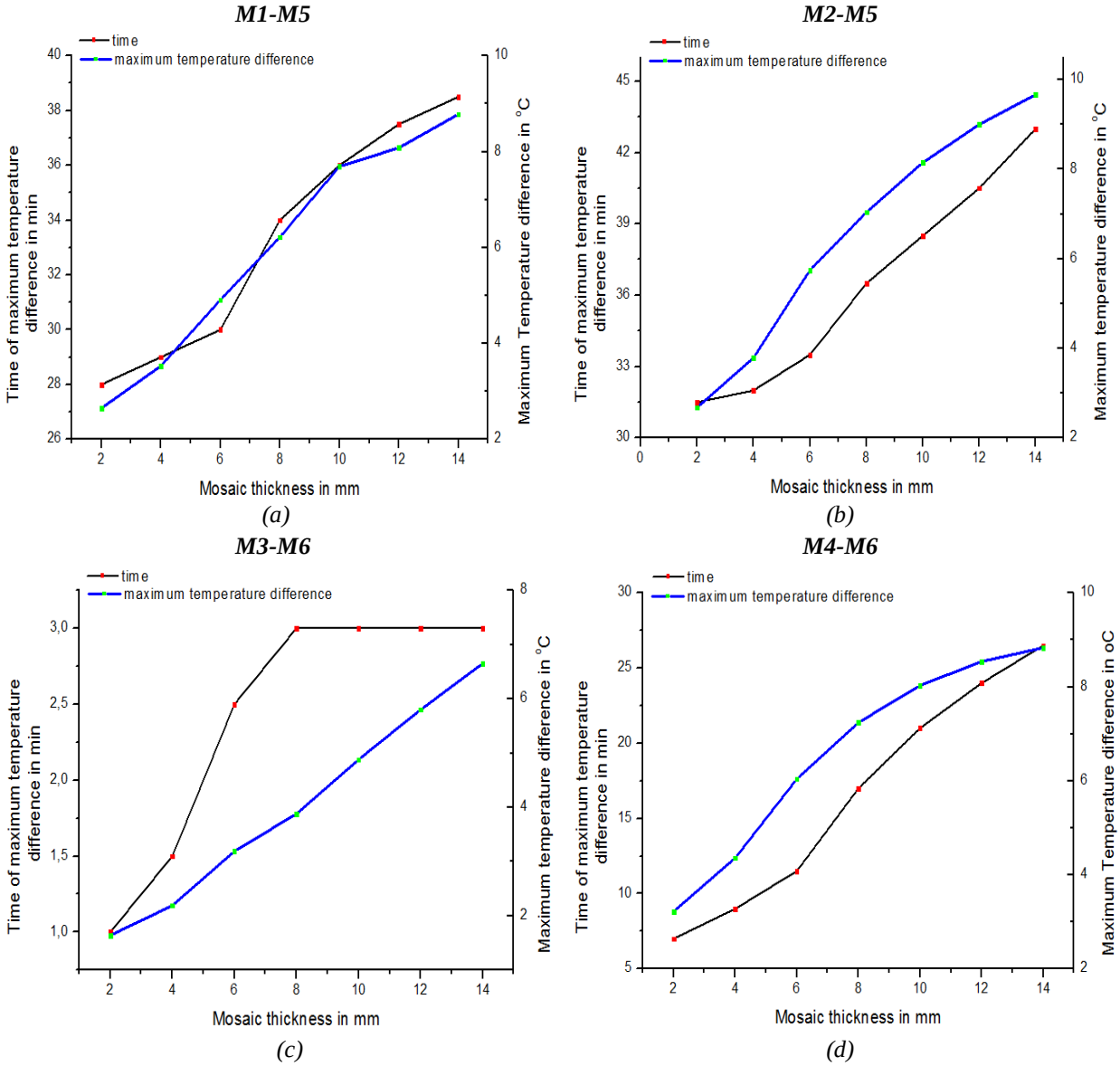

Fig.6.27: *Variation of maximum temperature differences and of the correspondent maximum times with respect to the mosaic layer thickness for (a) M1-M5, (b) M2-M5, (c) M3-M6 and (d) M4-M6 numerical simulations.*

Finally, the numerical studies conducted to evaluate the effect of mosaic thermal effusivity on its detection, indicated that as higher the thermal effusivity of the hidden mosaic the greater its detectability, verifying the enhanced detectability produced for the marble tiles with respect to that of

the glass tiles regardless the covering regime. As the effusivity of the covering layers remained constant, as greater was the thermal effusivity of the hidden feature the lower was its reaction in the conductive heat transfer back to the surface due to the produced temperature difference. In other words, the results verify that as higher is the thermal effusivity of the hidden layer with respect to that of the covering material, the greater is the heat accumulation in the hidden simulated mosaic layer.

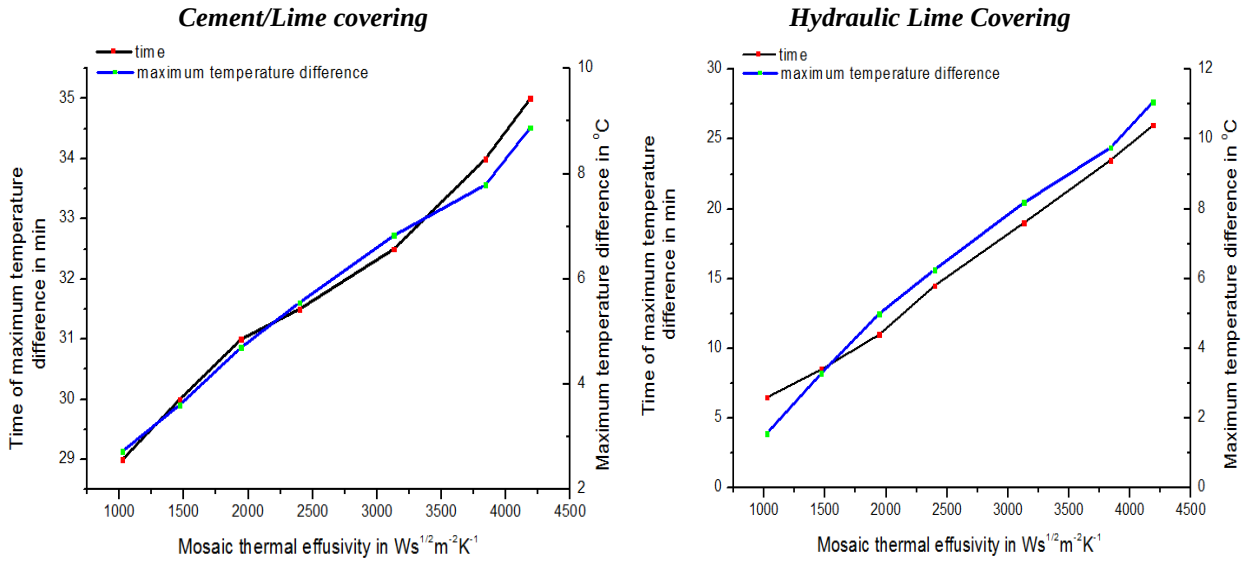

(a) *(b)*

Fig.6.28: *Variation of maximum temperature differences and of the correspondent maximum times with respect to the mosaic thermal effusivity for (a) lime/cement covering intervention and (b) hydraulic covering intervention.*

6.6 Experimental Results

As mentioned above, the experimental measurements were carried out by monitoring the cooling-down phase for 60 min after the application of a heat flux of 90 min duration on the investigated surfaces. The cooling down behaviour of the two panels was monitored acquiring time-history thermal data in a time interval of 30 s. In the following subsections, the results obtained characterising the thermal behaviour of each individual set, are interpreted in terms of thermal images, surface temperature decay and thermal contrast evolution curves. In particular, the main approach used in analysing the thermal data was to study the function of surface temperature decay vs. cooling time for selected points/areas with and without tesserae underneath them. These selected transient curves were compared and difference curves (between transients above a plastered mosaic area and above a mosaic-free reference area) were calculated in four control points and by measuring the average temperature on these respective surfaces, as presented in Figure 6.29.

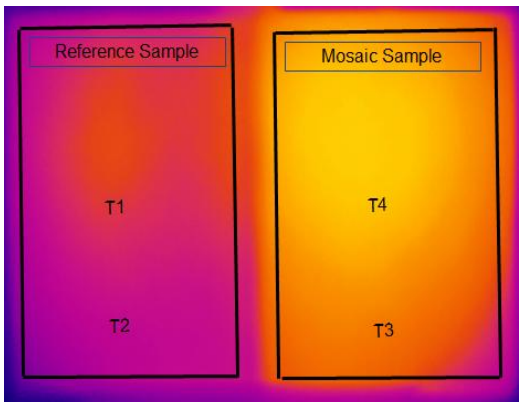

Fig. 6.29: *Selection of representative points and areas for the analysis of the experimental thermal data.*

6.6.1 Samples M1-M5

The first set of samples examined, was consisted of a two layers covering with cement and lime mortars respectively, which were hiding the mosaic layer made of glass tesserae with sheets of gold. Indicative thermal images from samples M1 and M5 obtained at the time points of 0, 10, 20, 30, 40, 60 min after the beginning of the cooling down procedure are presented in Figure 6.30, in which the right panel corresponds to the plastered mosaic and the left panel corresponds to the respective blank sample. As can be seen from the raw thermograms, increased thermal energy is deposited on the right surface with respect to the thermal energy deposited on the left surface. The different thermal responses detected over the two surfaces, are revealing the presence of the hidden mosaic layer beneath the coating plaster as the different type of material (mosaic layer) embedded into the structure is altering the cooling down behaviour on this respective area.

On the other hand, Figure 6.31 provides the temperature decay curves for both the mosaic and mosaic free pixels T4 and T1, along with the resulting thermal contrast curve. As can be seen, the temperature difference curve is characterised from a maximum ΔT_{max} at a distinct time t_{max}, revealing the point of maximum temperature contrast between the reference and the plastered mosaic pixels. More specifically, at the beginning of the cooling down process, the plot indicates a local negative ΔT value of -4.1^0C which has an upward trend, reaching initially zero three minutes after the beginning of the

cooling down recording, until its maximum value ΔT_{max} of 9.9 ^{0}C at t_{max} = 29.5 min. The signal after that slowly decays to a ΔT value of 7^{0}C at the end of the cooling down process. The aforementioned observations, derived from the temperature difference curve, can be confirmed by the representative thermal images acquired at 0, 10, 30 and 60 min (Figure 6.30). Initially, the surface temperature of the blank panel is greater to that of the mosaic sample (Figure 6.30a). However as the cooling down process is evolved (Figures 6.30b-f), this phenomenon is altered with the covered mosaic having increased thermal energy deposited on its surface and a slower heat loss rate. In other words, both the thermal images and the plot results are indicating that the reference sample M5 losses heat from its surface in a more rapid manner with respect to the specimen with the hidden mosaic (M1) underneath it.

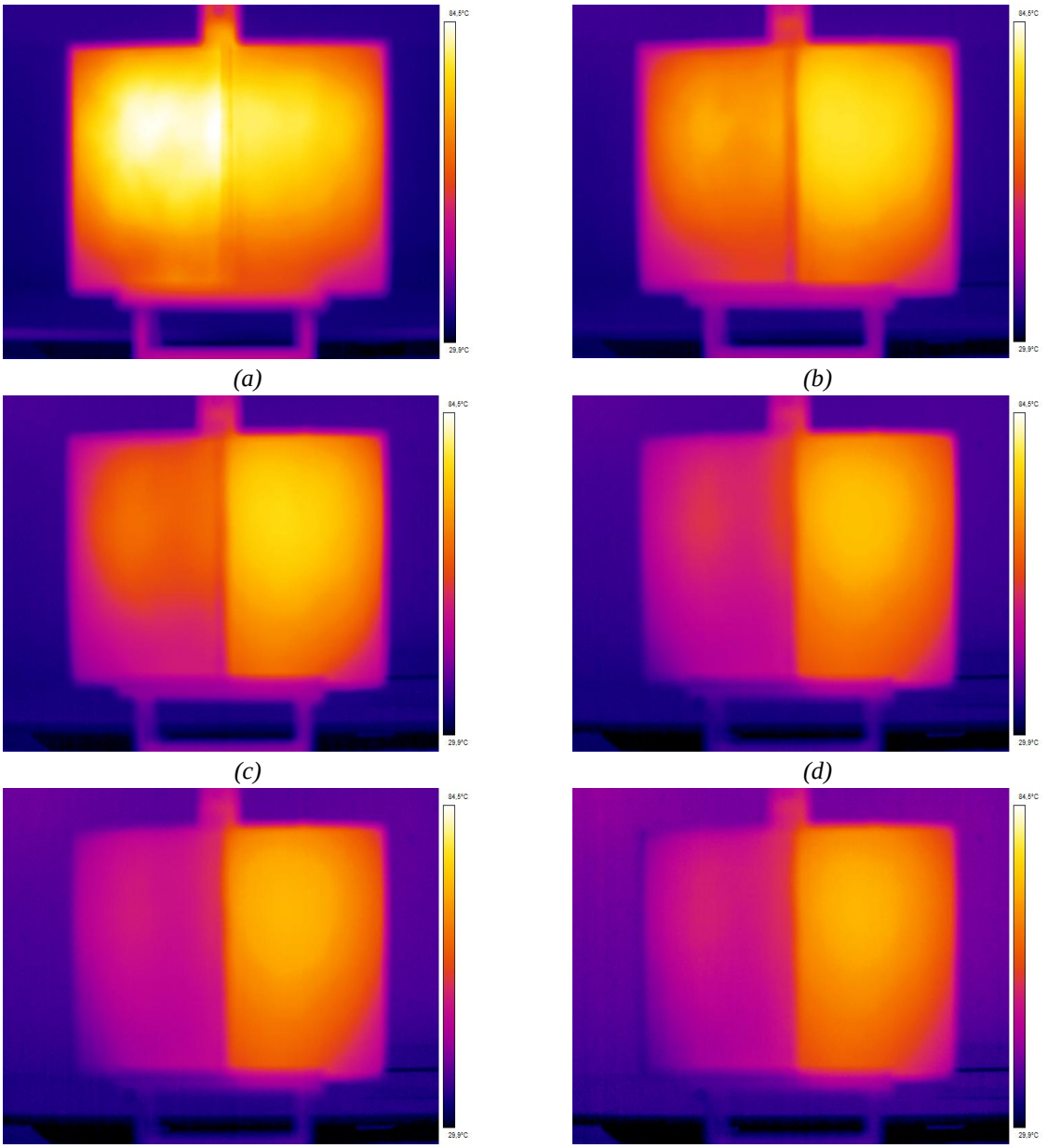

Fig. 6.30: *Thermal images of samples M1 – M5 at a) 0 min, b) 10 min, c) 20 min, d) 30 min, e) 40 min and f) 60 min after the beginning of the cooling down process. The left panel in each representative thermogram corresponds to the reference sample, whilst the right panel corresponds to the covered mosaic structure.*

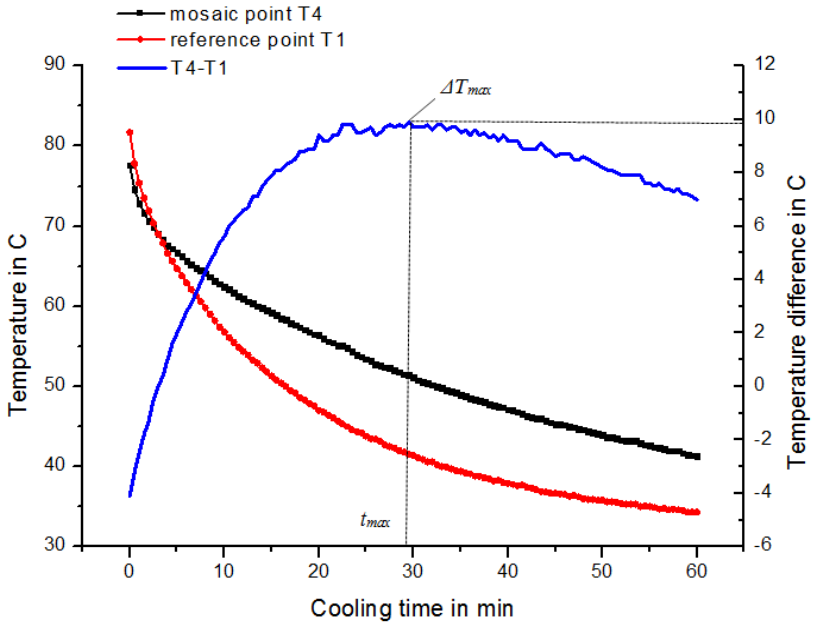

Fig. 6.31: *Transient curves above the reference point (T1) and above the mosaic covered point (T4) and the corresponding temperature difference curve with a maximum thermal contrast ΔT_{max} at a distinct time t_{max}.*

The thermal characterisation obtained from the second spot testing (T3/T2) and the measurement of the average temperatures over the investigated areas, produced similar results as in the case of T4/T1 spots analysis. The representative transient plots are illustrated in Figure 6.32. However, some small variations in terms of ΔT and t values were observed. In particular, at the beginning of the cooling down process, the local ΔT values of -2.5 °C and -3.3 °C respectively were distinguished, while nearly at the half of the process a ΔT_{max} of 8.2 °C at t_{max} = 28.5 min and a ΔT_{max} of 8 °C at t_{max} = 29 were detected for both the spot and area analyses respectively. The two thermal contrast curves after reaching their maximum values, they followed in a similar manner a slight decay to the ΔT values of 5.6 °C and 5.2 °C respectively.

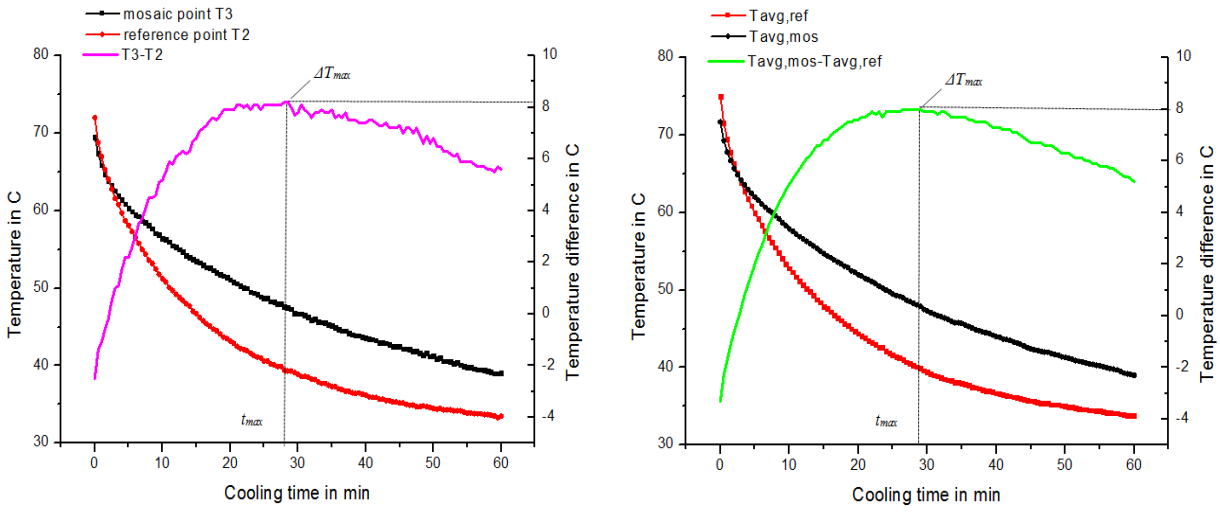

Fig. 6.32: *a) Transient curves above the reference point (T2) and above the mosaic covered point (T3) and the respective temperature difference curve with the corresponding maximum thermal contrast ΔT_{max} at the distinct time t_{max}. b) Thermal behaviour acquired after calculating the average temperatures over the investigated areas.*

The comparison of the above presented results from the three distinct data analysis procedures, verified that the cooling rate of the blank sample M5 was greater with respect to the cooling rate of the mosaic consisted sample and as the cooling down process was deployed, an enhanced contrast was presented. The temperature difference evolution curves were following the same gradient, with small differentiations as regards the ΔT and t values indicating that the quantity of heat delivered to the sample surface directly influences their temperature decays and in addition the resulting thermal contrasts. However in general it can be confirmed that cooling down thermography was able to qualitatively detect the glass tiles beneath the two layers of the covering intervention. The maximum thermal contrasts and the correspondent times of this occurrence acquired from the three different analysis procedures are summarized in Table 6.4.

Table 6.4: *Maximum temperature differences and the corresponding times of occurrence for M1-M5 set*

	T4-T1	***T3-T2***	$T_{avg,mos} - T_{avg,ref}$
ΔT_{max} in ^{0}C	*9.9*	*8.2*	*8*
t_{max} in min	*29.5*	*28.5*	*29*

6.6.2 Samples M2-M5

The next set of experimental measurements evaluated the potentiality of cooling down thermography to identify marble tesserae tiles beneath the cement/lime covering intervention. In particular, sample M2 was consisted of marble tesserae and tested in comparison with the respective two layers covering blank sample M5. As regards the heat emittance from the surface of the aforementioned panels, similar results were observed as in the case of the glass tesserae structure. This can be seen from Figure 6.33, which illustrates representative thermograms acquired at the beginning of the cooling down process and 20, 30, and 50 min as this process was evolved. Similarly to the previous measurement, increased thermal energy is deposited on the right panel in which the mosaic structure was embedded to, verifying the seeing -through condition of the marble tesserae layer under the cement/lime covering intervention.

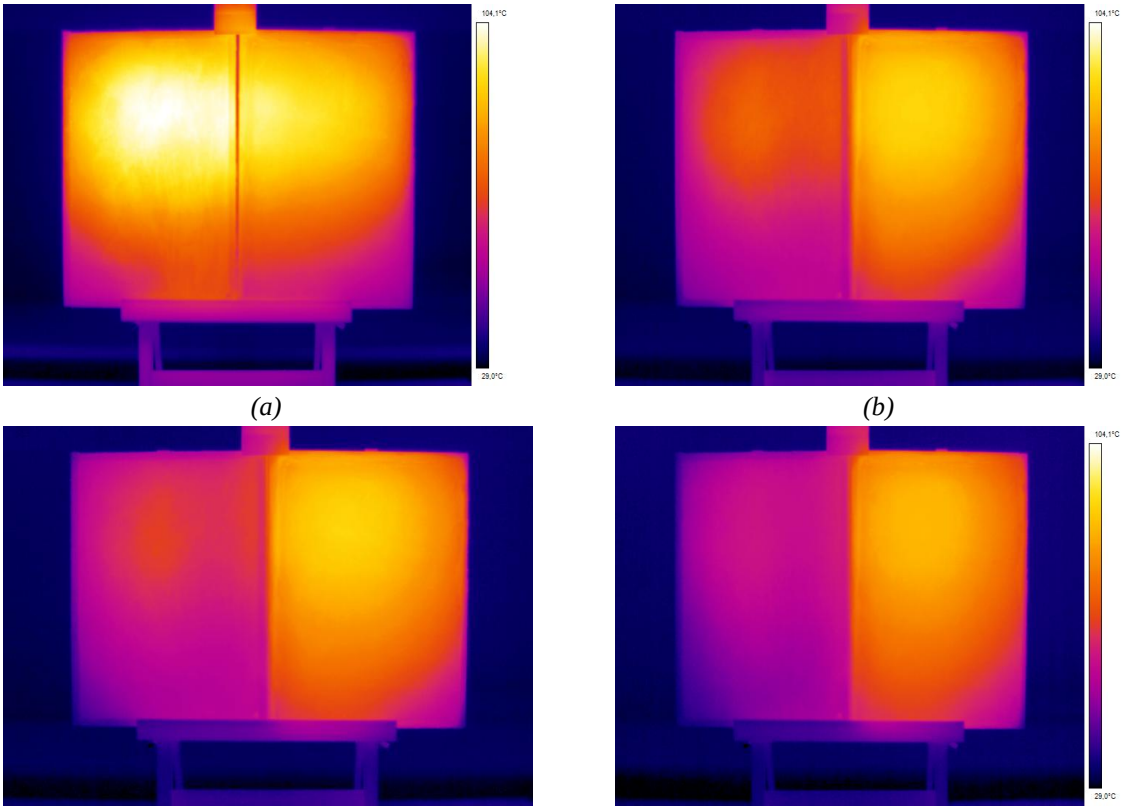

Fig. 6.33: *Thermal images of samples M2 – M5 at a) 0 min, b) 20 min, c) 30 min, and d) 50 min from the beginning of the cooling down process. The left panel in the thermal images corresponds to the reference sample, while the right panel corresponds to the covered mosaic structure.*

Figure 6.34 provides the plot results of the temperature decay curves and the representative thermal contrast evolution curves, acquired both from the spots and area analyses. During the cooling down process, it was observed that the temperature difference of the opposed accommodated pixels at the centres and the edges of the panels, while starting from -7.7 ° C and -2.3 °C respectively, after nearly the half of the cooling down they reached their maximum values of 12.4° C and 8.8 °C respectively, and finally the temperature differences followed a descending slope to 8.8° C and 5.8° C. Similarly, by measuring the average temperature over the two surfaces, the thermal contrast curve started from a negative value of -5.8 ^{o}C, until reaching its maximum value of 10.9° C, 32 min after the beginning of the cooling down and then followed a decay trend to 7.7°C. From the above description of the thermal contrast evolutions vs. cooling time, it can be seen that differences in thermal contrast levels were exhibited in this case as well (mainly between the two spot analyses) confirming the non uniformity of heat application on the investigated surfaces. However, despite the differentiations observed as regards the ΔT and t values, the three temperature difference curves were following the same behaviour verifying the detectability of the hidden mosaic produced though the thermal images elaboration.

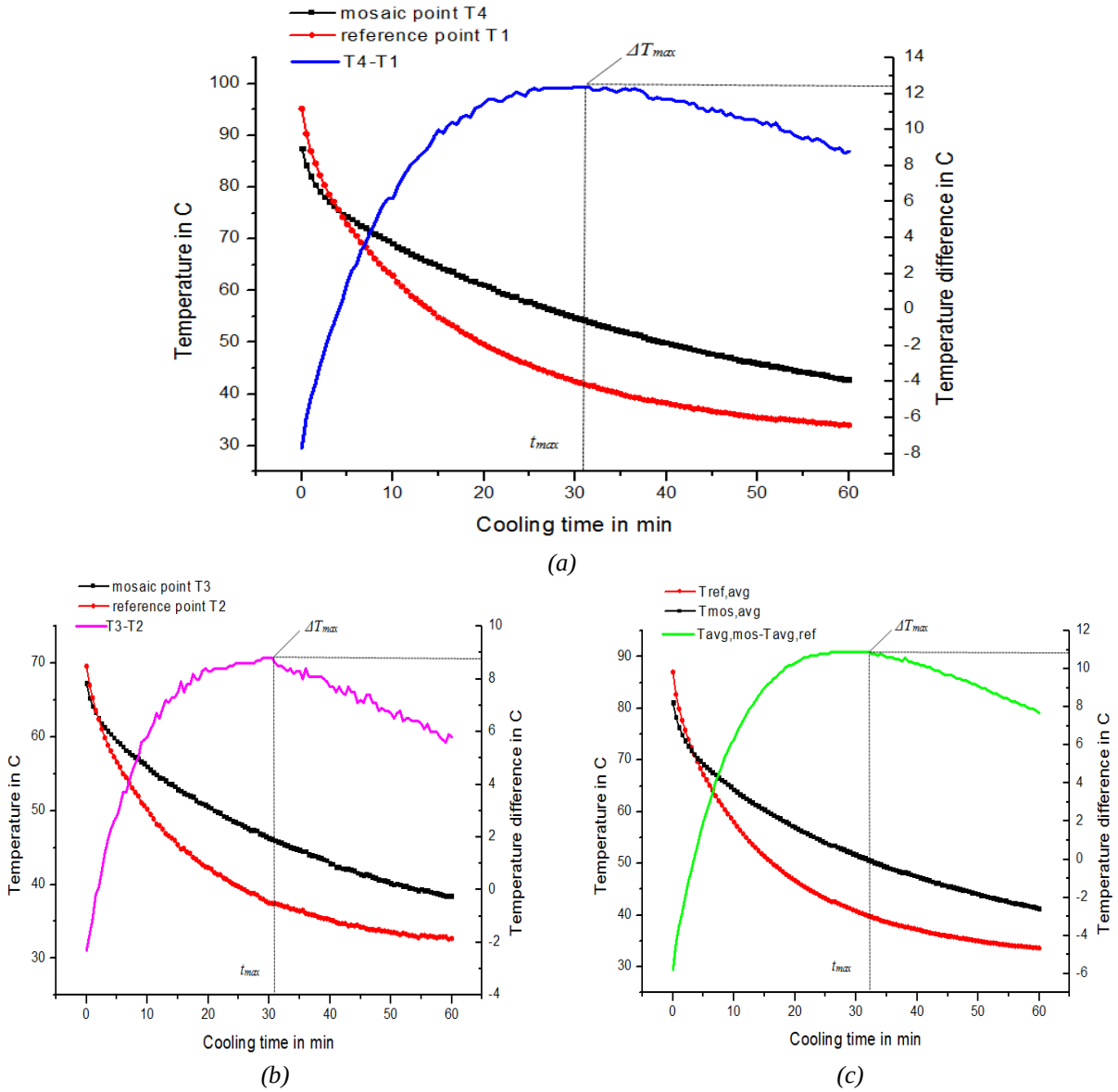

Fig. 6.34: *Transient curves above the reference panel and above the mosaic covered panel along with the representative temperature difference curve for M2-M5 specimens for a) T4-T1 b) T3-T2 and c) Tmos,avg – Tref,avg analyses.*

Comparing the thermal response of glass tesserae and marble tesserae under the two layers covering intervention, slightly increased thermal contrast levels, as well as longer times of the maximum contrast appearance were detected in the present test. As a result, since the only difference of the M2 investigated plastered mosaic from the respective one in the previous testing was the tesserae material, the small differences can be deduced to the presence of a different subsurface material (with dissimilar thermal properties) under the same layers of plaster, verifying the observation derived from the respective numerical simulations. The experimental results of maximum thermal contrast ΔT_{max} and the related maximum time points t_{max} monitored in M2-M5 test are summarized in the table below.

Table 6.5: *Maximum temperature differences and the corresponding times of occurrence for M2-M5 set*

	T4-T1	**T3-T2**	$T_{avg,mos} - T_{avg,ref}$
ΔT_{max} *in* ^0C	*12.4*	*8.8*	*10.9*
t_{max} *in min*	*31*	*30.5*	*32*

6.6.3 Samples M3-M6

The next set of experimental testing, evaluated the thermal behaviour of the glass tiles beneath a coating of hydraulic mortar. As can be observed from the representative thermal images of Figure 6.35, the replacement of the covering layer produced a different cooling down behaviour and thus different results as regards the identification of the hidden mosaic structure. More specifically from the representative thermal images, where the left panel corresponds to the plastered mosaic and the right panel corresponds to the blank sample, it was observed that the mosaic constructed panel cools down more rapidly contrary to the observed thermal responses of the plastered mosaics in the previous experimental measurements. In addition, along with the reverse cooling down behaviour exhibited in this case, a reduced contrast between the two areas of interest was observed, indicating the reduced visibility produced as well on the detection of the hidden tesserae structure.

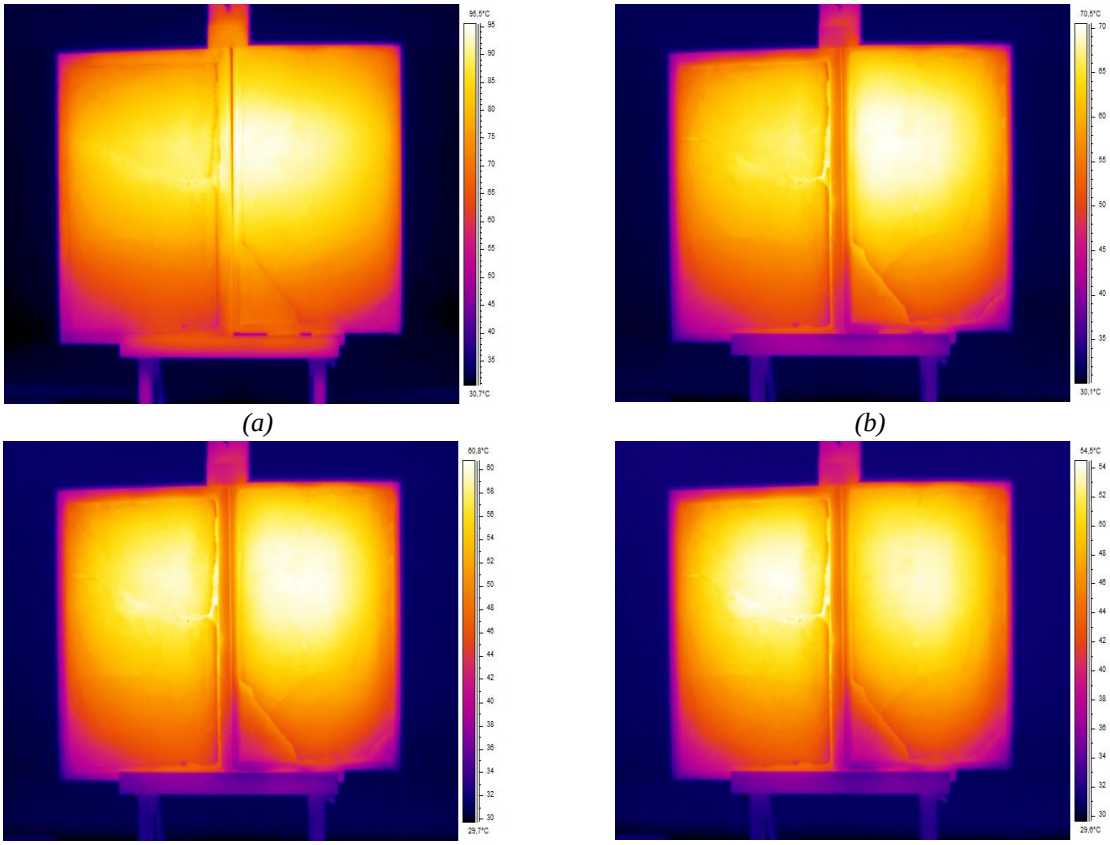

(a) *(b)*

(c) *(d)*

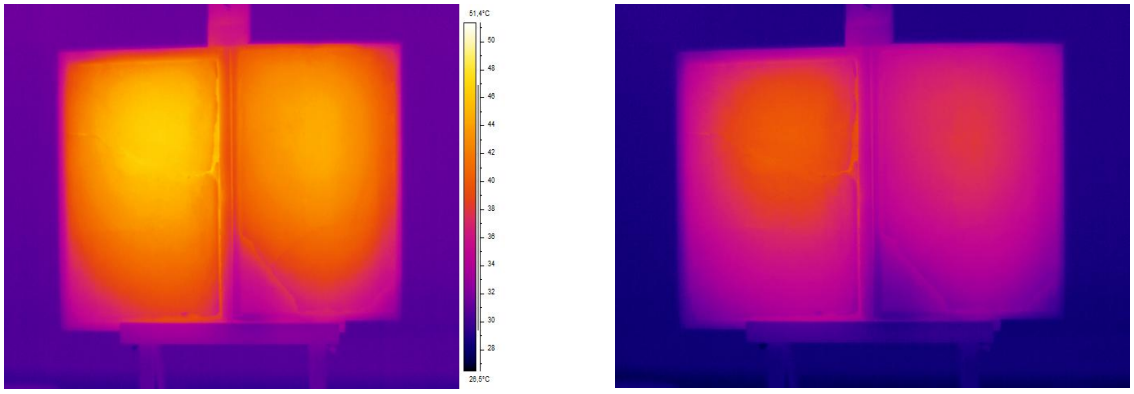

(e) *(f)*

Fig. 6.35: *Thermal images of samples M3 – M6 at a) 0 min, b) 10 min, c) 20 min, d) 30 min, e) 50 min and f) 60 min from the beginning of the cooling down procedure. The left panel in each representative thermogram corresponds to the mosaic sample, whilst the right panel corresponds to the reference structure.*

The dissimilar thermal behaviour detected on the M3-M6 pair can be further confirmed by the respective transient temperature plots, illustrated in Figure 6.36. The thermal contrast curves presented in this figure have been retrieved by subtracting the surface temperature of the mosaic sample from that of the reference sample. Thus, the temporal changes of the resulting thermal contrasts had the reverse responses during experimental testing than this presented in the plot. In particular, the first 30 min after the end of the heating up process, the surface temperatureT1 of the reference sample M6 was greater compared with the surface temperature T4 on the plastered mosaic (Figure 6.36a). Similarly as regards the edge pixels analysis (T3/T2), this phenomenon was occurred for the first 25 min (Figure 6.36b) and in the correspondent average temperature decay plot, this phenomenon was occurred for the first 27 min (Figure 6.36c). However, after these temporal points and until the end of the cooling down process, short temperature differences were detected with the temperature of the mosaic panel being slightly increased with respect the respective one of the blank surface, indicating that both panels loss heat from their surface with a similar rate. In terms of temperature contrast levels, the temperature difference of the opposed accommodated pixels at the centres and the edges of the panels, while starting from an value of 3.9 ^{0}C and 3.2 ^{0}C respectively, after 3 and 2.5 min respectively they reached their maximum absolute values of 4.4 ° C and 3.6 ° C and finally the temperature difference follows a decay slope and drops at -1.9° C and -1.6° C respectively. Similarly by calculating the average temperature over the areas of inspection, the thermal contrast curve reached a maximum value of 4.4 °C, 2.5 min after the beginning of the cooling down and then followed a decay trend to -1.9 ^{0}C. The plots indicate that the differentiations observed as regards the thermal contrast levels in the three inspection procedures are relatively short. Thus the thermal behaviour of the present inspected set does not seem to be a result of non uniform heat application, contrary it can rather be attributed to the thermal properties of the different layers which are composing this structure. As indicated through the numerical simulations, this specific thermal response of M3-M6 can be deduced to the relatively low thermal conductivity of the covering layer in addition with along the low heat absorption coefficient that glass tiles have. The low absorption coefficient that the glass tiles present, impede the heat diffusion into the mosaic layer

while the high thermal conductivity of the gold sheets facilitates the heat reflection to the surface of the panel. On the other hand, the heat accumulation observed on the blank region (similarly effects were produced in numerical analysis as well) can be deduced to the reduction of heat reflection rate back to the surface due to the low conductivity of hydraulic mortar used for the fabrication of these panels.

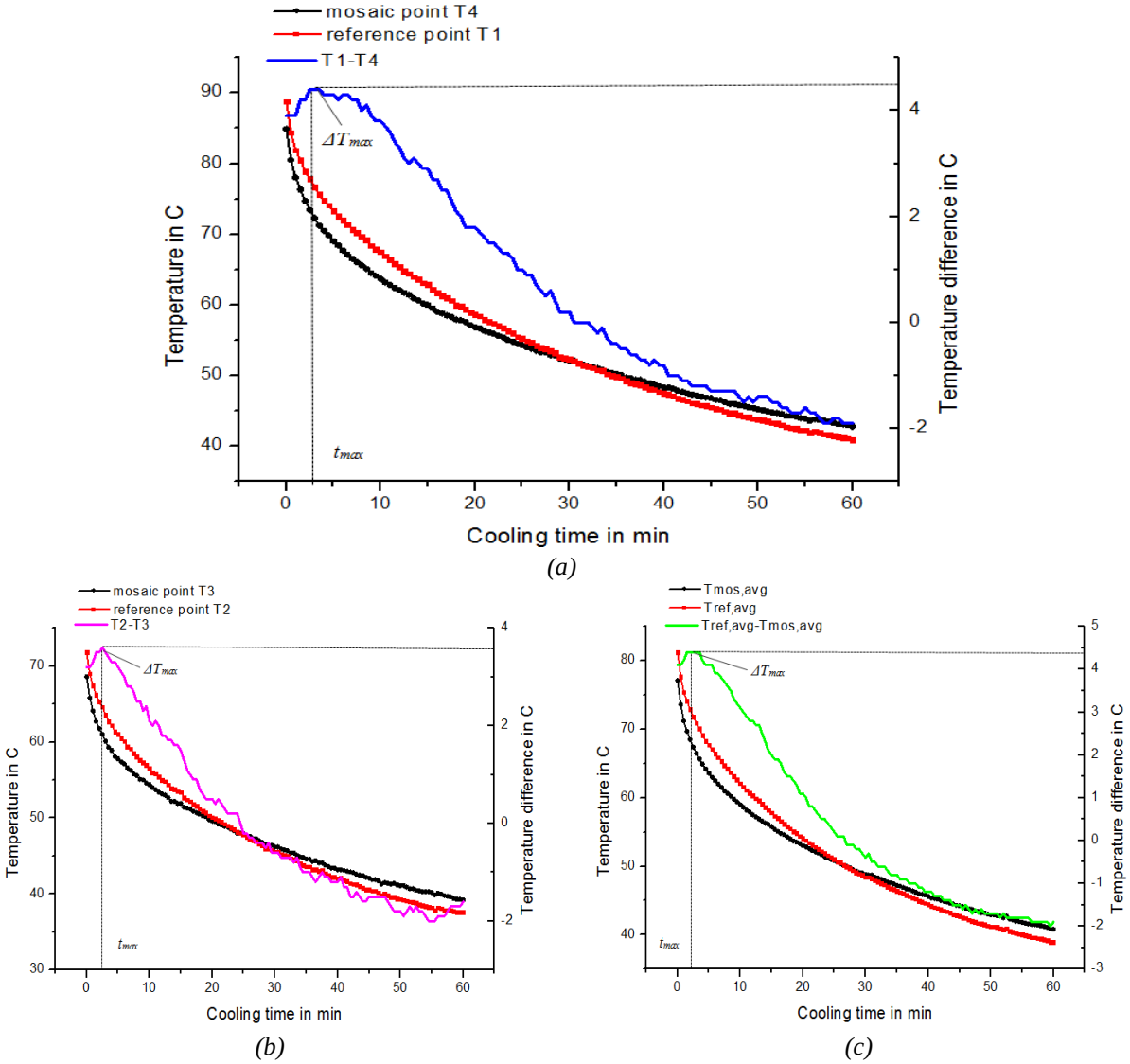

Fig. 6.36: *Transient curves above the reference panel and above the mosaic covered panel along with point the representative temperature difference curve with a maximum thermal contrast ΔT_{max} at a distinct time t_{max}. for a) T1-T4 analysis b) T2-T3 analysis and c)Tref,avg – Tmos,avg analysis.*

As mentioned above the thermal contrasts produced in this case, characterising the identification rate of the hidden glass mosaic, presented reduced values. This phenomenon was further accompanied with relatively short time points of the maximum thermal contrast appearance as summarised in Table 6.6. Thus, the best achieved visibility (the maximum thermal contrast) was detected nearly at the beginning of the cooling down process, indicating that the heat loss rate from the plastered mosaic surface was performed in a relatively rapid manner contrary to the other sets.

Table 6.6: *Maximum temperature differences and the corresponding times of occurrence for M3-M6 set*

	T1-T4	***T2-T3***	$T_{avg,ref} - T_{avg,mos}$
ΔT_{max} in ^{0}C	*4.4*	*3.6*	*4.4*
t_{max} in min	*3*	*2.5*	*2.5*

6.6.4 Samples M4-M6

The last experimental testing was performed for the marble fabricated panel covered with a layer of hydraulic plaster. By comparing the cooling down behaviour of the blank and mosaic consisted specimens, a seeing-through condition of the hidden marble tesserae layer was produced as indicated in the representative plots of the transient temperature and the resulting thermal contrasts curves on Figure 6.37. The temperature differences detected during the cooling down phase above the two areas of interest are indicating that increased thermal energy was accumulated on the plastered mosaic panel with respect to the energy deposited on the blank surface.

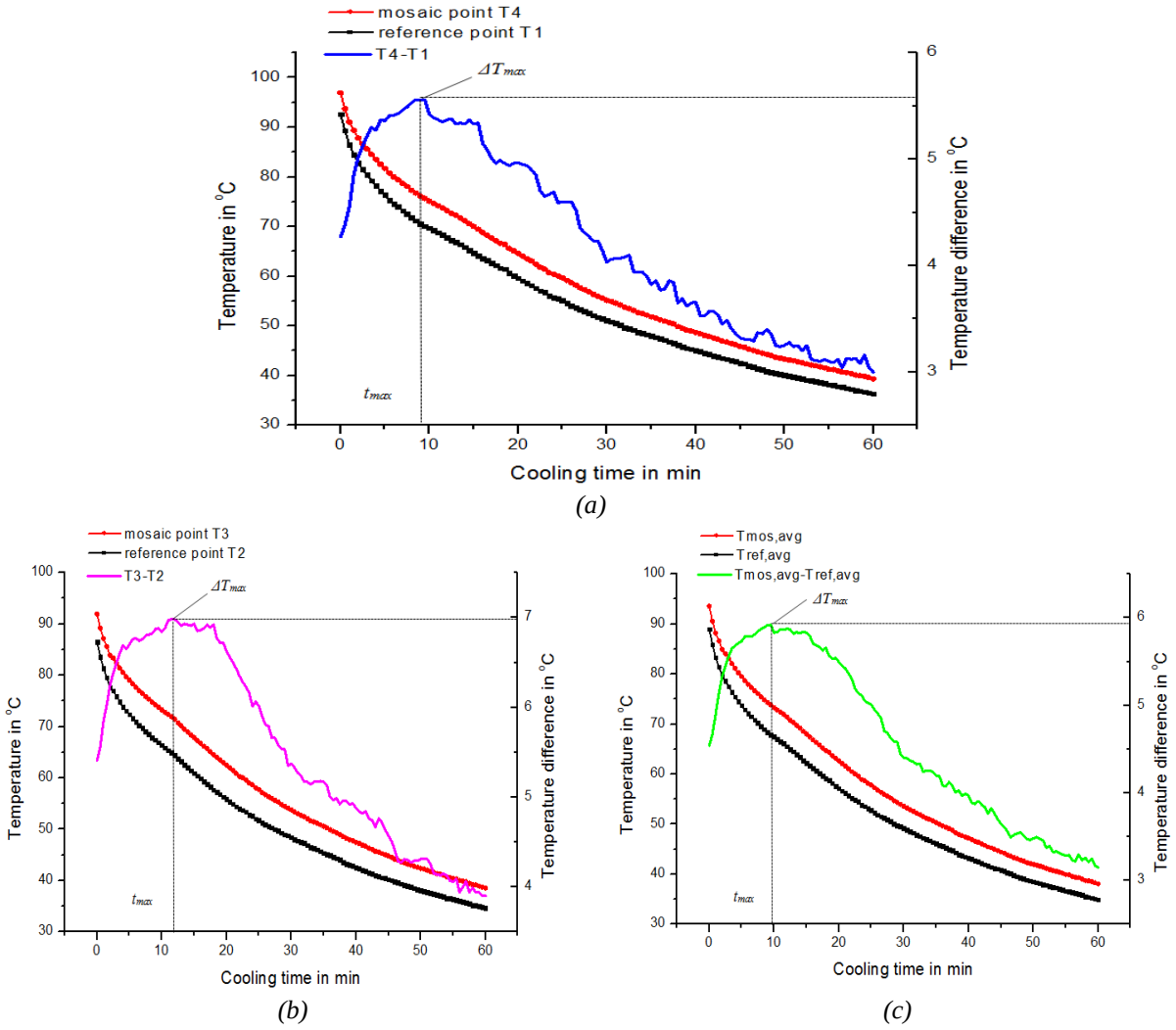

Fig. 6.37: *Transient curves above the reference panel and above the mosaic covered panel along with point the representative temperature difference curve with a maximum thermal contrast ΔT_{max} at a distinct time t_{max}. for a) T4-T1 analysis b) T3-T2 analysis and c)Tmos,avg – Tref,avg analysis.*

The thermal contrast evolutions derived from the different thermal data analyses followed the trend observed in the first two pairs of testing as the heat loss rate of the reference sample M6 was greater with respect to the heat loss rate of the plastered mosaic panel M4. More specifically as regards the T4-T1 analysis, a ΔT value of 4.27 ^{0}C was measured at the beginning of the cooling down process which has an upward trend reaching its maximum value of 5.56 ^{0}C at the time point of 9.5 min after the beginning of the cooling down process and then the signal decays to a temperature difference of 3 ^{0}C. Similar results were observed during the other spot and the area analyses procedures, with a ΔT_{max} of 6.98 ^{0}C at the time point of 11.5 min recorded for the T3-T2 analysis and a ΔT_{max} of 5.92 ^{o}C at the time point of 10 min recorded from the average temperature analysis.

The above results obtained made possible the detection of marble tesserae layer beneath the plaster, indicating as well the different tesserae material layered beneath the covering plaster as different cooling rates were detected on the surfaces of the hydraulic covering panels. In particular the marble tesserae absorb more heat from the glass tiles and the cooling rate of these structures is slower as a longer time of the maximum thermal contrast occurrence was observed in this case, revealing the different thermophysical properties of marble and glass tesserae structures. In Table 6.7, the experimental data of maximum of the temperature difference ΔT_{max} and the related time t_{max} are summarized for samples M4-M6.

Table 6.7: *Maximum temperature differences and the corresponding times of occurrence for M2-M5 set*

	T4-T1	***T3-T2***	$T_{avg,mos} - T_{avg,ref}$
ΔT_{max} **in ^{0}C**	*5.56*	*6.98*	*5.92*
t_{max} **in min**	*9.5*	*11.5*	*10*

6.6.5 Summary of experimental results

The experimental measurements, evaluating the potential of cooling down thermography for the reveal of plastered mosaics, were conducted in structures consisted of different tesserae materials, which were further covered by different layers of plaster. The seeing-through condition derived from the monitoring of the cooling down behaviour on selected spots and areas from the surface and the measurement of the resulting thermal contrasts in each particular test pair, was proven to be strongly related with the thermophysical properties of both the feature of interest and of the covering layer(s), something that initially was confirmed from the respective computational calculations. More specifically, the same type of tesserae layer has significantly different thermal responses when imbedded into different structures and vice versa. For instance, while in all the tested sets the mosaic panel were cooling down with a slower rate than the reference sample, in the case of the glass consisted panel beneath the hydraulic mortar, a reversed cooling-down behaviour was detected among reference and mosaic panel. The thermal contrast levels measured in each individual test configuration are summarised in Table 6.8, which provides the specific temperature difference values at the beginning

and at the end of the cooling down process as well as at the time point when the maximum thermal contrast was detected.

In the first two tests, investigating the detectability of glass and marble tesserae under the cement/lime covering intervention, it was observed that an increased amount of heat was accumulated on the covered mosaic sample, as during the cooling down process higher temperatures were monitored on its surface with respect to the correspondent temperatures monitored on the blank sample. As a result, since the thermophysical properties of the plaster layers were the same in both sets due to the presence of lime and cement mortars, the differentiations detected regarding the thermal contrast levels and their evolution in time, can be attributed to the presence of different types of materials beneath the plastering which was the major factor influencing the thermal response of these structures. Similar results can be extracted from the comparison of the two latter sets (M3-M6 and M4-M6), where the variations detected on the thermal contrasts levels can also be attributed to the presence of different materials under the hydraulic mortar. Nevertheless in the case of the glass consisted panel as stated above, a diversified thermal behaviour with respect to the other sets was detected confirming that the thermal behaviour of the structure is affected from both the thermal properties of the hidden tiles and of the covering layer(s). Probably, the diversified cooling down behaviour detected on M3-M6 set is due to the presence of an anisotropic regime which combines the relatively low thermal conductivity of the covering layer along with the low heat absorption coefficient that glass tiles have.

In addition from the above presented results, observations can be extracted regarding the influence of the covering material in the produced thermal contrast between reference and mosaic panels. More specifically, from the comparison of M1-M5 and M3-M6 sets, which both are constructed having a mosaic subsurface layer of glass with sheets of gold, the two layers covering seems to provide a more enhanced contrast. In addition, comparing the cooling rates of M1 and M3 samples, the first one cools down with a slower rate with respect to the latter one and this can be observed from the time points of the maximum thermal contrast appearance. Furthermore, an interesting observation derived from the comparison of the cooling rates of the aforementioned samples is that the glass tiles beneath different covering regimes seem to respond differently after the application of a thermal excitation. As the lime and hydraulic lime mortars have similar thermophysical properties, this can be attributed to the presence of the cement mortar in the two layers covering, providing a regime of higher thermal conductivity thus of a better heat flow through the specimen, which further creates an efficient heat accumulation in front of the mosaic layer. Simultaneously, the relatively low thermal conductivity of lime plaster in this structure avoids fast heat reflection flow back to the surface of the panel enabling an increased amount of heat energy to be deposited on the surface of the plastered mosaic. The above observation can also be confirmed from the comparison of the M2 and M4 cooling down responses, where the marble tiles under the two layers covering provided a more enhanced detectability with respect to the detectability observed on the hydraulic covering regime. In other words, a more efficient heat flow into the structure in the two layers covering was detected through cooling down thermographic monitoring.

Table 6.8: *Summary of experimental results*

Set of samples	**Materials mosaic / covering**	**Temperature Differences in ^{0}C**		
M1-M5	*glass/ cement, lime*	$\Delta T_{4,1}$ **t=0 (min)**	$\Delta T_{4,1}$ **Max**	$\Delta T_{4,1}$ **t=60 (min)**
		-4.1	*9.9/ t= 29.5*	*7*
		$\Delta T_{3,2}$ **t=0 (min)**	$\Delta T_{3,2}$ **Max**	$\Delta T_{3,2}$ **t=60 (min)**
		-2.5	*8.2/ t=28.5*	*5.6*
		ΔT_{avg} **t=0 (min)**	ΔT_{avg} **Max**	ΔT_{avg} **t=60 (min)**
		-3.3	*8/ t=29*	*5.2*
M2-M5	*marble/cement, lime*	$\Delta T_{4,1}$ **t=0 (min)**	$\Delta T_{4,1}$ **Max**	$\Delta T_{4,1}$ **t=60 (min)**
		-7.7	*12.4/ t= 31*	*8.8*
		$\Delta T_{3,2}$ **t=0 (min)**	$\Delta T_{3,2}$ **Max**	$\Delta T_{3,2}$ **t=60 (min)**
		-2.3	*8.8/ t=30.5*	*5.8*
		ΔT_{avg} **t=0 (min)**	ΔT_{avg} **Max**	ΔT_{avg} **t=60 (min)**
		-5.8	*10.9/ t=32*	*7.7*
*M3-M6**	*glass/hydraulic*	$\Delta T_{4,1}$ **t=0 (min)**	$\Delta T_{4,1}$ **Max**	$\Delta T_{4,1}$ **t=60 (min)**
		3.9	*4,4/ t= 3*	*-1,9*
		$\Delta T_{3,2}$ **t=0 (min)**	$\Delta T_{3,2}$ **Max**	$\Delta T_{3,2}$ **t=60 (min)**
		3.2	*3,6/ t=2.5*	*-1,6*
		ΔT_{avg} **t=0 (min)**	ΔT_{avg} **Max**	ΔT_{avg} **t=60 (min)**
		4.1	*4,4/ t=2.5*	*-1,9*
M4-M6	*marble/hydraulic*	$\Delta T_{4,1}$ **t=0 (min)**	$\Delta T_{4,1}$ **Max**	$\Delta T_{4,1}$ **t=60 (min)**
		4.27	*5.56/ t= 9.5*	*3*
		$\Delta T_{3,2}$ **t=0 (min)**	$\Delta T_{3,2}$ **Max**	$\Delta T_{3,2}$ **t=60 (min)**
		5.41	*6.98/ t=11.5*	*3.9*
		ΔT_{avg} **t=0 (min)**	ΔT_{avg} **Max**	ΔT_{avg} **t=60 (min)**
		4.54	*5.92/ t=10*	*3.15*

**ΔT in M3-M6 set corresponds to reference-mosaic*

6.7 Comparison of experimental and numerical results

In general, the results obtained by the numerical simulations -taking into account the limitations and simplifications considered- show quite similar behaviour when compared to the actual experimental results. Figure 6.38 indicates the comparison between numerical calculations and experimental measurements in terms of calculated and measured maximum temperature differences and the

correspondent time points of this maximum occurrence, for all the sets of investigated samples. As can be seen, the numerical calculations provided a reduced ΔT_{max} with respect to the maximum temperature differences monitored during the experimental cooling-down phase, mainly on the models simulating the cement/lime covering intervention. Contrary, a good correlation can be observed as regards the time points of maximum thermal contrast appearance obtained from numerical and experimental results.

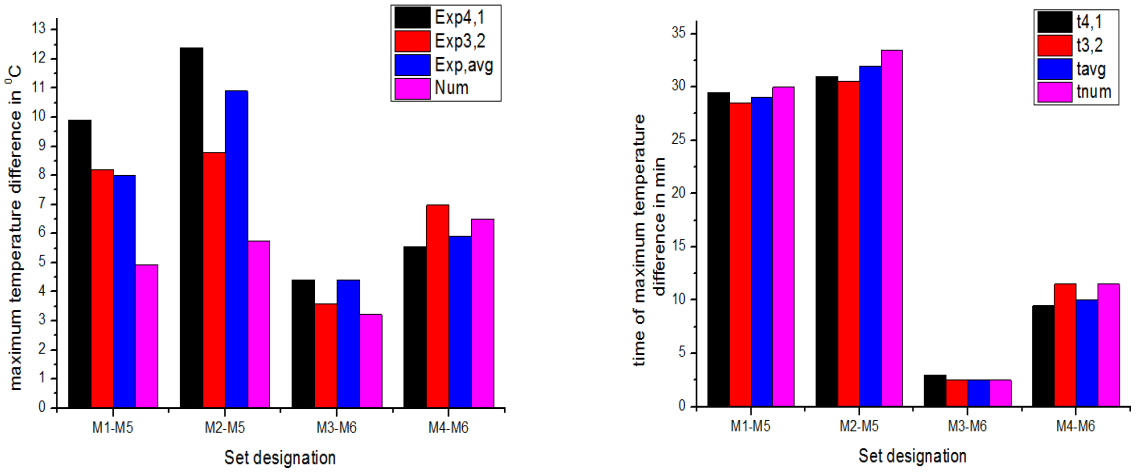

Fig. 6.38: *Comparison of numerical and experimental results in terms of (a) maximum temperature differences and (b) corresponding maximum time points.*

The reason of the ΔT_{max} variations observed can be attributed to a number of parameters affecting the comparison of experimental and numerical data. A very important issue when implementing thermographic investigations is the amount of heat energy delivered to the sample and the uniformity of the heating process, as these parameters during a testing procedure cannot be controlled precisely. A very small change between the distance of the heating source and the specimen surface can result in a significant change to its temperature evolution monitored on the surface of the panel. In addition, as presented on the experimental results and can be also verified from the respective histogram, the influence of non uniformity of heating produced differences regarding the temperature decays and the thermal contrast evolution curves through the different analysis procedures used for the retrieval of the thermal contrast curves. On the other hand, numerical simulations were conducted considering that the heating application was performed in a uniform manner, something that cannot be achieved on real experimental conditions. In addition, as described earlier, in the numerical model calculations the investigated structure was considered via only its thermophysical properties. However in actual conditions, when performing a thermographic survey apart from the thermophysical properties of the investigated material, there are several other factors that influence the output thermographic result such as the spectral properties of the material (i.e. emissivity, absorptivity and reflection coefficient) as well as material characteristics such as its porosity and surface geometry. Finally, another reason for the deviation of numerical and experimental results can be attributed to possible variations in the actual and defined from the literature thermophysical properties used to create the models. For instance, a single

standard value of cement mortar's thermal conductivity is unrealistic due to the multitude of different existed concrete kinds.

The above presented comparative results can be confirmed as well from the comparison of the thermal contrasts evolution curves in time, obtained experimentally and through simulations. The two plots in Figure 6.39 are presenting the comparison of M1-M5 and M2-M5 sets respectively, while Figure 6.40 illustrates the correspondent thermal contrast curves for the M3-M6 and M4-M6 sets. Comparing the results, it can be seen that in the four different testing procedures, the modeled and experimental obtained curves are exhibiting a similar trend despite the deviations in the temperature difference values observed mainly in the two layers covering intervention, which as discussed above can be attributed to a series of parameters affecting the numerical calculations of the surface thermal response. Furthermore, a slight difference can also be observed during the beginning of the cooling down process for the calculated and measured thermal responses of M4-M6 set. In particular, a negative thermal contrast was calculated at the first minutes of the simulated cooling down process contrary to the respective thermal contrasts measured on experimental conditions, which can be attributed to the short delay of the cooling down recording start during the measurements in real conditions.

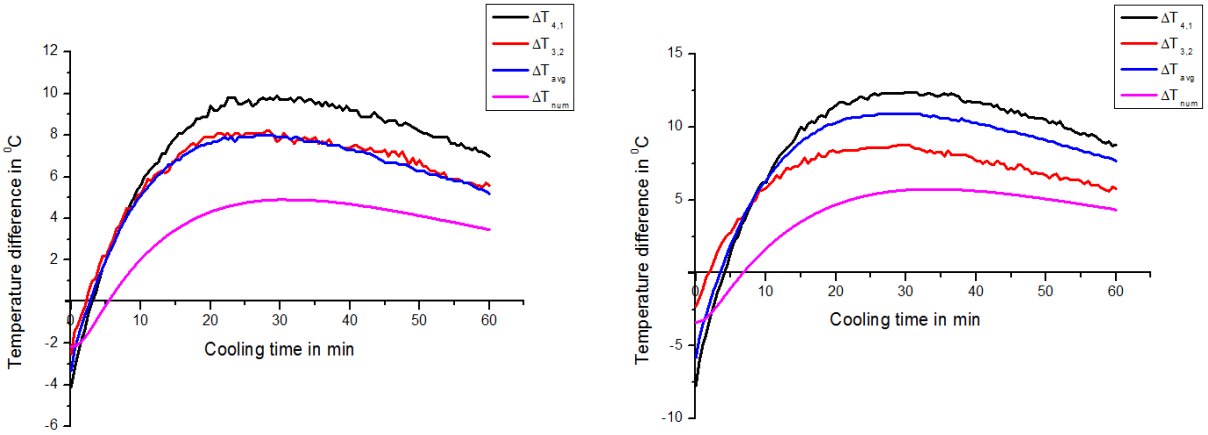

(a) *(b)*

Fig. 6.39: *Comparison of numerical and experimental thermal contrast evolution curves for (a) M1-M5, (b) M2-M5 sets.*

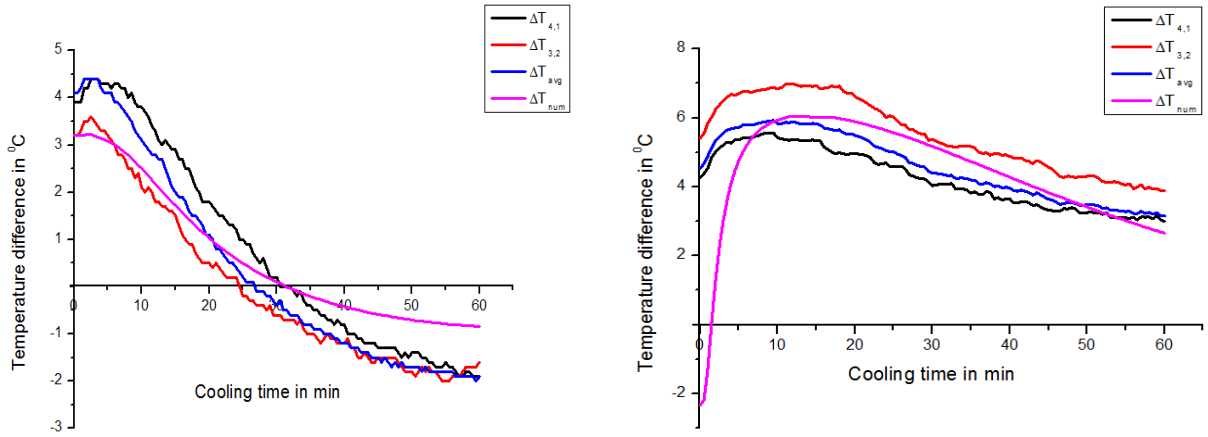

(a) *(b)*

Fig. 6.40: *Comparison of numerical and experimental thermal contrast evolution curves for (a) M3-M6, (b) M4-M6 sets.*

6.8 Quantitative analysis of plastered mosaics through the Inverse Problem Solution

Along with the qualitative characterisation of the plastered mosaic structures, quantitative information were retrieved correlating numerical and experimental results and by solving the Inverse Problem through the parameter estimation approach. More specifically, the temporal characteristics of the maximum temperature difference detected between the covered mosaics and the respective blank areas were used in order to predict the location and thickness of the mosaic layer as well as to characterise the material under the plaster through the estimation of its thermal effusivity and diffusivity, respectively. As a result, three different inverse problems were developed, where in the first problem the location of the mosaic layer (e.g. covering thickness) was estimated considering mosaic's thermophysical properties and thickness known, the second one was conducted for the estimation of mosaic thickness being known its location and its thermophysical properties and the last one predicted the thermophysical properties of the hidden mosaic being known the geometrical characteristics of the structure.

Due to the deviations observed on the calculated and measured temperature differences (derived from a series of several circumstances described above), quantitative analysis of the plastered mosaics was performed correlating the time of maximum thermal contrast occurrence with the parameter investigated in each particular inverse problem. As a result, least square fitting was used in order to find the best fitting function describing the evolution of the dependent variable of maximum time with respect to the parameter estimated (independent variable) in each individual inverse problem.

6.8.1 Quantitative evaluation of mosaic depth

Figure 6.46 and Figure 6.47 present the fit function of maximum thermal contrast appearance times related to the depth at which the mosaic is located to, for the cement/lime and hydraulic coverings respectively. As the fitting function plots present, and confirmed from the numerical simulations, the maximum time values are longer for increasing the covering thickness, following a second order polynomial fitting function. On the other hand, from the experimental data, the maximum of temperature difference ΔT_{max} (difference between blank and mosaic areas) and the related time point t_{max} have been determined. Using the diagrams of Figures 6.46 and 6.47, the experimental values can be connected to particular mosaic depths. This can be performed by searching the measured maximum time at the y-axis and reading the associated value on the x-axis.

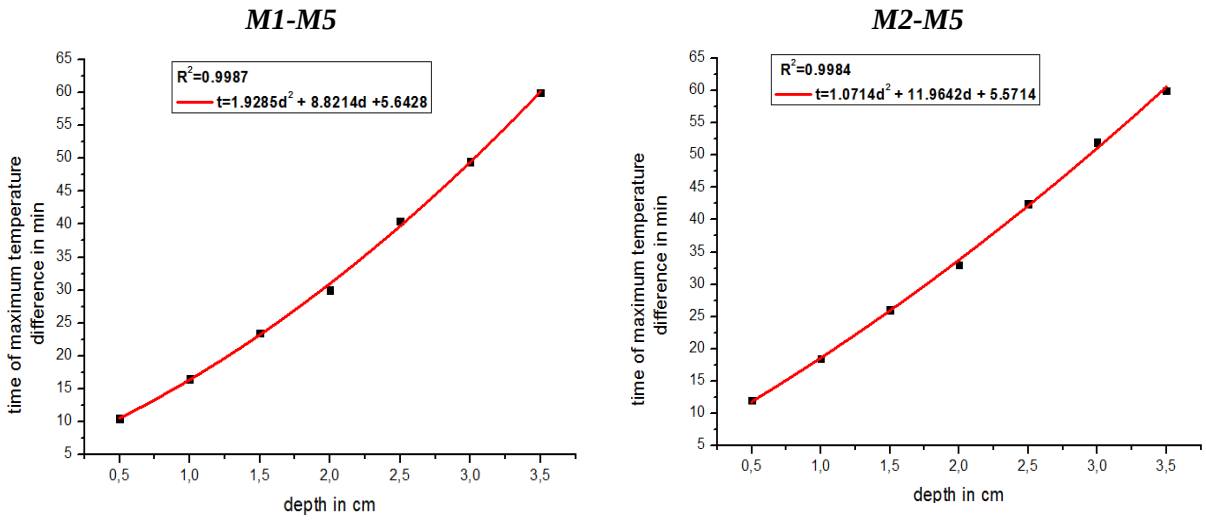

(a) *(b)*

Fig. 6.46: *Time of maximum temperature difference as a function of mosaic depth for (a) M1-M5 and (b) M2-M5 sets. Both curves are following a fitting function of a second order polynomial.*

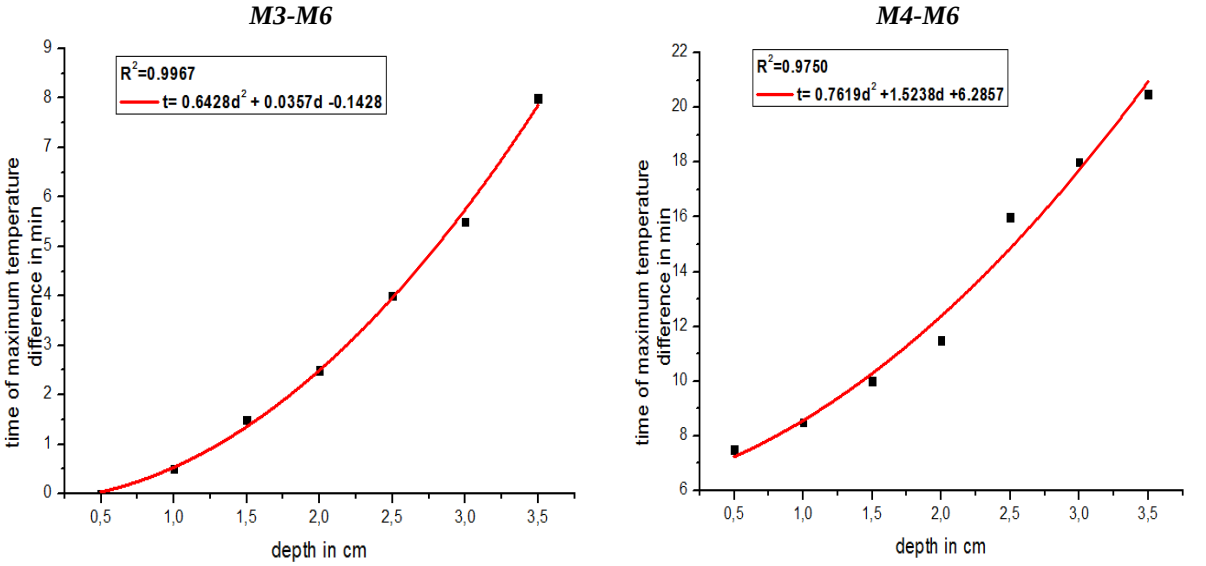

(a) *(b)*

Fig. 6.47: *Time of maximum temperature difference as a function of mosaic depth for (a) M3-M6 and (b) M4-M6 sets. Both curves are following a fitting function of a second order polynomial.*

The results obtained by solving the inverse problem for depth prediction are summarised in Table 6.9. The measured depths determined by the inverse solution differ from 0.8 mm to 4.7 mm to the nominal depth which in terms of error estimation can be deduced to a range from 4% to 23.5 %. The deviations on the estimated depth values from that of the actual depth in which the mosaic layer is located to are relatively short and can be attributed to two possible explanations. In particular, the simplifications adapted during numerical simulations could be a factor producing the above errors, while on the other hand similar deviations of the actual depth compared with the nominal depth of 2 cm could be produced during the plastering procedure.

Table 6.9: *Determination of mosaic depth by the Inverse Problem solution*

Mosaic	Nominal depth in cm	Estimated depth in cm		*Error (%)*
M1	2	Centre	**1.91**	*- 4.5*
		Edge	**1.85**	*-7.5*
		Average Area	**1.88**	*- 6*
M2	2	Centre	**1.83**	*-8.5*
		Edge	**1.80**	*-10*
		Average Area	**1.89**	*-5.5*
M3	2	Centre	**1.71**	*-14.5*
		Edge	**1.53**	-23.5
		Average Area	**1.53**	-23.5
M4	2	Centre	**1.78**	-11
		Edge	**2.3**	15
		Average Area	**1.92**	-4

As regards the comparison of depth information retrieval through the different analysis procedures, variations can be detected when using the experimental data derived from the correspondent pixels' analyses. For instance, the depth at which the mosaic subsurface layer is located to was estimated to be 1.78 cm at the centre of the panel M4 and at its edge it was estimated to be at a depth of 2.3 cm, while the corresponding average analysis produced an estimated depth of 1.92 cm. Similarly regarding the sample M2, while the pixels analyses produced depth results of 1.83 cm and 1.80 cm respectively, the temporal details from the average thermal contrast profile produced a depth result of 1.89 cm. The above observations indicate that the selection of the control points over the reference and the mosaic-consisted surfaces is a crucial parameter for the depth estimation procedure. As a result, in order to avoid inputting extra error from the information acquired due to an inappropriate control points' selection (temperature-time data can be easily affected by non uniform heating), the monitoring of the temperature-time history over an area rather than over a point should be adapted.

Finally, the comparison of the two covering interventions in terms of depth information retrieval are indicating that the cement/lime covering panels produced results which are fitted better to the nominal covering thickness. Contrary, the larger deviations were observed on sample M3 where the related time points of the maximum thermal contrast were detected nearly at the beginning of the cooling down process. For this reason, a new test reoptimising the experimental and numerical parameter used (i.e. a higher data acquisition rate and a shorter computation step of the numerical calculations), shall be performed to confirm if a greater accuracy on the determination of the characteristic maximum thermal contrast time can be achieved.

6.8.2 Quantitative evaluation of mosaic thickness

The second Inverse Problem investigated the correlation of numerical and experimental data in order to acquire quantitative information regarding the thickness of the hidden mosaic layer. Similarly to the depth parameter estimation, least square fitting was also used in order to describe the evolution of the maximum time points by increasing the thickness of the mosaic subsurface layer. Figure 6.48 and Figure 6.49 present the fit functions of time with respect to the tesserae thickness increase for all the samples sets, and Table 6.10 summarises the obtained results as regards the tesserae estimated thickness. As can be observed, the time evolution follows a linear fitting function in relation to the mosaic thickness increase, aside from M3 –M6 set where a second order polynomial fitting was used in order to describe better the influence of mosaic thickness on the temporal appearance of maximum thermal contrast.

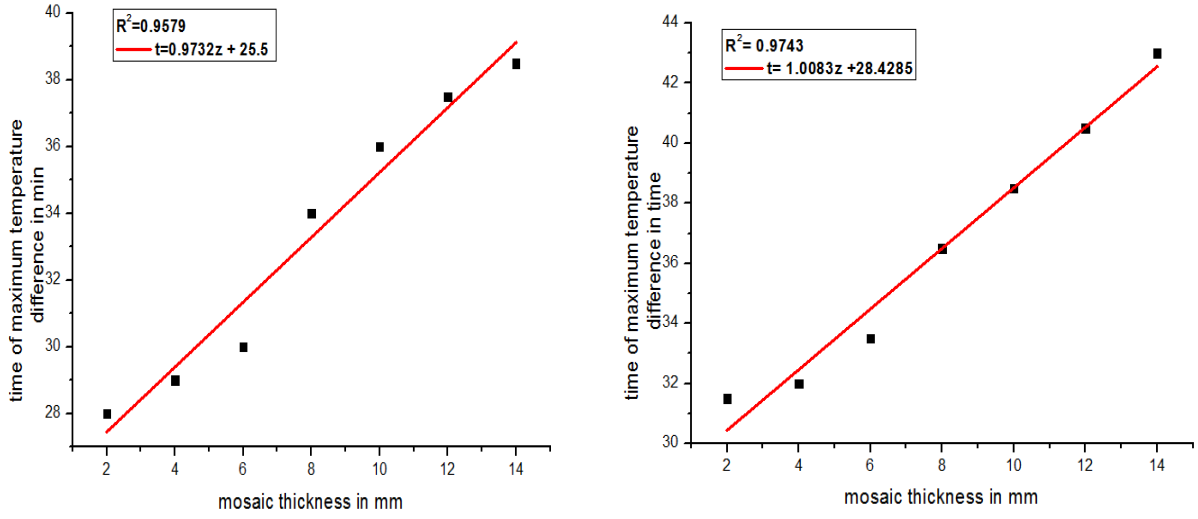

(a) *(b)*

Fig. 6.48: *Time of maximum temperature difference as a function of mosaic thickness for (a) M1-M5 and (b) M2-M5 sets.*

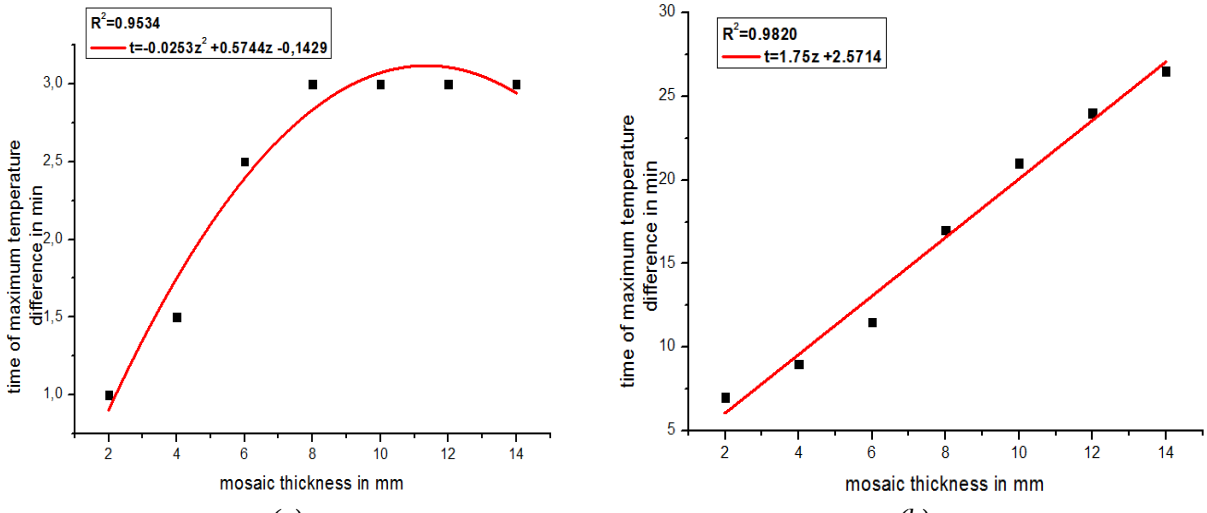

(a) *(b)*

Fig. 6.49: *Time of maximum temperature difference as a function of mosaic thickness for (a) M3-M6 and (b) M4-M6 sets.*

Table 6.10: *Determination of tesserae thickness by Inverse Solution*

Mosaic no.	Nominal thickness in mm	Estimated thickness in mm		*Error (%)*
M1	5	Centre	**4.11**	*-17.8*
		Edge	**3.08**	*-38.4*
		Average Area	**3.60**	*-28*
M2	5	Centre	**2.55**	*-49*
		Edge	**2.06**	*-58.8*
		Average Area	**3.54**	*-29.2*
M3	5	Centre	**9.21**	*84.2*
		Edge	**6.41**	*28.2*
		Average Area	**6.41**	*28.2*
M4	5	Centre	**3.96**	*-20.8*
		Edge	**5.09**	*1.8*
		Average Area	**4.24**	*-15.2*

From the results obtained and summarised in Table 6.10, it can be observed that the estimated thicknesses acquired through the inverse solution are differing from the nominal mosaic thickness from 0.09mm to 4.21 mm, which in terms of error it can be attributed in the range of 1.8% to 84.2%. In general, the acquired results predicting the mosaic thickness were able to provide estimations regarding the tesserae thickness, however larger prediction errors were produced in this case with respect to the mosaic depth inverse problem. Nevertheless, these deviations from the actual thickness can be possibly attributed, similarly to case of covering thickness estimation, to the different tiles thicknesses that can be encountered in such structures due to the inaccuracy of the cutting procedure.

The larger errors were produced for the mosaic layer of M3 sample (glass tiles under hydraulic mortar). In this investigation, numerical simulations showed that the time of maximum thermal contrast occurrence remained stable for increasing the thickness of the mosaic layer from 8 to 14 mm, while on the other hand the experimental measurements provided a relatively weak contrast aside from its early maximum appearance. As a result, in order to acquire quantitative information regarding the investigated feature, a relatively efficient contrast should be produced between this area and the reference. The above observation can be further confirmed from the results acquired regarding the covering thickness estimation, where the greater deviations were also observed in this set of samples.

However, despite the error produced in this case, a comparison of the results acquired from the different data analysis procedures revealed, as in the case of the covering thickness estimation, that the monitoring of the average surface temperature to time provided results more closely to the nominal mosaic thickness, while the pixel analyses had great divergences between them. In particular, comparing the pixels' analyses it can be observed that great deviations on the results can be acquired in all the sets of samples investigated. For instance, as can be seen from the results acquired regarding the

M2 measurements, while the pixels analyses produced errors of 49% and 58% respectively, the average data analysis estimated the mosaic thickness to be 3.54 mm, producing an error of 29.2%.

6.8.3 Determination of mosaic thermophysical properties

The classical thermophysical properties of a material that are characterising its response to a heat flux are the thermal conductivity k, the specific heat c_p and its mass density ρ. The last two can be combined to the heat capacity which is a material property derive from the product of specific heat and density ($c_p \cdot \rho$). As stated above these thermophysical properties in a transient thermal regime can be considered in two other material properties, this of thermal effusivity ($e = \sqrt{k\rho c_p}$) and this of thermal diffusivity ($\alpha = k/\rho c_p$) respectively. Thus, by determining the aforementioned thermal properties, estimations regarding the thermal conductivity and the heat capacity of the investigated feature can be obtained, according to:

$$k = \sqrt{\alpha} e \quad \text{and} \quad \rho c_p = e/\sqrt{a}$$

Taking into consideration the aforementioned, the third inverse problem was created in order to fit the temporal characteristics of thermal contrast evolution with respect to the mosaic's thermal effusivity and thermal diffusivity changes. Thus, following a similar procedure as in the cases of the two previous inverse problems, Figure 6.50 presents the fit function of the maximum time points with respect to the mosaic thermal effusivity and diffusivity increase in the two layers covering regime, while Figure 6.51 presents the same fit functions for the hydraulic lime covering intervention. As can be observed from the aforementioned figures, the dependent variable of maximum time is following a linear fitting function with respect to the thermal effusivity and a fitting function of a second polynomial order with respect to the thermal diffusivity. Using these diagrams the experimental maximum temporal values can be connected to the particular mosaic thermal properties and additionally its thermal conductivity and heat capacity can be estimated using the analytical formulas presented above.

Cement/lime covering intervention

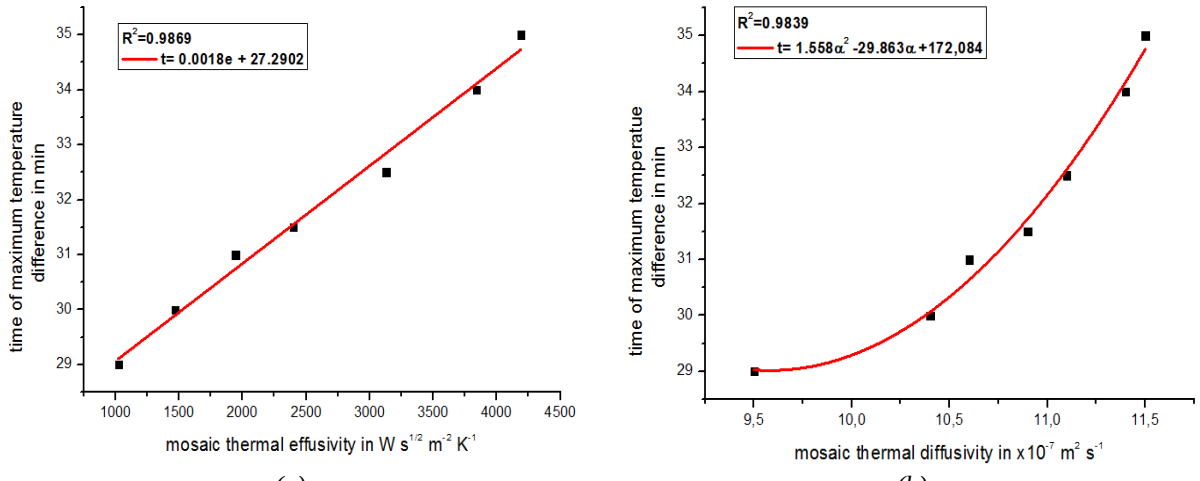

(a) *(b)*

Fig. 6.50: *Time of maximum temperature difference as a function of (a) mosaic thermal effusivity and (b) mosaic thermal diffusivity for the two layers covering intervention.*

Hydraulic lime covering intervention

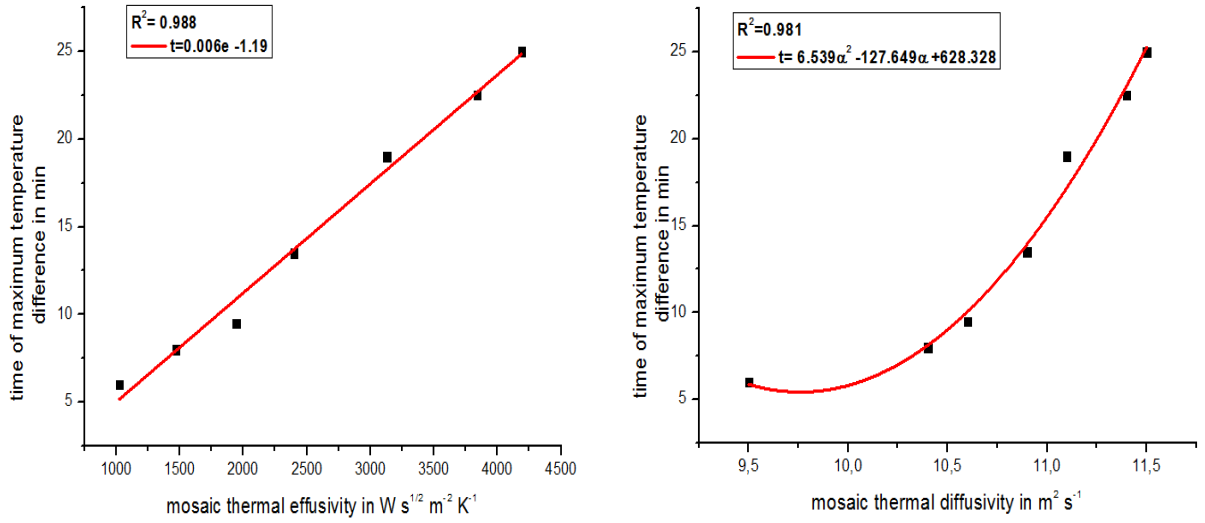

(a) *(b)*

Fig. 6.51: *Time of maximum temperature difference as a function of (a) mosaic thermal effusivity and (b) mosaic thermal diffusivity for the hydraulic lime covering intervention.*

In this point it should be mentioned, that the indirect characterisation of the mosaic nature though the estimation of its thermophysical properties, was performed implementing the inverse problem procedure described above, only for the marble tesserae consisted panels, as this mosaic layer has the same thermophysical properties in all of its directions (volume fraction). The results obtained by solving the inverse problem for thermal effusivity and thermal diffusivity prediction are summarised in Table 6.11. Contrary, regarding the glass mosaic layer which can be characterised as a two layers structure, both the glass and gold materials are producing thermal effects affecting in a completely different manner as stated above, the thermal response of the structure. Additionally, based on the observations stated above concerning the influence of a single pixel selection on the recovery of quantitative information, the results presented on this table, have been acquired through the temporal information derived from the average temperature data analyses.

Table 6.11: *Determination of mosaic thermal effusivity and thermal diffusivity by the Inverse Problem solution*

Mosaic No.	**Nominal thermal effusivity in W $s^{1/2}$ m^{-2} K^{-1}**	**Estimated thermal effusivity in W $s^{1/2}$ m^{-2} K^{-1}**	**Nominal thermal diffusivity in ($x10^{-7}$) m^2 s^{-1}**	**Estimated thermal diffusivity in ($x10^{-7}$) m^2 s^{-1}**
M2	*2715*	***2616***	*13.4*	***10.97***
M4		***1865***		***10.60***

As can be seen from the above presented results an estimation concerning thermal effusivity and thermal diffusivity of the hidden mosaic layer can be performed through the inverse problem solution in transient thermal regimes, where an efficient amount of heat is applied to the inspected sample. The results coming from the fitting function involving the maximum time evolution with respect to the independent variable of thermal diffusivity seems to be unaffected from the covering regime. Contrary efficient result regarding the thermal effusivity estimation was obtained on the two layers regime, as a noticeable deviation from the nominal thermal effusivity was detected on the hydraulic covering

procedure. In Table 6.12 the results acquired regarding the thermal conductivity and heat capacity of the marble mosaic layer are presented, as calculated through their correlation on the above analytical expressions.

Table 6.12: *Derived results for the mosaic thermal conductivity and mosaic heat capacity*

Mosaic No.	**Nominal thermal conductivity in W m^{-1} K^{-1}**	**Estimated thermal conductivity in W m^{-1} K^{-1}**	**Error (%)**	**Nominal heat capacity in KJ m^{-3} K^{-1}**	**Estimated heat capacity in KJ m^{-3} K^{-1}**	**Error (%)**
M2	*3.14*	***2.74***	*-12.7*	*2349*	***2515***	***7***
M4		***1.92***	*-38.8*		***1828***	*-22.1*

From the results presented on the above table, it can be observed that a rough estimation of a detected hidden mosaic layer through cooling down thermography can be performed. By defining the thermal properties of conductivity and heat capacity, these can be combined searching in the literature to match both values with a specific material. In this point it should be mentioned that the nominal values of the thermal properties, are actually the values that have been used in order to create the numerical simulations and have been retrieved from the literature as non individual measurement was performed to evaluate the actual thermal properties of each individual subsurface layer. However a search in the literature exhibited, that the different types of marble exist have different thermophysical properties. For instance according to the type of marble used its thermal conductivity can vary from 2.08 to 3.34 [18]. Contrary more efficient results were acquired concerning the prediction of heat capacity, which nominal value has also been defined from the literature.

6.9 Conclusions

From the above presented study, the potential of cooling down thermography has been numerically and experimentally demonstrated on revealing hidden mosaic layers made of different materials and additionally located beneath different covering interventions. Images seeing-through the mortar on plastered mosaic surfaces were obtained using the principles of cooling down thermography, as this technique was efficiently applied providing an enhanced detectability of the subsurface layers (i.e. tesserae), under the specific testing conditions adapted for this survey. Furthermore, quantitative information regarding the hidden structures were retrieved through the monitoring of the surface temperature decay over a reference and a mosaic consisted area and the calculation of the resulting thermal contrast evolution to time. Conclusively, cooling down thermography ought to be considered as a valuable appraisal tool in the investigation of plastered mosaic surfaces, while the combination of experimental and numerical data can expand its capabilities for quantification purposes.

The methodology presented above was consisted of three different distinct phases, this of the experimental testing, this of the simulated parametric studies conduction for the effect evaluation of specific parameters alterations on the thermal response of the structures, and the development of the Inverse Problems in order to correlate numerical and experimental results.

Starting from the experimental phase, the implementation of Cooling-Down Thermography was proven to be very well suited for this specific application -investigation of plastered mosaics-. As the experimental results demonstrated, thermal contrasts among mosaic-consisted and mosaic-free areas were detected in all the panels pairs inspections, after the application of a long heating pulse. More specifically, it was observed that the marble tiles present a more enhanced detectability regardless the covering intervention, while the covering intervention of the two layers regime produced a more enhanced detectability of the hidden mosaic layer regardless the material from which it was made of [19]. However, for the best possible understanding of the detected thermal effects and the best possible interpretation of the acquired results, a thorough knowledge of the history of the investigated structure is required. For instance, while in all the above presented investigations, an increased amount of thermal energy deposited on the surface of the mosaic panel was detected with respect to the correspondent thermal energy deposited on the reference surface, the reverse condition was observed on the structure consisted of glass tiles under a covering procedure with hydraulic lime mortar. The above observation confirms that the thermal response of the structure is strictly related to the thermophysical properties that each of its layers renders and a precise knowledge of these properties can provide a greater accuracy on the explanation of the results [20]. Finally, cooling down thermography can be implemented studying the thermal contrasts on areas instead on points, as the results acquired from the average analyses in the presented study, seem to provide results less affected by the non uniform heat application.

On the other hand numerical computations, simulating the transient thermal inspection problem are able to provide information about the thermal response of the investigated structure and confirm or predict the results acquired through experimental testing. In the present study, the numerical calculations were proven to match efficiently with the experimental results, confirming the reliability of the experimental procedure for the investigation of plastered mosaic. In addition, the use of the numerical simulation programs are able to provide information regarding the influence of specific parameters variations to the produced detectability of the covered mosaic layer as well as to estimate the detection limits under the specific testing configurations. In particular, in the present study it was observed that temperature differences on the surface of the investigated structure can be produced for coverings up to 3.5 cm and for a covering intervention with 2cm of thickness layer, a tesserae layer of 2mm can be revealed. Thus, as far as the numerical model is considered, it should be defined in such a way that it allows for correct description of the real sample and despite the applied simplifications that may used, the model shall be sufficiently close to the real sample in order to provide the results enabling the establishment of the correspondence between the experimental and numerical data. In other words, as more precise in terms of actual conditions and thermophysical properties definition is the model setup, this can act as an important tool both for predicting the thermal response of the inspected structure and acquiring quantitative information from the combination of numerical and experimental results.

The above methodology for the retrieval of quantitative information and the indirect characterisation of the hidden mosaic layer through the estimation of its thermophysical properties can provide efficient results when the experimental and numerical tests have been conducted with accuracy. However, a limitation characterising this approach could be the fact that it can be applied in cases where only an unknown parameter is missed. In other words, in order to estimate the covering thickness the thermophysical properties and the thickness of the mosaic layers have to be known and so on. However, this approach in cases of cultural heritage investigations can be applied efficiently, as because very often the ultimate goal of an inspection concept is the acquisition of knowledge for the missed history of the artefact. In other word this procedure can be followed in cases where a detail is missing from the archives documenting the artifact. In addition, recently developed procedures for the depth estimation in long pulsed heating techniques can provide depth information, involving the results acquired from the experimental measurements, while FWHM approach can be also used to define the lateral dimensions of a detected feature of interest. The results acquired through experimental data can be inputted on the model and thus the above stated limitation can be overcome.

6.10 References

[1] E. Grinzato, C. Bressan, F. Peron, P. Romagnoni, A.G. Stevan (2000). *Indoor climatic conditions of ancient buildings by numerical simulation and thermographic measurements.* In R.B. Dinwiddie, D.H. Le Mieux (Eds.): Proc. of SPIE- The International Society for Optical Engineering, Thermosense XXII, Vol. 4020, Orlando, Florida, 2000, pp. 314-323.

[2] M. Volinia (2000). *Integration of qualitative and quantitative infrared surveys to study the blaster conditions of Valentino Castle.* In R.B. Dinwiddie, D.H. Le Mieux (Eds.): Proc. of SPIE- The International Society for Optical Engineering, Thermosense XXII, Vol. 4020, Orlando, 2000, pp. 324-334.

[3] E. Grinzato (2012). *IR thermography applied to the cultural heritage conservation.* In Proc. of the 18th World Conference on Nondestructive Testing- WNDT, Durban, South Africa, 2012, CD-ROM.

[4] T. Kauppinen, C. Maierhofer, H. Wiggenhauser, D. Arndt (2000). *The use of cooling down thermography in locating below-surface defects of building facades.* In R.B. Dinwiddie, D.H. Le Mieux (Eds.): Proc. of SPIE- The International Society for Optical Engineering, Thermosense XXII, Vol. 4020, Orlando, 2000, pp. 314-323.

[5] M. Krishnapillai, R. Jones, I.M. Marshall, M. Bannister, N. Rajic (2006). *NDTE using pulse thermography: Numerical modelling of composite subsurface defects.* In J. Composite Structures, Vol. 75, pp. 241-249.

[6] C. Maierhofer, A. Brink, M. Rolling, H. Wiggenhauser (2005). *Quantitative impulse-thermography as non-destructive testing method in civil engineering - Experimental results and numerical simulations.* In J. of Construction and Building Materials, Vol. 19, pp. 731-737.

[7] C. Maierhofer, M. Rollig (2009). *Active thermography for the characterisation of surfaces and interfaces of historic masonry structures.* In Proc. of Non-Destructive Testing In Civil Engineering Conference- NDTCE'09, Nantes, France, June 30th-July 3rd 2009, CD-ROM.

[8] N.P. Avdelidis, D.P. Almond (2004). *Transient thermography as a through skin imaging technique for aircraft assembly: modelling and experimental results.* In Infrared Physics & Technology, Vol. 45, pp. 103-114.

[9] S. Danesi, A. Salerno, D. Wu, G. Busse (1998). *Cooling down thermography: principle and results for NDE.* In J.R. Snell, R.N. Wurzbach (eds.): Proc. of SPIE- The International Society for Optical Engineering, Thermosense XX, Vol. 3361, pp. 266-274.

[10] E. Rosina, N. Ludwig, V. Radaelli, S. Della Torre, S. D' Ascola, M. Catalano, C. Faliva (2005). IRT analysis on historic buildings: Towards a controlled convection heating. In G.R. Peacock, D.D. Burleigh, J.J. Miles (eds.): Proc. of SPIE- The International Society for Optical Engineering, ThermosenseXXVII, Vol. 5782, pp.153 – 163.

[11] N.P. Avdelidis, (2002). *Applications of infrared thermography for the investigation of*

materials and structures. PhD Thesis, NTUA.

[12] Ch. Maierhofer, A. Brink, M. Rollig, H. Wiggenhauser, (2003). *Detection of shallow voids in concrete structures with impulse thermography and radar*. In J. NDT&E. International, Vol. 36, pp. 257-263.

[13] M. Koui, N.P. Avdelidis, Ch. Arvanitis, (2004). *Transient thermographic evaluation of plastered mosaics.* in D. Balageas, G. Busse, G.M. Carlomagno, J.-M. Buchlin (eds.) : Proc. of the 7th International Conference on Quantitative Infrared Thermography (QIRT7), Brussels ,Belgium, pp. I.6.1-I.6.6.

[14] N.P. Avdelidis, M. Koui, C. Ibarra-Castanedo, X. Maldague, (2007).*Thermographic studies of plastered mosaics.* In J. Infrared Physics and Technology, Vol. 49, pp. 254-256.

[15] X. Maldague (2001). *Theory and Practice of Infrared Technology for Non Destructive Testing.* John-Wiley & Sons, New York.

[16] ThermoCalc 3D Software operating manual. Version 2.0, Innovation Inc., 1998.

[17] D.P. Almond, P.M. Patel (1996). *Photothermal Science and Techniques.* Chapman &Hall, London.

[18] http://www.engineeringtoolbox.com/thermal-conductivity-d_429.html

[19] P. Theodorakeas , N.P. Avdelidis, M. Koui, C. Ibarra – Castanedo , E. Cheilakou, A. Bendada, K. Ftikou ,X.P.V. Maldague (2010). *Active thermographic NDT approaches for the assessment of plastered mosaics.* In M. Koui, F. Zezza, P. Koutsoukos (eds): Proc. of the 8th International Symposium on the Conservation of Monuments in the Mediterranean Basin (MONUBASIN8), Patras, Greece, Vol. 2, pp. 442-456 .

[20] P. Theodorakeas , C. Ibarra-Castanedo, S. Sfarra, N. P. Avdelidis, M. Koui, X. Maldague, D. Paoletti, D. Ambrosini(2012). *NDT inspection of plastered mosaics by means of Transient Thermography and Holographic Interferometry*. In J. NDT&E International, Vol. 47, pp. 150-156.

Chapter 7

General Conclusions

and

Future Perspectives

7.1 General conclusions

In the present thesis, the capabilities of two different quantification methods were examined, for the assessment of the inspected targets' internal configurations. More specifically, the experimental determination of the peak slope time and blind frequency informative parameters and their correlation to analytical formulas were used to estimate the depth of Teflon insertions embedded into CFRP composites, while the correlation of numerical and experimental results was used in order to acquire quantitative information from plastered mosaic regimes. The reliability and effectiveness of pulsed thermography was assessed as a function of:

- the geometry of the inspected surfaces
- the depth of the internal features
- the size of the internal features

Similarly, the reliability and effectiveness of cooling down thermography was numerically and experimentally assessed as a function of:

- the covering layer thickness
- the mosaic layer thickness
- the thermal properties of both the plastered and covered mosaic layers

The aim of this thesis was to achieve a greater understanding regarding the application of active infrared thermography, as a NDT&E technique on different inspection problems. The results of this study showed that active thermal imaging can be successfully applied for the structural integrity assessment of different materials and structures, acting as a useful tool able to provide a sufficient internal detectability and/or quantitative estimations. These two objectives can be achieved through two different data manipulation procedures, this of qualitative and this of quantitative analysis respectively. However, the testing scenario deployment can vary for different applications, and either focusing on qualitative or quantitative information retrieval, this shall be properly defined according to the thermal properties of the inspected material, the temporal and spatial resolution of the imaging equipment and the way that the inspected target shall be stimulated. In other words, as different materials response differentially to a thermal excitation, its characteristic shall be conformed according to the test piece and the expected desirable results. The two case studies showed that the knowledge of the thermal properties can provide initial estimations regarding the amount of heat required in order to internally stimulate the sample as well as how fast or slow the heat diffusion into the material bulk can penetrate. These initial estimations will enable the operator to define the proper experimental conditions and sufficiently monitor this phenomenon and the potential produced thermal effects.

Furthermore, some general conclusions derived from both the results of pulsed and cooling down thermographic inspections are presented, providing some general remarks that have to be considered when infrared thermography is applied as an inspection technique. These general remarks are

simultaneously correlated with the results produced in each individual study. Thus, in a qualitative thermographic assessment, these are:

- The initial resulting output, this of the unprocessed raw temperature image can contain the complete information of the tested material based on the thermal effects that embedded features with different thermal properties than the background, can produce. – *The thermal effects from the different thermal properties that each of the investigated covered mosaics had, produced a surface temperature difference easily detected from the acquired thermographs.*- However, these thermal effects can be extremely small or undistinguishable for deep and/or small probing, leading to the loss of information- –*The thermal effects produced from small and deep insertions into the CFRP coupons, in some instances were undetectable while in some others they had a very weak contrast incommoding their detection. Additionally numerical modelling revealed that as deeper was the location of the internal mosaic layer as reduced was the resulted thermal contrast on the produced model.*– This loss of information can be further enhanced from a non uniform heat application process.- *The non uniform heat deposition on the planar CFRP composite produced limited detectability regarding its embedded insertions identification.*-
- On the other hand, the information retrieval from the unprocessed thermographic signal can be importantly improved through the application of advanced signal processing routines. These algorithms are enhancing the thermal *"footprints"* mainly of deep and/or small defects, while by countering the problems affecting the raw temperature data, a greater amount of information is retrieved with enhanced visual appearance and reliable quality –*Advanced signal processing techniques produced efficient results for the identification of the embedded insertions in the CFRP composites, revealing all the internal inserts in some instances*.- A more detailed study of the produced quality contrast through SNR calculation proved that despite the enhanced visibility that advanced signal processing techniques provide, these can be properly manipulated according to the probing criteria and the user's demands. –*The results produced regarding the performance of each processing algorithm were equivalent for deeper probing on the CFRP specimens, however shallower probing produced a better quality through TSR and synthetic PPT analysis.*-

As regards the quantitative estimation procedures, these are:

- Analytical methods based on the determination of a characteristic point either working in the time or the frequency domain can provide results in a straightforward manner. – *The determination of the peak slope time and of the blind frequency values were inputted into the correspondent formulas and insertions depth was retrieved.*- Contrary the correlation of numerical simulations and experimental results require both the theoretical and experimental assessment of the inspection problem. –*Plastered mosaics were numerically and experimentally*

assessed in order to produce the correspondent inverse problems.- Nevertheless, the joint methodology correlating numerical and experimental information can quantitatively evaluate more informative parameters than the quantification methods based on exclusively experimental results –*The correlation of numerical and experimental results was able to estimate the thickness of the mosaic layer and its thermophysical properties. On the other hand no analytical formulas have been suggested for the straightforward measurements of this informative characteristics when embedded features have to be characterised*.-

- Analytical methods involving peak slope time and blind frequency were proven to be unaffected from the shape of the inspected surface and consequently the non uniformity of heat deposition on the inspected surface –*The depth results produced from the quantitative analysis of the CFRP specimens in the time domain were equally good or bad regardless the geometry of inspected sample. Similarly, the enhanced depth prediction manipulating phase data, provided approximately the same depth results on the planar trapezoid and curved panels*.- Contrary when numerical simulations are implemented for quantification purposes, these shall be defined in such a manner that they allow for a precise description of the real sample and of the testing scenario. –*The transient thermographic problem of the plastered mosaics was modelled considering a uniform stimulation procedure something that cannot be achieved on real experimental conditions. Furthermore, the investigated structures were considered via only their thermophysical properties in numerical calculations. However in actual conditions apart from the thermophysical properties, the spectral properties of the material are also considered*.-
- Of prime importance when quantitative analysis shall be performed is the proper definition of the experimental conditions. Time resolution has a great impact on the determination of temporal informative characteristics from which quantitative information can be acquired. As more accurate is the time resolution, the sufficient will be the quantitative result. – *The larger error prediction on the plastered mosaic investigations was produced for the mosaic having its peak thermal contrast appearance on a relatively short time point*.- Additionally, another factor of great importance is the definition of the truncated parameters in the case where processing limitations exhibit. - *The peak slope times for the shallowest defects on the CFRP specimens were measured at the lower time interval of the truncated sequence*-. The above described parameters either sampling resolution or truncated resolution should be defined according to the inspected depth and the inspected material/defect thermal properties. Fast phenomena require a high temporal resolution and a high sampling frequency and vice versa.
- When quantification methods have to be implemented, based on intensity-contrast techniques, the selection of a sound area is considered to be essential for the sufficient quantitative information retrieval. –*Time domain quantification on the CFRP panels was performed selecting different sound areas as non uniform heating deposition was observed on the*

respective surfaces. - However the selection of a large area as a sound area and the computation of its average intensity can greatly enhanced the acquired quantitative information. – *Depth quantification through the measurement of the average phase intensity on the CFRP specimens produced enhanced accuracy of the measured internal inserts depth. On the other hand, the average temperature monitoring over the plastered surfaces provided results closer to the nominal informative parameters or it reduced the divergences between the acquired results from the correspondent pixels analyses.-*

7.2 List of research contributions

The results derived from the two different thermographic investigations, resulted to the following research contributions:

- From the application of different signal processing routines to handle pulsed thermographic data, it was proven that the shape of the investigated surface has an important impact when qualitative information are retrieved from raw temperature data and low but not negligible when the same information are retrieved from processed results.
- The comparative study of different signal processing algorithms on defect detectability on CFRP components showed that higher detectability gradient was produced through Principal Component Thermography (PCT) and through Pulsed Phase Thermography (PPT) either on raw or synthetic temperature data.
- The study of the produced quality contrast through SNR calculations proved that despite the enhanced visibility that advanced signal processing techniques provide, these can be properly manipulated according to the probing criteria and the user's demands.
- From the quantitative assessment both on temporal and frequency domain analyses, it was proven that the shape of the investigated surface has a negligible impact on the retrieval of depth information.
- From the numerical investigation of different mosaics covered with various plaster layers, it was proven that a mosaic surface can be detected beneath a covering layer of 3.5 cm while thin mosaic layers of 2 mm can be detected beneath a covering layer of 2 cm.
- The produced thermal contrasts over a mosaic-free and mosaic-consisted surface as well as its temporal evolution are characteristic of the materials used to build the respective structure.
- A procedure was proposed providing quantitative information in terms of depth, thickness and thermophysical properties estimation of the hidden features through the setup of the respective inverse problem.

- For quantification purposes based on intensity-contrast techniques, it was proven that the selection of a large area as a sound area and the computation of its average intensity can greatly enhanced the acquired quantitative information

7.3 Future research perspectives

There are two principal directions suggested for the continuation of this research. The first recommendation concerns the use of pulsed thermography for the inspection of composite materials, while the second one concerns the integration of the numerical/experimental joint methodology under varied circumstances.

As regards the former recommendation, the present study showed that the implementation of advanced signal processing along with the enhanced visibility and internal features detectability that it produces, it can further provide accurate quantitative information regarding the depth of the detected features (e.g. quantitative PPT). However in order to complete the quantitative characterisation, the lateral dimensions of the detected feature should also be determined. A statistical approach in order to implement this step is this of *Full Width at Half Maximum* (FWHM), which is based on the identification of potential intensity variations upon a line profile that bisects the area of interest. Once the pixels presenting this variation are determined, these can be transformed to the physical quantity of length. Nevertheless, as the informative parameter in this technique is the magnitude contrast produced between the defect and the background, the lateral heat diffusion around the feature may lead to an inaccurate estimation of this parameter.

In order to avoid this phenomenon, research studies have proposed to estimate the lateral dimensions of a detected feature on early time intervals when temperature data have to be manipulated (see ref. 70 from Chapter 4). On the other hand, the qualitative results from this study showed that imaging results through the application of advanced signal processing techniques can produce seeing-through conditions of enhanced geometry, which are much less affected from the negative effects of lateral heat diffusion. As a result, a research study combining FWHM approach with the advantages of post processing analyses shall be performed, investigating the impact degree of 3D conduction effects on the accuracy of the produced quantitative size estimations. Following the above described procedure, defect size can be extracted from the analysis of derivative data, or phase data manipulation in the frequency spectrum where a defect is visible. The estimation of the lateral size and the monitoring of its variations as a function of time or frequency will produce results regarding:

- The effect of 3D conduction problem on post processed data manipulations
- The appropriate time and/or frequency range in which size estimations shall be performed
- The influence of defect depth and size (correlated with the produced intensity variations), when enhanced imaging outputs have to be manipulated for quantitative size estimations.

Additionally in this study, a SNR evaluation was conducted, using a specific experimental configuration and studying internal simulated delaminations of different sizes and depths. For each particular internal insertion, SNR computations were performed in all the frames of the truncated sequence, searching for its maximum value which corresponds to an optimum defect contrast image. As a result, based on the SNR analysis, a research study focusing on CFRP materials, can be conducted for

the development of a database which will provide information regarding the time points of the best detectability, for predefined structural characteristics (i.e. common defect modes and irregularities) and for specified experimental conditions (i.e. pulsed excitation, long pulsed excitation etc.). This will optimise the inspection procedures as a single image after the flash initiation can be recorded which will be able to provide the operator the best visual output and thus the optimum defect detectability according to its depth, dimensions and nature. In order to produce the aforesaid database, the parameters that shall be considered and correlated with the SNR metric are:

- the thermal properties of the inspected material
- the type of the defect
- the thermal properties of the defects
- the size of the defect
- the depth of the defect
- the heating application procedure
- the data manipulation domain

As regards, cooling down thermographic inspection, further aims for the possible continuation of this research include:

- The investigation on the effectiveness and reliability of cooling down Thermography with lower stimulation times.

  An important issue when applying active infrared thermography, is the amount of heat that has to be delivered with respect to the preservation of the non destructive nature of this technique. When dealing with real constructions and especially with cultural heritage assets, the amount of heat delivered to the surface shall be absolutely controlled avoiding any possible excessive supply of heat which may create further damage to the artefact. As a result, the effects of heat supply on the accuracy of results should be studied investigating different times. This can further correlate the detection limits of this technique with respect to the heating up procedure and the geometrical specifications of the materials inspected.

- The investigation of lateral heat diffusion on quantitative information retrieval through the correlation of numerical and experimental results.

  In the present study the covered mosaic area occupied a large region (the half) with respect to the entire area examined. So the 3D conduction problem did not adversely affect the setup of the inverse problems and the recovery of quantitative information. As a result the accuracy produced from the joint numerical/experimental methodology shall be examined considering internal features of interest of smaller dimensions. A comparative research will provide information regarding the quantitative information retrieval limits of this procedure with respect to the lateral dimension of the feature detected.

- The investigation of different materials for their characterisation, through the determination of their thermophysical properties.

  In the present study it was shown that the thermal properties of effusivity and diffusivity can be properly used in transient regimes, where long heating times are required in order to produce an indirect characterisation of the embedded materials through its thermophysical properties estimation. However a further validation of this procedure is required, studying different materials under the same structure and assessing their thermal effects both numerically and experimentally.

LIST OF PUBLICATIONS

Publications in Refereed Journals:

1. S. Sfarra, P. Theodorakeas, N.P. Avdelidis, M. Koui (2013). *Thermographic, Ultrasonic and Optical Methods: A New Dimension in Veneered Wood Diagnostics*. In Russian J. of Nondestructive Testing, Vol. 49 (4), pp. 234-250.

2. P. Theodorakeas , C. Ibarra-Castanedo, S. Sfarra, N. P. Avdelidis, M. Koui, X. Maldague, D. Paoletti, D. Ambrosini(2012). *NDT inspection of plastered mosaics by means of Transient Thermography and Holographic Interferometry*. In J. NDT&E International, Vol. 47, pp. 150-156.

3. S. Sfarra, P. Theodorakeas, C. Ibarra-Castanedo, N. P. Avdelidis, A. Paoletti, D. Paoletti, K. Hrissagis, A. Bendada, M. Koui, X. Maldague (2012). *Evaluation of defects in panel paintings using infrared, optical and ultrasonic techniques*. In J. Insight, Vol. 54(1), pp. 21-27.

Publications in Refereed Conference Proceedings:

4. P. Theodorakeas, S. Sfarra, C. Ibarra-Castanedo, N.P. Avdelidis, M. Koui, X.P.V. Maldague, D. Ambrosini, D. Paoletti (2013). *The use of Pulsed Thermography for the investigation of art and cultural heritage objects.* In Proc. of the 5th International Conference on NDT of HSNT-IC MINDT 2013, Athens, Greece, art. no. P.2.5, CD ROM.

5. E. Cheilakou, P. Theodorakeas, M. Koui, S. Moustakidis, C. Zeris (2013). *Determination of reinforcement and tendon ducts positions on pre-stressed concrete bridges by means of Ground Penetrating Radar (GPR).* In Proc. of the 5th International Conference on NDT of HSNT- IC MINDT 2013, Athens, Greece, art. no P.10.5, CD ROM.

6. S. Sfarra, N.P. Avdelidis, C. Ibarra-Castanedo, P. Theodorakeas, A. Bendada, D. Paoletti, M. Koui, X.P.V. Maldague (2013). *A promising method for the detection of subsurface defects in impacted composites materials made of natural fibres*. In Proc. of 9th International Conference on Composite Science and Technology -ICCST9, Sorrento, Italy, CD ROM.

7. E. Cheilakou, P. Theodorakeas, M. Koui, S. Moustakidis, C. Zeris (2012). *Application of Ground Penetrating Radar as a diagnostic technique in concrete bridges inspection.* In Proc. of 42nd International Conference and NDT Exhibition NDE for Safety 2012 / Defektoskopie 2012, Sec, Czech Republic, pp. 107- 114.

8. P. Theodorakeas, N.P. Avdelidis, K. Hrissagis, C. Ibarra-Castanedo, M. Koui, X. Maldague (2011). *Automated transient thermography for the inspection of CFRP structures: experimental results and developed procedures.* In Proc. of SPIE- The International Society

for Optical Engineering, Thermosense XXXIII, Orlando, Florida, Vol. 8013, pp. 8013W1-11.

9. S. Sfarra, P. Theodorakeas, C. Ibarra-Castanedo, N. P. Avdelidis, A. Paoletti, D. Paoletti, K. Hrissagis, A. Bendada, M. Koui, X. Maldague(2011). *Importance of integrated results of different non-destructive techniques in order to evaluate defects in panel paintings: the contribution of infrared, optical and ultrasonic techniques*. In Proc. of SPIE- The International Society for Optical Engineering, Optical Metrology Conference 8084, Münich, Germany, Vol. 8084, art no. 80840R.

10. S. Sfarra, C. Ibarra-Castanedo, P. Theodorakeas, N.P. Avdelidis, A. Paoletti, D. Paoletti, K. Hrissagis, A. Bendada, M. Koui, X. Maldague (2011). *Holographic Interferometry (HI), Active Infrared Thermography (IRT) and Ultrasound Testing (UT) for the nondestructive assessment of esteemed hand-painted ceramic sample panels*. In Proc. of the 6th International Workshop "NDT in progress 2011", Prague, Czech Republic, CD ROM.

11. S. Sfarra, P. Huke, P. Theodorakeas, D. Paoletti,N. P. Avdelidis, D. Ambrosini, R. Klattenhoff, M. Koui, R. B. Bergmann (2011). *Non-Destructive Testing (NDT) Methods used for the Study of Stone Frescoes.* In Proc. of the 6th International Workshop "NDT in progress 2011", Prague, Czech Republic, CD ROM.

12. N.P. Avdelidis, C. Ibarra-Castanedo, P. Theodorakeas, A. Bendada, E. Saarimaki, T. Kauppinen, M. Koui, X.P.V. Maldague (2010). *NDT characterisation of carbon-fibre and glass-fibre composites using non-invasive imaging techniques*. In Proc. of the 10th Quantitative Infrared Thermography Conference (QIRT), Quebec City, Canada, pp. 703-710.

13. N.P. Avdelidis, E. Saarimäki, T. Kauppinen P. Theodorakeas, A. Tati, E. Cheilakou, S. Fanou, M. Koui, C. Ennaceur (2010). *LWIR and MWIR thermography tools for composites assessment.* In proc. of SPIE- The International Society for Optical Engineering, Orlando, Florida, Thermosense XXXII, Vol. 7661, pp.76610P1-11.

14. P. Theodorakeas , N.P. Avdelidis, M. Koui, C. Ibarra – Castanedo , E. Cheilakou, A. Bendada, K. Ftikou ,X.P.V. Maldague (2010). *Active thermographic NDT approaches for the assessment of plastered mosaics*. In Proc. of the 8th International Symposium on the Conservation of Monuments in the Mediterranean Basin- MONUBASIN8, Patras, Greece, Vol. 2, pp. 442-456.

15. E. Cheilakou, P. Papandreopoulos, P. Theodorakeas, N.P. Avdelidis, D. Sideris, M. Koui (2010). *The ancient theatre of Sikyon: Preliminary Studies on the structural materials and the decay patterns – proposals for prompt protection*. In Proc. of the 8th International Symposium on the Conservation of Monuments in the Mediterranean Basin- MONUBASIN8, Patras, Greece, Vol. 1, pp.129-148.

16. E. Ftikou, E. Cheilakou P. Theodorakeas, N.P. Avdelidis, K. Roumpopoulos, M. Koui (2010).

The Mycenaean tomb 'Treasury of Minyas': Conservation problems and evaluation of deterioration phenomena.. In Proc. of the 8th International Symposium on the Conservation of Monuments in the Mediterranean Basin- MONUBASIN8, Patras, Greece, Vol.1, pp 207-222.

17. P. Theodorakeas M. Koui, (2010). *Conservation procedures for the reburials of mosaic pavements: A review of materials and techniques.* In Proc. of the 8th International Symposium on the Conservation of Monuments in the Mediterranean Basin -MONUBASIN8, Patras, Greece, Vol. 3, pp. 589- 604.